

DYNAMICS AND STRUCTURE
FROM
MOLECULAR BEAM EXPERIMENTS

A thesis submitted to
The Australian National University
for the degree of Doctor of Philosophy

Peter Frederic Vohralík

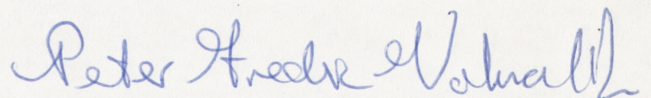
March 1986



STATEMENT

Except where acknowledgements are made in the text and in the present statement the candidate was responsible for all of the work reported in this thesis.

The spectra reported in Figure 6.2 and Sections 6.5 and 6.6 were measured by Dr G. Fischer and Dr R.E. Miller.



Peter Frederic Vohralík

Canberra, March 4, 1986.

"And hast thou slain the Jabberwock?

Come to my arms, my beamish boy!

O frabjous day! Callooh! Callay!"

He chortled in his joy.

Acknowledgements

I wish to thank my supervisor Dr R.O. Watts for his constant encouragement and expert supervision. It was a pleasure working with him.

I would also like to thank Dr R.E. Miller for numerous discussions and many helpful suggestions.

I am grateful to Dr R.W. Crompton and the members of the Electron and Ion Diffusion Unit, the Research School of Physical Sciences, for giving me the opportunity to study at the Australian National University. Thanks also go to the following for their assistance and encouragement during my stay at the Australian National University: Dr J. Reimers, Dr D.F. Coker, Mr G. Bryant, Mr F. Claremont, Dr M.T. Elford, Mr C.V. Boughton and Mr L. Mitchell.

I would like to thank Prof. K. Takayanagi and Prof. M.H. Alexander for providing the results of their calculations prior to publication.

Special thanks go to the technical staff of the Electron and Ion Diffusion Unit and to the members of the Electronics Unit for their valuable support. The assistance of the programmers and operators of the Computer Services Centre is also gratefully acknowledged. For help with the typing of this manuscript I am indebted to Mrs A. Duncanson and Mrs L. Robins.

Financial support from a Commonwealth Postgraduate Research Award is gratefully acknowledged.

I wish to thank all of my friends for their support and encouragement and for making my stay in Canberra a pleasant one.

Finally, I thank my parents, my brother and my sister-in-law for their friendship and understanding during the course of this work.

Abstract

Molecular beam scattering methods and laser-bolometer spectroscopic techniques were used to investigate the dynamical behaviour of a number of atom-molecule and molecule-molecule systems. Extensive scattering calculations were carried out for both He-HF and Ar-HF in order to assess the ability of available intermolecular potential functions to predict the measured total scattering intensities. The coupled states approximation was used to study the inelastic integral and differential cross sections for these systems. Total differential cross sections for He-HF scattering are adequately described using the spherical part of the interaction potential. This is not the case for Ar-HF, for which the anisotropies in the potential play a major role in determining the scattering behaviour.

A colour centre laser was used in conjunction with molecular beam techniques to measure the infrared spectra of small clusters of acetylene, methyl acetylene and ethylene. By recording spectra for a wide range of molecular beam conditions it was possible to assess the contributions to the observed spectra from the different cluster sizes present in the beams. Infrared cluster dissociation spectra were studied under both low resolution (0.4 cm^{-1}) and high resolution (0.0001 cm^{-1}). Lifetimes of the initially excited clusters determined from the homogeneous widths of the individual rovibrational transitions range from 1 ps for ethylene to $>80 \text{ ns}$ for acetylene.

A combination of spectroscopic and scattering techniques was used to investigate the transfer of rotational energy between HF molecules in the ground vibrational state. Resonant rotational energy transfer

processes which are dipole allowed to first order were found to dominate the observed scattering. A lower bound of 310 \AA^2 was obtained for the $j_1=0, j_2=1 \rightarrow j_1=1, j_2=0$ cross section.

The work described in this thesis has been reported in several publications:

Miller R.E., Vohralík P.F. and Watts R.O. (1984), "Sub-Doppler resolution infrared spectroscopy of the acetylene dimer: A direct measurement of the predissociation lifetime", J. Chem. Phys. 80, 5453.

Fischer G., Miller R.E., Vohralík P.F. and Watts R.O. (1985), "Molecular beam infrared spectra of dimers formed from acetylene, methyl acetylene, and ethene as a function of source pressure and concentration", J. Chem. Phys. 83, 1471.

Vohralík P.F. and Miller R.E. (1985), "Resonant rotational energy transfer in HF", J. Chem. Phys. 83, 1609.

Boughton C.V., Miller R.E., Vohralík P.F. and Watts R.O. (1986), "The helium-hydrogen fluoride differential scattering cross section", accepted for publication in Molecular Physics.

An additional manuscript describing the work reported in Chapter 5 is being prepared.

TABLE OF CONTENTS

STATEMENT		(ii)
ACKNOWLEDGEMENTS		(iv)
ABSTRACT		(v)
TABLE OF CONTENTS		(vii)
TABLE AND FIGURE CAPTIONS		(xi)
<u>CHAPTER 1</u>	Introduction	1
<u>CHAPTER 2</u>	EXPERIMENTAL TECHNIQUES	6
2.1	The Beam Chamber	7
2.2	Phase Sensitive Detection	9
2.3	The Quadrupole Mass Spectrometer	10
2.4	Bolometric Detection	11
2.5	The Colour Centre Laser	15
	(a) Low Resolution Scanning	16
	(b) High Resolution Scanning	17
	(c) Frequency Stabilized Operation	19
2.6	Quantum State Distributions in Molecular Beams	25
2.7	Differential Scattering Cross Section Measurements	27
2.8	Time-of-Flight Measurements	29

<u>CHAPTER 3</u>	SCATTERING CALCULATIONS	34
3.1	Introduction	35
3.2	Atom-Diatom Scattering	41
3.3	The Spherical Potential Approximation	49
3.4	The Infinite Order Sudden Approximation	50
3.5	The Coupled States Approximation	52
3.6	The Matrix Elements of the Potential	56
3.7	Solution of the Coupled States Equations	58
3.8	On the Comparison Between Theory and Experiment	61
<u>CHAPTER 4</u>	HELIUM-HYDROGEN FLUORIDE SCATTERING CROSS SECTIONS	68
4.1	Introduction	69
4.2	Experimental Results	77
4.3	The He-HF Interaction Potential	79
4.4	A Comparison between the Present Coupled States Calculations and Previous Close Coupled Results	82
4.5	A Comparison between Coupled States, IOS and Spherical Potential Calculations	85
4.6	Inelastic Cross Sections within the Coupled States Approximation	88
4.7	Comparing Theory with Experiment	93
4.8	Conclusions	99

<u>CHAPTER 5</u>	ARGON-HYDROGEN FLUORIDE SCATTERING CROSS SECTIONS	100
5.1	Introduction	101
5.2	Experimental Results	109
5.3	The Ar-HF Interaction Potential	112
5.4	A Comparison between Spherical Potential, Infinite Order Sudden and Coupled States Calculations	115
5.5	Comparing Theory with Experiment	122
5.6	State-to-state Cross Sections within the Coupled States Approximation	125
5.7	Partial Integral Cross Sections	130
5.8	Conclusions	136
<u>CHAPTER 6</u>	INFRARED SPECTROSCOPY OF SMALL CLUSTERS OF ACETYLENE, METHYL ACETYLENE AND ETHYLENE	138
6.1	Introduction	139
6.2	Monomer Spectroscopy	148
6.3	Experimental	150
6.4	Acetylene Clusters	154
6.4.1	Large Clusters of Acetylene	154
6.4.2	High Resolution Spectroscopy of Small Clusters of Acetylene	158
6.4.3	Pressure Dependence of the Spectra of Small Acetylene Clusters	166
6.5	Methyl Acetylene Clusters	173
6.6	Ethylene Clusters	176
6.7	Summary and Conclusions	178

<u>CHAPTER 7</u>	RESONANT ROTATIONAL ENERGY TRANSFER IN HF	181
7.1	Introduction	182
7.2	Experimental	189
7.3	Results	194
7.4	Kinetic Model	199
7.5	Analysis and Discussion	202
7.6	Conclusions	212
<u>CHAPTER 8</u>	SUMMARY AND CONCLUSIONS	213

REFERENCES

Table 2.1 Operating point parameters for bolometer B corresponding to the I-V characteristics (labelled A through H) shown in Figures 2.7 and 2.8. The data labelled C through H were obtained under conditions similar to those existing when the spectroscopic studies reported in this thesis were carried out and the pressures P are typical 310 K helium beam stagnation pressures corresponding to these data. (I_0, V_0) is the operating point and S_0 is the zero frequency responsivity.

13b

Table 2.2 Frequency response characteristics of some of the components of the laser system. FSR = free spectral range and FWHM = full width at half maximum of the response profile.

17b

Table 2.3 Parameters describing the geometry of the experimental arrangement used to obtain the total differential scattering cross sections (see Figure 2.18).

27b

Table 2.4 Parameters of the velocity distributions obtained from the analysis of the measured time-of-flight spectra. T_0 is the nozzle temperature; v_s and v_w are the stream velocity and width parameter; v_{mp} is the most probable velocity of the v^3 maxwellian distribution; Δv is the FWHM of this distribution; T' is the nozzle temperature corresponding to the stream velocity if one assumes an ideal isentropic expansion (see Eqs. (2.13) and (2.14)); and E is the mean kinetic energy of the atoms/molecules in the beam.

32c

Table 2.5 Mean collision energies for a number of beam-beam and beam - (300 K Boltzmann gas) combinations. The results in the upper part of the

table are all for beams of pure gases. '(Boltz)' indicates that the results are for a Boltzmann distribution of velocities. The velocity distributions used for the beams are those given in Table 2.4. Apart from the HF and He(80K) beams, the nozzles used to form the expansions were maintained at 310 K. See the text for more details.

Figure 2.1 A schematic diagram of the crossed molecular beam apparatus. In the elevation view A and B denote the far and near cryostat positions, C is the molecular beam chopper, F is the molecular beam flag, N is the nozzle, S is the skimmer and A.T. is the alignment telescope. In the plan view, B is the bolometer, PBC is the primary beam chamber and SBC is the secondary beam chamber.

7a

Figure 2.2 Details of the nozzle and skimmer geometries. The outside diameter of the nozzle is 1/4". Region A contains the gas of interest at the stagnation pressure P_0 and temperature T_0 . The supersonic expansion takes place in region B, and region C is the main scattering chamber. $\alpha = 60^\circ$ or 90° ; the nozzle diameter d is usually in the range 30-80 μm ; the skimmer diameter D is generally between 200 and 600 μm ; and β and γ are 26° and 30° respectively.

7b

Figure 2.3 A schematic diagram of the bolometer cryostat assembly. 11a

Figure 2.4 The circuit used to operate the bolometer detector. 12a

Figure 2.5 The circuit used to measure the I-V characteristics (ie. load curves) of the bolometer. 12b

Figure 2.6 I-V characteristic for bolometer A. $(I_0, V_0) = (0.69 \mu\text{A}, 5.33 \text{V})$ is the operating point defined by the load line shown and $V_a = 3.15 \text{V}$. The load line is given by $V(V) = 8.8 - 5xI(\mu\text{A})$. 12c

Figure 2.7 I-V characteristic for bolometer B as supplied by Infrared

Laboratories. The operating point defined by the load line shown [$V(V) = 8.8 - 5xI(\mu A)$] is (1.58 μA , 0.90 V) and the V-intercept of the tangent to the load curve at the operating point is $V_a = 0.755$ V.

12d

Figure 2.8 I-V characteristics for bolometer B as a function of the heat flux reaching the bolometer. Curves B and C were measured in the absence of direct molecular beam flux reaching the detector (although the background radiation and molecular fluxes were almost certainly not the same). Characteristics D through H show the changes resulting from increasing the flux of the helium beam used to heat the detector. Also shown are the zero frequency responsivities (in V/mW) at the operating points determined by the load line [$V(V) = 8.8 - 5xI(\mu A)$]. The operating points are given in Table (2.1).

13a

Figure 2.9 Changes in the output of the bolometer B - LIA detection system (for a small, chopped IR signal of unvarying amplitude) as a function of the helium beam gas load reaching the bolometer.

14a

Figure 2.10 A comparison between the measured response of the bolometer B -LIA detection system and the predicted responsivity of bolometer B obtained from the I-V characteristics as a function of the voltage at the operating point. The shapes of the response profiles are similar, indicating that, as expected, the overall response of the bolometer-LIA system is determined by the response of the bolometer.

14b

Figure 2.11 A simplified energy level diagram of an $F_A(II)$ colour centre

(adapted from Mollenauer (1985)).

15a

Figure 2.12 A schematic diagram of the FCL cavity.

16a

Figure 2.13 An illustration of the frequency response profiles of the FCL cavity, the intracavity etalon and the cavity grating. The response profiles are not drawn to the same scale.

17a

Figure 2.14 The experimental setup used to obtain high resolution IR - molecular beam spectra with the FCL. D1 and D2 are IR detector/amplifier units and LIA1 and LIA2 are lock-in amplifiers.

18a

Figure 2.15 Experimental arrangement used to obtain feedback stabilised single frequency operation with the FCL. D1 and D2 are IR detector /amplifier units and LIA1 and LIA2 are lock-in amplifiers.

20a

Figure 2.16 Gas cell absorption profiles as observed on CO_2 .

21a

Figure 2.17 Curves A and B are the frequency response profiles of the 150 MHz etalon transmission signal at the extremities of the 600 Hz oscillation applied to it. The lower curve is the output of the LIA which is used as the feedback signal.

22a

Figure 2.18 A schematic diagram of the experimental arrangement used to measure total differential scattering cross sections. N1 and N2 are the nozzles; S1, S1' and S2 are the skimmers; C is the rotating secondary beam chopper; F is the primary beam flag; SC is the scattering centre; B is the

bolometer; and A1 and A2 are the apertures in the bolometer cryostat shields. Values of the parameters describing the geometry appear in Table 2.3.

27a

Figure 2.19 A schematic diagram of the experimental setup used to obtain the time-of-flight distributions of the molecules in the beams. E is the electron ionization region; A represents the field used to inject the positive ions into the quadrupole region Q; and D is the multi-dynode ion detector.

29a

Figure 2.20 Corrected experimental TOF distributions (dots) for the gases studied. The solid curves are the fitted TOF distributions discussed in the text.

32a

Figure 2.21 v^3 maxwellian distributions corresponding to the TOF distributions given in Figure 2.20. They have been normalized to have the same area.

32b

Table 3.1 The equations required to effect the angle transformation from the centre of mass reference frame to the laboratory reference frame.

62a

Figure 3.1 An illustration of the coordinates used to describe the atom-diatom collision problem.

41a

Figure 3.2 Newton diagram for in-plane scattering.

61a

Figure 3.3 Variables used to account for the detector geometry.

64a

Figure 3.4 An illustration of the technique used to account for the divergence of the primary beam.

66a

Table 4.1 Measured scattering intensities for the He-HF system as a function of the laboratory scattering angle (in degrees). Results are shown for two mean collision energies corresponding to different primary (helium) beam conditions. The numbers in parentheses represent two standard deviations in the scatter of values obtained at the corresponding angles. "(-)" indicates that only two measurements were made at the corresponding angle.

77a

Table 4.2 Experimental conditions used to obtain the differential scattering intensities reported in this chapter. The velocity fitting parameters v_s , v_w and v_{mp} have estimated uncertainties of $\pm 0.5\%$. These velocity parameters, which were reported in Chapter 2, are duplicated here for convenience.

77b

Table 4.3 Energies (E_j) and asymptotic wavevectors (k_j) and wavelengths (λ_j) for the basis set used in the CS calculations at a total energy of 313 K.

82a

Table 4.4 Centre of mass frame integral cross sections for He-HF at a total energy of 313 K obtained using the rigid rotor and vibration dependent HFD1 potentials. The close coupled results are those of Battaglia et al. (1984b). Details of the CS calculations are given in the text. The cross sections are in square Ångstroms.

82a

Table 4.5 Total integral cross sections obtained using the CS, IOS, spherical potential (quantum) and spherical potential (WKB) approximations.

87b

Table 4.6 Energies (E_j) and asymptotic wavevectors (k_j) and wavelengths (λ_j) for the basis sets used in the CS calculations at a collision energy of 480 K.

88c

Table 4.7 Energies (E_j) and asymptotic wavevectors (k_j) and wavelengths (λ_j) for the basis sets used in the CS calculations at a collision energy of 950 K.

88d

Table 4.8 (a) Centre of mass frame integral cross sections for He-HF scattering obtained using the vibration dependent HFD1 potential and the CS approximation for a collision energy of 480 K. The cross sections are in square Ångstroms.

(b) The results in this table were obtained by multiplying the cross sections shown in Table 4.8a by the populations of their initial j states in the HF beam. They are expressed as percentages of the total population weighted cross section.

89a

Table 4.9 (a) and (b) As for Table 4.8a, except these results are for a collision energy of 950 K.

89b

Table 4.10 Contributions to the total differential cross section from both the sum of all inelastic processes and selected individual inelastic transitions at a collision energy of 950 K. In the second, third and fourth columns are given the percentage contributions at the first three minima of the total differential cross section. The last column gives these percentage contributions at a laboratory scattering angle of 32 degrees. All the cross sections have been weighted by the relevant HF

rotational state populations.

90a

Table 4.11 Properties of the spherical terms of the potential surfaces used to analyse the experimental He-HF scattering data. σ is the value of r for which $V(r)=0$, r_m is the position of the minimum in the potential, ϵ is the well depth and $\Delta r_{\frac{1}{2}}$ is the width of the attractive part of the potential at half its maximum depth. S(516) and S(990) are the fitting parameters, defined by Eq. (3.72) at the two experimental collision energies. The smaller the value of S, the better the fit.

BFW is the Barker potential discussed in the text.

HFD2-A is the HFD2 model with the spherical C_6 term increased by 24 %.

HFD2-B is the HFD2 model with the spherical C_6 term increased by 18 % and all other dispersion coefficients recalculated using the method discussed by Rodwell *et al.* (1982).

HFD1-A is the HFD1 model with the spherical C_6 term increased by 18 %.

HFD- ρ is the HFD1 model with the value of ρ (see Eq. (4.4)) increased by 11 %.

94a

Table 4.12 Parameters of the Barker potential (BFW) used to represent the spherical part of the He-HF interaction.

96a

Figure 4.1 He-Ar total differential scattering cross section. Experimental points are represented as diamonds and the solid curve is calculated using the potential of Aziz et al. (1979). The value of the fitting parameter S given by Eq. (3.72) is 2.8×10^{-3} . 78a

Figure 4.2 Cross sections through the HFD1 potential reported by Rodwell et al. (1982) for different values of the potential angle. These cross sections are for the full potential, which depends upon the HF separation. The HF bond length was fixed at its equilibrium value. 80a

Figure 4.3 A comparison between the close coupled results of Battaglia et al. (1984b) and the present CS results for He-HF scattering at a total energy of 313 K. The CC results (-----) are for the rigid rotor HFD1 potential. The CS cross sections (————) for the same potential appear on the left half of the figure and those for the vibration dependent HFD1 potential are shown on the right. 82b

Figure 4.4 Total differential scattering cross sections for He-HF predicted by the HFD1 potential using the CS method (————), the IOS approximation (.....), an exact single channel calculation with the spherical part of the potential (-----) and a single channel WKB computation with the same spherical potential (— — — —). 86a

Figure 4.5 An enlargement of part of Figure 4.4. In this figure the spherical potential semiclassical results have been omitted. 87a

Figure 4.6 The Newton diagram for the collision geometry used in the CS calculations at a kinetic energy of 480 K. See the text for details. 88a

Figure 4.7 The Newton diagram for the collision geometry used in the CS calculations at a kinetic energy of 950 K. See the text for details. 88b

Figure 4.8 Population weighted differential scattering cross sections calculated from the full HFD1 potential using the CS method at collision energies corresponding to the mean experimental energies. Notice that whereas Figure 4.3 shows cross sections calculated at the same total energy, in this figure the collision energies are fixed. No averaging over experimental parameters has been done. See the text for details. 89c

Figure 4.9 A comparison between the experimental total differential cross sections (diamonds) and those obtained from a number of different potential surfaces using spherical potential approximation and semiclassical techniques. 93a

Figure 4.10 The spherical potential functions used to obtain the theoretical cross sections shown in Figure 4.9. 96b

Table 5.1 Measured scattering intensities for the Ar-HF system as a function of the laboratory scattering angle (in degrees). Estimates of the uncertainties associated with the reported intensities are given for a few of the scattering angles. See the text for a discussion of these estimates. The experimental conditions are summarised in Table 5.2.

109a

Table 5.2 Experimental conditions used to obtain the differential scattering intensities reported in Table 5.1. The velocity fitting parameters v_s , v_w and v_{mp} have estimated uncertainties of $\pm 0.5\%$. These velocity parameters, which were reported in Chapter 2, are duplicated here for convenience.

109b

Table 5.3 Equations and parameters defining the M5 potential.

112a

Table 5.4 Energies (E_j) and asymptotic wavevectors (k_j) and wavelengths (λ_j) for the basis set used in the coupled states calculations.

116a

Table 5.5 Total integral cross sections computed using the spherical potential, infinite order sudden and coupled states approximations. The coupled states results were obtained summing the population weighted state-to-state cross sections. Upper figures were obtained by summing values of 1 from 0 to 220. The lower values were determined by summing values of 1 from 0 to 300.

117e

Table 5.6 Integral cross sections calculated using the spherical potentials obtained by fixing the potential angle γ for the three potentials. By multiplying the cross sections by the weights given in the

table and summing these weighted values one obtains the corresponding IOS integral cross sections. 119a

Table 5.7 Coupled states integral cross sections for the three potentials considered in this study. The summed cross sections for scattering from the given initial HF rotational states are also given. 128a

Figure 5.1 Typical classical trajectories in the centre-of-mass frame for the scattering resulting from an interaction with a strong attractive part. The circle gives an indication of the size of the repulsive core of the potential.

101a

Figure 5.2 Sections of the ArHF-HFD1 potential for fixed values of the potential angle. Note that the vertical scale is logarithmic for energies greater than 50 K. The dashed curve is the spherical average of the interaction potential.

112b

Figure 5.3 The same as Figure 5.2, except for the ArHF-HFD2 potential.

112c

Figure 5.4 The same as Figure 5.2, except for the M5 potential.

112d

Figure 5.5 The Newton diagram for the collision geometry used in the coupled states and some of the other calculations. The final velocity vectors for the 0→1 and 1→0 transitions terminate on the labelled curves.

117a

Figure 5.6 A comparison between the total differential scattering intensities calculated using the spherical potential (— — —), infinite order sudden (— — —) and coupled states (————) approximations. These results were obtained from Eq. (3.59) (in Å² per steradian), and have been multiplied by $\sin\theta.\theta^{4/3}$. They have also been smoothed out using a 2 degree angular window to damp the diffraction oscillations. The coupled states state-to-state cross sections were weighted by the populations of the initial rotational states and added to give the results shown in the figure.

117b

Figure 5.7 As for Figure 5.6, except for the ArHF-HFD2 potential. 117c

Figure 5.8 The same as Figure 5.6, except for the M5 potential. 117d

Figure 5.9 In this figure we show the total population weighted differential cross section for the ArHF-HFD2 potential obtained using the coupled states approximation. The results in the upper half of the figure have been multiplied by $\sin\theta.\theta^{4/3}$, and those in the lower half have not. Neither of the cross sections were angle averaged in order to smooth out the diffraction oscillations.

118a

Figure 5.10 The partial IOS cross sections are shown, as a function of the potential angle γ , for the three potentials considered in this study. These integral cross sections were obtained from JWKB and Born phase shifts for the (spherical) potentials determined from the full potentials by fixing the potential angle.

119b

Figure 5.11 A comparison between the velocity averaged IOS cross section (for the case of right angle collisions) and the single energy IOS cross section for the ArHF-HFD2 potential. These cross sections are shown as solid curves. The diffraction oscillations of the averaged cross section are almost completely damped out, whereas the shape of the rainbow oscillation have not been affected. All of the cross sections shown in this figure have been smoothed out using a two degree angular window. The solid curves were obtained using the velocity distributions given in Table 5.2. The dashed curve shows a single energy IOS cross section (for the same potential) obtained for the velocities used in the coupled states

calculations, which differ slightly from the most probable experimentally determined velocities. 122a

Figure 5.12 A comparison between the population weighted coupled states cross sections for the ArHF-HFD1 (— — —), ArHF-HFD2 (- - -) and M5 (————) potentials and the experimentally determined scattering intensities (diamonds). The uncertainties associated with experimental points for angles less than 10 degrees are smaller than the diamonds. Error bars corresponding to the estimated uncertainties (given in Table 5.1 and discussed in the text) are shown to scale in the lower part of the diagram at a number of angles. 123a

Figure 5.13 As for Figure 5.12, except this time the factor $\sin\theta.\theta^{4/3}$ was not used to weight the scattered intensities. 123b

Figure 5.14 Inelastic state-to-state differential scattering cross sections for the ArHF-HFD1 potential calculated using the coupled states approximation. They have been weighted by the measured HF rotational populations, multiplied by $\sin\theta.\theta^{4/3}$, and angle averaged using a two degree window. The three solid curves (from top to bottom) are the total cross section, the sum of the elastic cross sections, and the sum of the inelastic cross sections. The dashed curves, in order of increasing dash length, correspond to the 0→1, 1→0, 1→2, 0→2 and 2→3 transitions. 125a

Figure 5.15 As for Figure 5.14, except for the ArHF-HFD2 potential. 125b

Figure 5.16 The same as Figure 5.14, but this time for the M5 potential. 125c

Figure 5.17 This is Figure 5.16 without the $\sin\theta.\theta^{4/3}$ weighting. 125d

Figure 5.18 Total scattering cross sections for initial HF rotational states $j=0,1,2$ and 3 calculated using the coupled states approximation for the ArHF-HFD1 potential. The four pairs of solid curves (from top to bottom) are the total $j \rightarrow \sum j'$ and elastic $j \rightarrow j$ cross sections for $j=0,1,2$ and 3 respectively. Results have been population weighted, averaged using a 2 degree window and multiplied by $\sin\theta.\theta^{4/3}$. The $0 \rightarrow 0$ and $0 \rightarrow \sum j'$ curves have been moved up half a decade for clarity. The un-shifted $0 \rightarrow \sum j'$ cross section is also shown (the dashed curve) so that its magnitude can be compared with the other population weighted results. 126a

Figure 5.19 The same as Figure 5.18, except this time for the ArHF-HFD2 potential. 126b

Figure 5.20 As for Figure 5.18, except for the M5 potential. 126c

Figure 5.21 Opacity functions for the $0 \rightarrow j$ (upper half of figure) and $1 \rightarrow j$ (lower half of figure) state-to-state cross sections calculated using the coupled states approximation for ArHF-HFD1 potential. The elastic opacities are the largest curves in both cases. The double peaked curves which attain their maxima near $l=100$ are the $0 \rightarrow 1$ and $1 \rightarrow 0$ opacity functions. Opacity functions for the $j \rightarrow 2$, $j \rightarrow 3$ and $j \rightarrow 4$ transitions define areas of decreasing magnitude above the l -axis. These results have not been weighted by the measured rotational populations. The areas under these curves give the corresponding integral cross sections. 130a

Figure 5.22 As for Figure 5.21, except for the ArHF-HFD2 potential. 130b

Figure 5.23 The same as Figure 5.21, but this time for the M5 potential. 130c

Figure 5.24 In the lower half of this figure are shown the opacities calculated using the spherical potential approximation for the ArHF-HFD2 potential. The collision speeds used are those which were used for the coupled states calculations. Differential cross sections obtained by summing values of l from 0 to 85, 110 and 300 appear in the upper half of the figure. See the text for more details. 132a

Figure 5.25 Opacity functions for the ArHF-HFD2 integral cross sections given in Table 5.6. Curves labelled (a) through (h) correspond to potential angles of 84.5, 73.6, 63.3, 51.8, 41.0, 30.0, 19.1 and 8.5 degrees respectively. 133a

Table 6.1 Monomer transitions for acetylene, methyl acetylene and ethylene in the range 3000 to 3300 cm^{-1} . The centre frequencies of the cluster absorptions for ethylene are taken from Fischer et al. (1983). Those for methyl acetylene are from Figures 6.18 and 6.19 of this thesis. The frequencies of the acetylene cluster bands are given in Table 6.2. "inactive" denotes that the band is infrared inactive in the monomer. The monomer data are taken from the paper by Fischer et al. (1983) and the tables of Shimanouchi (1972).

148a

Table 6.2 A summary of the full widths at half maximum of the homogeneous components of the individual rovibrational transitions observed in each of the six cluster dissociation bands of acetylene. The results were obtained by convoluting the monomer lineshapes with Lorentzians to fit the cluster absorption profiles.

165b

Table 6.3 The slopes of the $\log(\text{signal})$ vs $\log(\text{source pressure})$ plots for the intensities of the infrared signals observed for the low resolution acetylene cluster spectra shown in Figure 6.13. Cluster sizes suggested by these slopes are also given.

169c

Figure 6.1 A schematic of the beam apparatus showing the position of the multipass mirrors and the bolometer as used to measure the infrared spectra reported in this chapter. See the caption to Figure 2.1.

151a

Figure 6.2 A series of low resolution predissociation spectra obtained for an 11% mixture of acetylene in helium measured using bolometer A. Spectra are plotted in arbitrary units with a positive signal representing a decrease in the energy of the molecular beam. The source pressures used (in kPa) were: A 480, B 685, C 800, D 915, E 1100, F 1240, G 1490, H 1680, and I 1890. The arrows labelled A and B are the positions of the Fermi shifted monomer absorptions for the $\nu_2+\nu_4^1+\nu_5^1$ and ν_3 bands of acetylene respectively. The arrow marked SOLID indicates the absorption frequency of solid acetylene (Bottger and Eggers (1964)).

154a

Figure 6.3 Log(signal) vs log(source pressure) plots of the mass signals seen near the acetylene monomer, dimer and trimer masses for beams formed from a mixture of 11% acetylene in helium. The symbols represent the experimental points. Lines of best fit are also shown. Slopes of the lines of best fit are 0.5, 2.4 and 6.0 respectively. See the text for more details.

155a

Figure 6.4 Log(signal) vs log(pressure) plots for the three mass peaks seen near the dimer mass for the 11% acetylene in helium mixture. Slopes of the lines of best fit are 1.5, 1.7 and 4.2 for the mass peaks observed at 49, 50 and 51 amu respectively.

156a

Figure 6.5 The concentration and source pressure dependence of the low resolution spectrum of acetylene clusters. The upper spectra were measured using bolometer A. Bolometer B was used to record the lowest scan. Note that the top scan is that spectrum labelled A in Figure 6.2. Under the conditions used to obtain these spectra the dimer, and possibly trimer, were the only clusters present.

156b

Figure 6.6 The concentration and source pressure dependence of the low resolution spectrum of acetylene clusters measured using bolometer B. See the text for more details.

157a

Figure 6.7 A low resolution spectrum of a 1% acetylene in helium mixture at a source pressure of 1160 kPa. High resolution (single mode) scans from each band are shown as inserts with the frequency scales expanded by a factor of 155. A series of etalon transmission peaks separated by 150 MHz and a monomer absorption, plotted using the same frequency scale as the other inserts, are shown in insert G. All the high resolution scans were obtained using multiple near orthogonal laser - molecular beam crossings. The spectra are plotted so that a laser induced decrease in the molecular beam energy is seen as an upward going transition.

158a

Figure 6.8 A composite high resolution scan of about 0.4 cm^{-1} from acetylene cluster band D. The downward going spikes are attributed to monomer absorptions. Eleven single high resolution scans were required to piece together this portion of the spectrum of band D. The upper trace shows frequency markers separated by 150 MHz. Wavelength increases from left to right.

160a

Figure 6.9 An example of the convolution technique used to obtain the homogeneous broadening component of the cluster absorption lineshapes. Two Gaussians were used to fit the Doppler broadened monomer lineshape shown. The fitted monomer profile was then convoluted with a Lorentzian to obtain the fit to the cluster absorption, shown as the upper trace. Solid curves represent the experimental data and broken curves are the fitted lineshapes. The results were obtained using multiple near orthogonal laser - molecular beam crossings.

165a

Figure 6.10 Monomer and dimer spectra obtained using a single orthogonal laser - molecular beam crossing. The full width at half maximum of the monomer transition is 4 MHz.

166a

Figure 6.11 A mass spectrum of the 1% acetylene in helium mixture obtained at a source pressure of 1100 kPa. The energy of the ionizing electrons was set at 30 eV. The mass scale shown corresponds to the mass readout of the mass spectrometer.

167a

Figure 6.12 Source pressure dependence of the mass peaks shown in Figure 6.11. The slopes of these curves at the low pressure limit are 0.83, 2.8, 2.8 and 4.35 for the mass 25, 49, 50 and 51 signals respectively.

167b

Figure 6.13 Source pressure dependence of the low resolution spectrum of the 1% acetylene in helium mixture. The vertical scales for the individual spectra have been adjusted for clarity.

168a

Figure 6.14 Log(signal) vs log(pressure) data for the intensities of the cluster absorption bands shown in Figure 6.13. In this figure the experimental data have been joined by straight line segments. 169a

Figure 6.15 As for Figure 6.14, except this figure gives the best least squares linear fits to the data. For bands A and B the lowest pressure datum was not used in the fit. 169b

Figure 6.16 Low resolution spectra for a 2.5% methyl acetylene in helium mixture at various source pressures. 173a

Figure 6.17 Low resolution spectra for a 1% methyl acetylene in helium mixture at various source pressures. Note the change in the frequency scale from Figure 6.16. At the lowest pressure the dimer, and possibly trimer, would have been the only clusters present. 173b

Figure 6.18 A low resolution infrared spectrum of small methyl acetylene clusters near 3300 cm^{-1} . Note the change in the frequency scale from Figure 6.17. 174a

Figure 6.19 A single mode scan of a portion of band A_2 of the methyl acetylene spectrum. The frequency scale was calibrated using a 150 MHz free spectral range confocal etalon. The experimental points are shown as dots. The solid curve is a best least squares fit to the data using three independent Lorentzians. 174b

Figure 6.20 The concentration and source pressure dependence of the low resolution spectrum of ethylene clusters. The upper spectrum was obtained using bolometer A, and the lower ones were measured with bolometer B. Vertical scales for the spectra are not the same.

Table 7.1 Parameters describing various beam-beam and beam-gas collisions. HF(beam) refers to a pure HF secondary beam supersonic expansion at a nozzle temperature of about 500 K. HF(boltz) denotes a gaseous sample of HF at a temperature of 300 K. He, HF/He, and HF/Ar refer to supersonic expansions of pure He, 1% HF in He and 2% HF in Ar at nozzle temperatures of 310 K. The characteristics of the supersonic expansions have been given in Chapter 2. In this table μ is the reduced mass, \bar{v} is the mean collision speed, v_{rms} is the root mean square speed and E is the mean collision energy.

192a

Table 7.2 Rotational state distributions are given for a Boltzmann distribution of HF at 300 K, for the secondary beam supersonic expansion of pure HF, and for the various primary beam supersonic expansions of 1% HF in helium. All populations are expressed as percentages. The upper figures for the primary beam data were obtained with the secondary beam operating at the largest nozzle-skimmer separation. The lower numbers, in parentheses, were determined by extrapolating the attenuation data to zero attenuation, and are therefore estimates of the primary beam populations in the absence of scatterers. A room temperature pyroelectric detector was used to obtain the secondary beam populations.

194a

Table 7.3 Cross sections fitted to each of the four sets of data corresponding to different primary beam source pressures. In this case the ratios of the first order cross sections were determined by Eq. (7.9) and the second order ones were assumed to be equal. The labels A,B,C and D refer to primary beam pressures of 2170,1480,655 and 310 kPa respectively.

205a

Table 7.4 The same as Table 7.3, except this time the second order cross sections were also scaled according to Eq. (7.9). 205a

Table 7.5 Best fit cross sections determined by simultaneously fitting to all four sets of data. The two sets of results correspond to choosing the second order cross sections to be equal or scaling them according to Eq. (7.9). In both cases the ratios of first order cross sections were determined by Eq. (7.9). \sum is the sum of square relative deviations, which can be compared with the \sum 's in Table 7.6. 205b

Table 7.6 Best fit cross sections obtained by fixing the size of the second order cross sections and allowing the first order ones to vary independently. In each case, the second order cross sections were chosen to be equal and the $34+43$ cross section was made equal to the $23+32$ cross section. The fitting was performed simultaneously to all four sets of data. \sum is the sum of square relative deviations for the best fit in each case. 207b

Figure 7.1 A schematic diagram of the experimental arrangement. 189a

Figure 7.2 Secondary beam angular profiles for various nozzle-skimmer separations as recorded with the mass spectrometer. A pure argon supersonic expansion at a source pressure of about 175 kPa and a nozzle temperature of 310 K was used. The nozzle diameter was 70 μm . Curves 1 through 5 are in order of decreasing nozzle-skimmer separation. At the nozzle-skimmer separation corresponding to curve 5, the attenuation of the primary beam HF was about 15% (relative to the secondary beam not operating) for the case of an HF (rather than argon) secondary beam. 191a

Figure 7.3 Plots of $\ln[(2j+1)P_0/P_j]$ vs $j(j+1)$ for the secondary HF beam and the four primary beams. The primary beam populations extrapolated to zero attenuation were used. SB labels the secondary beam data and A,B,C and D are the four sets of primary beams data, labelled as in Table 7.2. 194b

Figure 7.4 Attenuation curves for the $j=0,1,2$ and 3 states obtained at the primary beam source pressures shown in Table 7.2. The sets of curves labelled A through D correspond to source pressures of 2170,1480,655 and 310 kPa respectively. The experimental points are shown as diamonds. The solid lines represent the fit to the experimental data obtained using the best fit cross sections given in Table 7.5 for the case in which the second order cross sections were scaled according to Eq. (7.9). The straight lines drawn for $j=0$ and 1 show the behaviour expected when all of the rotational transfer cross sections are zero. Populations are expressed as percentages of the total primary beam HF population at zero attenuation ($\alpha=0$). 196a

Figure 7.5 Plots of the summed rotational state populations, $\sum P_j(\alpha)$, as a function of α for the four primary beam pressures. 197a

Figure 7.6 Results obtained for $j=0,1$ and 2 when an argon secondary beam was used. The primary beam source pressure was 930 kPa. 197b

Figure 7.7 A comparison between fits to the $j=3$ population curve at a primary beam pressure of 1480 kPa obtained using different magnitudes of the second order resonant cross sections. The curves labelled $1,2,4,6$ and 7 correspond to the similarly labelled cross sections listed in Table 7.6

207a

Chapter One

Introduction

The use of supersonic expansions to form intense beams of neutral atoms and/or molecules was first reported by Kantrowitz and Grey (1951) and Kistiakowsky and Slichter (1951). High intensities in the forward direction and narrow velocity distributions result from the hydrodynamic flow of gas through a suitable opening into a sufficiently high vacuum. To achieve hydrodynamic flow, the mean free path of the gas on the upstream side of the opening must be smaller than the size of the opening. The properties of beams formed from supersonic expansions are well understood. See, for example, the investigations by Anderson and Fenn (1965), Toennies and Winkelmann (1977), Beijerinck and Verster (1981) and Engelhardt et al. (1985).

By varying both the conditions under which the molecular beam is formed and the composition of the gas mixture used to form it, one can control (to a useful degree) (1) the most probable speed of the atoms/molecules in the beam, (2) the effective temperature of the molecules in the beam, and (3) the degree of clustering resulting from the expansion (Fluendy and Lawley (1973), Bernstein (1982)). The majority of investigations carried out using molecular beam techniques can be classified either as scattering experiments or spectroscopic studies, or a combination of the two. The results of beam-beam collision experiments in which one measures the angular distribution of the atoms or molecules in one beam which have been scattered from those in the other often yield detailed information about the relevant interaction potential (Buck (1971),

Buck and Pauly (1971), Pack et al. (1982a,1982b)). In many cases the dependence of the scattering upon the initial and/or final states of the collision partners can be resolved. If one uses small amounts of the molecules of interest seeded in a light carrier gas, say helium or hydrogen, one can obtain supersonic beams in which the molecules of interest have very low effective temperatures (less than 10 K). Such beams are ideal for carrying out spectroscopic investigations of the molecules, or clusters of molecules (van der Waals clusters), present in the beam (Travis et al. (1977), Gough et al. (1977), Levy (1981), Janda (1985)). The combination of continuously tunable narrow bandwidth lasers and highly sensitive molecular beam techniques allow the measurement of high resolution spectra free from the effects of Doppler broadening (Gough et al. (1977), Bernstein (1982)). From spectra of this kind one can often obtain information about the dynamical processes occurring in the systems being studied.

The simplest scattering experiments use a crossed molecular beam configuration and a suitable detector to measure the total scattered intensity as a function of the scattering angle. Early experiments of this kind were carried out using surface ionisation detectors to detect alkali atoms (Morse and Bernstein (1962), Pauly and Toennies (1968)). Other techniques for detecting scattered particles include (1) bolometric detection, in which one measures the total energies (internal + kinetic) of the detected particles (Cavallini et al. (1967,1971a,1971b), Boughton et al. (1985)), (2) mass spectrometry, with the possibility of using time-of-flight techniques to resolve inelastic scattering events (Andres et al. (1982), Buck et al. (1983b), Hoffbauer et al. (1983a)), and (3) laser-induced fluorescence detection, which can also be used to obtain

information about inelastic scattering via time-of-flight techniques (Serri et al. (1980), Bergmann et al. (1980)). These methods can also be used to record detailed spectroscopic information about the species present in a given molecular beam. By intersecting the molecular beam with a suitable source of laser radiation prior to bolometric detection one is able to measure the laser-induced change in the molecular beam energy as a function of the laser frequency (Gough et al. (1977,1983), Boughton et al. (1982)). The high sensitivity of bolometer detectors makes them ideal for measuring the spectra of the molecules and van der Waals clusters present in a given molecular beam (Miller (1980)). Mass spectrometry and laser-induced fluorescence detection have also been used to monitor molecular beams which have been excited by suitable laser radiation (Brinza et al. (1983,1984), Vernon et al. (1982b), Liu et al. (1984), Page et al. (1984), Hoffbauer et al. (1983b,1983c), Haynam et al. (1983), Smalley et al. (1978)). By combining state-selective methods (such as laser excitation, electrostatic quadrupole state selection, or the time-of-flight methods noted above) with molecular beam scattering techniques, it is possible to investigate both integral and differential scattering cross sections as functions of the initial and/or final states of the collision partners (Barnes et al. (1982), Borkenhagen et al. (1979), Bergmann et al. (1980), Andres et al. (1980), Buck et al. (1984), Wilcomb and Dagdigian (1977), Dagdigian et al. (1979)).

Results of experimental scattering and spectroscopic studies can be used either to develop or refine interaction potentials for the systems under study, or to test the accuracy of available potential surfaces (Hutson and Howard (1981,1982a), Pack et al. (1982a,1982b,1984), Buck and Pauly (1971), Buck and Schleusener (1981), Boughton et al. (1985)). The

aims of such investigations are (1) to characterise the interaction potentials as accurately as possible, and (2) to understand the dynamical processes involved. Both the complexity of the molecules and the nature of the dynamical processes being investigated will determine the amount of information which can be obtained from studies of this kind.

Detailed experimental and computational studies of the dynamical behaviour of a number of small atom-molecule and molecule-molecule systems are reported in this thesis. Both molecular beam scattering methods and infrared laser spectroscopic techniques were used in combination with bolometric detection during the course of these investigations. The experimental techniques are described in Chapter 2. In Chapter 3 are described both the approximations used to calculate the cross sections reported in this thesis and the method used to compare these cross sections with the measured differential scattering intensities. The results of the research are described and discussed in Chapters 4, 5, 6 and 7. Each of these chapters includes an introduction to the topics discussed therein. An outline of the work reported in these chapters is given below.

The results of a computational study of the scattering of helium from hydrogen fluoride are discussed in Chapter 4. Total differential cross sections predicted using the single channel, infinite order sudden and coupled states approximations are compared with each other and with the available experimental data (Boughton (1986)) for a number of model potentials. An analytic, spherically symmetric potential function is determined by fitting to the measured intensities. Coupled states calculations of the inelastic cross sections are reported for the ab initio potential developed by Rodwell et al. (1981).

An experimental and computational study of the scattering of argon

from hydrogen fluoride is reported in Chapter 5. Detailed scattering calculations were carried out using the single channel, infinite order sudden and coupled states approximations for the Ar-HF interaction potentials developed by Hutson and Howard (1982b) and Douketis et al. (1984). The calculated cross sections are compared with the measured differential scattering intensities and with previously reported integral cross sections (Barnes et al. (1982)).

The results of an infrared laser - molecular beam spectroscopic investigation of small clusters of acetylene, ethylene and methyl acetylene are presented in Chapter 6. A continuously tunable colour centre laser was used to measure cluster dissociation spectra under both high (0.4 cm^{-1}) and low (0.0001 cm^{-1}) resolution in the vicinity of 3000 cm^{-1} . A discussion of the possible structural and dynamical implications of the measured spectra is given.

An experimental study of the resonant transfer of rotational energy between HF molecules is reported in Chapter 7. By combining molecular beam scattering methods and infrared laser spectroscopic techniques it was possible to estimate the magnitudes of the resonant transfer cross sections. These cross sections correspond to processes in which the colliding HF molecules exchange their rotational quantum numbers, and are determined primarily by the long range dipole-dipole interaction.

Finally, a summary of the results reported in this thesis and the conclusions drawn from these results is given in Chapter 8.

Chapter TwoExperimental Techniques

In this chapter we describe the equipment and techniques used to obtain the experimental results presented in this thesis. The following topics are discussed : the beam chamber, phase sensitive detection, the quadrupole mass spectrometer, the bolometer detection system, the colour centre infrared laser and associated spectroscopic techniques, the measurement of a total differential scattering cross section and the time-of-flight determination of the velocity distribution of the molecules in a given beam.

2.1 The Beam Chamber

The molecular beam system used in the present investigations has been described by Boughton et al. (1982) and Miller et al. (1984a). A schematic diagram of the apparatus is shown in Figure 2.1. It consists of a stainless steel chamber and a rotatable base flange between which a conventional O-ring seal is located. Mounted on the base flange are the primary and secondary supersonic molecular beam source chambers which are pumped by an unbaffled 5300 l/s and an unbaffled 2400 l/s oil diffusion pump respectively. Monel nozzles mounted on xyz translation stages are used to form supersonic expansions of the gas mixtures of interest which are then sampled by conical brass skimmers, as shown schematically in Figure 2.2. Typical operating pressures in the primary and secondary chambers lie in the range 10^{-3} to 10^{-4} torr. After passing through the skimmers the beams enter the scattering chamber, which is pumped by two 1600 l/s oil diffusion pumps to maintain an operating pressure of about 10^{-6} torr. The four diffusion pumps are backed by a common 50 l/s rotary pump.

An alignment telescope is used to locate the skimmers so that, by suitably adjusting the nozzle positions, it is possible to obtain beams which lie in a plane with the detectors and meet at 90° on the axis of rotation of the base flange. By using heating tape or a liquid nitrogen cooled copper sleeve it is possible to vary the nozzle temperature from 80 K to 550 K. The beams can be modulated by rotating mechanical choppers which are placed either before or after the skimmers. It is also possible to block the primary beam altogether using a flag located outside the primary beam chamber.

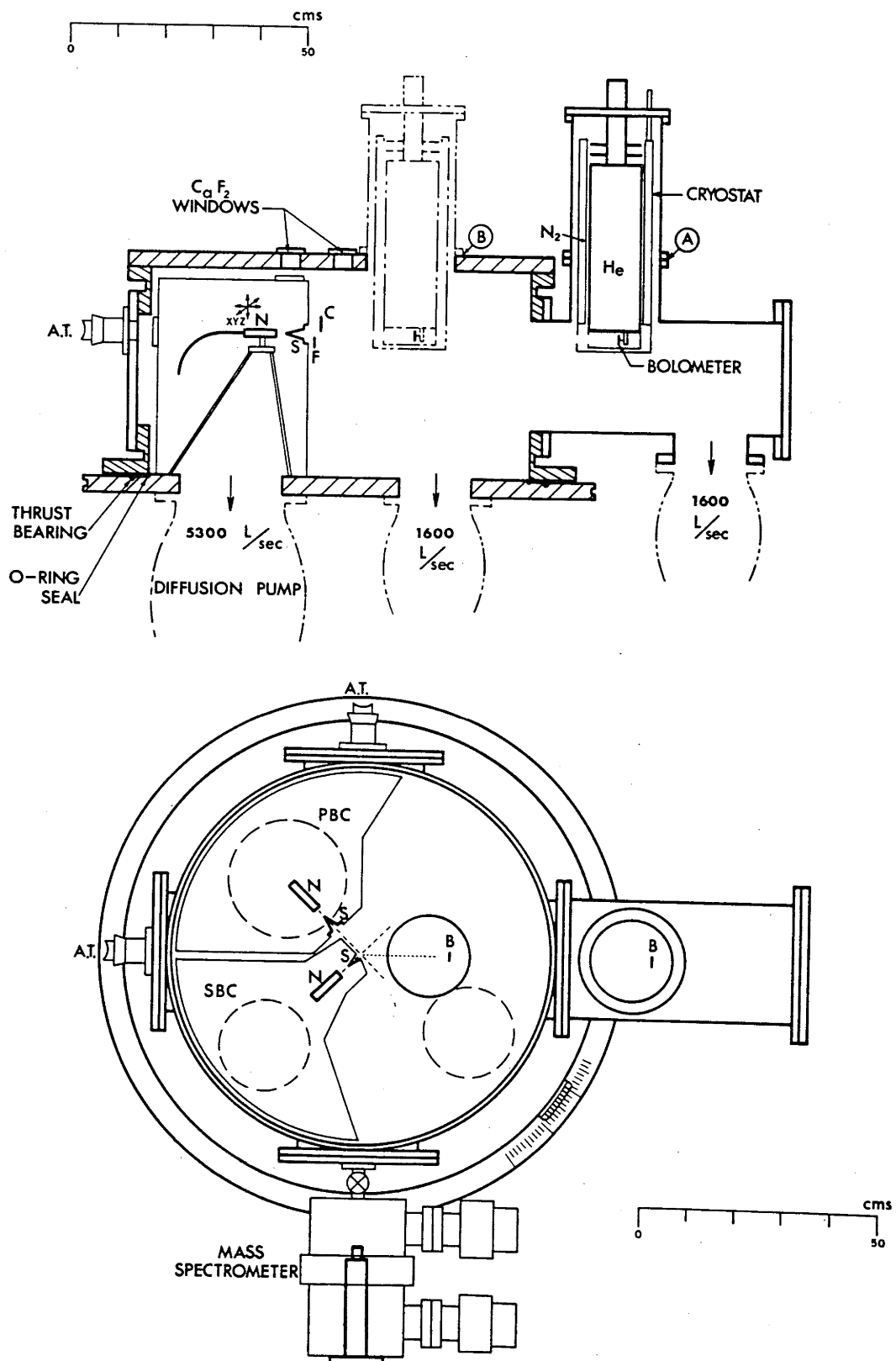


Figure 2.1

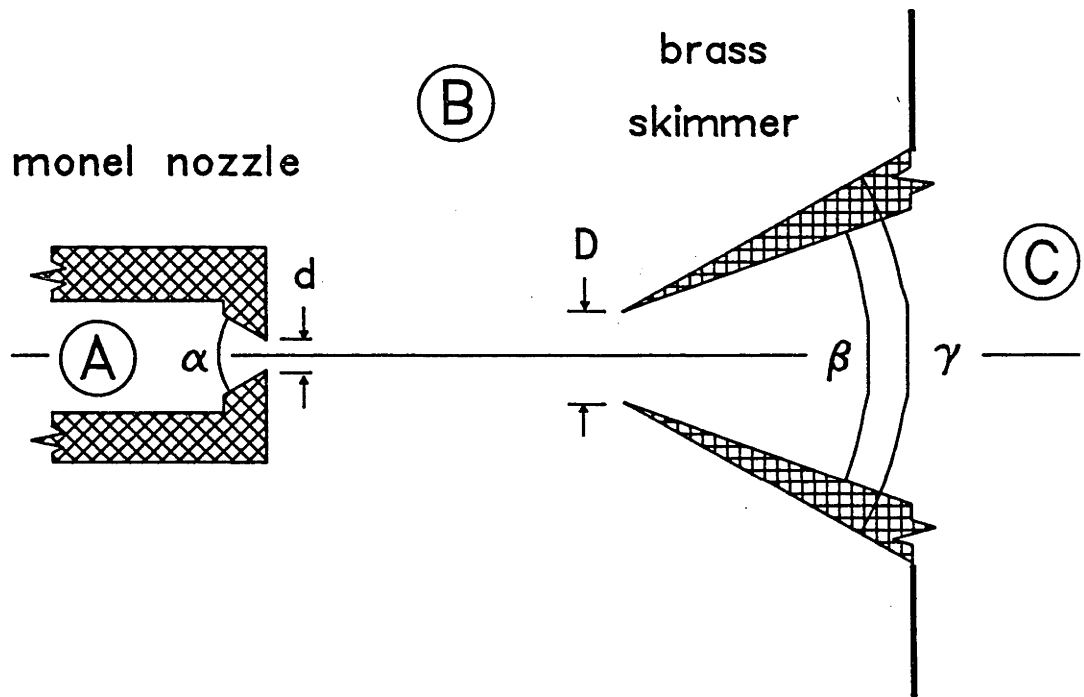


Figure 2.2

The beams are formed either from pure gases or from mixtures of the gas of interest in helium or argon. The rated purities of the gases used were : helium 99.99 % ; argon 99.99 % ; hydrogen 99.98 %; hydrogen fluoride 99.9 % ; and acetone free acetylene (C_2H_2) in helium mixtures of a high but unspecified purity. The helium was used both in the pure form and to make low dilutions of hydrogen fluoride and acetylene in helium. Although no further purification of the gases was performed, they were passed through 7 micron sintered stainless steel filters before they reached the nozzles. The gas handling system was constructed from 1/4 inch O.D. stainless steel tubing and both stainless steel and monel bellows valves. Mattheison regulators were used to control the pressures of the gas mixtures which reached the nozzles. These stagnation pressures ranged from about 0.5 to 30 atm (50 to 3000 kPa).

2.2 Phase Sensitive Detection

Phase sensitive detection was used to detect the small signals typical of many molecular beam scattering or spectroscopic studies. The technique involves modulating the process of interest and using a lock-in amplifier (LIA) to determine an average value of the change in the signal resulting from the modulation. Princeton Applied Research model 124-A and 128-A lock-in amplifiers were used in the studies reported in this thesis.

In the beam-beam total differential scattering experiments the secondary beam was modulated and the corresponding change in the number of primary beam particles detected at the desired scattering angle was measured. For the spectroscopic studies the laser beam was chopped and the change in the energy of the molecular beam caused by laser excitation was observed. In both cases rotating mechanical choppers with duty cycles of 50% were used. Typical modulation frequencies ranged from 30 Hz to 80 Hz, depending upon the frequency response characteristics of the detector and the prevailing noise spectrum.

By using phase sensitive detection with a liquid helium cooled bolometer detector it is possible to measure very small changes in an otherwise large signal. For example, we have recorded infrared spectra with peak signals as small as a few hundred nV in a total molecular beam signal of about 0.3 V.

2.3 The Quadrupole Mass Spectrometer

A commercially available electron impact ionization quadrupole mass spectrometer (UTI 100c), housed in an ultra-high differentially pumped enclosure, was used to mass resolve the molecules in a given beam. A buffer chamber, pumped by a 125 l/s turbo-molecular pump, separates the scattering chamber from the mass spectrometer chamber, which is pumped by a 175 l/s turbo-molecular pump. Two 5 mm circular apertures allow the molecular beam to pass through the buffer chamber. Typical operating pressures in the final chamber lie in the range 10^{-8} to 10^{-9} torr. By chopping the molecular beam and using phase-sensitive detection the effects of background gas in the system are minimised.

The energy of the ionizing electrons can be varied from 30 eV to 70 eV. When studying beams which contain weakly bound van der Waals molecules a low electron energy is used to minimise problems associated with cluster fragmentation resulting from electron impact.

By scanning the mass spectrometer from 0 to its maximum of 300 amu it is possible to determine both the chemical composition of the beam and the degree of clustering occurring in the supersonic expansion. One can also monitor the change in a particular mass signal as a function of, for example, the secondary beam intensity or the primary beam gas pressure. Time-of-flight measurements used to obtain the velocity distributions of the mass components of a given beam are discussed in a later section.

2.4 Bolometric Detection

A bolometer is a detector constructed from a material with a large temperature coefficient of resistivity. It is possible to detect very small changes in the incident energy flux by monitoring the resistance of the device. A liquid helium cooled bolometric detection system was used to obtain the total differential scattering cross sections and to perform the infrared spectroscopic measurements reported in this thesis. One of the earliest applications of bolometric detection to the measurement of total differential cross sections was reported by Cavallini et al. (1967,1971a, 1971b). Miller (1980), Gough et al. (1977,1983) and Boughton et al. (1982) discuss the use of bolometers in conjunction with laser - molecular beam spectroscopic techniques.

The cryostat assembly housing the detector is shown schematically in Figure 2.3. The bolometer is mounted onto a copper block which is in good thermal contact with the inner liquid helium dewar. By pumping on the dewar it is possible to attain an operating temperature of 1.8 K. A copper shield in contact with the inner cryostat and an outer shield attached to the liquid nitrogen cryostat are used to prevent stray radiation or molecules from reaching the bolometer. Two apertures allow the molecules of interest to pass through the shields to the detector. The aperture in the outer shield is a 3x6 mm rectangular slot, with its long axis vertical, and the inner shield has a circular aperture 6 mm in diameter. Metallic baffles in the neck of the helium dewar prevent stray radiation from reaching the liquid helium during operation. A single transfer enables up to 15 hours of continuous operation. The bolometer cryostat assembly can be mounted either in the near position (shown dashed in Figure 2.1) or in

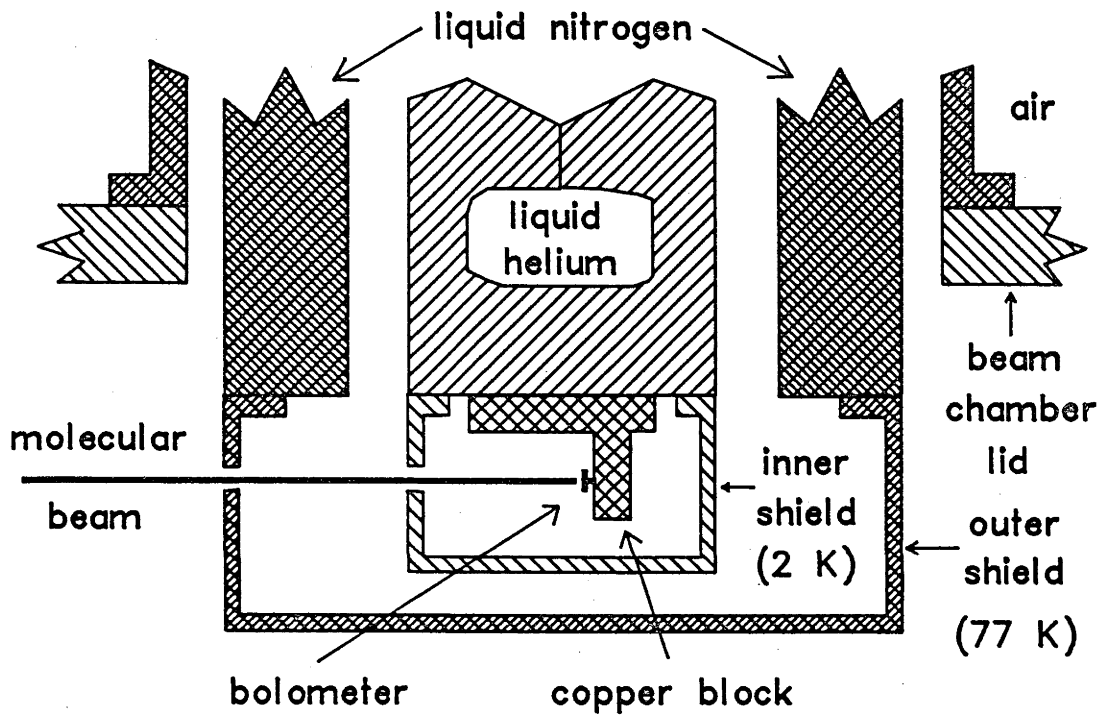


Figure 2.3

the far position (shown in solid lines).

The bolometer is operated in series with a mercury cell of ~ 8.8 V and a load resistor of ~ 5 M Ω , as shown in Figure 2.4. In this way the changes in bolometer resistance are observed as voltage changes across the bolometer. The response of the bolometer to a change in the incident energy flux can be determined from the load curve, or I-V characteristic, of the device. Figure 2.5 shows the circuit used to obtain the load curve. By fixing V_S and measuring I one obtains the corresponding bolometer voltage from $V_b = V_S - IR_e$, where R_e is the series resistance of the electrometer.

Two different bolometers were used to obtain the experimental results reported in this thesis. The first, bolometer A, is an antimony-doped silicon chip (1.97 x 4.27 x ~ 0.5 mm) onto which are spot welded two 0.13 mm diameter gold wires. These are indium soldered to copper wires which are in good thermal contact with, but electrically isolated from, the copper block attached to the helium dewar.

Bolometer B, which was obtained from Infrared Laboratories Inc., consists of a very small gallium doped germanium element thermally bonded onto a 2x5 mm blackened diamond absorber which is in thermal contact with the cold copper block. Load curves for the two bolometers are shown in Figures 2.6 and 2.7. The data in Figure 2.7 are the calibration data supplied by Infrared Laboratories. These curves were obtained in the absence of molecular beam or laser related energy impinging upon the detectors, although there was almost certainly some residual background radiation or molecular flux reaching the bolometer. The zero frequency responsivity S_0 is obtained from (see Jones (1953))

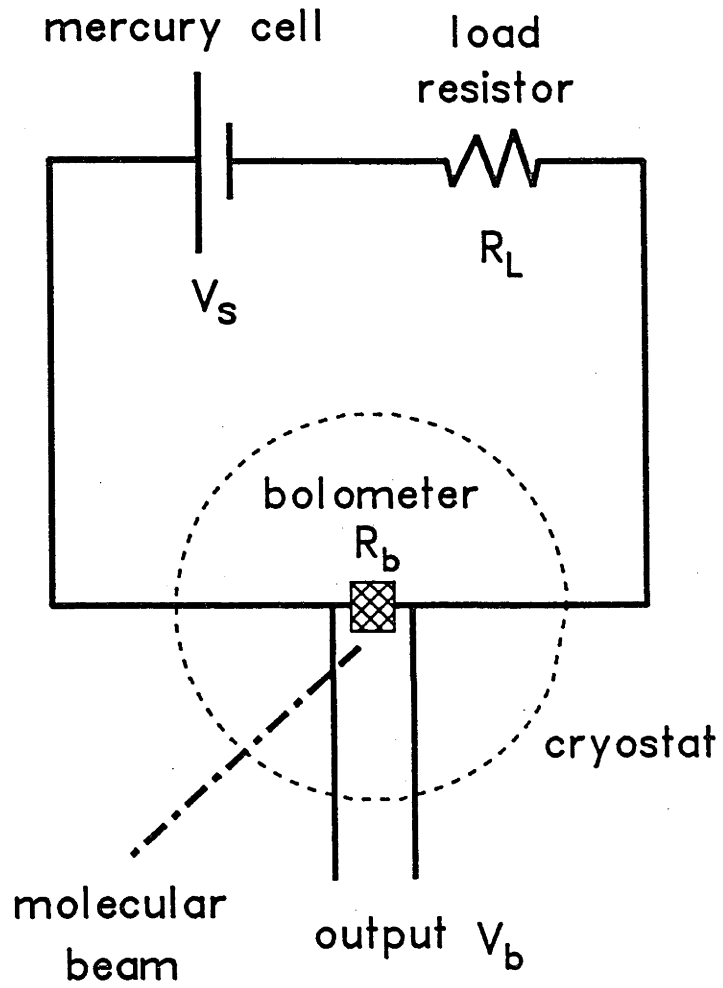
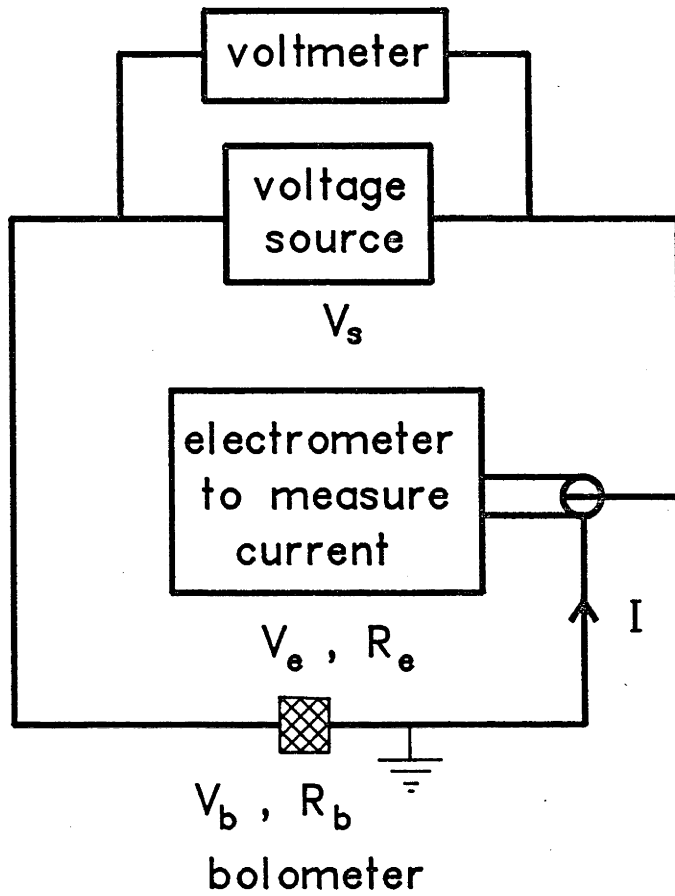


Figure 2.4

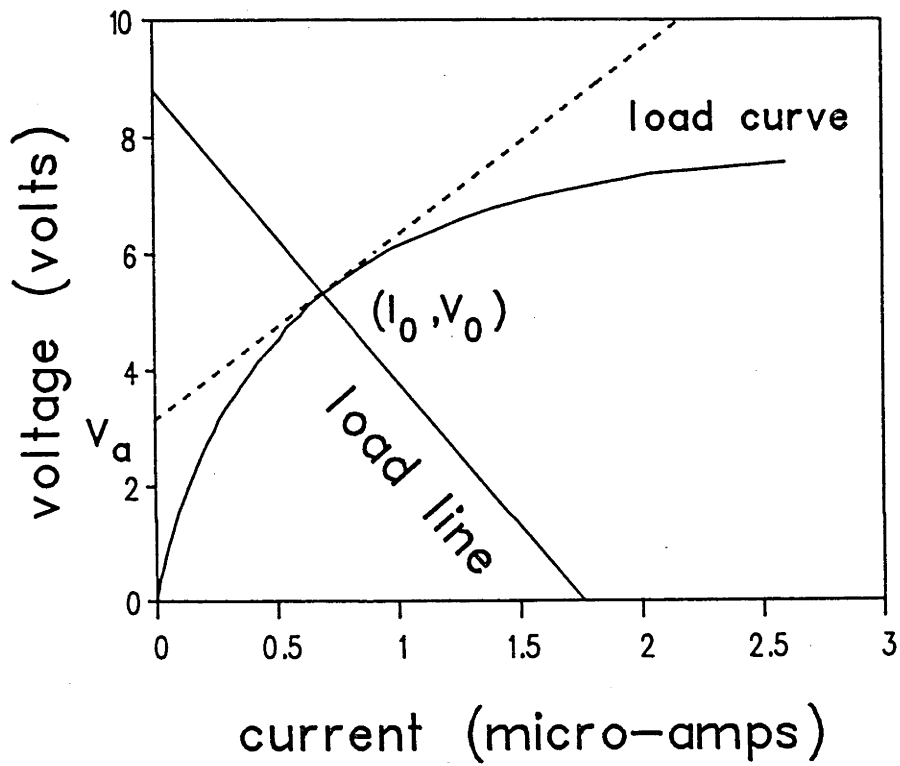


$$V_b = V_s - IR_e$$

Figure 2.5

bolometer A

I-V characteristic

Figure 2.6

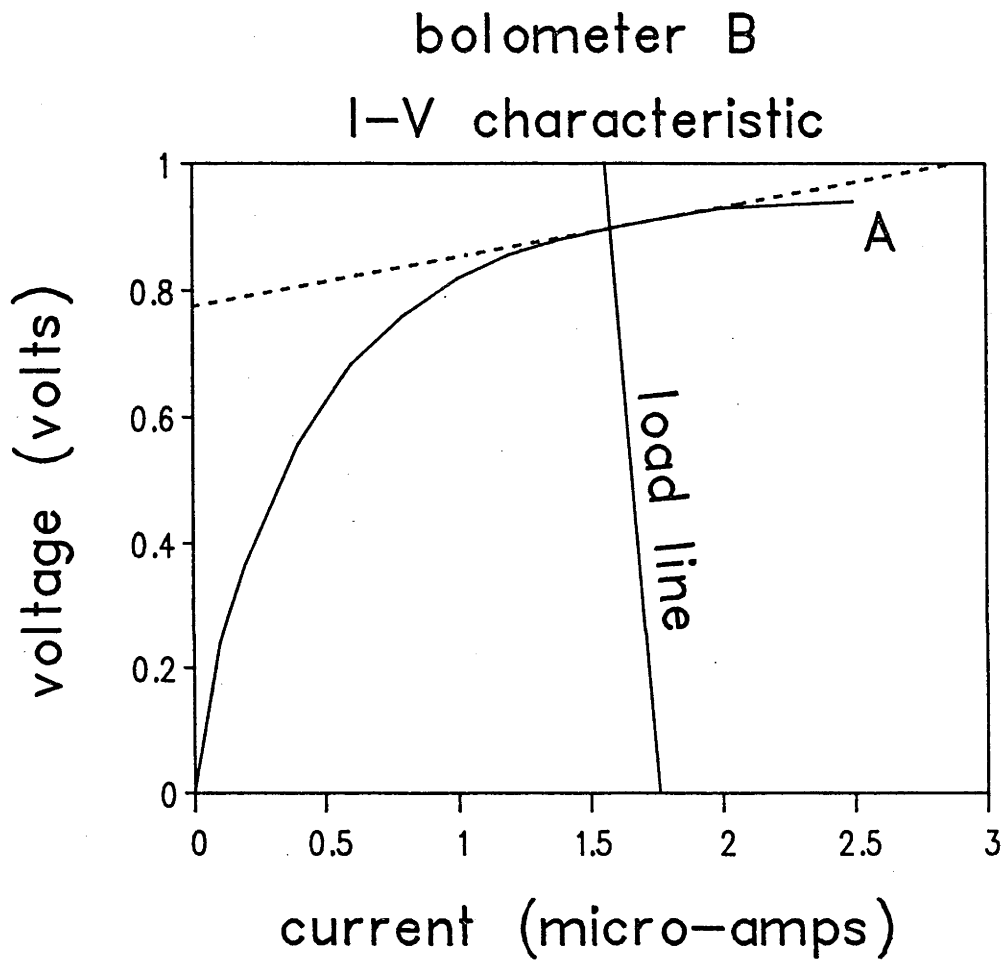


Figure 2.7

$$S_0 = \frac{Z_0 - R_0}{2V_0} = \frac{V_a}{2V_0 I_0} \quad (2.1)$$

where: the operating point (I_0, V_0) is given by the intersection of the load line $V = V_S - IR_L$ with the load curve; $Z_0 = dV/dI(I_0, V_0)$; $R_0 = V_0/I_0$; and V_a is the V-intercept of the tangent to the load curve at the operating point (see Figure 2.6). S_0 determines the change in voltage ΔV caused by a change ΔE in the total energy incident upon the bolometer, as long as the energy change does not substantially alter the load curve (ie. the position of the operating point), but says nothing about how small a signal one is able to detect. The noise equivalent power (NEP) is the incident power required to produce a unity signal-to-noise ratio for unity bandwidth. The NEP's for bolometers A and B, determined under conditions for which no external radiation or molecular beam flux reaches the detector, are approximately $3 \cdot 10^{-12}$ and $5 \cdot 10^{-14}$ $\text{WHz}^{-\frac{1}{2}}$ respectively. In principle, therefore, bolometer B can be used to observe signals as small as 1/60 times the smallest observable signal using bolometer A.

The responsivities obtained from the load curves of Figures 2.6 and 2.7 are $430 \mu\text{V/nW}$ and $270 \mu\text{V/nW}$ for bolometers A and B respectively. It was found that the responsivity of bolometer A remained essentially constant as a function of the total molecular flux reaching the bolometer. For device B, on the other hand, the responsivity varied considerably with the gas load. Figure 2.8 shows the load curves for bolometer B obtained with different constant gas loads reaching the bolometer. The conditions at the operating points determined by the load line shown in the figure are given in Table 2.1. In order to measure the change in responsivity as a function of gas load a small (constant) chopped IR signal was trained at the bolometer and the output of the bolometer-LIA detection system was

bolometer B

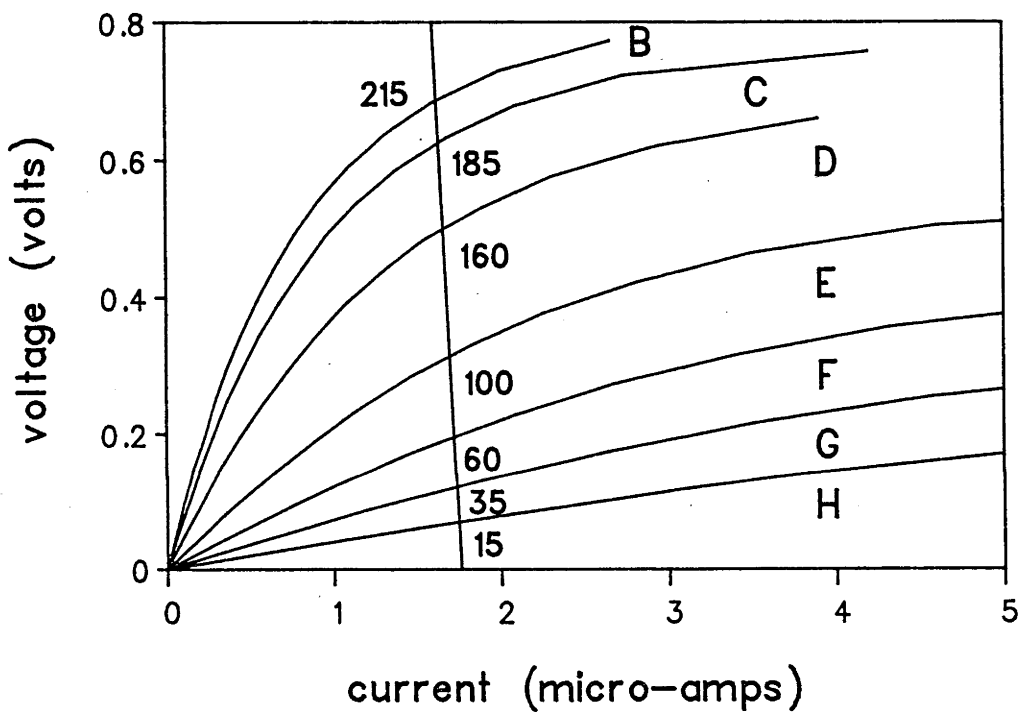
Figure 2.8

Table 2.1

load curve	I_0 (μA)	V_0 (V)	S_0 (V/mW)	P (kPa)
A	1.580	0.900	270	-
B	1.622	0.690	215	zero
C	1.633	0.626	185	zero
D	1.659	0.504	160	100
E	1.696	0.318	100	400
F	1.721	0.196	60	750
G	1.735	0.124	35	1200
H	1.746	0.070	15	> 2000

monitored as a function of the gas load. A pure helium beam was used and the experimental arrangement was similar to that existing during the spectroscopic studies reported in this thesis. The results of these investigations are shown in Figure 2.9. A plot of the responsivity (obtained from the load curves) vs V_0 appears in Figure 2.10 together with the experimentally measured response (in arbitrary units) of the detector-amplifier system. The measured response was used as a first order correction when comparing data obtained with different molecular beam intensities reaching the bolometer. It should be noted that bolometer B was used exclusively for on-beam spectroscopic studies. Typical primary beam source pressures corresponding to the various operating points are shown in Table 2.1. These pressures were also determined under conditions similar to those existing during the spectroscopic studies.

The response times for bolometers A and B are approximately 20 ms and 10 ms. These are the times required for the output signals to reach 63% of their final values after instantaneously applying (small) constant energy fluxes to the bolometers. Typical modulation frequencies used in conjunction with phase sensitive detection were 35 Hz and 80 Hz for bolometers A and B.

We note here that a Molelectron P1-71 pyroelectric detector was used in place of the bolometer when studying beams of pure HF. The NEP of this detector is $\sim 3 \cdot 10^{-10} \text{ WHz}^{-\frac{1}{2}}$ (ie., about two orders of magnitude lower than for bolometer A). Phase sensitive detection was used in a similar manner as with the bolometer to monitor the laser-induced changes in the molecular beam energy. The use of this detector in conjunction with infrared laser - molecular beam techniques has been discussed by Miller (1982).

bolometer B

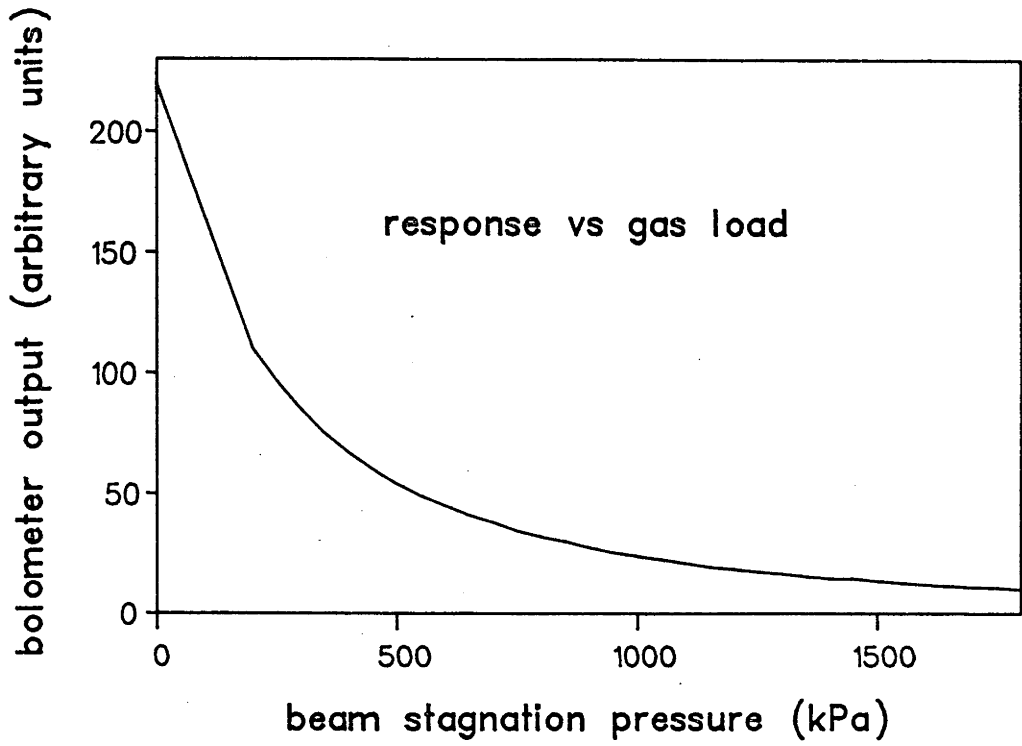


Figure 2.9

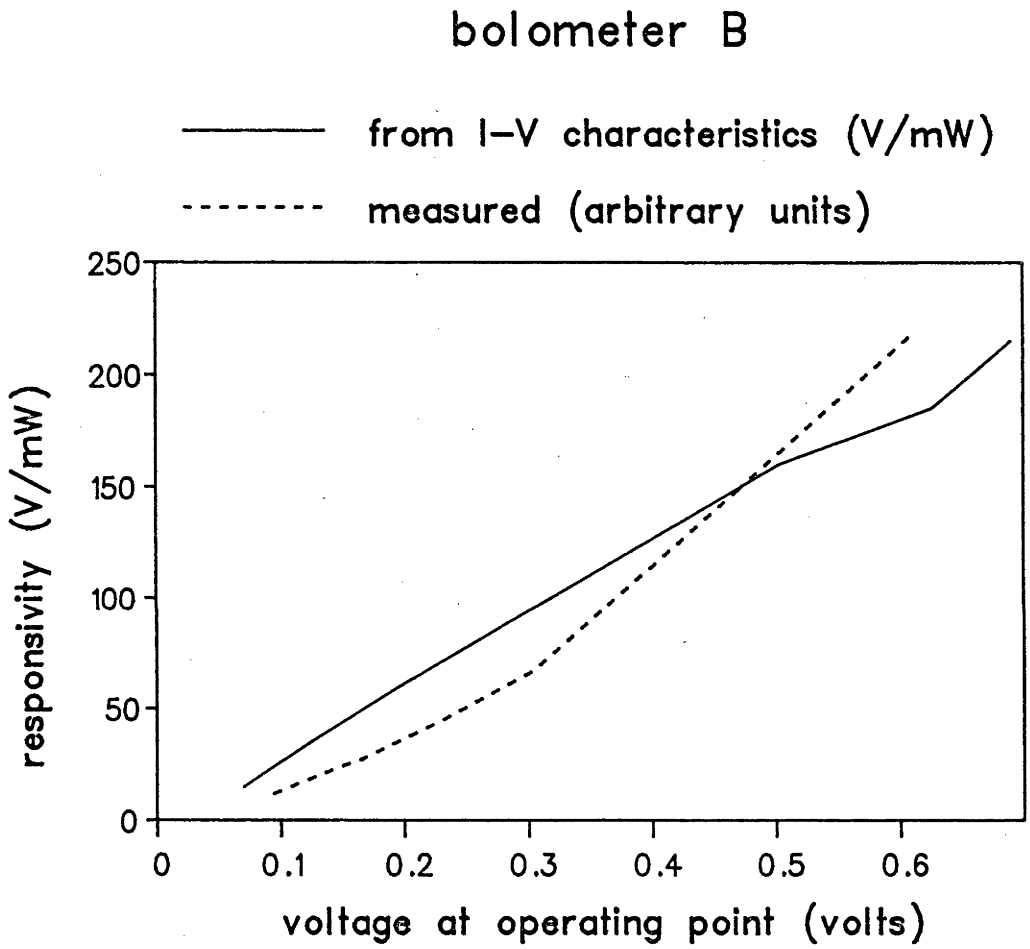


Figure 2.10

2.5 The Colour Centre Laser

A Burleigh FCL-20 colour centre laser (FCL), pumped by a Spectra Physics 171 krypton ion laser, produces useful radiation in the 2.3 to 3.3 micron wavelength range (4400 to 3000 cm^{-1}). A multipass device consisting of two parallel gold-coated mirrors is used to achieve multiple near-orthogonal laser-molecular beam crossings. By modulating the laser output with a 50% duty cycle rotating chopper and monitoring the excited molecular beam with the bolometer-lock-in-amplifier system it is possible to observe the net laser-induced change in the energy of the molecular beam. When making such measurements the bolometer cryostat is mounted in the far position (see Figure 2.1) and the multipass mirrors are located in the near position. A thorough review of colour centre lasers is given by Mollenauer (1985). In this section we briefly describe the colour centre laser used in these investigations and outline the techniques used to tune and monitor its output.

The lasing medium is a doped metal halide crystal which is kept at 77 K. To excite HF ($v=0 \rightarrow v=1$) transitions near $2.5\text{ }\mu\text{m}$ (4000 cm^{-1}) a Li doped KCl crystal is used. Li doped RbCl is used to excite ro-vibrational states in acetylene near $3\text{ }\mu\text{m}$ (3330 cm^{-1}). In these crystals, laser action results from the so-called $F_A(\text{II})$ colour centres, which consist of a single electron trapped in an anion vacancy where one of the metal ions adjacent to the vacancy has been replaced by a lithium ion (see Figure 2.11). The pump beam ($\sim 647\text{ nm}$) excites the electron in the anion vacancy, after which a fast, radiationless, rearrangement of the crystal lattice takes place. The desired IR photon is emitted when the excited electron, now in the relaxed vacancy, returns to the ground state of this (relaxed) vacancy. A

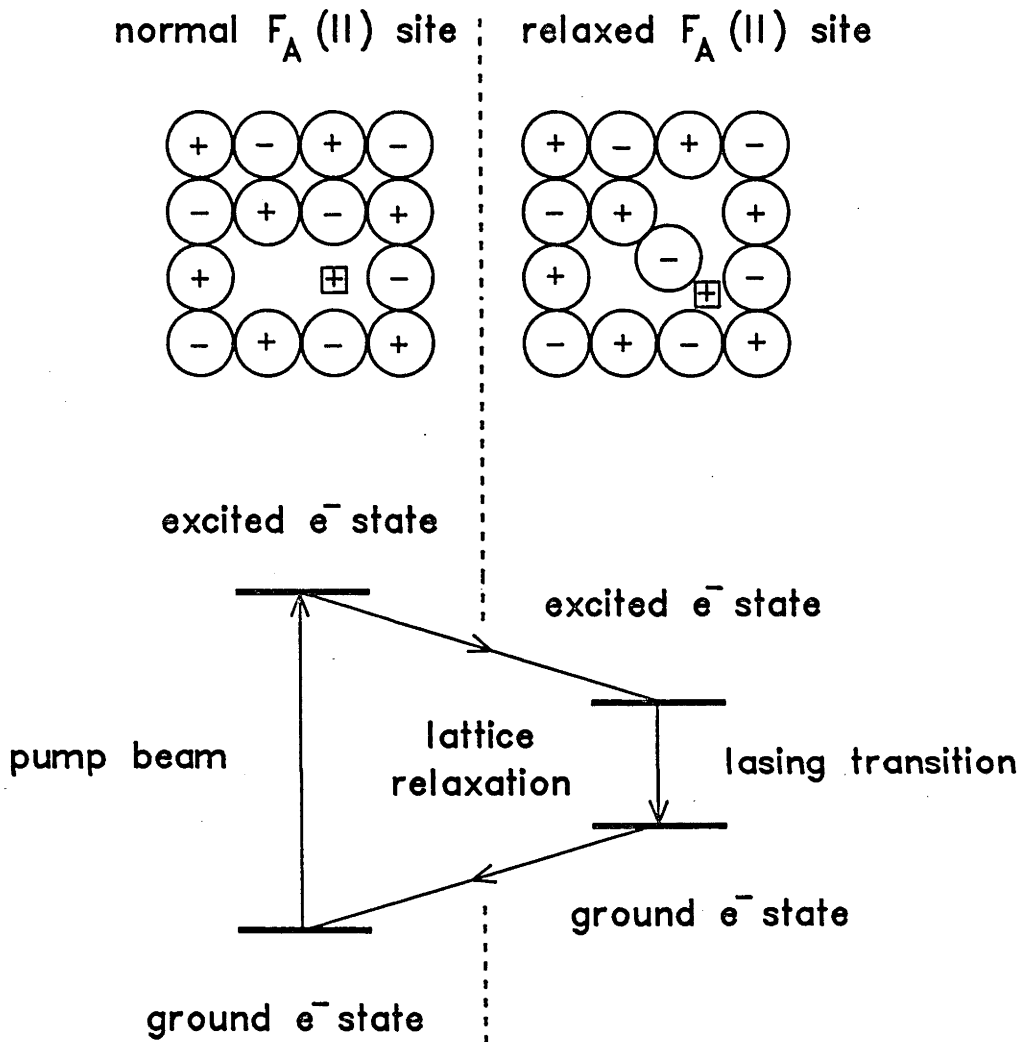


Figure 2.11

second fast, radiationless, lattice re-arrangement returns the system to its original configuration.

A schematic diagram of the FCL cavity is shown in Figure 2.12. The free spectral range (FSR) of the cavity is 300 MHz (0.01 cm^{-1}). In this section we discuss the techniques used to obtain low resolution scans (resolution $\approx 10 \text{ GHz}$ or $1/3 \text{ cm}^{-1}$), high resolution scans (resolution $\approx 1 \text{ MHz}$ or 0.00003 cm^{-1}) and frequency stabilized operation.

(a) Low Resolution Scanning

When operated without the cavity etalon lasing occurs on two cavity modes separated by 10 GHz ($1/3 \text{ cm}^{-1}$). One of these is the fundamental mode and the other is the spatial hole-burning mode, which has its maximum power density in those regions of the crystal for which the fundamental mode has its lowest power densities. Rotating the grating causes the lasing modes to jump discontinuously from one cavity mode to the next. It should be noted that the FWHM of each cavity mode is $\leq 1 \text{ MHz}$. In practice there may be 2 or 3 modes lasing simultaneously at both the fundamental and the spatial hole-burning wavelengths. Typical output powers obtained range from 10 to 15 mW. The overall laser resolution in this scanning mode is approximately 10 GHz ($1/3 \text{ cm}^{-1}$). A Grubb Parsons monochromator is used to calibrate the absolute frequency of the low resolution scans to within about 0.5 cm^{-1} .

The rotating mechanical chopper which is used to modulate the IR radiation before it crosses the molecular beam can be placed either between the krypton ion laser and the FCL or after the FCL. By chopping the pump laser the heating of the FCL crystals is reduced (for a given pump power)

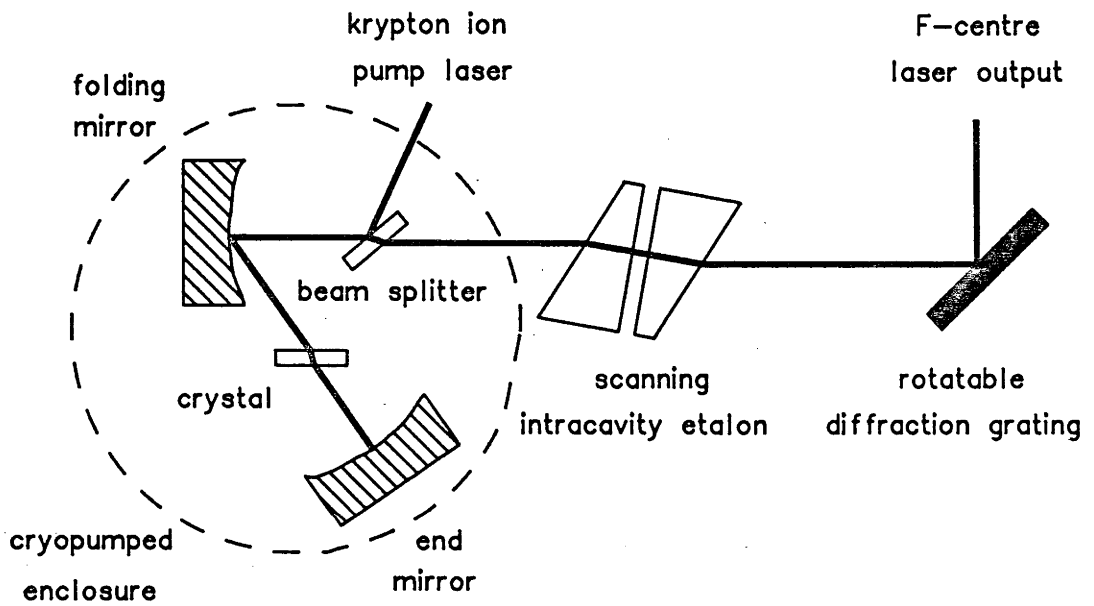


Figure 2.12

and one is able to use higher pump powers with a corresponding increase in useful IR output power.

(b) High Resolution Scanning

In order to achieve single mode operation a 20 GHz FSR temperature stabilized etalon is installed in the laser cavity. This suppresses the spatial hole burning mode associated with a given lasing cavity mode. Tuning of the FCL is accomplished by piezo-electrically controlling the folding mirror position and the cavity etalon spacing as well as rotating the grating. Figure 2.13 illustrates schematically the frequency response of the grating and of the cavity etalon in relation to the allowed cavity modes. By rotating the grating or ramping the cavity etalon or folding mirror piezo-electric translators (PZT's) it is possible to continuously scan the respective response profiles as a function of frequency.

A 7.5 GHz FSR confocal etalon is used to monitor the output of the FCL. By ramping the etalon, passing a portion of the FCL radiation through it, and observing the intensity of the transmitted radiation on a CRO it is possible to follow changes in the frequency and mode structure of the FCL output. To calibrate the high resolution spectra the laser light reflected off the rotating mirrored chopper is passed through a 150 MHz FSR temperature stabilized confocal etalon and the intensity of the transmitted light is detected using phase sensitive detection. In this way one obtains frequency markers at 150 MHz (0.005 cm^{-1}) intervals when the laser frequency is scanned continuously as discussed below. The frequency responses of the various elements are given in Table 2.2.

Ideally, the only cavity mode lasing for a given setting of the

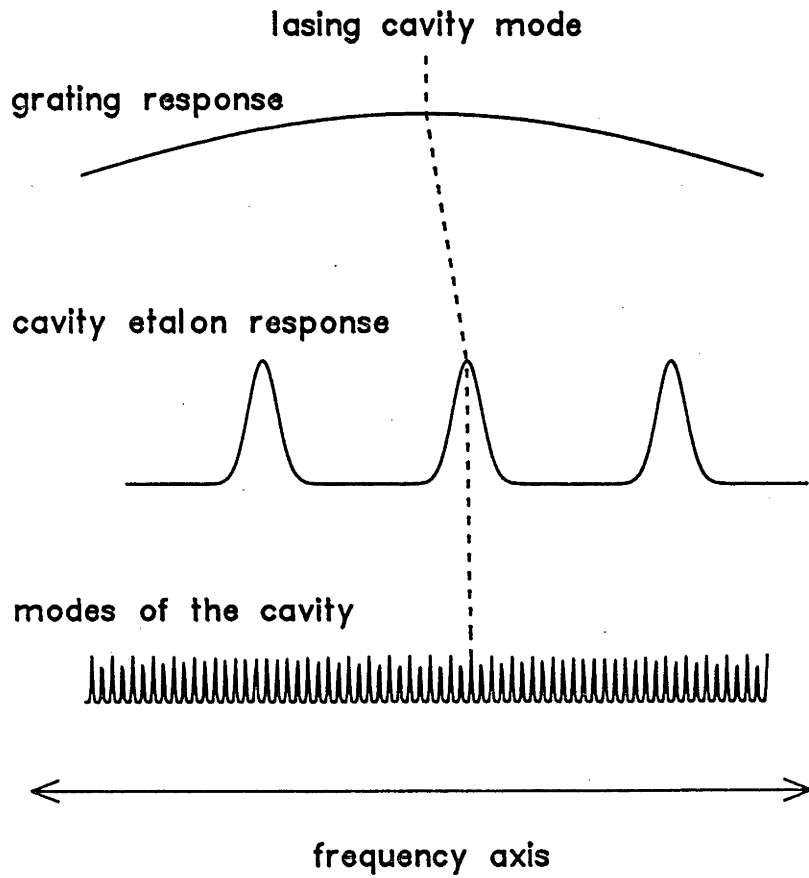


Figure 2.13

Table 2.2

frequency response characteristics

component	FSR	FWHM	finesse
FCL cavity	300 MHz	< 1 MHz	> 300
FCL cavity etalon	20 GHz	≈ 600 MHz	≈ 30
7.5 GHz etalon	7.5 GHz	≈ 250 MHz	≈ 30
150 MHz etalon	150 MHz	< 1.2 MHz	> 125
FCL cavity grating	-	≈ 50 GHz	-

three tuning elements will be that mode which has the highest overall transmission as determined by the grating and cavity etalon response profiles. Single mode scanning is realized as follows :

(1) Align the optics as shown in Figure 2.14. Leave all ramp generators on but unramped. The mirrored chopper should be rotating.

(2) Ramp the 7.5 GHz analyser etalon and observe the intensity of the transmitted laser radiation on a CRO.

(3) Adjust the FCL to obtain single mode behaviour.

(4) Apply a full linear ramp to the folding mirror PZT. The ramp generators used in these studies (Burleigh RC-43 and RC-45) have a maximum amplitude of 1000 V, corresponding to the maximum PZT excursion.

(5) Use the folding mirror ramp output $\div 100$ as input to the cavity etalon PZT ramp generator as shown in Figure 2.14. [Because the laser cavity is substantially longer than the cavity etalon spacing, the frequency shift caused by a given PZT excursion will be larger for the latter than for the former. This is the reason for dividing the folding mirror ramp by 100 before using it as input to the cavity etalon PZT ramp controller.]

(6) Adjust the amplitude (i.e. gain) of the cavity etalon ramp until the cavity mode observed on the CRO is scanning continuously. If the cavity etalon is being ramped too far or not far enough the mode on the CRO will jump discontinuously from one cavity mode to another. It may be necessary to optimize the bias voltage of the cavity etalon ramp to ensure that its frequency response profile is centred upon the lasing cavity mode. At this stage the desired single mode scanning has been achieved.

The length and speed of such a scan are controlled by the

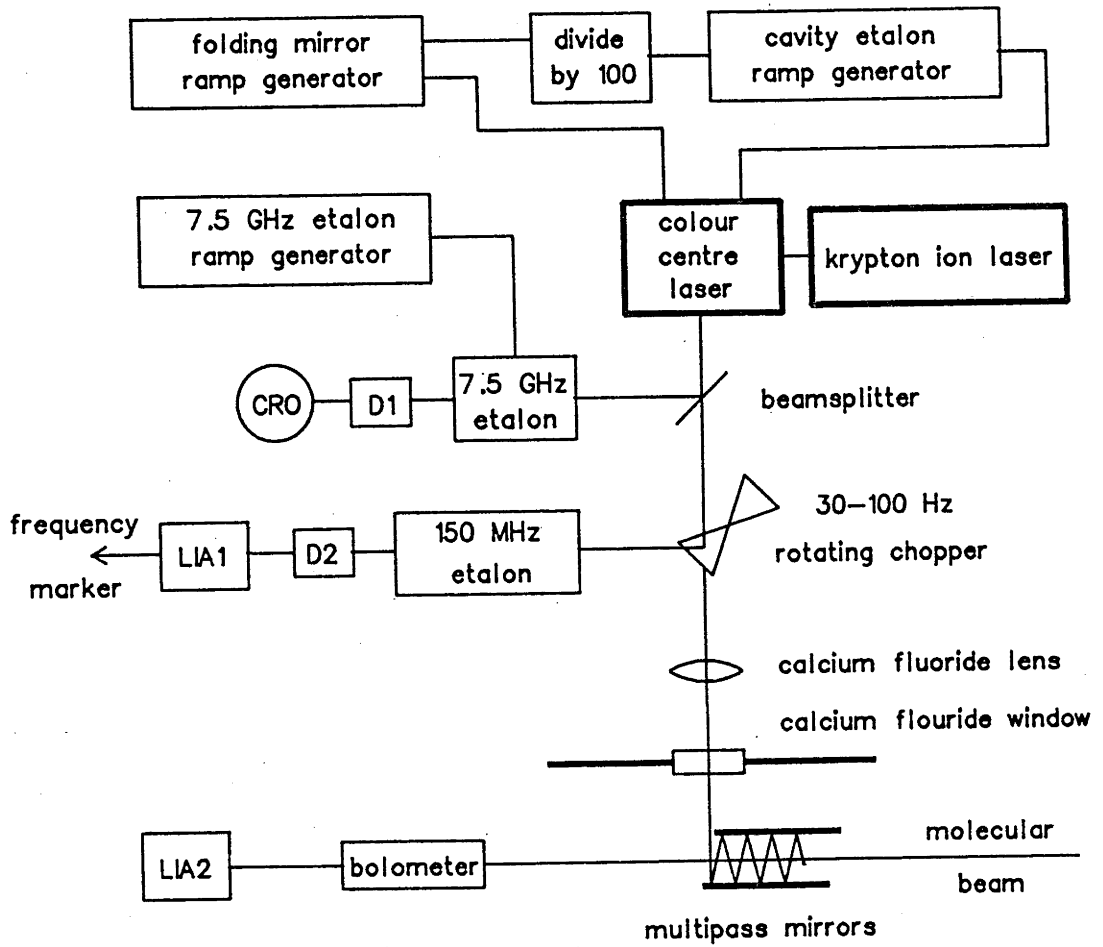


Figure 2.14

amplitude and duration of the folding mirror ramp. The maximum length of a single scan is determined by the maximum travel of the folding mirror and is approximately 3000 MHz (0.1 cm^{-1}). In practice, mode instabilities limited the maximum scan to about 2000 MHz (0.07 cm^{-1}).

It is possible to obtain longer continuous spectra by using features in the spectrum to splice together a series of consecutive, overlapping scans. To do this one adjusts the bias voltage applied to the cavity etalon PZT at the beginning of a new scan so that the (new) cavity mode being followed overlaps initially with the end of the previous scan. The maximum travel of the cavity etalon PZT and/or the position of the grating determine how many times this procedure can be repeated without having to re-optimize the grating position. The longest continuous single mode spectrum obtained in these studies was 0.4 cm^{-1} . If a sufficiently accurate absolute frequency calibration (for example, a wavemeter) had been available it would have been possible to routinely obtain extensive single mode spectra without having to rely on features in the spectra to match up consecutive scans.

By combining the narrow laser linewidth of $\leq 1 \text{ MHz}$ with the small transverse Doppler widths attainable with molecular beams it is possible to obtain spectra with an overall instrumental resolution as small as 3 MHz (0.0001 cm^{-1}) FWHM. Examples of such spectra are presented in Chapter 6. Typical single mode output powers are in the range 2-6 mW.

(c) Frequency Stabilized Operation

One way to monitor the number of molecules in a given quantum state in a molecular beam is by interrogating the beam with radiation which

can be absorbed by the quantum state in question. The total energy absorbed by the beam is directly proportional to the number of molecules which can absorb the radiation. By correcting such absorption signals for laser power variations, dipole oscillator strengths, degeneracies and saturation effects it is possible to obtain relative populations of different quantum states in a molecular beam. The details of these corrections are given in Section 2.6.

To make such measurements over an extended period of time the laser frequency must be accurately maintained at the centre of the desired absorption. This is done by dynamically adjusting the voltages applied to the folding mirror and cavity etalon PZT's to keep the frequency of the FCL output locked to that of the temperature stabilized 150 MHz etalon. The following procedure is used to obtain frequency stabilized operation :

- (1) Align the optics as shown in Figure 2.15. Leave the ramp generators on but unramped. A beamsplitter located before the mirrored chopper should direct a portion of the FCL output through the 150 MHz confocal etalon. The mirrored chopper should be off and positioned so that the reflected FCL output passes through the empty gas cell. A constant DC output should be seen on CRO2.

- (2) Apply a full amplitude linear ramp to the cavity etalon PZT. Use the ramp trigger to trigger the gas cell CRO. A series of steps (300 MHz wide) should be observed on the CRO as the laser hops from one cavity mode to the next. Allow a small amount of gas into the gas cell and rotate the grating until an absorption signal is seen on the CRO.

- (3) By decreasing the amplitude of the cavity etalon ramp to zero and simultaneously adjusting the ramp bias to keep the mode at the bottom of

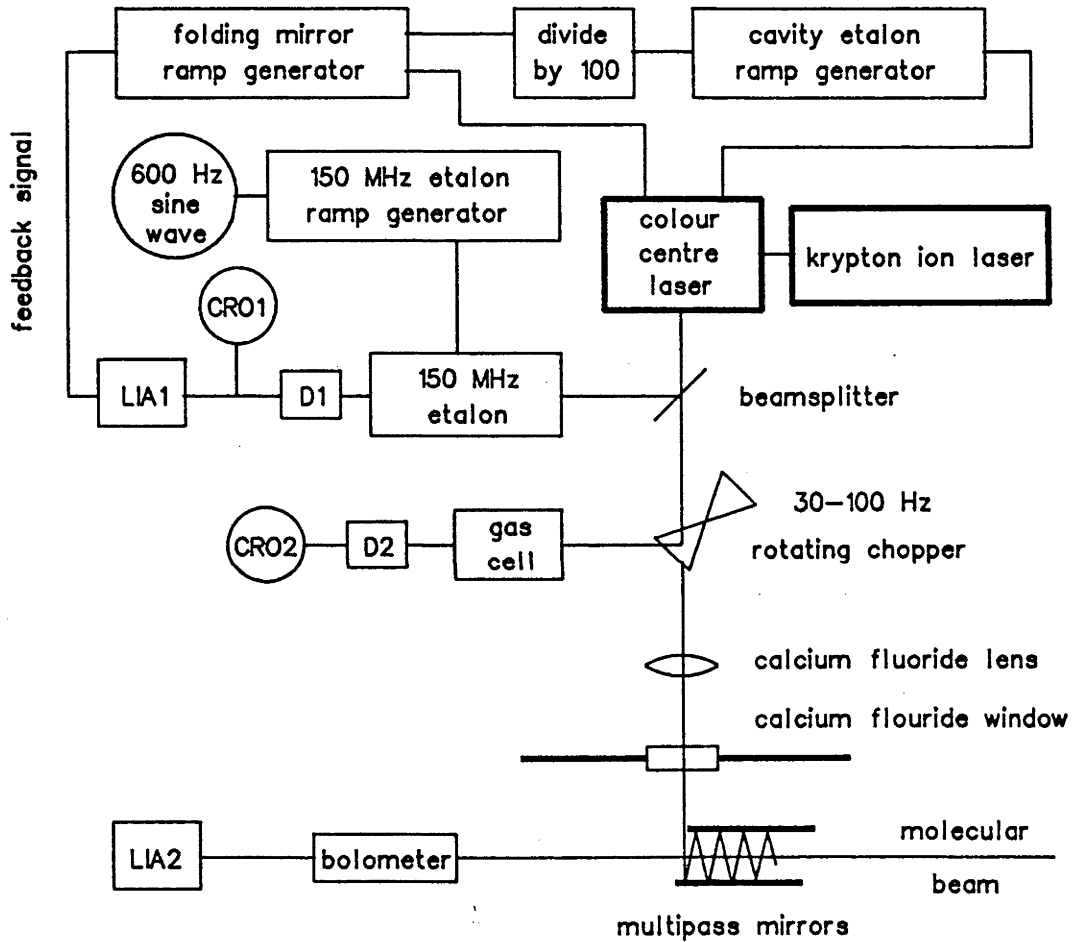


Figure 2.15

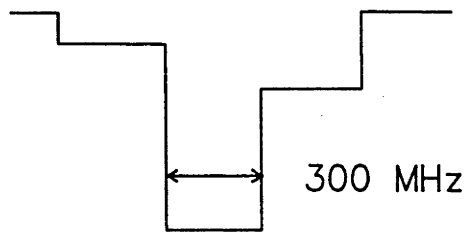
the absorption centred on CRO2 the resulting etalon separation is such that the FCL is lasing on a cavity mode located at the centre of the absorption. Turn off the internal ramp control for the cavity etalon PZT. A typical signal on CRO2 for an intermediate ramp amplitude is shown in the upper half of Figure 2.16.

(4) Apply a full linear ramp to the folding mirror PZT. Use the ramp trigger to trigger the gas cell CRO. Take the folding mirror ramp ± 100 and use it as the external input to the cavity etalon PZT controller. Increase the amplitude of the cavity etalon PZT controller until a continuous absorption profile, as shown in the lower half of Figure 2.16, is seen on CRO2. It may be necessary to make small changes to the cavity etalon bias to achieve this. Adjust the amount of gas in the gas cell until the absorption only just reaches 100% at line centre. [At this stage the ramps being applied to the cavity etalon and folding mirror PZT's have been locked together so that a single cavity mode is being scanned through the Doppler broadened absorption of the transition of interest.]

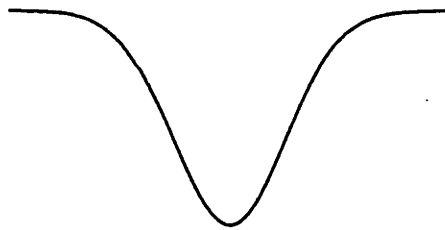
(5) Reduce the amplitude of the folding mirror ramp to zero while simultaneously adjusting its bias to keep the centre of the absorption centred on CRO2. Turn off the internal ramp of the folding mirror PZT controller. [The FCL is now lasing single mode at the centre of the desired transition. It is possible to continuously tune the laser through the absorption by adjusting the bias control of the folding mirror PZT controller. Alternatively, by applying a small amplitude ramp to the folding mirror PZT one can repeatedly scan through a small portion of the absorption.]

(6) Turn the chopper on. Make sure that no scattered laser radiation is reaching the detector. Adjust the folding mirror PZT bias voltage and

gas cell absorption profiles



ramping cavity etalon only



ramping cavity etalon and folding mirror together

Figure 2.16

align the laser-molecular beam crossing until the desired laser-induced molecular beam signal is observed. Thermal drift of the laser output is likely to move the frequency away from the desired absorption. At this stage one must lock the FCL output to the 150 MHz etalon.

(7) Apply a small amplitude audio frequency signal (a 600 Hz sine wave is adequate) to the external ramp input of the 150 MHz etalon PZT controller. Use the same signal to drive the reference channel of the lock-in amplifier which is used to monitor the intensity of the IR transmitted by the etalon. Connect the output of the LIA to the external input of the folding mirror PZT controller, making sure that its internal ramp generator is off and that its ramp amplitude is reduced to zero. By adjusting the bias of the 150 MHz etalon controller it is possible to scan a transmission peak of the etalon through the frequency of the FCL, which should still be freely drifting. Set the amplitude on the 150 MHz etalon ramp controller so that, as the etalon is scanned through the lasing mode, the signal observed on the LIA resembles the derivative of the etalon transmission profile. In achieving this it may be necessary to optimize the phase control of the LIA. Figure 2.17 shows typical transmission profiles (curves A and B) of the 150 MHz etalon at the extremities of the ramp applied to it. The output of the LIA (as a function of the FCL frequency) is proportional to the difference between these transmission signals (lower curve). When the signal transmitted by the etalon is observed directly on CRO1 it should resemble the signal used to ramp the etalon PZT except when the centre of the etalon transmission profile coincides with the FCL frequency, in which case one should observe a waveform whose frequency is twice the ramp frequency (see the figure). If the amplitude of the ramp is too large the transmitted waveform will not

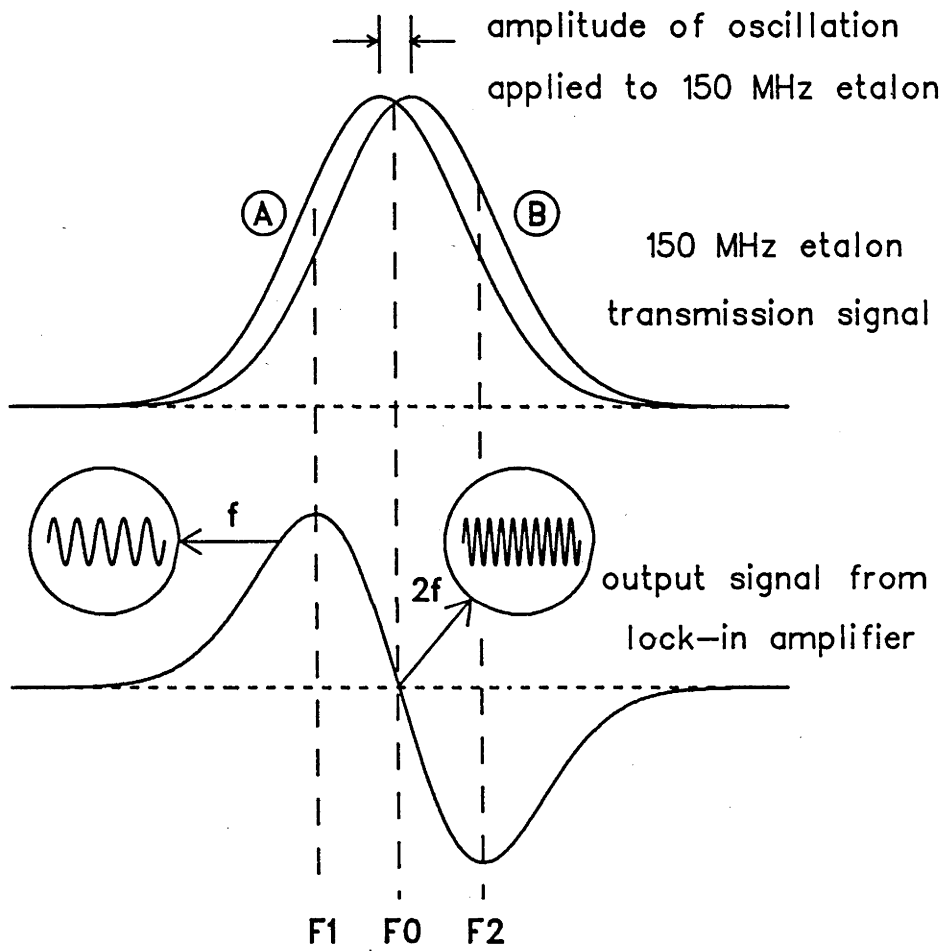


Figure 2.17

resemble the ramp signal and (in the extreme case) the corresponding LIA output will consist of two separated peaks. When correctly optimized, the LIA output is the desired error signal which will be used to lock the FCL frequency to that of the etalon.

(8) Adjust the bias voltage on the 150 MHz etalon ramp to centre the transmission profile about the lasing cavity mode. Now increase the folding mirror ramp amplitude (which controls the degree of feedback) to lock the FCL frequency to that of the etalon transmission peak. Note that, if the sign of the LIA output is incorrect, the feedback signal will drive the FCL frequency away from that of the 150 MHz etalon. The output of the LIA will change in order to compensate for frequency changes in the FCL output. The voltage applied to the folding mirror PZT is the sum of the feedback signal and the internal bias voltage of its ramp controller. Any small change made to this bias voltage will be compensated for by an identical change (of opposite sign) in the feedback signal. The feedback circuit is such that there is a maximum feedback signal which can be generated. Frequencies F1 and F2 in Figure 2.17 correspond to the maximum +ve and -ve feedback signals possible. It is therefore necessary to periodically shift the bias voltage on the folding mirror PZT controller to keep the feedback voltage below its maximum value in order to maintain the desired frequency lock.

(9) Having locked the FCL to the 150 MHz etalon, its frequency can be varied by adjusting the bias on the 150 MHz etalon PZT controller. This shifts the frequency of the etalon mode to which the FCL is locked. Although the cavity etalon was originally centred on the lasing cavity mode, thermal drift in the FCL may destroy this coincidence, with the result that the FCL will mode hop to an adjacent cavity mode. To return

the FCL to the original cavity mode and re-establish the frequency lock the cavity etalon transmission profile is shifted by altering the bias voltage of the cavity etalon PZT controller. If the frequency lock is lost, it can be regained by adjusting the folding mirror bias voltage in order to shift the cavity mode until it once again coincides with the transmission frequency of the 150 MHz etalon.

In summary, the FCL can be used in conjunction with molecular beam techniques and phase sensitive bolometric detection to : (1) obtain low resolution ($\sim 0.5 \text{ cm}^{-1}$) infrared spectra of the species in the beam, (2) obtain high resolution (a few MHz) single mode scans of individual transitions and (3) determine the relative populations of the quantum states of molecules in the beam.

2.6 Quantum State Distributions in Molecular Beams

It was mentioned in the previous section that by tuning the colour centre laser to particular molecular absorptions and measuring the energy absorbed by the molecular beam it is possible to determine the relative populations of the ground states of the probed transitions. During the course of this thesis such measurements were performed for hydrogen fluoride. The colour centre laser is tuned so that it excites a single vibrational quantum ($v=0 \rightarrow v=1$) either in the $P(j \rightarrow j+1)$ or the $R(j \rightarrow j-1)$ branch. The energy E_i absorbed by the molecular beam, assuming that saturation effects are negligible, is given by

$$E_i \propto (N f_i) P |\mu_{ij}|^2 \lambda^{-2} \quad (2.2)$$

where N is the molecular flux of the species of interest (in molecules/m²/sec) whose trajectories pass through the laser beam and terminate at the bolometer, f_i is the fraction of these molecules in the ground state of the transition of interest, P is the laser power available for excitation, λ is the wavelength of the transition and $|\mu_{ij}|^2$ is the square of the dipole moment transition matrix element. For R-branch transitions one has

$$|\mu_{ij}|^2 = \mu_{0 \rightarrow 1}^2 \left(\frac{j+1}{2j+1} \right) \quad (2.3)$$

and for P-branch transitions

$$|\mu_{ij}|^2 = \mu_{0 \rightarrow 1}^2 \left(\frac{j+1}{2j+3} \right) \quad (2.4)$$

where $\mu_{0 \rightarrow 1}^2$ is the dipole oscillator strength for the $v=0$ to $v=1$ vibrational transition. The product Nf_i is proportional to the total molecular flux at the point of laser excitation in the ground state of the excited transition. By taking the ratios of Eq. (2.2) for different transitions $i \rightarrow j$ it is possible to determine the relative populations, proportional to Nf_i , of the rotational states of a given beam. To check the accuracy of the technique, the results obtained using P and R branch transitions, which should coincide, can be compared.

2.7 Differential Scattering Cross Section Measurements

The total differential scattering cross section measurements reported in this thesis were obtained using bolometer A (described in Section 2.4) with the cryostat was mounted in the near position, as shown in broken lines in Figure 2.1. A schematic diagram of the experimental arrangement is shown in Figure 2.18 and values of the parameters describing the geometry are given in Table 2.3. In all cases the secondary beam divergence was such that all points on the surface of the bolometer had an unobstructed view of the whole scattering volume. A narrow primary beam (FWHM = 1.5°) is obtained by using a second skimmer to further collimate the primary beam. This beam is intersected with a chopped secondary beam (angular FWHM in the range $5-12^\circ$) at the axis of rotation of the base flange. The beams are formed from supersonic expansions of the (pure) gases of interest, with the lighter mass species in the primary beam. Scattered primary beam molecules can be detected at different laboratory scattering angles θ_L by rotating the base flange, onto which the beam sources are fixed, in order to vary the orientation of the beams with respect to the bolometer.

By chopping the secondary beam using a 50% duty cycle rotating chopper, and using the chopping frequency as the reference to the lock-in amplifier used to monitor the bolometer output, one obtains a signal which depends upon the number of primary beam molecules scattered to the detector by colliding with secondary beam molecules. A microcomputer is used integrate (ie. average) the output of the lock-in amplifier for each individual measurement. Integration times vary between 15 seconds and about 10 minutes, depending upon the signal-to-noise ratio of the lock-in

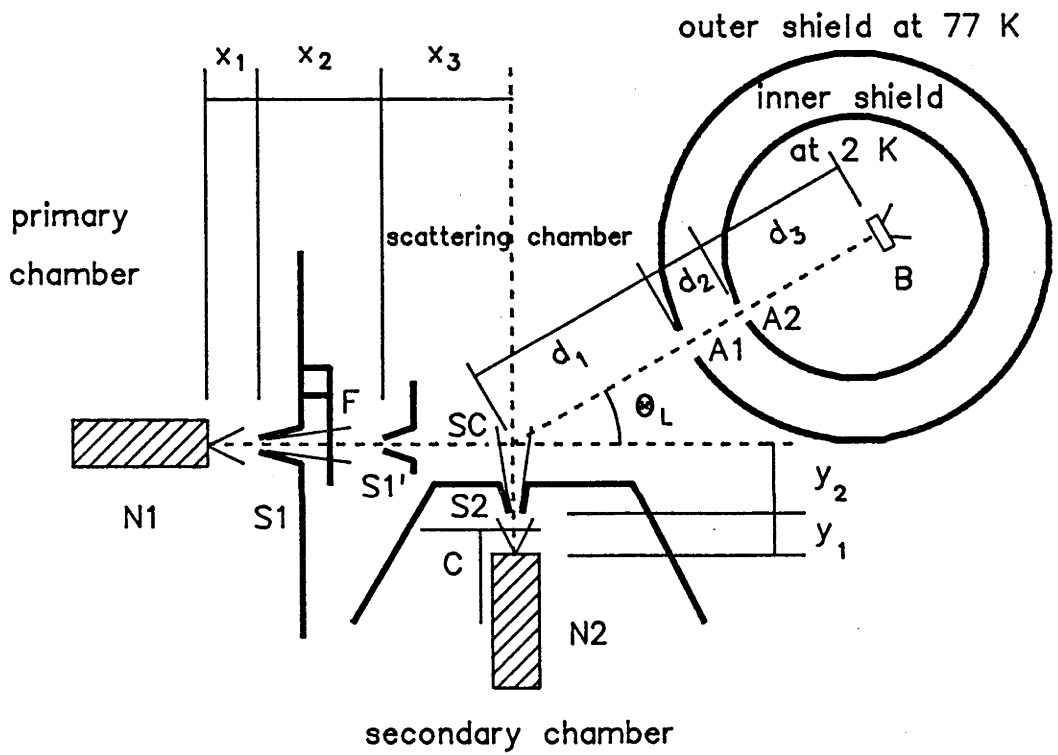


Figure 2.18

Table 2.3

parameter	value (mm)
x_1	10-15
x_2	50
x_3	50
$L=x_2+x_3$	100
y_1	10-15
y_2	18.3
d_1	56
d_2	30
d_3	66
$D=d_1+d_2+d_3$	152

aperture A1 : rectangular 3x6 mm

long axis vertical

aperture A2 : circular, 7 mm diameter

amplifier output. In order to eliminate any contribution to the bolometer signal which does not result from scattered primary beam molecules, the measurements are carried out with and without the primary beam blocked and the resulting signals are subtracted. To correct the experimental data for any slow variations in either the intensities of the beams or the responsivity of the bolometer, the scattering signal at 5 degrees is remeasured periodically and all recorded data are normalized to these values. It should be noted that, except at very large scattering angles, the number of secondary beam molecules scattered onto the bolometer as a result of collisions with primary beam molecules is negligible. If the mass of the secondary beam molecules is sufficiently large there may be no such contribution at all.

The bolometer, being an energy detector, has a detection efficiency which is proportional to mv^2 , where m and v are the mass and speed of the detected particle. When comparing experiment with theory this needs to be taken into account. The techniques used to compare a theoretical cross section with an experimental one are discussed in Chapter 3.

2.8 Time-of-flight Measurements

A rotating slotted-disc chopper was used with the mass spectrometer and a multichannel analyser (MCA) to obtain the velocity distributions of the molecules in the beams. A schematic diagram of the experimental arrangement is shown in Figure 2.19, where $R = 53$ mm, $w = 0.8$ mm, $d \approx 700$ mm and $q \approx 180$ mm. Two rectangular slots are centred on opposite ends of a diameter of the disc. As one slot coincides with the molecular beam the other one activates an emitter-detector which is used to trigger the MCA sweep. The bin separation of the MCA is $10 \mu\text{s}$. The chopper was operated at 400 Hz, resulting in molecular pulses $6 \mu\text{s}$ wide separated by 1.25 ms. As a pulse of molecules travels to the ionizer, at the front end of the mass spectrometer, it spreads out as a result of the distribution of the velocities of the molecules. By analysing the distribution of the detected molecules as a function of time one can obtain the mean speed and the FWHM of the velocity distribution (see, for example, Anderson and Fenn (1965)).

In practice the emitter-detector is not perfectly located, resulting in a slight offset between the trigger pulse and the molecular pulse start time. The size of the offset is determined by comparing the arrival time spectrum for clockwise disc rotation and triggering on the leading edge of the emitter-detector pulse with the one obtained using anti-clockwise rotation and triggering on the trailing edge of the emitter-detector pulse. It is also necessary to subtract the mass dependent ion flight time through the quadrupole region. In terms of the ion energy $E_i = 15$ eV upon entering the quadrupole region the transit time is

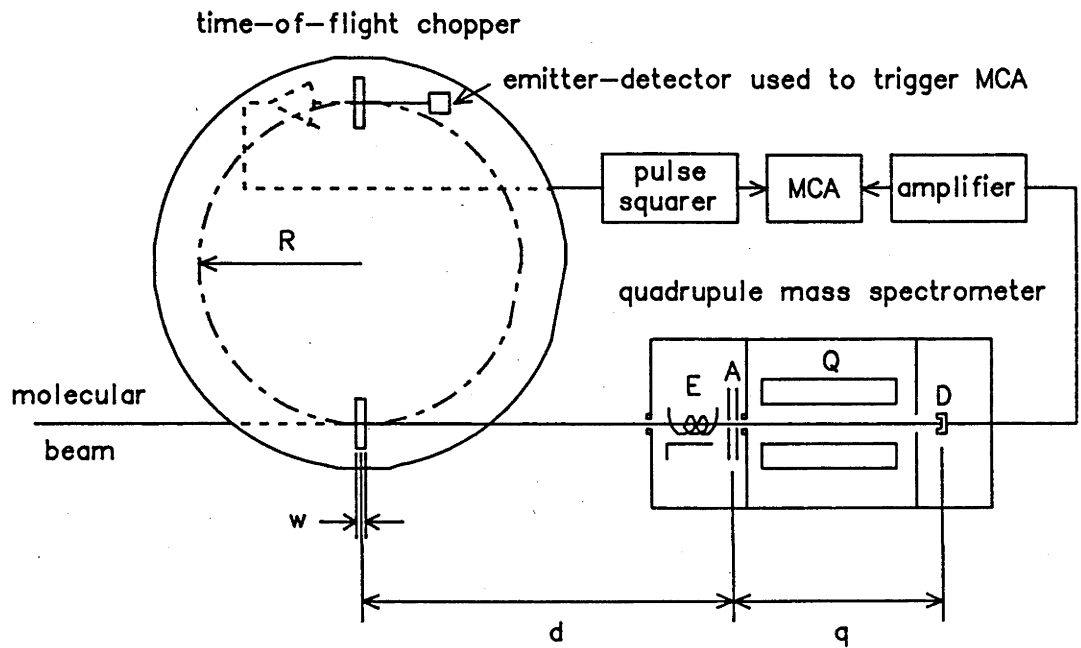


Figure 2.19

$$t_q = q / v_q \quad (2.5)$$

where

$$v_q = (2E_i / m)^{1/2} \quad (2.6)$$

After making these two corrections to the flight time the resulting time-of-flight spectra can be deconvoluted to obtain the desired velocity distributions. The velocity of a molecule is related to its flight time over the distance d by

$$v = d/t \quad \text{and} \quad dv/dt = -d/t^2 \quad (2.7)$$

Assuming that the molecules in the beam obey a shifted v^3 Maxwell-Boltzmann distribution, and correcting for the $1/v$ ionization efficiency, the resulting velocity distribution is

$$f(v) = A v^2 \exp[-((v-v_s)/v_w)^2] \quad (2.8)$$

The corresponding TOF spectrum is

$$f(t) = B t^{-4} \exp[-f (1/t - g)^2] \quad (2.9)$$

where A , v_s , v_w , B , f and g are constants which specify the distributions. The values of B , f and g are related to those of A , v_s and v_w . By fitting a function of the form of Eq. (2.9) to the corrected TOF spectrum it is

possible to obtain estimates of v_s , the stream velocity, and v_w , the width parameter. The most probable speed v_{mp} of the corresponding v^3 Maxwell-Boltzmann distribution is given by

$$v_{mp} = \frac{1}{2} \left[v_s + \left(v_s^2 + 6v_w^2 \right)^{\frac{1}{2}} \right] \quad (2.10)$$

To account for the 10 μ s bin separation of the MCA and the 6 μ s widths of the initially formed pulses of molecules the calculated TOF distributions were also averaged in time. The functions which were fitted to the experimental distributions had the form

$$f_0(t) = \int_{-8 \mu s}^{8 \mu s} f(t+t') dt' \quad (2.11)$$

with $f(t)$ given by Eq. (2.9). In all cases least squares minimization of the sum of squared deviations was used to obtain the desired fits. It is also necessary, in principle, to account for the finite length of the ionizing region. This requires that one calculate TOF spectra for a range of flight distances d , which appears explicitly in Eq. (2.7), and then average these spectra over d . The inclusion of this latter correction was found to have a negligible effect upon the results of the analysis, primarily because of the long flight distance (~ 70 cm) compared to the length of the ionizing region (≤ 2 cm).

The effective flight distance d was determined by equating the stream velocity obtained from the TOF distribution for the pure helium expansion at 310 ± 2 K with that calculated by assuming an ideal isentropic expansion at the same temperature. For such an ideal expansion the stream velocity v_s is given by (Bernstein (1982))

$$v_s = \left[\frac{2kT}{m} \frac{\gamma}{\gamma-1} \right]^{\frac{1}{2}} \quad (2.12)$$

where $\gamma = C_p/C_v$ is the specific heat ratio. For a monatomic gas one has

$$v_s = 203.889 \left(\frac{T(K)}{m(\text{amu})} \right)^{\frac{1}{2}} \quad (2.13)$$

and for a diatomic

$$v_s = 241.245 \left(\frac{T(K)}{m(\text{amu})} \right)^{\frac{1}{2}} \quad (2.14)$$

The stream velocity for an ideal helium expansion at 310 ± 2 K is $v_s = 1794 \pm 6$ m/s. By equating this with the stream velocity obtained from the corresponding experimental TOF spectrum the effective flight distance d was found to be 70.30 ± 0.35 mm.

The experimental TOF distributions for the gas mixtures of interest are shown in Figure 2.20 together with the resulting theoretical fits. Velocity distributions corresponding to these spectra appear in Figure 2.21 and the parameters describing these distributions are given in Table 2.4, along with the nozzle temperatures T_0 . As expected, the results were found to be almost independent of the stagnation pressure for the range of pressures used. In Table 2.5, the root-mean-square collision speeds g_{rms} and the mean collision energies are given for a number of beam-beam and beam-(300 K Boltzmann gas) collision pairs. For the beam-beam results, g_{rms}^2 was assumed to be the sum of the mean square speeds of the beam velocity distributions. This approximation is expected to be good for the case of right angle collisions and narrow velocity

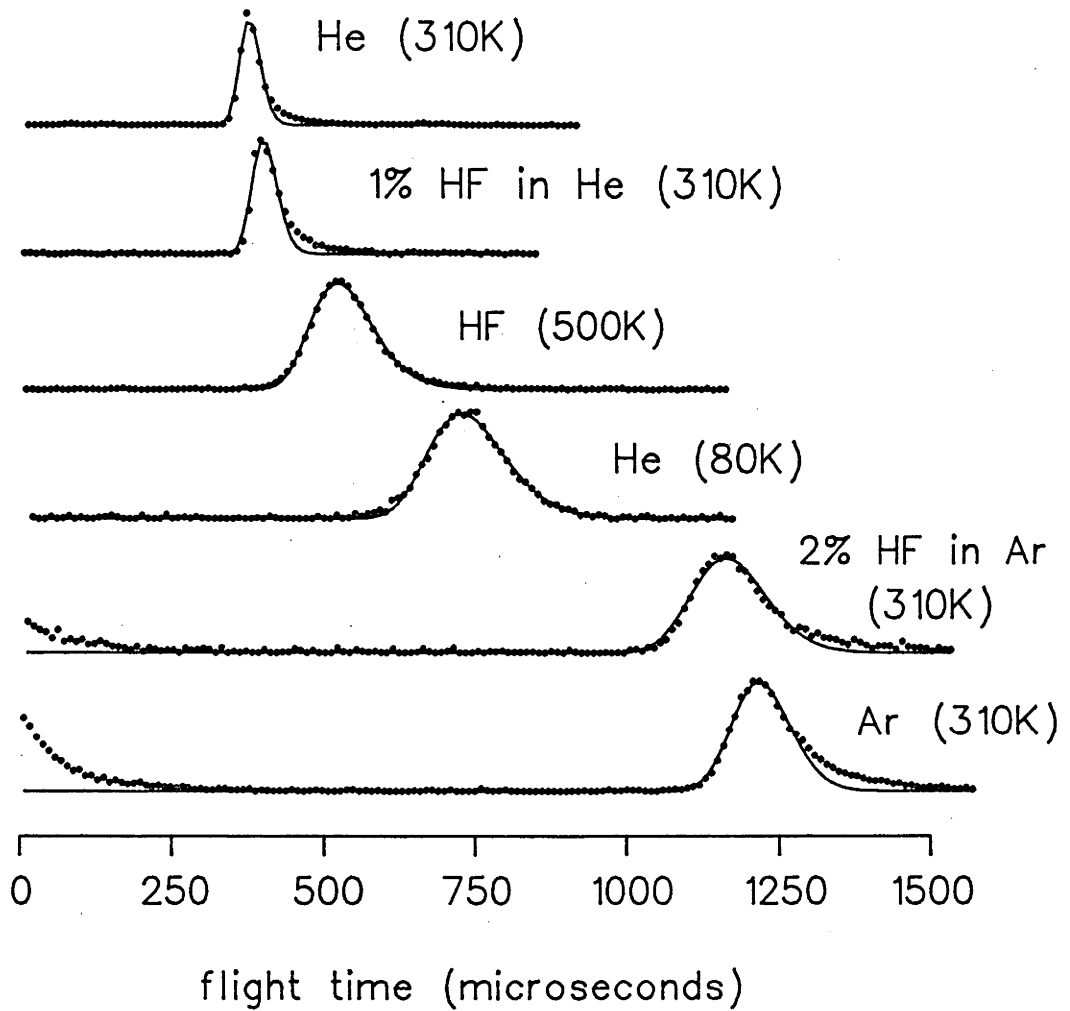


Figure 2.20

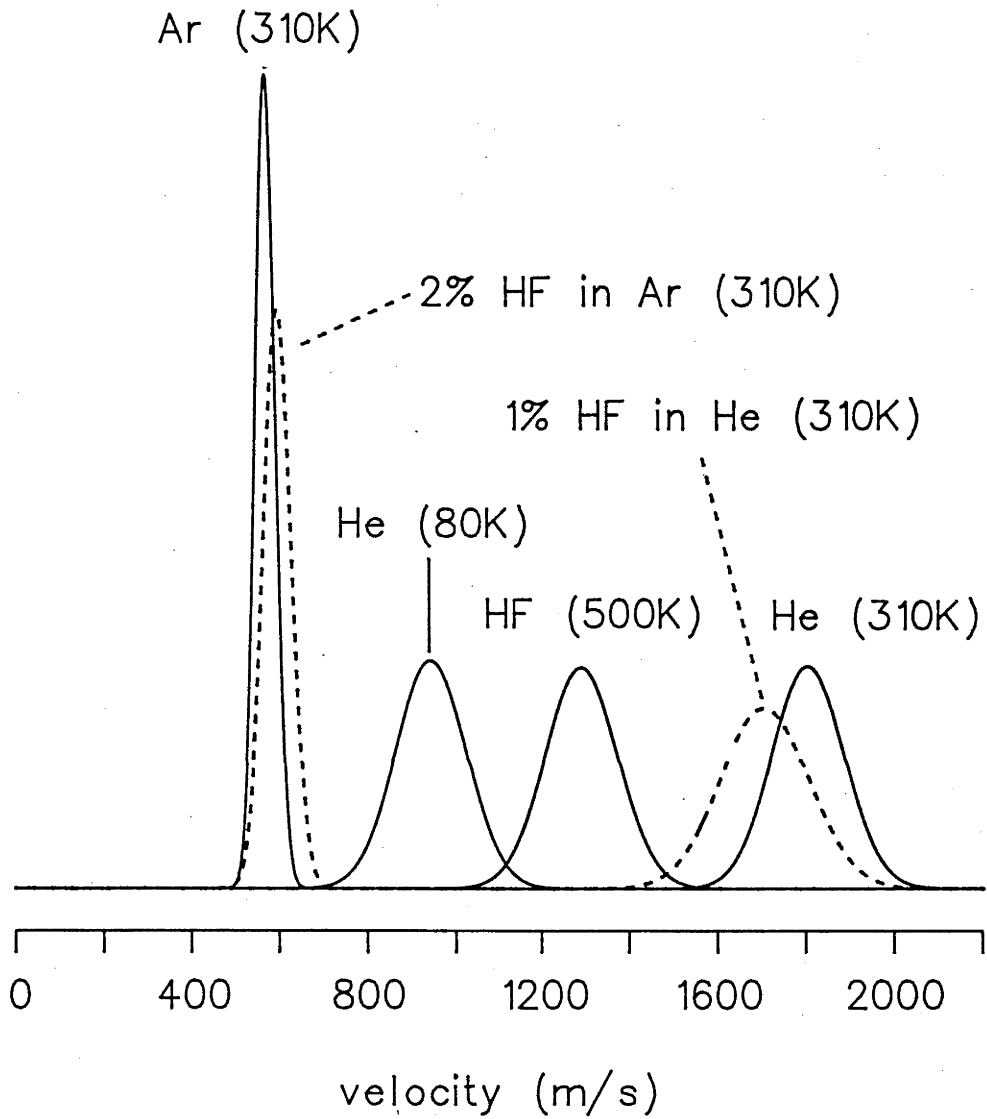


Figure 2.21

Table 2.4

gas	T ₀ (K)	v _S (m/s)	v _W (m/s)	v _{mp} (m/s)	Δv(%)	T'(K)	S	E(K)	E(meV)
Ar	310	571	32	574	9	313	17.8	792.	68.2
N ₂	310	788	78.5	800	16	299	10.0	1082.	93.2
He	≈ 80	927	114	948	20	83	8.1	218.	18.8
HF	≈ 500	1273	177	1289	22	557	7.2	2008.	173.0
He	310	1794	116	1805	14	310	15.5	786.	67.7
H ₂	310	2845	138	2855	8	278	20.6	982.	84.6
HF/Ar [†]	310	595	45	600	12	-	13.2	434.	37.4
HF/He [†]	310	1688	143	1706	14	-	11.8	3513.	302.7

[†] these mixtures are 2 % HF in Ar and 1 % HF in He. The results are for the HF component.

Table 2.5

collision pair	$\mu(\text{amu})$	E(K)	E(meV)	$g_{\text{rms}}(\text{m/s})$
He - Ar	3.64	787	67.8	1869
He(80K) - HF	3.34	516	44.5	1604
He - HF	3.34	990	85.3	2221
H ₂ - N ₂	1.87	988	85.2	2967
H ₂ - HF	1.82	1075	92.6	3136
HF - HF	10.00	2008	173.0	1827
Ar - HF	13.33	1602	138.0	1414
HF/He - HF(beam)	10.00	2142	238.0	2760
HF/Ar - HF(beam)	10.00	1221	105.0	1425
HF/He - HF(Boltz)	10.00	1985	171.0	1817
HF/Ar - HF(Boltz)	10.00	446	38.4	861

distributions. The beam-(Boltzmann gas) values were obtained by averaging over both the possible collision angles and the relevant speed distributions.

Chapter ThreeScattering Calculations

In order to study the scattering processes in a given atom-diatom system it is necessary to solve the Schrödinger equation for that system. The formulation of this problem and its solution are well documented in the literature. See, for example, the books by Bernstein (editor) (1979), Child (1974), Farina (1973), Fluendy and Lawley (1973), and the references contained therein. In this thesis the coupled states (CS), infinite order sudden (IOS) and spherical potential approximations have been used to investigate the total and inelastic cross sections for the He-HF and Ar-HF systems. An outline of the approximations and the techniques used to perform the calculations is presented in this chapter.

After an introduction to the scattering problem for the case of a spherical interaction potential the following topics are discussed: atom-diatom scattering; the spherical potential approximation; the IOS method; the coupled states approximation; the matrix elements of the atom-diatom interaction potential in the CS approximation; the solution of the CS equations; and the comparison of a calculated differential cross section with an experimentally determined one.

3.1 Introduction

In this section we consider the scattering of two unlike particles A and B with no internal degrees of freedom interacting via the spherical potential $V(r)$, where r is the distance between the particles. The Schrödinger equation for the two particles is (Watts and McGee (1976))

$$\left[-\frac{\hbar^2}{2m_A} \nabla_{\underline{r}_A}^2 - \frac{\hbar^2}{2m_B} \nabla_{\underline{r}_B}^2 + V(|\underline{r}_A - \underline{r}_B|) \right] \Psi_T(\underline{r}_A, \underline{r}_B) = E_T \Psi_T(\underline{r}_A, \underline{r}_B) \quad (3.1)$$

where \underline{r}_A and \underline{r}_B are the positions of the particles, E_T is the total energy, Ψ_T is the total wavefunction and \hbar is Planck's constant divided by 2π . Let \underline{R}_{cm} denote the centre of mass coordinate and \underline{r} the relative separation. By assuming that Ψ_T can be written as the product of functions of \underline{R}_{cm} and \underline{r} as

$$\Psi_T(\underline{r}_A, \underline{r}_B) = \Psi_{cm}(\underline{R}_{cm}) \Psi(\underline{r}) \quad (3.2)$$

Eq. (3.1) can be factorized into an equation for $\Psi_{cm}(\underline{R}_{cm})$,

$$-\frac{\hbar^2}{2(m_A+m_B)} \nabla_{\underline{R}_{cm}}^2 \Psi_{cm}(\underline{R}_{cm}) = E_{cm} \Psi_{cm}(\underline{R}_{cm}) \quad (3.3)$$

and an equation for the relative motion in the centre of mass frame

$$\left[-\frac{\hbar^2}{2\mu} \frac{1}{r} \frac{\partial^2}{\partial r^2} r + \frac{\hat{l}^2}{2\mu r^2} + V(r) \right] \Psi(\underline{r}) = E \Psi(\underline{r}) \quad (3.4)$$

where $E_T = E_{cm} + E$, E is the relative collision energy and μ is the reduced

mass. If \underline{v}_A and \underline{v}_B are the velocities before the collision then $E = \frac{1}{2}\mu v_r^2$, where $\underline{v}_r = \underline{v}_A - \underline{v}_B$ is the initial relative velocity. The orbital angular momentum operator \hat{l} is related to the Laplacian ∇_r^2 by

$$-\frac{\hbar^2}{2\mu} \nabla_r^2 = -\frac{\hbar^2}{2\mu} \frac{1}{r} \frac{\partial^2}{\partial r^2} r + \frac{\hat{l}^2}{2\mu r^2} \quad (3.5)$$

We now express Eq. (3.4) in terms of spherical polar coordinates $\underline{r} = (r, \theta, \phi)$ and, using the technique of separation of variables, attempt to find a solution of the form

$$\phi(\underline{r}) = \frac{1}{r} T(\theta) P(\phi) u(r) \quad (3.6)$$

where the term $1/r$ has been included because it will lead to simpler equations in the subsequent analysis. If $\phi(\underline{r})$ is substituted into Eq. (3.4) then the resulting equations can be solved for the angular functions, with the general solutions being (Edmonds (1974))

$$T(\theta) P(\phi) = Y_{lm}(\theta, \phi) \quad (3.7)$$

where the Y_{lm} are the spherical harmonics and are the simultaneous eigenfunctions of \hat{l}^2 and $\hat{l}_z = -i\hbar\partial/\partial\phi$, the z-component of the orbital angular momentum operator. l is the orbital angular momentum quantum number and m is the z-component of the orbital angular momentum. We choose the z-axis to lie along the initial relative velocity so that the orbital angular momentum vector will always be perpendicular to the z-axis and we need therefore consider only those spherical harmonics with $m=0$.

The next step is to use these angular eigenfunctions to expand the desired solution $\Psi(\underline{r})$ to Eq. (3.4) according to

$$\Psi(\underline{r}) = \sum_l A_l \frac{1}{r} P_l(\cos\theta) u_l(r) \quad (3.8)$$

noting the result $Y_{10}(\theta, \phi) = P_1(\cos\theta)$, where P_1 is a Legendre polynomial (Edmonds (1974)). The radial functions $u_l(r)$ are determined by the requirement that $\Psi(\underline{r})$ be a solution to Eq. (3.4) and the coefficients A_l are chosen to ensure that $\Psi(\underline{r})$ has the asymptotic (large r) form

$$\Psi(\underline{r}) \sim e^{i\underline{k} \cdot \underline{r}} + F(\Omega) \frac{e^{ikr}}{r} \quad (3.9)$$

where $\hbar \underline{k} = \mu \underline{v}_r$ defines the initial wavevector \underline{k} for the collision. It can be shown (Farina (1973)) that both terms of Eq. (3.9) are solutions to Eq. (3.4) for large r . $e^{i\underline{k} \cdot \underline{r}}$ represents a plane wave travelling with the initial relative momentum $\hbar \underline{k}$ and corresponds to a constant flux of unscattered particles. The second term is an outgoing spherical wave and represents the outward flux of particles resulting from the interaction $V(r)$. The differential scattering cross section in the direction $\Omega = (\theta, \phi)$ is related to the scattering amplitude $F(\Omega)$ by (Farina (1973))

$$\frac{d\sigma}{d\Omega}(\Omega) = |F(\Omega)|^2 \quad (3.10)$$

where $\Omega = (\theta, \phi)$ is the scattering angle in the centre of mass reference frame.

To proceed further one substitutes the expansion given by Eq. (3.8) into Eq. (3.4), multiplies the equation by $P_l(\cos\theta)$, integrates $\int_{-1}^1 \dots d\cos\theta$ and replaces l' by l to obtain the following equation for the radial wavefunction $u_l(r)$:

$$\left[-\frac{\hbar^2}{2\mu} \frac{d^2}{dr^2} + \frac{l(l+1)\hbar^2}{2\mu r^2} + V(r) \right] u_l(r) = E u_l(r) \quad (3.11)$$

where we have used the orthogonality of the Legendre polynomials (Edmonds (1974))

$$\int_{-1}^1 P_l(\cos\theta) P_{l'}(\cos\theta) d\cos\theta = \frac{2\delta_{ll'}}{(2l+1)} \quad (3.12)$$

and the fact that

$$\hat{l}^2 Y_{lm}(\theta, \phi) = l(l+1)\hbar^2 Y_{lm}(\theta, \phi) \quad (3.13)$$

If $V(r) \rightarrow 0$ faster than $1/r^2$ as $r \rightarrow \infty$ then the general solution to Eq. (3.11) is, for sufficiently large r , (Fluendy and Lawley (1973))

$$u_l(r) \sim B_l \hat{j}_l(kr) + C_l \hat{n}_l(kr) \quad (3.14)$$

where \hat{j}_l and \hat{n}_l are Ricatti-Bessel functions (Abramowitz and Stegun (1970)) and B_l and C_l are constants. For $u_l(r)$ to represent a physically meaningful solution we require that $u_l(r) \rightarrow 0$ as $r \rightarrow 0$. The asymptotic forms $\hat{j}_l(kr) \sim \sin(kr + l\pi/2)$ and $\hat{n}_l(kr) \sim \cos(kr + l\pi/2)$ determine the large r behaviour of $u_l(r)$.

Consider first the case where $V(r) = 0$ for all r . The solution to Eq. (3.11) is then given by Eq. (3.14) for all r . Noting that $\hat{j}_l(x) \sim x^l$ and $\hat{n}_l(x) \sim 1/x^{l+1}$ as $x \rightarrow 0$, it is necessary to choose $C_l = 0$ so that $u_l(r) \rightarrow 0$ as $r \rightarrow 0$. The asymptotic form of $u_l(r)$ is therefore

$$u_l(r) \sim B_l \sin(kr - l\pi/2) \quad (3.15)$$

When $V(r)$ is non-zero the value of C_l in Eq. (3.14) is in general

not zero, resulting in the asymptotic form (after simplification)

$$u_1(r) \sim D_1 \sin(kr - l\pi/2 + \eta_1) \quad (3.16)$$

where $D_1 = B_1/\cos\eta_1$ and the phase shift η_1 is given by

$$\eta_1 = \tan^{-1}(C_1/B_1) \quad (3.17)$$

The effect of the potential $V(r)$ is therefore to introduce shifts η_1 to the phases of the radial waves.

Having determined the radial wavefunctions $u_1(r)$ by integrating the radial equations, the final step in the solution is to relate the phase shifts η_1 to the scattering amplitude $F(\Omega)$. To do this one substitutes Eq. (3.16) into Eq. (3.8) and chooses the coefficients A_1 in such a way that the asymptotic behaviour of $\Psi(\underline{r})$ is given by Eq. (3.9). If the $u_1(r)$ are normalized so that the D_1 in Eq. (3.16) are unity then the desired large r behaviour will result if the A_1 are chosen according to (Farina (1973))

$$A_1 = \frac{1}{k} (2l+1) i^l e^{i\eta_1} \quad (3.18)$$

The corresponding expression for the scattering amplitude, which is independent of ϕ if $V(r)$ is spherically symmetric, is

$$F(\theta) = \frac{1}{2ik} \sum_l (2l+1) [e^{2i\eta_1} - 1] P_l(\cos\theta) \quad (3.19)$$

The differential cross section can be obtained from Eq. (3.10) and the integral cross section is given by

$$\sigma = \frac{4\pi}{k^2} \sum_1 (2l+1) \sin^2 \eta_l \quad (3.20)$$

In summary, the cross sections for spherical potential scattering in the centre of mass frame are obtained by : (1) integrating the radial wave equations, Eq. (3.11), for the radial wave functions $u_l(r)$, (2) matching these solutions to the asymptotic form (3.14), (3) computing the phase shifts from Eq. (3.17) and (4) using Eqs (3.10) and (3.20) to evaluate the desired cross sections.

This concludes our summary of the scattering resulting from a spherical potential. In the remainder of this chapter we turn our attention to the calculation of the scattering behaviour of atom-diatom systems. The analysis of atom-diatom scattering closely parallels that presented in this section for a spherical interaction potential.

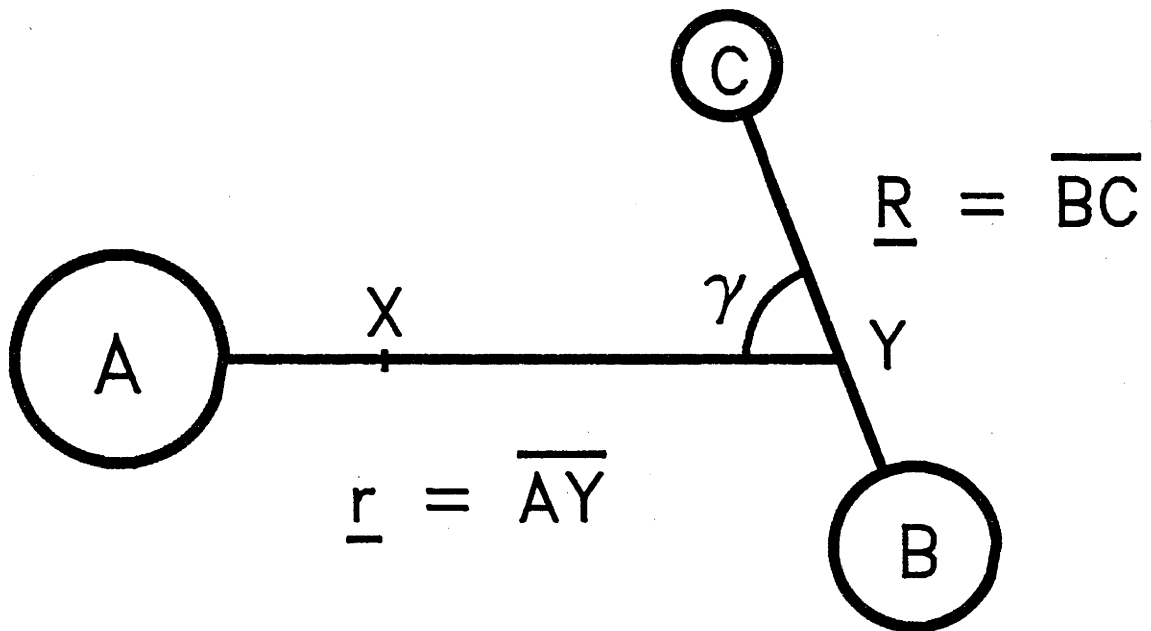
3.2 Atom-Diatom Scattering

The theory of atom-diatom scattering is discussed in most books on scattering theory and is reviewed in many of the publications in the field. A summary of the theory following the treatment of Arthurs and Dalgarno (1960) is presented in this section.

Figure 3.1 shows the coordinates describing an atom-diatom system. \underline{r} is the vector joining the atom A to the diatom centre of mass and \underline{R} is the diatom coordinate vector. The interaction potential for the system is written as $V(r,R,\cos\gamma)$, where $\cos\gamma = \hat{\underline{r}} \cdot \hat{\underline{R}}$. One obtains the scattering cross sections by solving the Schrödinger equation for the atom-diatom system. In a non-rotating centre of mass coordinate system the Schrödinger equation describing the interaction is

$$\left[-\frac{\hbar^2}{2\mu} \frac{1}{r} \frac{\partial^2}{\partial r^2} r + \frac{\hat{l}^2}{2\mu r^2} + V(r,R,\cos\gamma) \right. \\ \left. + \left(-\frac{\hbar^2}{2\mu_{BC}} \frac{1}{R} \frac{\partial^2}{\partial R^2} R + \frac{\hat{j}^2}{2\mu_{BC} R^2} + W(R) \right) \right] \Psi(\underline{r},\underline{R}) = E \Psi(\underline{r},\underline{R}) \quad (3.21)$$

where $W(R)$ is the isolated diatom potential, E is the sum of the initial relative kinetic energy and the initial diatom internal energy, \hat{l}^2 is the square of the orbital angular momentum operator, \hat{j}^2 is the square of the diatom rotational angular momentum operator and μ_{BC} and μ are the reduced masses of the diatom and of the A-BC system respectively. The scattering from a given initial diatom state (labeled by i) is obtained from that solution of Eq. (3.21) whose asymptotic (large r) behaviour is (compare with Eq. (3.9))



X = Centre of mass of ABC

Y = Centre of mass of diatom BC

Figure 3.1

$$\Psi_i(\underline{r}, \underline{R}) \sim e^{i\mathbf{k}_i \cdot \underline{r}} \chi_i(\underline{R}) + \sum_f \frac{e^{ik_f r}}{r} F(f; i | \Omega) \chi_f(\underline{R}) \quad (3.22)$$

where $\chi_i(\underline{R})$ and $\chi_f(\underline{R})$ represent the initial and possible final eigenstates of the diatom, $k_\alpha^2 = 2\mu(E - E_\alpha) / \hbar^2$ defines the wavevector corresponding to the diatom state with internal energy E_α and $\hbar \mathbf{k}_i = \mu \mathbf{v}_r$, where \mathbf{v}_r is the initial relative velocity. The diatom states are described by the quantum numbers v, j and m , the component of j along the initial relative momentum \mathbf{k}_i , which is chosen to coincide with the z axis. The first term in Eq. (3.22) is the system eigenstate in the absence of scattering and the second term represents the scattered intensity. Note that Eq. (3.22) includes only those diatom states for which $k_\alpha^2 > 0$. These are referred to as the open channels. Although states for which $E_\alpha > E$ are not present in the asymptotic form Eq. (3.22), they must in principle be considered in solving Eq. (3.21). For such states, which are referred to as the closed channels, one defines $k_\alpha = |k_\alpha^2|^{1/2}$. The differential cross section for scattering in the direction $\Omega = (\theta, \phi)$ corresponding to the diatom transition $i \rightarrow f$ can be expressed in terms of the scattering amplitude $F(f; i | \Omega)$ as (compare with Eq. (3.10))

$$\frac{d\sigma_{f \leftarrow i}}{d\Omega}(\Omega) = \left(\frac{k_f}{k_i}\right) |F(f; i | \Omega)|^2 \quad (3.23)$$

We begin the solution of Eq. (3.21) by first obtaining a set of eigenfunctions $\phi^{JM}(\underline{r}, \underline{R})$ of Eq. (3.21), described by total angular momentum quantum numbers J and M , in terms of which the desired solutions $\Psi_i(\hat{\underline{r}}, \hat{\underline{R}})$ will then be constructed. Expand $\phi^{JM}(\underline{r}, \underline{R})$ in the angular eigenfunctions $Z^{JM}_{j, 1}(\hat{\underline{r}}, \hat{\underline{R}})$ of the total angular momentum and the vibrational

eigenfunctions $H_{v',j'}(R)$ of the rotating diatom in the form

$$\Phi^{JM}(\underline{r}, \underline{R}) = \frac{1}{r} \sum_{v',j',l'} Z_{j',l'}^{JM}(\hat{r}, \hat{R}) H_{v',j'}(R) u_{v',j',l'}^{JM}(r) \quad (3.24)$$

where the $u_{v',j',l'}^{JM}(r)$ are as yet undetermined radial wavefunctions. Until one specifies the $u_{v',j',l'}^{JM}(r)$, Φ^{JM} represents a completely general solution to Eq. (3.21) for which J and M are good quantum numbers. l' is the orbital angular momentum of the A-BC system. The functions $Z_{j',l'}^{JM}(\hat{r}, \hat{R})$ can be written as sums of products of spherical harmonics Y_{lm} and Clebsch-Gordan coefficients $(\quad | \quad)$ (Edmonds (1974) and Arthurs and Dalgarno (1960)) as

$$Z_{j',l'}^{JM}(\hat{r}, \hat{R}) = \sum_{m_1 m_2} (j' l' m_1 m_2 | j' l' J M) Y_{j',m_1}(\hat{R}) Y_{l',m_2}(\hat{r}) \quad (3.25)$$

By substituting Eqs (3.24) and (3.25) into Eq. (3.21), multiplying by $(Z_{j',l'}^{JM}(\hat{r}, \hat{R}) H_{v',j'}(R))^*$ and integrating over the coordinates \hat{r} and \hat{R} one obtains the following set of equations, called the close-coupled (CC) equations, for the radial wavefunctions :

$$\left[\frac{d^2}{dr^2} - \frac{l(l+1)}{r^2} + k_{vj}^2 \right] u_{vj,l}^J(r) - \frac{2\mu}{\hbar^2} \sum_{v',j',l'} \langle vj,l | V | v'j',l' \rangle u_{v',j',l'}^J(r) = 0 \quad (3.26)$$

where the r dependent matrix elements of the interaction potential are given by

$$\langle vj,l | V | v'j',l' \rangle = \int (H_{vj}(R) Z_{j',l'}^{JM}(\hat{R}))^* V(r, R, \cos \gamma).$$

$$\cdot H_{v'j'l'}(R) Z_{j'l'}^{JM}(\hat{R}) d\hat{r} dR \quad (3.27)$$

The evaluation of the potential matrix elements $\langle |V| \rangle$ is discussed in Section 3.6 for the CS approximation. The M label of the radial wavefunction has been omitted because the potential matrix elements, and therefore Eq. (3.26), are independent of M. For any given J, Eq. (3.26) represents a set of coupled second order linear DE's, one for each allowed vjl triplet. Corresponding to each of these equations one can find solution vectors $\underline{u}^{Jvj'l}(r) = \{ u^{Jvj'l}_{v'j'l'}(r) \}$ which describe the scattering from an initial state vjlJ to final states v'j'l'J. It is convenient to write these radial wavefunctions in matrix form as $\underline{u}^J(r)$, where each column represents a solution vector $\underline{u}^{Jvj'l}(r)$. The close-coupled equations can then be expressed in matrix form as

$$\frac{d^2}{dr^2} \underline{u}^J(r) + \underline{k}_J^2(r) \underline{u}^J(r) = \underline{0} \quad (3.28)$$

where

$$\begin{aligned} (\underline{k}_J^2)_{v'j'l'J;vj'lJ} &= \left(k_{vj}^2 - \frac{l(l+1)}{r^2} \right) \delta_{ll'} \delta_{vv'} \delta_{jj'} \\ &- \left(\frac{2\mu}{\hbar^2} \right) \langle v'j'l'J | V | vjlJ \rangle \end{aligned} \quad (3.29)$$

and the rows and columns are labeled by quantum numbers v'j'l' and vjl respectively. In practice one numerically integrates Eq. (3.26) using real arithmetic subject to the initial condition $\underline{u}^J(0) = 0$. The form of $\underline{u}^J(r)$ at large r can be expressed in terms of the (real) reaction matrix \underline{K}^J (see Johnson (1973) and compare with Eq. (3.14)) as

$$\underline{\underline{u}}^J(r) \sim \underline{\underline{J}}(r) + \underline{\underline{N}}(r) \underline{\underline{K}}^J \quad (3.30)$$

where

$$\left(\underline{\underline{J}} \right)_{if} = \delta_{if} k_i^{-1/2} \hat{j}_{l_i}(k_i r) \quad (3.31)$$

$$\left(\underline{\underline{N}} \right)_{if} = \delta_{if} k_i^{-1/2} \hat{n}_{l_i}(k_i r)$$

for open channels (with $k_i^2 > 0$) and

$$\left(\underline{\underline{J}} \right)_{if} = \delta_{if} (k_i r)^{1/2} I_{l_i+1/2}(k_i r) \quad (3.32)$$

$$\left(\underline{\underline{N}} \right)_{if} = \delta_{if} (k_i r)^{-1/2} K_{l_i+1/2}(k_i r)$$

for closed channels (with $k_i^2 \leq 0$). The subscripts i and f refer to states labeled by quantum numbers vjl and J . \hat{j} and \hat{n} are Ricatti-Bessel functions and I and K are modified spherical Bessel functions of the first and third kinds (Abramowitz and Stegun (1970)). By matching the solution matrix $\underline{\underline{u}}^J(r)$ to the asymptotic form Eq. (3.30) one obtains the matrix $\underline{\underline{K}}^J$, from which, as we show below, the desired scattering cross sections can be calculated.

In the case of a spherically symmetric potential (Section 3.1) one obtained a set of phase shifts η_l which were used to compute the cross sections. To describe the scattering from an anisotropic interaction potential it is useful to define the so-called S-matrices $\underline{\underline{S}}^J$ (Child (1974)). The S-matrix element $S^J(v'j'l';vjl)$, which determines the probability of the transition $vjlJ \rightarrow v'j'l'J$, is defined by that solution

vector $\underline{u}_0^{Jvj1}(r)$ of Eq. (3.26) whose asymptotic form possesses an incoming spherical wave only for the state $vj1$ and outgoing spherical waves for all other states :

$$\begin{aligned} u_0^J(v'j'l';vj1|r) &\sim \delta_{vv'}\delta_{jj'}\delta_{ll'} e^{-i(k_{vj}r - l\pi/2)} \\ &- \left(\frac{k_{vj}}{k_{v'j'}}\right)^{1/2} S^J(v'j'l';vj1) e^{i(k_{v'j'}r - l'\pi/2)} \end{aligned} \quad (3.33)$$

where we have written the elements of the vector $\underline{u}_0^{Jvj1}(r)$ as $u_0^J(v'j'l';vj1|r)$. The delta functions ensure that an incoming spherical wave exists only when $v'j'l'$ coincide with the quantum numbers $vj1$ of the initial state.

By forming suitable linear combinations of the solution vectors $\underline{u}^{Jvj1}(r)$, which are the columns of the matrix $\underline{u}^J(r)$ obtained by integrating Eq. (3.28), and noting the asymptotic form given by Eq. (3.30), it is possible to construct solutions $\underline{u}_0^{Jvj1}(r)$ with asymptotic forms given by Eq. (3.33). In doing so one is able to express the S matrices in terms of the K matrices. One finds that (see Child (1974))

$$\underline{S}^J = (\underline{1} - i\underline{K}_0^J)^{-1} (\underline{1} + i\underline{K}_0^J) \quad (3.34)$$

where \underline{K}_0^J is that submatrix of \underline{K}^J obtained by deleting rows and columns corresponding to closed channels.

It now remains to express the cross-sections in terms of the S matrices. To do this one first substitutes the solution vectors $\underline{u}_0^{Jvj1}(r)$ into Eq. (3.24) to obtain a set of eigenfunctions $\phi_{vj1}^{JM}(\underline{r}, \underline{R})$ of Eq. (3.21) for which $JMvj1$ are good quantum numbers. These are the eigenfunctions

which are used to construct the desired solution of Eq. (3.21), $\Psi_{\underline{v}j\mathbf{m}}(\underline{r}, \underline{R})$, which corresponds to an initial diatom state $\phi_{\underline{v}j\mathbf{m}}(\underline{R})$ and has the asymptotic form of Eq. (3.22). Written in terms of the elements of the $u_0^{Jvj1}(\underline{r})$ the final expression is (Arthurs and Dalgarno (1960))

$$\Psi_{\underline{v}j\mathbf{m}}(\underline{r}, \underline{R}) = \left(\frac{\pi^{1/2}}{k_{\underline{v}j} r} \right) \sum_{\substack{JM1 \\ v'j'l'}} i^{l+1} (2l+1)^{1/2} (jlm0|j1JM) Z_{j'l'}^{JM}(\hat{r}, \hat{R}) \cdot H_{\underline{v}'j'l'}^J(R) u_0^J(v'j'l'; vj1|r) \quad (3.35)$$

By combining Eqs (3.33) and (3.35) and comparing the result with Eq. (3.22) one finds that (Fitz et al. (1981))

$$F(v'j'm'; vjm|\Omega) = \pi(k_{\underline{v}j} k_{\underline{v}'j'})^{-1/2} \sum_{l'} g_{l'}(v'j'm'; vjm) Y_{l'}^{m-m'}(\theta, \phi) \quad (3.36)$$

where

$$g_{l'}(v'j'm'; vjm) = \sum_{J1} i^{l-l'+1} (2l+1)^{1/2} (2J+1) \begin{pmatrix} j & l & J \\ m & 0 & -m \end{pmatrix} \begin{pmatrix} j' & l' & J \\ m' & m-m' & -m \end{pmatrix} \cdot [\delta_{\underline{v}\underline{v}'}, \delta_{j j'}, \delta_{l l'}, - S^J(v'j'l'; vj1)] \quad (3.37)$$

In the above equations the m 's are the projections of the j 's along the initial relative momentum, the $(:::)$ are Wigner 3-J symbols (Edmonds (1974)) and $\Omega = (\theta, \phi)$ defines the scattering angle. The differential cross sections are obtained using Eq. (3.23) and the integral cross sections can be written as

$$\sigma(v'j'm';vjm) = \left(\frac{\pi}{k_{vj}}\right) \sum_{l'} |g_{l'}(v'j'm';vjm)|^2 \quad (3.38)$$

It should be noted that these cross sections are valid in the centre of mass reference frame. The problem of transforming them to the laboratory reference frame is discussed in a later section.

In summary, the scattering behaviour for a given atom-diatom system is obtained by (1) solving Eq. (3.28) for the radial wavefunction matrices $\underline{u}^J(r)$, (2) obtaining the K and S matrices from the large r behaviour of the $\underline{u}^J(r)$ and (3) using Eqs (3.23) and (3.36-38) to determine the cross sections. The approximations and numerical methods used to solve these equations are outlined in later sections.

3.3 The Spherical Potential Approximation

For systems with small anisotropies, accurate total scattering cross sections can often be obtained by performing an angular average of the interaction potential and then solving the scattering equations for the resulting spherical potential using the methods discussed in Section 3.1. In the present thesis we refer to this method as the spherical potential approximation. Calculations based upon the spherical potential approximation are often referred to as single channel calculations. The phase shifts η_1 can be determined either by direct quadrature of Eq. (3.17) or by using the WKB or Born approximations. The details of the WKB and Born calculations are well documented and will not be reproduced here. See, for example, Child (1974), Fluendy and Lawley (1973), Bernstein (1960), Smith (1964), Smith and Munn (1964), Munn et al. (1964) and Hepburn and LeRoy (1978).

3.4 The Infinite Order Sudden Approximation

A simple way of including the anisotropy of a given potential $V(r, R, \cos\gamma)$ in a calculation of the scattering cross sections, other than by first obtaining an effective spherical potential, is to use the infinite order sudden (IOS) approximation. The approximation is derived and discussed by Parker and Pack (1978) and Goldflam *et al.* (1977b). One obtains the IOS Schrödinger equation by replacing the angular momentum operators \hat{l}^2 and \hat{j}^2 in Eq. (3.21) by $\bar{l}(\bar{l}+1)\hbar^2$ and $\bar{j}(\bar{j}+1)\hbar^2$ respectively. The resulting equations depend upon angular coordinates only through the angle γ which appears in the interaction potential. For the case of rigid rotor scattering, in which the interaction potential is independent of R , the substitution of $u_{\bar{l}\gamma}(r)/r$ into the IOS Schrödinger equation leads to the following equation for the IOS radial wavefunction $u_{\bar{l}\gamma}(r)$ (Parker and Pack (1978))

$$u_{\bar{l}\gamma}(r) + \left(k^2 - \frac{\bar{l}(\bar{l}+1)}{r^2} \right) u_{\bar{l}\gamma}(r) = \frac{2\mu}{\hbar^2} V(r, \cos\gamma) u_{\bar{l}\gamma}(r) \quad (3.39)$$

where k is the wavevector corresponding to the collision energy. Eq. (3.39) has the same form as Eq. (3.11) except that the potential term has been replaced by $V(r, \cos\gamma)$. As a result of removing the angle dependence from the Hamiltonian, the radial equations now depend parametrically upon the angle γ . That is, it is possible to solve Eq. (3.39) for any fixed value of γ . This parametric dependence upon γ is shown by writing the radial wavefunction as $u_{\bar{l}\gamma}(r)$. Scattering cross sections can be obtained for any given γ by solving Eq. (3.39) using the methods discussed in Section 3.1.

Parker and Pack (1978) have shown that the IOS approximations to the total differential and total integral cross sections are obtained from the following average of the spherical potential cross sections $\Lambda(\gamma)$ computed at fixed potential angles γ :

$$\Lambda_{\text{IOS}} = \int_{-1}^1 \Lambda(\gamma) d\cos\gamma \quad (3.40)$$

In the above equation Λ can be taken to represent either a total differential or total integral cross section. This result makes the calculation of such approximate cross sections a straight forward exercise.

The IOS approximation should be accurate whenever the kinetic energy is large compared to the diatom rotational energy spacing and the differences between the centrifugal potentials of the coupled channels in Eq. (3.26) are small (Parker and Pack (1978)).

We note that the IOS approximation can also be used to approximate the individual inelastic cross sections. As calculations of this type are not reported in this thesis, however, the details of such calculations are not discussed.

3.5 The Coupled States Approximation

The coupled states (CS) approximation (Khare et al. (1980) and Fitz et al. (1981)) is useful in the study of systems for which an IOS treatment is inadequate and a full solution to the close coupled equations impractical. During the 1970's and early 1980's numerous investigations of the CS approximation appeared. See, for example, the works by Fitz et al. (1981), Khare et al. (1978,1980,1981), Khare (1977), Kouri et al. (1976a,1976b), Khare and Kouri (1978), Kouri and Shimoni (1976,1977), Shimoni and Kouri (1976a,1976b,1977a,1977b), Parker and Pack (1977), Pack (1973), McGuire (1973,1975), McGuire and Kouri (1974), Kouri (1975), Secrest (1975), Goldflam et al. (1977a) and Goldflam and Kouri (1977). As a result of these studies it became clear that great care was required in the use and interpretation of the technique. Rather than presenting a rigorous derivation of the CS approximation, we indicate how one obtains the CS equations and give a summary of the method for atom-diatom scattering using the interpretation of the approximate S matrices given by Khare et al. (1980,1981) and Fitz et al. (1981).

In Section 3.1 we discussed the solution to the scattering problem in a non-rotating centre-of-mass reference frame. A number of the earlier studies of the CS approximation (Pack (1973), McGuire (1975), Kouri (1974), McGuire and Kouri (1974)) began by transforming the Schrödinger equation to a rotating centre of mass reference frame whose z axis coincides with the vector \underline{r} . The radial wavefunction in this rotating reference frame, $\underline{w}^J(r)$, is the solution to the following equations (compare with Eqs (3.28) and (3.29))

$$\frac{d^2}{dr^2} \underline{w}^J(r) + \underline{k}_J^2(r) \underline{w}^J(r) = \underline{0} \quad (3.41)$$

and

$$\left(\underline{k}_J^2 \right)_{v'j'm_r'; J; vjm_r J} = k_{vj}^2 \delta_{vv'} \delta_{jj'} \delta_{m_r m_r'} - \delta_{vv'} \delta_{jj'} \langle vjm_r' | \frac{\hat{l}_J^2}{\hbar^2 r^2} | vjm_r \rangle - \frac{2\mu}{\hbar^2} \delta_{m_r m_r'} \langle v'j'm_r' | V | vjm_r \rangle \quad (3.42)$$

where m_r takes the place of l in the non-rotating frame equations and represents the projection of the diatom rotational angular momentum on the new (rotating) z axis. Note that the eigenstates $|vjm_r\rangle$ do not depend upon J , and therefore all of the J dependence results from the rotating frame \hat{l}_J^2 operator. For details of the transformation to the rotating reference frame see McGuire (1975).

In the non-rotating frame, the coupling between the $vj1$ states is solely a result of the potential (see Eq. (3.29)). In the rotating frame, however, the potential only mixes different vj states. Coupling between m_r states results from the operator \hat{l}_J^2 . The coupled states equations are obtained by approximating the operator \hat{l}_J^2 by $\bar{l}(\bar{l}+1)\hbar^2$. Eq. (3.41) is then independent of J and uncoupled in m_r , resulting in one set of equations, coupled only in v and j by the potential, for each pair of $\bar{l}\bar{m}$ values. We use \bar{m} to denote the value of m_r which appears in the potential matrix elements. The CS radial wavefunctions $w^{\bar{l}\bar{m}}(v'j'; vj|r)$ are solutions to the CS equations (McGuire and Kouri (1974) and Khare (1977)), written here in matrix form

$$\frac{d^2}{dr^2} \underline{w}^{\bar{l}\bar{m}}(r) + \underline{k}_{CS}^2(r) \underline{w}^{\bar{l}\bar{m}}(r) = \underline{0} \quad (3.43)$$

and

$$\left(\underline{k}_{CS}^2 \right)_{v'j';vj} = \left(k_{vj}^2 - \frac{\bar{l}(\bar{l}+1)}{r^2} \right) \delta_{vv'} \delta_{jj'} - \frac{2\mu}{\hbar^2} \langle v'j'\bar{m} | V | vj\bar{m} \rangle \quad (3.44)$$

where the potential matrix elements are given by

$$\langle v'j'\bar{m} | V | vj\bar{m} \rangle = \int \left(H_{v'j'}(R) Y_{j'\bar{m}}(\hat{R}) \right)^* V(r, R, \cos\beta) \cdot H_{vj}(R) Y_{j\bar{m}}(\hat{R}) dR \quad (3.45)$$

β is the angle between the (rotating) z axis and the diatom vector \underline{R} .

As was done in the previous section for the close-coupled theory, (see Eqs (3.30) to (3.32)), one can define matrices $\underline{K}^{\bar{l}\bar{m}}$ in terms of the asymptotic behaviour of the $\underline{w}^{\bar{l}\bar{m}}(r)$. In this case, however, the l_i which appear in the Bessel functions are replaced by the CS orbital angular momentum parameter \bar{l} . One can similarly define CS S matrices $\underline{S}^{\bar{l}\bar{m}}$, (see Eq. (3.33)), and express them in terms of the $\underline{K}^{\bar{l}\bar{m}}$ using the analogue of Eq. (3.34). The final step is to use the $\underline{S}^{\bar{l}\bar{m}}$ to approximate the full S matrices \underline{S}^J . Following the discussions of Khare *et al.* (1980), the most general CS approximation to \underline{S}^J is

$$S_{CS}^J(v'j'l';vj\bar{l}) = \frac{a_{\bar{l}}}{a_{\bar{l}}} i^{l'-\bar{l}} \sum_{\bar{m}} \left[(2l+1)(2l'+1) \right]^{1/2} \begin{pmatrix} j & 1 & J \\ \bar{m} & 0 & -\bar{m} \end{pmatrix} \cdot \begin{pmatrix} j' & 1' & J \\ \bar{m} & 0 & -\bar{m} \end{pmatrix} S^{\bar{l}\bar{m}}(v'j';vj) \quad (3.46)$$

where \bar{l} depends upon l and l' such that when $l=l'$ then $\bar{l}=l=l'$ and the a_l are complex phase factors with moduli of one. The accuracy of the resulting cross sections depends crucially upon the choices of both \bar{l} and a_l .

Although some early studies of the CS approximation used the choices $a_l = i^{-l}$ and $\bar{l} = l$ or l' , it was found that the positions of the diffraction oscillations of the differential cross sections for odd Δj transitions were incorrectly predicted (Khare et al. (1980,1981) and Fitz et al. (1980)). By insisting that the $\underline{\underline{S}}_{CS}^J$ have the correct time reversal symmetry, which requires that they be symmetric (Khare and Kouri (1980a,1980b)), it follows that $a_l = i^{+l}$ (the "correct phase" choice of Khare et al. (1980)) and that \bar{l} be a symmetric function of l and l' . The l -average choice, $\bar{l} = (l+l')/2$, together with the "correct phase" choice represent one of the most promising CS approximations studied to date (Khare et al. (1980,1981) and Fitz et al. (1981)). With these choices, the factor which appears outside the summation in Eq. (3.46) becomes unity. Most of the CS results presented in this thesis were obtained using these latter choices, which have been shown to correct the previous errors in the odd Δj differential cross sections. The use of the l -average choice for the calculation of inelastic IOS cross sections has been discussed by Fitz (1978). Finally, we note that although these choices lead to approximate S matrices $\underline{\underline{S}}_{CS}^J$ which do satisfy time reversal symmetry, these matrices do not satisfy unitarity (ie. flux conservation) (Khare et al. (1981)). Efforts to develop a CS approximation which results in $\underline{\underline{S}}_{CS}^J$ which satisfy both time reversal symmetry and unitarity were being made in the early eighties by Khare et al. (1981).

3.6 The Matrix Elements of the Potential

In solving the CS equations (3.43) one must evaluate the coupling terms given by Eq. (3.45). This is most easily done by expanding the potential in terms of Legendre polynomials as

$$V(r, R, \cos\gamma) = \sum_{\lambda} V_{\lambda}(r, R) P_{\lambda}(\cos\gamma) \quad (3.47)$$

It can then be shown that

$$\begin{aligned} \langle v' j' \bar{m} | V | v j \bar{m} \rangle &= (-1)^{\bar{m}} \sum_{\lambda} [(2j+1)(2j'+1)]^{1/2} \begin{pmatrix} j & \lambda & j' \\ 0 & 0 & 0 \end{pmatrix} \\ &\quad \cdot \begin{pmatrix} j & \lambda & j' \\ -\bar{m} & 0 & \bar{m} \end{pmatrix} \langle v' j' | V_{\lambda} | v j \rangle \end{aligned} \quad (3.48)$$

where

$$\langle v' j' | V_{\lambda} | v j \rangle = \int H_{v', j'}^*(R) V_{\lambda}(r, R) H_{v j}(R) R^2 dR \quad (3.49)$$

The $H_{v j}(R)$ are obtained by solving the Schrödinger equation for the isolated diatom. In the case of rigid rotor scattering, where $V_{\lambda}(r, R) = V_{\lambda}(r)$, $\langle v' j' | V_{\lambda} | v j \rangle$ is equal to $V_{\lambda}(r)$. Note that the matrix elements for $+\bar{m}$ and $-\bar{m}$ are equal. As a result, the CS equations need only be solved for $\bar{m} \geq 0$.

For potentials which depend upon R , the $V_{\lambda}(r, R)$ are expanded according to

$$V_{\lambda}(r, R) = \sum_{n=0}^3 \left(\frac{R-R_e}{R_e} \right)^n V_{n\lambda}(r) \quad (3.50)$$

where R_e is the equilibrium diatom bond length. Then

$$\langle v'j' | V_{\lambda} | vj \rangle = \sum_n V_{n\lambda}(r) \langle v'j' | \left(\frac{R-R_e}{R_e} \right)^n | vj \rangle \quad (3.51)$$

The Hamiltonian for the rotating diatom is

$$H_j = W(R) + \frac{\hbar^2}{2\mu} \left[\frac{1}{R} \frac{\partial^2}{\partial R^2} R + \frac{j(j+1)}{R^2} \right] \quad (3.52)$$

Let $|u_{vj}\rangle$ correspond to the eigenfunctions of H_j when $W(R)$ is approximated by a Morse potential. Since the Morse eigenfunctions can be expressed analytically in terms of the Laguerre polynomials, one can readily calculate matrix elements in the $|u_{vj}\rangle$ basis. The energies E_{vj} are given by the eigenvalues of $\langle u_{v'j} | H_j | u_{vj} \rangle$ and the corresponding eigenmatrices $\langle u_{v'j} | v''j \rangle$ can be used to evaluate the required matrix elements of $\left((R-R_e)/R_e \right)^n$:

$$\langle v'j' | \left(\frac{R-R_e}{R_e} \right)^n | vj \rangle = \sum_{v_1 v_2} \langle v'j' | u_{v_1 j'} \rangle \langle u_{v_1 j'} | \left(\frac{R-R_e}{R_e} \right)^n | u_{v_2 j} \rangle \cdot \langle u_{v_2 j} | vj \rangle \quad (3.53)$$

The equations presented in this section can be used to evaluate the CS potential matrix elements. In the next section, the numerical solution of the CS equations is discussed.

3.7 Solution of the Coupled States Equations

The CS calculations reported in this thesis were performed using the log-derivative (LOGD) and variable-interval variable-step (VIVAS) algorithms. These methods are discussed by Johnson (1973,1977), Parker et al. (1979,1980a,1980b), Thomas et al. (1981) and Alexander (1984). The S matrices are obtained from the log-derivative matrices, which result from integrating the CS equations. An outline of the algorithms and the evaluation of the S matrices is given in this section. As the techniques discussed in this chapter are applicable to both the CC and CS methods, the labels J, \bar{l} and \bar{m} have been omitted for convenience. We first discuss the LOGD algorithm.

Rather than directly solving the CS matrix equations (Eq. (3.43)), in the LOGD method one solves for the log-derivative matrix $\underline{y}(r)$, which can be written in terms of the wavefunction matrix $\underline{u}(r)$ as

$$\underline{y}(r) = \frac{d}{dr} \log(\underline{u}(r)) = \frac{d}{dr} \underline{u}(r) \cdot \underline{u}^{-1}(r) \quad (3.54)$$

and satisfies the matrix Ricatti equation (Johnson (1973))

$$\underline{y}'(r) + \underline{k}^2(r) + \underline{y}^2(r) = \underline{0} \quad (3.55)$$

By replacing \underline{y} in Eq. (3.55) by $\underline{u}'\underline{u}^{-1}$ one does indeed obtain an equation of the form of Eqs (3.28) or (3.43). Define $r_n = r_0 + nh$, where r_0 is the starting point of the integration and h is the step size. Let N (even) be the total number of steps. If one defines $\underline{z} = h\underline{y}$, then the LOGD algorithm is obtained by applying the following recursive formula :

$$\underline{z}_n = \left(\underline{1} + \underline{z}_{n-1} \right)^{-1} \underline{z}_{n-1} - \left(\frac{\hbar^2}{3} \right) \underline{u}_n \quad (3.56)$$

where

$$\underline{u}_n = \begin{cases} \underline{k}^2(r_n) & , n = 0, N \\ 2 \underline{k}^2(r_n) & , n \text{ even} \\ 4 \left[\underline{1} + \left(\frac{\hbar^2}{6} \right) \underline{k}^2(r_n) \right]^{-1} \underline{k}^2(r_n) & , n \text{ odd} \end{cases} \quad (3.57)$$

and $\underline{k}^2(r)$ is given by Eq. (3.44) for the CS approximation.

As initial conditions one chooses r_0 well inside the classically forbidden region and sets $\underline{z}_0 = \infty \underline{1}$, where ∞ is taken to mean a suitably large number such as 10^{40} . The log-derivative matrix at r_N is given by $\underline{y}(r_N) = \underline{z}_N/h$. The LOGD method is most efficient when the potential is a rapidly changing function of r .

In the VIVAS method one solves the radial equations in the form of Eq. (3.43). The integration region is divided into a series of variable length intervals which are then further subdivided into steps. The potential matrix is diagonalized at the midpoint of each interval and a set of piecewise-constant potentials are used to approximate the potential over the steps. Perturbation techniques are used to propagate the solution over the steps in an interval and an R matrix evaluation (where $\underline{R} = \underline{y}^{-1}$) coupled with a suitable basis transformation is used to stabilize the solution and transform it from one interval to the next. The details of the VIVAS method are well documented in the references cited previously and will not be given here.

Unlike the LOGD method, the VIVAS method is most efficient when the potential is slowly varying with r or the de Broglie wavelength is

small. By using the LOGD method for small r and the VIVAS method to extend the solution to large r one obtains an efficient algorithm for integrating the CC or CS equations (Parker et al. (1980a)). Both the LOGD algorithm and the combined LOGD-VIVAS algorithm were used to obtain the CS results presented in this thesis.

The K matrices, which are used to calculate the S matrices, are obtained from the $\underline{y}(r)$ at large r by substituting the asymptotic form Eq. (3.30) into Eq. (3.54). One finds that

$$\underline{K} = - [\underline{y}(r) \underline{N}(r) - \underline{N}'(r)]^{-1} [\underline{y}(r) \underline{J}(r) - \underline{J}'(r)] \quad (3.58)$$

Having determined the K matrices, the S matrices and cross sections can be evaluated as discussed earlier in this chapter.

The log-derivative algorithm can readily be applied to solving the spherical potential or IOS equations, which have the form of Eq. (3.11). By performing such calculations it is possible to test the accuracy of the WKB and other approximate methods used to solve these single channel equations.

3.8 On the Comparison Between Theory and Experiment

The cross sections obtained using the equations presented earlier in this chapter are valid in the centre of mass reference frame. To compare a calculated differential scattering cross section with one determined experimentally, one must calculate the cross section as a function of the laboratory scattering angle. The total differential cross section in the laboratory frame is obtained by transforming the individual elastic and inelastic cross sections to the laboratory frame and then summing their appropriately weighted intensities. In this section we first outline the transformation from the centre of mass frame to the laboratory frame, following Morse and Bernstein (1962), and then discuss the algorithm used to average the laboratory frame cross section over the molecular beam parameters and the detector geometry. Details of such transformation and averaging procedures are given by Morse and Bernstein (1962), Helbing (1968) and Pack (1984).

Consider an in-plane collision between two molecules having masses m_1, m_2 and velocities $\underline{v}_1, \underline{v}_2$ respectively. Let ΔE be the change in the total internal energy of the molecules as a result of the collision. We denote laboratory and centre of mass frame velocities by \underline{v} and \underline{w} respectively. Primed quantities refer to post-collision values. The Newton diagram for such an event is shown in Figure 3.2.

The velocity of the centre of mass, \underline{v}_{cm} , is represented by the vector \overline{LC} joining the laboratory origin L to the centre of mass origin C. The relative velocity $\underline{g} = \underline{v}_2 - \underline{v}_1$ corresponds to the vector \overline{PQ} . θ_L and θ_C are typical laboratory and centre of mass scattering angles. Given $m_1, m_2, \underline{v}_1, \underline{v}_2, \Delta E$ and θ_L one needs to determine the corresponding values of

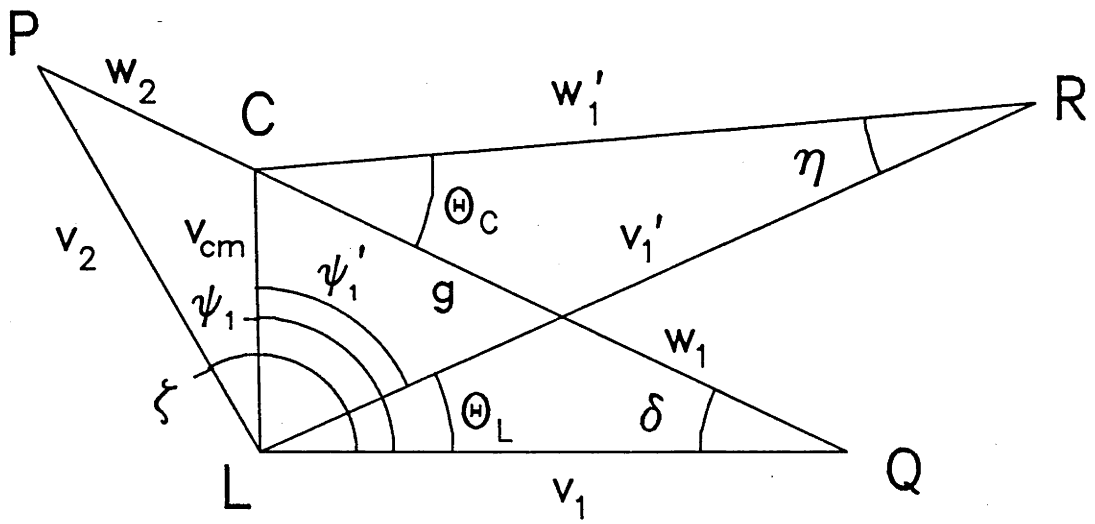


Figure 3.2

θ_C and $d\Omega_C/d\Omega_L$, the Jacobian for the solid angle transformation between the laboratory and centre of mass frames.

The equations required to perform the transformation are given in Table 3.1. Note that if $w_1' < v_{cm}\sin\alpha_1'$ then there are no particles scattered to laboratory angle θ_L ; if $v_{cm}\sin\alpha_1' < w_1' < v_{cm}$ then both signs in Eq. (T3.1.11) lead to forward scattering at laboratory angle θ_L ; and if $w_1' > v_{cm}$ then only the "+" sign is to be used.

Most of the laboratory frame coupled states differential cross sections presented in this thesis assume the ideal situation of monoenergetic beams of zero angular divergence colliding at 90° . The usefulness of this assumption in representing an experimentally measured cross section is investigated by performing fully averaged calculations using the spherical potential or IOS methods and comparing them with the corresponding unaveraged ones. The algorithms used to perform the averaging, discussed by Boughton *et al.* (1986), are summarised below. A similar averaging procedure was used by Boughton (1986) to analyse measured differential scattering intensities for He-Ar, He-HF and CH₄-CH₄.

Suppose that $I_C(g, \theta_C)$ is the differential scattering cross section in the centre of mass frame calculated at a collision energy of $E_C = \frac{1}{2}\mu g^2$ using an assumed potential surface. In order to relate this function to the experimental measurements it is necessary to transform to the laboratory frame, as outlined above, and average over the beam velocity distributions and the geometry of the detector. Any variation of the detector efficiency with particle velocity must be included in this average. The quantity to be averaged over the experimental parameters to obtain a laboratory frame cross section for comparison with the experimentally measured intensities is

Table 3.1

Given : m_1 , \underline{v}_1 , m_2 , \underline{v}_2 , ΔE , θ_L

Aim : to find $\theta_C(\theta_L)$ and $d\Omega_C/d\Omega_L$

Method :

$$\cos \zeta = \hat{\underline{v}}_1 \cdot \hat{\underline{v}}_2 \quad (T3.1.1)$$

$$g^2 = v_1^2 + v_2^2 - 2v_1v_2 \cos \zeta \quad (T3.1.2)$$

$$w_1 = gm_2 / (m_1 + m_2) \quad (T3.1.3)$$

$$\cos \delta = (v_1^2 + g^2 - v_2^2) / (2v_1g) \quad (T3.1.4)$$

$$v_{cm}^2 = w_1^2 + v_1^2 - 2v_1w_1 \cos \delta \quad (T3.1.5)$$

$$\mu = m_1m_2 / (m_1 + m_2) \quad (T3.1.6)$$

$$E_0 = \mu g^2 / 2 \quad (T3.1.7)$$

$$w_1' = w_1 (1 - \Delta E / E_0) \quad (T3.1.8)$$

$$\cos \psi_1 = (v_{cm}^2 + v_1^2 - w_1^2) / (2v_1v_{cm}) \quad (T3.1.9)$$

$$\cos \psi_1' = \cos(\psi_1 - \theta_L) \quad (T3.1.10)$$

$$v_1' = v_{cm} \cos \psi_1' \pm (w_1'^2 - v_{cm}^2 \sin^2 \psi_1')^{1/2} \quad (T3.1.11)$$

$$\cos \theta_C = (w_1^2 + w_1'^2 - v_1^2 - v_1'^2 + 2v_1v_1' \cos \theta_L) / (2w_1w_1') \quad (T3.1.12)$$

$$\cos \eta = (v_1'^2 + w_1'^2 - v_{cm}^2) / (2v_1'w_1') \quad (T3.1.13)$$

$$d\Omega_C/d\Omega_L = (v_1'/w_1')^2 / |\cos \eta| \quad (T3.1.14)$$

$$I_L^0(\underline{v}_1, \underline{v}_2, \theta_L, \phi_L) = \sum_{\theta_C} \frac{g}{v_1} \left(\frac{v_1'}{v_1}\right)^2 \left[\left(\frac{v_1'}{w_1}\right)^2 \frac{1}{|\cos\eta|} \right] I_C(g, \theta_C) \quad (3.59)$$

where the term in square brackets is the Jacobian for the angle transformation and the sum is over those centre-of-mass angles θ_C which result in scattering through angles θ_L and ϕ_L in the laboratory frame. ϕ_L is the angle between the plane of the incident beams and the final velocity \underline{v}_1' and θ_L is the angle between \underline{v}_1 and the projection of \underline{v}_1' onto the plane of the incident beams. During the course of this analysis it will be assumed that $\phi_L=0$, corresponding to the case of in-plane scattering. To account for the fact that the bolometer is an energy sensitive, rather than a flux sensitive, device the term $(v_1'/v_1)^2$ appears in Eq. (3.59). The most probable primary beam velocity, v_1 , is included so that $I_L^0(\underline{v}_1, \underline{v}_2, \theta_L, \phi_L)$ has the same units as the centre-of-mass frame cross section $I_C(g, \theta_C)$.

The cross section obtained by averaging $I_L^0(\underline{v}_1, \underline{v}_2, \theta_L, \phi_L)$ over the molecular beam parameters ($\int d\zeta \int d\delta \int dg$) and the detector geometry ($\int d\alpha \int dh$) is

$$I_{av}(\theta_L) = \frac{1}{N} \int d\zeta \int d\delta \int dg \left(\frac{g}{\sin\zeta}\right) f_1(v_1) f_2(v_2) s(\zeta) \times \int d\alpha \int dh w(\zeta, h, \alpha) I_L^0(\underline{v}_1, \underline{v}_2, \theta, \phi) \quad (3.60)$$

where the normalization integral N is given by

$$N = \int d\zeta \int d\delta \int dg \left(\frac{g}{\sin\zeta}\right) f_1(v_1) f_2(v_2) s(\zeta) \times \int d\alpha \int dh w(\zeta, h, \alpha) \quad (3.61)$$

and $(g/\sin\zeta)$ is the Jacobian for the transformation from the coordinates

(v_1, v_2, ζ) to the coordinates (g, δ, ζ) . From Figure 3.2 it can be seen that the velocities v_1 and v_2 are related to the integration variables by

$$v_1 = \frac{g \sin(\zeta + \delta)}{\sin \zeta}; \quad v_2 = \frac{g \sin \delta}{\sin \zeta} \quad (3.62)$$

In our analysis it was assumed that the primary and secondary beam velocity distributions, $f_1(v_1)$ and $f_2(v_2)$, were of the form (see Chapter 2)

$$f_i(v) = v^3 \exp\left[- \left(\frac{v - v_s}{v_w} \right)^2 \right] \quad (3.63)$$

with v_s the stream velocity, as determined by time-of-flight measurements, and v_w determined from the width of the distribution. It was also assumed that the primary beam had zero angular divergence and that the angular divergence of the secondary beam was given by

$$s(\zeta) = \exp\left[- \ln 2 \left(\frac{\pi/2 - \zeta}{\zeta_0} \right)^2 \right] \quad (3.64)$$

with ζ_0 the half-width at half maximum. Values of the parameters describing the velocity distributions of the beams used to obtain the differential scattering cross sections presented in this thesis are given in Chapter 2.

For a given collision geometry, determined by ζ , δ and g , one must integrate the differential cross section $I_L^0(\underline{v}_1, \underline{v}_2, \theta, \phi)$ over the coordinates describing the detector geometry, namely α and h . α fixes the lateral position of the point of interest on the bolometer surface, as shown in Figure 3.3, and h is its position above or below the plane of the initial beams. The laboratory scattering angles are given by $\theta = \theta_L + \alpha$ and $\tan \phi = h \cos \alpha / a$, where the ranges of α and h are determined by the dimensions

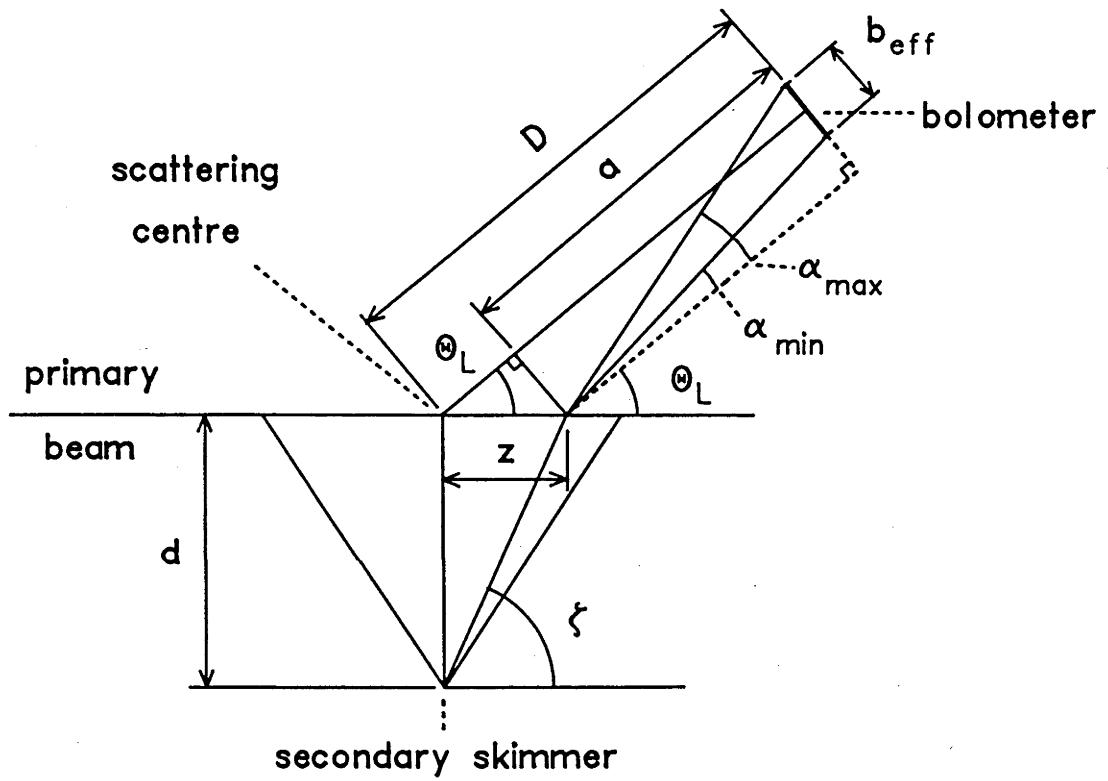


Figure 3.3

of the detector. $w(\zeta, h, \alpha)$ relates the infinitesimals $d\alpha dh$ to the element of solid angle dS subtended at the collision point (Bordenave-Montesquieu et al. (1980))

$$dS = w(\zeta, h, \alpha) d\alpha dh \quad (3.65)$$

where

$$w(\zeta, h, \alpha) = a^2 \cos\alpha (a^2 + h^2 \cos^2\alpha)^{-3/2} \quad (3.66)$$

and, from Figure 3.3,

$$a = D - z \cos\theta_L \quad (3.67)$$

with

$$z = d \tan(\pi/2 - \zeta) \quad (3.68)$$

By choosing $\phi=0$ in Eq. (3.60) $I_L^0(\underline{v}_1, \underline{v}_2, \theta, \phi)$ becomes independent of h and the integral over h can be done analytically yielding (Bordenave-Montesquieu et al. (1980))

$$\int_{-h_{\text{eff}}/2}^{h_{\text{eff}}/2} w(\zeta, h, \alpha) dh = h_{\text{eff}} \cos\alpha (a^2 + h_{\text{eff}}^2 \cos^2(\alpha)/4)^{-1/2} \quad (3.69)$$

where h_{eff} is the effective height of the bolometer (discussed below). It is reasonable to neglect the h -dependence of $I_L^0(\underline{v}_1, \underline{v}_2, \theta, \phi)$ since the range of centre-of-mass angles corresponding to the h integral is less than 10 % of that corresponding to the α integral for the range of scattering angles and collision geometries considered in this thesis. In practice it was found that neglecting the dependence of the h -integral upon ζ , α and θ_L (ie., assuming it was constant) had a negligible effect upon the averaged cross sections. We note here that all points on the surface of the detector have an unobstructed view of the whole scattering volume.

Thus far the divergence of the primary beam has been neglected.

It was included in the analysis by incorporating it into the average over the detector surface area. An effective width for the detector was defined by adding to its real width ($b_0 = 1.93$ mm for bolometer A, as discussed in Chapter 2) the projection of the primary beam width at the scattering centre onto the plane of the detector (see Figure 3.4), giving

$$b_{\text{eff}} = b_0 + 2L \tan(\Delta/2) \cos\theta_L \quad (3.70)$$

with Δ the divergence (FWHM) of the primary beam and L the distance between the scattering centre and the aperture of the first primary beam skimmer.

An effective height was defined in a similar fashion

$$h_{\text{eff}} = h_0 + 2L \tan(\Delta/2) \quad (3.71)$$

where $h_0 = 4.27$ mm (for bolometer A). Given this somewhat ad hoc method used to include the divergence of the primary beam, Δ was used as a free parameter in fitting to the He/Ar total differential scattering measurements, which were used to test and calibrate the experimental and theoretical techniques discussed in this thesis. The results of this study are reported in Chapter 4.

A 12 point Gauss-Chebyshev quadrature was used to evaluate the ζ , δ and g integrals and a 4 point Gauss-Legendre rule was used for the α integral. For each set of ζ , δ , g values a laboratory frame cross section $I_L^0(\underline{v}_1, \underline{v}_2, \theta, \phi=0)$ was calculated at 0.25 degree intervals and a four point Lagrange formula was used to interpolate between these points. The limits on the ζ , δ and g integrals and the numbers of quadrature points used were chosen to converge the averaged cross sections to within the accuracy of the experiments.

Finally, the averaged cross section $I_{\text{av}}(\theta_L)$ was compared with the experimental cross section by scaling the latter in order to minimize the quantity

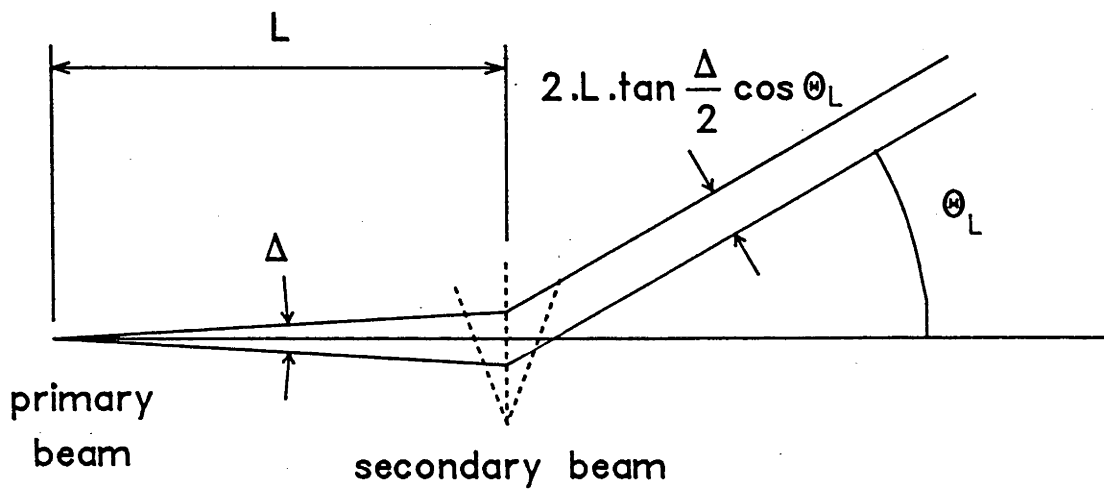


Figure 3.4

$$S = \frac{1}{N} \sum_{i=1}^N \left(\frac{C_i - \lambda E_i}{\lambda E_i} \right)^2 \quad (3.72)$$

where the E_i are the experimental points, C_i the corresponding theoretical estimates and λ is an adjustable scaling parameter.

The discussions thus far have assumed that the the initial internal state of the diatom can be uniquely specified. In practice the diatom beam may contain molecules in a number of rovibrational states. In the absence of state selection before or after the collision, the cross sections for scattering from these initial states to all possible final states must be calculated and weighted according to the measured relative internal state populations of the diatom beam before the collision. The determination of such rotational state distributions is discussed in Chapter 2. Lastly, given the fact that the bolometer is an energy detector, one also needs to consider contributions from the internal energies of the detected particles, (ie. rovibrational energies in the case of diatomic molecules), and the energies of accomodation on the surface of the bolometer. These matters are discussed elsewhere in this thesis.

Chapter FourHelium - Hydrogen Fluoride Scattering Cross Sections

In this chapter we present the results of coupled states, infinite order sudden and spherical potential scattering calculations for the He-HF system. The aim of the study was to assess the accuracy of the approximations in predicting total differential scattering cross sections and to investigate the role of the inelastic processes using the coupled states method. A re-analysis of the total differential scattering experiments of Boughton (1986) is also reported.

After a brief introduction we discuss: the experimental results obtained by Boughton (1986); the interaction potentials used to model the He-HF system; a comparison between the present coupled states results and previously reported close coupled and infinite order sudden calculations; the validity of the spherical potential and IOS approximations in determining the He-HF total differential scattering cross sections; the coupled states results obtained for He-HF at two collision energies; the analysis of the measured total differential scattering cross sections; and the conclusions drawn from the present investigations.

4.1 Introduction

Experimentally determined differential scattering cross sections provide a stringent test for proposed intermolecular potential functions. By combining such measurements with accurate scattering calculations it is possible to refine, and in some cases construct, potential surfaces describing the observed interactions. The amount of information that can be obtained from such a procedure depends upon the complexity of the system being studied, the accuracy of the calculations, and the quality of the experimental data. Exact scattering calculations can easily be done for atom-atom systems. Early scattering experiments were done using effusive, rather than supersonic, beams of alkali atoms, for which efficient surface ionisation detectors were available. Some of these investigations are discussed in the review by Pauly and Toennies (1968). In one such study, Morse and Bernstein (1962) and Morse et al. (1962) investigated the differential scattering of velocity selected beams of K and Cs by a beam of mercury atoms. A technique for inverting atom-atom differential scattering cross sections to obtain the corresponding interaction potentials, reported by Buck and Pauly (1969) and Buck (1971), was used to obtain intermolecular potentials for Na-Hg (Buck and Pauly (1971)), Cs-Hg and K-Hg (Buck et al. (1972)), and Li-Hg (Buck et al. (1974)). Differential scattering measurements have also been used to develop and test interaction potentials for the noble gases, as described in the book by Watts and Mc Gee (1976). Subsequent studies include those by Smith et al. (1977) for He-Ar, Kr and Xe, by Aziz et al. (1979b) and (1979a, 1983) for He-Ar and Ar-Kr respectively, and by Pack et al. (1982a) for Ar-Xe and Kr-Xe.

The study of atom-molecule or molecule-molecule scattering is more

complicated. For a start, the interaction potentials are no longer isotropic. Secondly, the internal states of one or both of the structured scattering partners may change, resulting in rotationally and/or vibrationally inelastic collisions. Differential cross sections for inelastic processes are usually much smaller than for the elastic processes, with the result that rather sensitive techniques are required to distinguish and resolve the former. Pulsed molecular beams coupled with mass dependent time-of-flight detection were developed by Gentry and Giese (1977) to measure rotationally inelastic differential cross sections for He-HD. Hoffbauer et al. (1983a) used the same method to investigate the Ar-Cl₂ interaction.

Laser techniques can also be used to obtain partially resolved cross sections $\sigma_{v_j \rightarrow v'j'}$ as a function of the scattering angle. Bergmann et al. (1980) used dye laser excitation to prepare a sodium dimer containing beam before crossing it with a helium beam, and then used argon ion laser induced fluorescence to monitor the states of the scattered dimers as a function of angle. Serri et al. (1980,1981) used similar methods to study inelastic differential cross sections for Na₂-Ar using two dye lasers. In both sets of experiments the results were seen to reflect the repulsive nature of the potentials.

Hydrogen (and its deuterated counterparts) and the hydrogen halides have received substantial attention from both experimentalists and theoreticians. The large rotational constants of these molecules mean (1) that time-of-flight spectra resulting from collisions with them will be well resolved, and (2) that few internal states will be needed when performing quantum mechanical calculations of their scattering behaviour. Buck and coworkers have made many experimental and computational studies of

H₂, HD and D₂ containing systems using time-of-flight mass spectrometry to resolve the inelastic scattering (Buck (1982)). Atom-diatom combinations investigated include Ne-HD (Buck et al. (1980)), Ne-D₂ (Andres et al. (1980)) and Ar-D₂ (Buck et al. (1984)). For Ar-D₂ the repulsive part of the potential was obtained from the inelastic and total differential cross sections and the attractive region was determined by the analysis of infrared spectra of the Ar-H₂ van der Waals molecule. Diatom-diatom systems studied include HD-D₂ (Buck et al. (1981,1983b)), D₂-CO (Andres et al. (1982)), and H₂-D₂ (Buck et al. (1983a)). In all cases it was possible to obtain detailed information about the anisotropic components of the interactions. Potentials derived using such data are often able to accurately predict properties other than those to which the fits were made, such as diffusion coefficients, integral cross sections and other inelastic differential cross sections.

Other systems for which time-of-flight measurements of inelastic cross sections have been used to investigate interaction potentials include He-O₂ (Faubel et al. (1983)), He-N₂ (McCourt et al. (1984)), and He-C₂H₆ (Faubel et al. (1985)). It is not always possible, however, to resolve inelastic differential cross sections because either (1) they are too small, or (2) the techniques required to resolve them (in principle) are not available. Even so, one may still be able to extract useful information about the relevant potential surface. See, for example, the investigations by Parker et al. (1983) for He-CO₂, N₂O and C₂N₂, by Pack et al. (1982b) and (1984) for SF₆-Ar,Kr and SF₆-He,Ne respectively, by Becker et al. (1979) for Xe-HF, by Farrar and Lee (1974), Buck and McGuire (1976) and Buck and Schleusener (1981) for Ar-HCl, by Boughton (1986) for HF-He,Ne and CH₄-CH₄, and by Held et al. (1980) for He-HCl,HBr. The

$\text{CH}_4\text{-CH}_4$, Ne and Ar total differential cross sections have also been measured and analysed to obtain effective spherical potentials (O'Loughlin et al. (1985) and Ried et al. (1985)). Total differential scattering measurements for atom-molecule or molecule-molecule systems (1) provide a good test for existing potential functions, (2) often yield effective spherical potentials, and (3) less often allow a quantitative determination of the anisotropic components of the potential surface. Further examples of the variety of techniques used and systems studied are given in the following books and reviews (to name but a few): Faubel (1983), Bernstein (1982), Loesch (1980), Bernstein (1979), Thuis et al. (1979) and Faubel and Toennies (1978).

In Chapters 4 and 5 of this thesis we present and discuss the results of experimental and computational studies of the scattering of helium and argon from hydrogen fluoride. Details of the approximations used to calculate the cross sections are given in Chapter 3. There have been a number of studies of the integral and differential cross sections for (noble gas) - (alkali halide) collisions. Held et al. (1980) measured total differential cross sections for He-HCl and He-HBr at collision energies of about 75 meV and used spherically symmetric potentials to give good representations of the experimental data. A study of the Xe-HF interaction based upon measured total differential scattering cross sections at collision energies of 44 and 153 meV was given by Becker et al. (1979). Although it was possible to obtain a reliable estimate of the spherical part of the potential, it was not possible to determine the potential anisotropy from the measurements.

The Ar-HCl and Ar-HF systems have been studied both experimentally and theoretically. Holmgren et al. (1978) used experimentally determined

structural data for the Ar-HCl van der Waals molecule to obtain an anisotropic potential function. Interaction potentials for a number (noble gas)-HF, HCl pairs were determined by Hutson and Howard (1980, 1981, 1982a, 1982b) by fitting simultaneously to available spectroscopic, pressure broadening and virial coefficient data. More recently, Douketis et al. (1984) calculated potentials for Ar-HCl and Ar-HF using semi-empirically determined damping functions to combine the results of SCF calculations for small r (the atom-diatom separation) with dispersion series expansions for large r . By increasing the dispersion coefficients of the HFD model (Hartree Fock with damped Dispersion) for Ar-HF beyond those determined by combining the Ar-Ar and HF-HF values, it was possible to obtain a potential surface which, although it differed from the previously reported M5 potential (Hutson et al. (1982b)), was never-the-less able to reproduce all of the available experimental data. In Chapter 5 of this thesis we present calculations of the differential scattering cross sections of Ar-HF using the available potentials and compare them with experimentally measured total scattering intensities.

Farrar and Lee (1974) measured the total differential cross sections for Ar-HCl and used an effective spherical potential to analyse their results. The measured cross section showed a resolved primary rainbow maximum which enabled the well depth of the effective spherical potential to be determined reasonably accurately. Rainbow phenomena are discussed by Loesch (1980) and in Chapter 5 of this thesis. Buck and McGuire (1976) added anisotropic components to the spherical potential determined by Farrar and Lee (1974) and used coupled states calculations to assess the role of inelastic processes in determining the total differential cross section. A few years later, Buck and Schleusener (1981)

remeasured this cross section and compared their results with those predicted using the potentials developed by Holmgren et al. (1978) and Hutson and Howard (1982a). Although both potentials correctly predicted the position of the observed rainbow maximum, neither was able to give a good representation of the measured cross section. Large differences were found between the cross sections calculated using the isotropic parts of the potentials and those obtained from coupled states studies using the full potentials, stressing the importance of inelastic processes in determining the scattering behaviour of the Ar-HCl system.

Differential scattering cross sections form but a small part of the arsenal of experimental data available to test, develop and refine intermolecular potentials. Other sources of useful information include: (1) measurements of total integral cross sections as a function of collision energy, as used by Thuis et al. (1980) to obtain anisotropic potentials for NO-Ar, Kr and Xe, and by Linse et al. (1979a, 1979b) and van den Bisen et al. (1980, 1982a, 1982b) to study (noble gas)-(noble gas) interactions; (2) structural and spectroscopic properties of van der Waals complexes of the molecules of interest (see Chapter 6 of this thesis), as used by Holmgren et al. (1978), Hutson and Howard (1980, 1981, 1982a, 1982b) and Douketis et al. (1984) to investigate (noble gas)-HCl, HF interactions; and (3) state resolved integral cross sections (see Chapter 7 of this thesis), as measured for HF-Ne, Ar and Kr by Barnes et al. (1980, 1982). Pressure broadening cross sections, virial coefficients and other transport data can also be used to assess intermolecular potentials, depending upon the information content of the experimental data and the accuracy of the computations used to analyse them. In the remainder of this introduction we discuss the behaviour of the He-HF system.

Although little experimental data is available for He-HF, there have been many computational/theoretical studies. Collins and Lane (1975,1976) performed close coupled and coupled states calculations of inelastic integral cross sections using an ab initio model potential. The same potential was used by Mullaney and Truhlar (1979) to investigate the convergence properties of close coupled calculations of integral cross sections as a function of the basis set used. In other studies, Battaglia and Gianturco (1981) evaluated vibrational relaxation rate constants for HF colliding with helium, obtaining reasonable agreement with available experimental results, and Procaccia and Levine (1976) considered an information theoretic approach to determine rotational excitation in (rare gas) - (hydrogen halide) collisions.

In 1982 Rodwell et al. (1981) reported extensive large basis set Hartree Fock calculations of the He-HF potential surface as a function of the orientation, the intermolecular separation and the HF bond length. These results were combined with the dispersion coefficients determined by Mulder et al. (1980) to give estimates of the full potential surface. Two potentials, referred to as the HFD1 and HFD2 potentials, were reported. They differ in the way the small r behaviour was combined with the dispersion expansion. Both rigid rotor and vibration dependent forms of the HFD1 and HFD2 potentials were generated. The vibration dependent HFD1 potential was used by Tennyson and Sutcliffe (1983) to predict the vibrational energy levels of the He-HF van der Waals molecule, and by Gianturco et al. (1983,1984) to investigate vibrationally inelastic energy transfer. Collision energies used in the latter studies ranged from 500 meV up to 4.5 eV.

Of more relevance to the investigations reported in this chapter

are the close coupled and infinite order sudden (IOS) studies of low energy rotationally inelastic cross sections for He-HF reported by Battaglia et al. (1984a,1984b). The rigid rotor HFD1 potential of Rodwell et al. (1982) was used. Inelastic differential cross sections calculated using the IOS approximation differ markedly from the exact close coupled results. In Section 4.4 we compare the CC and IOS results of Battaglia et al. (1984a,1984b) with our own coupled states calculations in order to assess the accuracy of the latter for the weakly anisotropic He-HF system.

Finally, we note that Frick (1984) measured total differential scattering cross sections for He-HF, HCl, C₂H₆, C₂F₆, CF₄, SF₆ and Ne-SF₆ in the range 69 to 95 meV. Battaglia et al. (1984b) compared the He-HF cross section measured by Frick (1984) with IOS calculations using the HFD1 rigid rotor potential. The agreement between theory and experiment was not bad.

4.2 Experimental Results

Measurements of the total differential cross section for He-HF were carried out by Boughton (1986) at mean collision energies of 990 and 516 K (85.3 and 44.5 meV). These results, which are given in Table 4.1, were obtained using the crossed beam apparatus and techniques described in Chapter 2 of this thesis. In these experiments a pure helium primary beam was crossed with a secondary beam of pure HF and bolometer A (see Chapter 2) was used to record the scattering intensities. Prior to measuring the cross sections reported in Table 4.1, the He-Ar cross section was measured and analysed. The results of this study are summarised below. Characteristics of the expansions used are given in Table 4.2.

The HF secondary beam was obtained by expanding pure HF at its vapour pressure through a nozzle heated to about 500 K. Under these conditions it was determined, using the quadrupole mass spectrometer, that the concentration of HF clusters was insignificant. The populations of the HF rotational states present in the beam were determined using the techniques described in Chapter 2 from monomer absorption intensities measured by Boughton (1986). For the first five rotational states we obtained: $j=0$ - 36.21% ; $j=1$ - 42.37% ; $j=2$ - 16.48% ; $j=3$ - 3.80% ; and $j=4$ - 1.14%. These populations, which have been scaled so that their sum is 100%, can be described reasonably well using a Boltzmann rotational distribution corresponding to a temperature of 70 K.

As mentioned in Section 2.7, the internal energies of the detected particles and their adsorption energies must, in principle, be considered. All of the differential cross sections reported in this chapter, however, were obtained by using the bolometer to detect scattered helium atoms, for

Table 4.1

Lab Angle (degrees)	Collision Energy		Lab Angle (degrees)	Collision Energy	
	990 K	516 K		990 K	516 K
2.5	-	51.76 (-)	15.0	2.28 (.2)	1.10 (.1)
3.0	128.20 (7.)	38.16 (3.8)	15.5	2.48 (-)	1.13 (.1)
3.5	93.78 (2.8)	28.08 (1.6)	16.0	2.47 (-)	.95 (.16)
4.0	64.92 (4.2)	20.53 (.9)	16.5	2.56 (.2)	1.01 (.1)
4.5	43.28 (1.7)	15.61 (.4)	17.0	2.40 (-)	.91 (.24)
5.0	25.42	12.47	17.5	2.17 (.2)	.81 (.12)
5.5	12.72 (.5)	9.99 (.4)	18.0	2.13 (.2)	.81 (.16)
6.0	6.52 (.3)	7.98 (.8)	18.5	1.95 (.1)	.67 (.22)
6.2	5.65 (.5)	-	19.0	1.89 (.1)	
6.5	5.93 (.9)	5.92 (.8)	19.5	1.87 (.1)	
7.0	7.85 (1.)	4.11 (.6)	20.0	2.00 (.1)	
7.5	9.99 (1.3)	2.69 (.5)	20.5	1.90 (.1)	
8.0	10.84 (.8)	2.01 (.3)	21.0	1.83 (.1)	
8.5	9.58 (.6)	1.70 (.3)	21.5	1.90 (-)	
9.0	7.06 (.4)	1.82 (.4)	22.0	1.78 (.1)	
9.5	4.39 (.2)	2.07 (.3)	22.5	1.75 (-)	
10.0	2.96 (.2)	2.21 (.5)	23.0	1.74 (.1)	
10.5	2.73 (.5)	2.27 (.2)	23.5	1.80 (-)	
11.0	3.15 (.5)	2.05 (.2)	24.0	1.75 (.01)	
11.5	3.90 (.5)	1.81 (.3)	25.0	1.69 (.02)	
12.0	4.31 (.3)	1.37 (.4)	26.0	1.65 (.1)	
12.5	4.14 (.2)	.96 (.18)	27.0	1.59 (.1)	
13.0	3.50 (.2)	.82 (.18)	28.0	1.61 (-)	
13.5	2.85 (.1)	.90 (.12)	29.0	1.46 (-)	
14.0	2.40 (.2)	.89 (.28)	30.0	1.45 (.2)	
14.5	2.23 (.2)	1.01 (.1)			

Table 4.2

Property	Experiment					
	He-Ar		He-HF		He-HF	
Mean collision						
energy (K)	787 ± 8		990 ± 10		516 ± 5	
(meV)	67.8 ± 0.7		85.3 ± 0.9		44.5 ± 0.4	
Gas used	He	Ar	He	HF	He	HF
Source pressure (kPa)	1200	200	1200	100	1000	100
Source temperature (K)	310	310	310	~500	~80	~500
Stream velocity v_S (m/s)	1794	571	1794	1273	927	1273
Most probable						
velocity v_{mp} (m/s)	1805	574	1805	1289	948	1289
Velocity width						
parameter v_W (m/s)	116	32	116	177	114	177
Velocity spread						
FWHM (%)	13	9	13	22	20	22
Beam divergence						
FWHM (degrees)	1.5	5	1.5	11	1.5	11
Nozzle diameter (μm)	35	40	35	80	35	80
First skimmer						
diameter (μm)	200	500	200	500	200	500
Second skimmer						
diameter (μm)	800	-	800	-	800	-

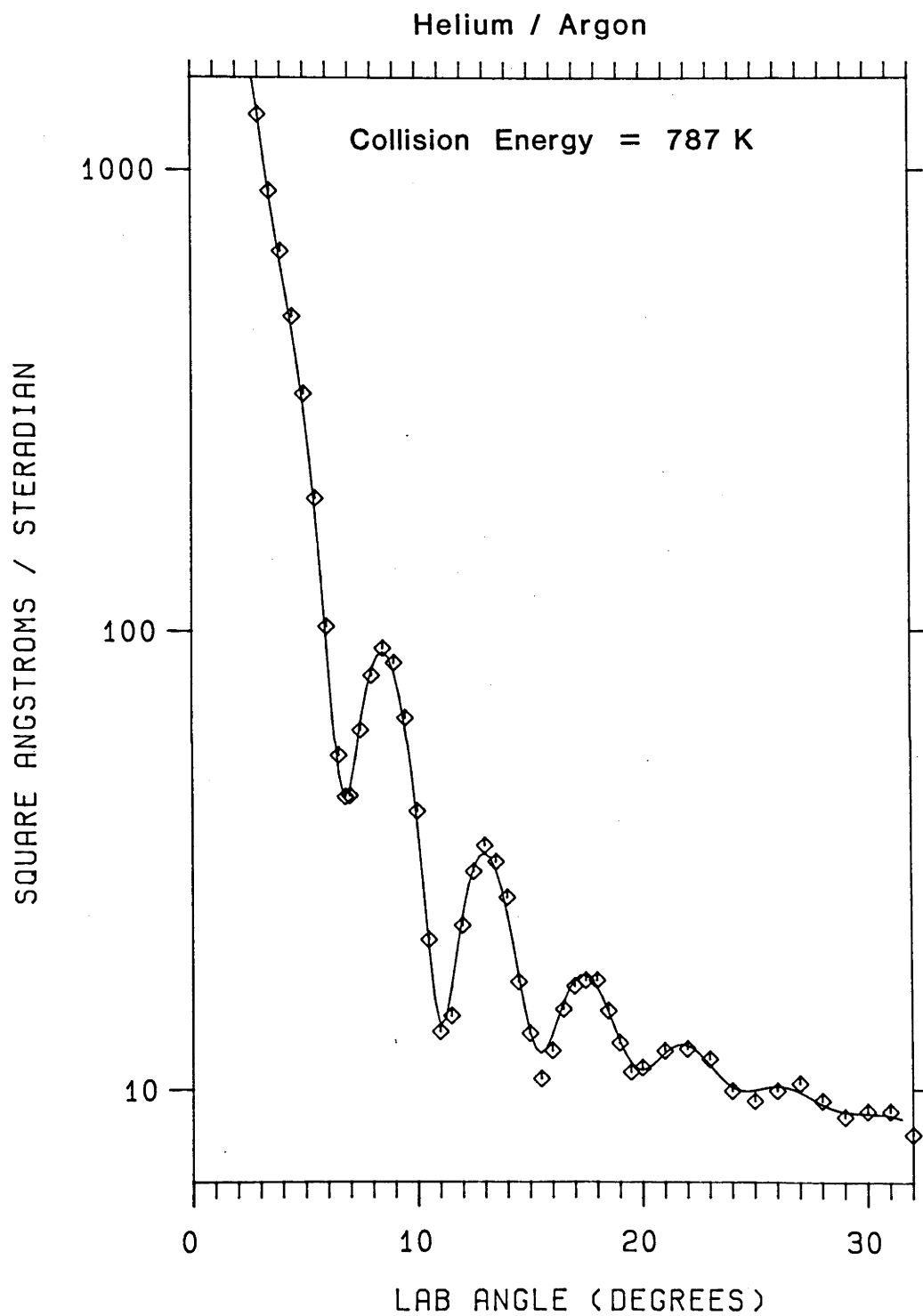


Figure 4.1

4.3 The He-HF Interaction Potential

Most of the scattering calculations reported in this chapter were done using the HFD potentials described by Rodwell et al. (1981). These surfaces were constructed by combining the results of large basis set Hartree Fock (HF-) calculations with accurate values of the dispersion coefficients (---D) using formulae described by Douketis et al. (1984). Briefly, the HFD surfaces take the form

$$V(\text{HFD}) = V(\text{Hartree Fock}) + \sum_n F_n(\rho) V_n(\text{Dispersion}) \quad (4.1)$$

where the individual terms $V_n(\text{Dispersion})$ of the dispersion series are multiplied by damping functions $F_n(\rho)$ which approach zero for sufficiently small He-HF separations and approach unity for large separations. Full details, including values of the dispersion coefficients, are given by Rodwell et al. (1981). For the present purpose it is sufficient to note that the two potential surfaces reported by Rodwell et al. (1981), referred to as the HFD1 and HFD2 potentials, were determined by different choices of the parameter ρ which appears in the damping function and has been shown explicitly in the simplified Eq. (4.1).

As mentioned in the introduction, Rodwell et al. (1981) reported two sets of calculations, one based on the rigid rotor approximation, and the other taking into account the vibrational motion of the HF molecule. The rigid rotor potentials were expanded in terms of Legendre polynomials

$$V(r, \cos\gamma) = \sum_{\lambda=0}^8 V_{\lambda}(r) P_{\lambda}(\cos\gamma) \quad (4.2)$$

with r the distance between the helium atom and the centre of mass of the HF molecule, and γ the angle between the HF bond and the line of centres

(see Figure 3.1). The vibration dependent potential surfaces were represented as double expansions

$$V(r, R, \cos\gamma) = \sum_{\lambda=0}^6 \sum_{n=0}^3 V_{n\lambda}(r) s^n P_{\lambda}(\cos\gamma) \quad (4.3)$$

with $s = (R - R_e)/R_e$ being the relative displacement of the HF bond from its equilibrium value R_e . Coefficients $V_{\lambda}(r)$ and $V_{n\lambda}(r)$, tabulated by Rodwell et al. (1981) at 0.01 atomic unit intervals in the range 3 to 11 atomic units, were used in the investigations reported in this chapter in conjunction with a four point Lagrange interpolation formula. A dispersion series was used to evaluate the interaction potential at large r (see Rodwell et al. (1981)). As will become apparent in Section 4.7, the fits obtained to the measured cross sections could be improved either by altering the dispersion coefficients or by changing the parameter ρ which appears in Eq. (4.1). These modifications required that the interpolation tables be regenerated from the original data of Rodwell et al. (1981). Cuts through the HFD1 R-dependent potential are shown in Figure 4.2 with $R = R_{eq} = 1.7328$ atomic units (0.091696 Å) and different values of the potential angle. Zero degrees corresponds to the collinear He-H-F geometry.

The scattering calculations based on the HFD1 potential of Rodwell et al. (1981) show that the anisotropic components of the He-HF potential surface make only a small contribution to the total differential scattering cross section (see the following sections). In Section 4.7 we present an analytic, spherically symmetric interaction potential which is consistent with the measured scattering intensities. The model chosen was that used by Barker and Pompe (1968), Barker and Bobetic (1970) and Barker et al. (1971) to describe rare gas interactions:

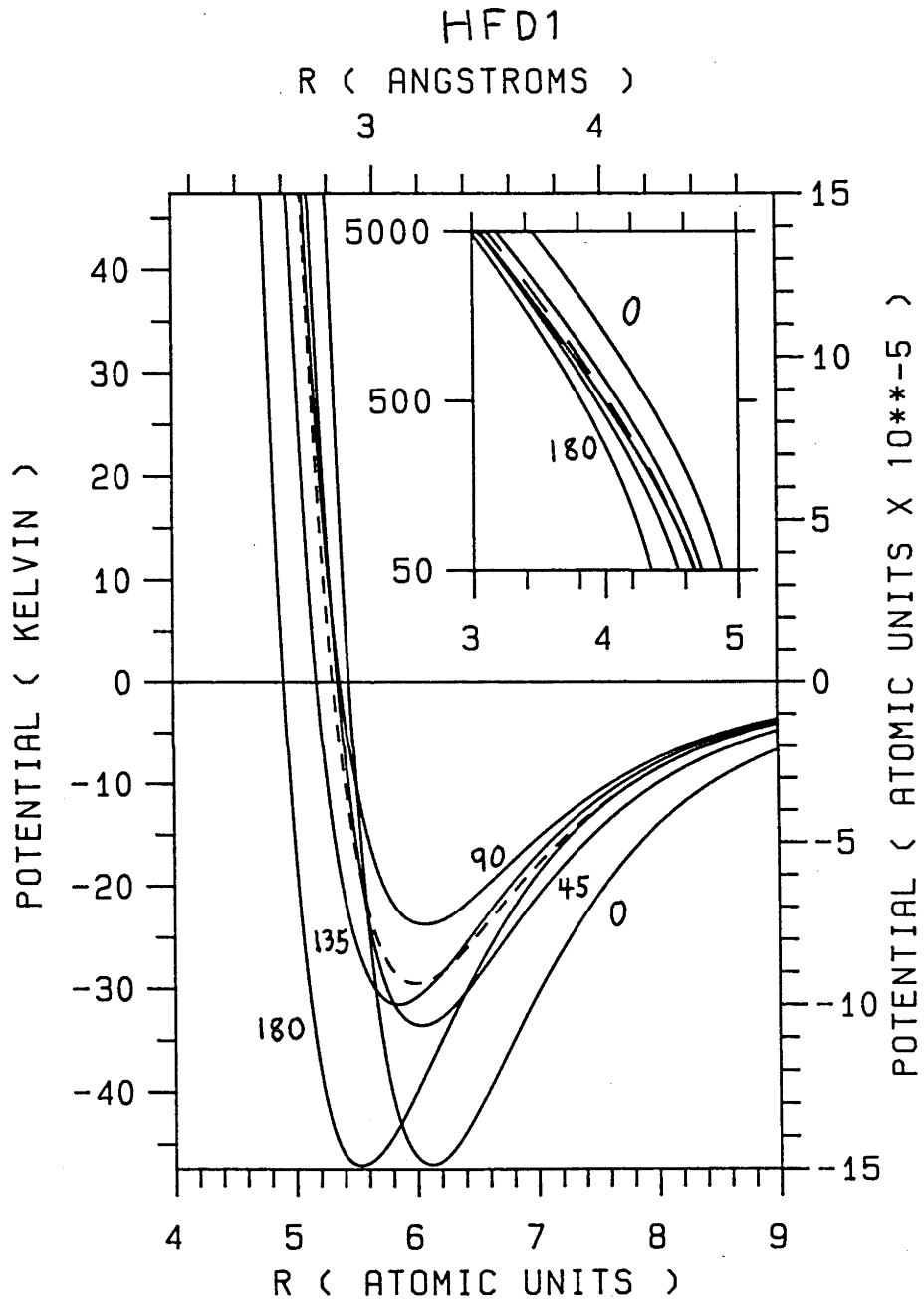


Figure 4.2

$$V(r) = \epsilon \left[\exp(\alpha(1-x)) \sum_{n=0}^3 A_n (x-1)^n - \frac{C_6}{x^{6+\delta}} - \frac{C_8}{x^{8+\delta}} \right] \quad (4.4)$$

with $x = r/r_m$, ϵ the well depth and r_m the position of the minimum. Values of the parameters used to describe the He-HF potential are reported in Section 4.7.

The coupling between channels in the CS approximation requires the evaluation of matrix elements of the form $\langle v'j' | ((R-R_e)/R_e)^n | vj \rangle$ for $v=v'=0$ (see Section 3.6). As suggested by Rodwell et al. (1981), the perturbed Morse oscillator potential reported by Huffaker (1977) was used to characterise the HF vibration. For each j the exact eigenfunctions $|vj\rangle$ (ie. the solutions of the relevant Schrödinger equation) were expanded in terms of a Morse basis $\{ |v\rangle : v=0, \dots, 9 \}$ and the eigenvectors were used to transform the matrix $\langle v' | ((R-R_e)/R_e)^n | v \rangle$, evaluated by direct integration, to obtain the desired matrix elements. The corresponding eigenvalues are the rovibrational energies of the isolated HF molecule, which were also needed for the coupled states studies.

4.4 A Comparison Between the Present Coupled States Calculations and Previous Close Coupled Results

Battaglia et al. (1984a,1984b) calculated both close coupled and infinite order sudden cross sections for low energy He-HF collisions using the rigid rotor HFD1 potential. Assuming that the CC results are converged, they represent the exact values for the given interaction potential. We report l-average CS calculations at the same total energy of 313 K (27.0 meV) (relative to the $v=0, j=0$ state of HF) and compare our results with those of Battaglia et al. (1984a,1984b). It is stressed that these calculations were carried out at a fixed total energy, as opposed to a fixed kinetic energy (also referred to as the collision energy). The log-derivative method was used to integrate the CS equations from $r = 2$ atomic units (0.106 nm) to 60 atomic units (3.175 nm) with a step size of 0.02 atomic units (0.001 nm). Values of the total angular momentum from $J=0$ to 80 were summed. Two closed channels were included in the integrations, along with the three energetically open channels which exist at this energy. The asymptotic energies and wave vectors are given in Table 4.3. All cross sections were averaged over the initial m states and summed over all possible values of m' (see Section 3.5). Under these conditions we expect to obtain CS cross sections converged to within at worst 0.5 % of their exact values. To obtain CS cross sections which can be compared with the CC results, a calculation was made using the rigid rotor HFD1 potential. Next, the effect of including the zero-point vibrational motion was assessed by calculating CS cross sections for the full vibration dependent HFD1 potential for with $v=0$.

In Table 4.4 and Figure 4.3 we compare our CS integral and

Table 4.3Basis set for CS calculations at a collision energy of 313 K

j	E_j (K)	k_j^2 (\AA^{-2})	k_j (\AA^{-1})	λ_j (\AA)
0	0.	43.03	6.561	0.958
1	59.15	34.91	5.907	1.064
2	177.4	18.65	4.318	1.163
3	354.5	-5.710	2.391	-
4	590.4	-38.15	6.176	-

Table 4.4

j→j'	Rigid rotor		Vibration included
	CC	CS	CS
0→0	69.6	70.7	70.6
1→1	77.3	78.3	78.4
2→2	107.0	107.8	108.5
0→1	3.38	3.27	3.86
0→2	.23	.21	.32
1→2	1.60	1.65	1.99

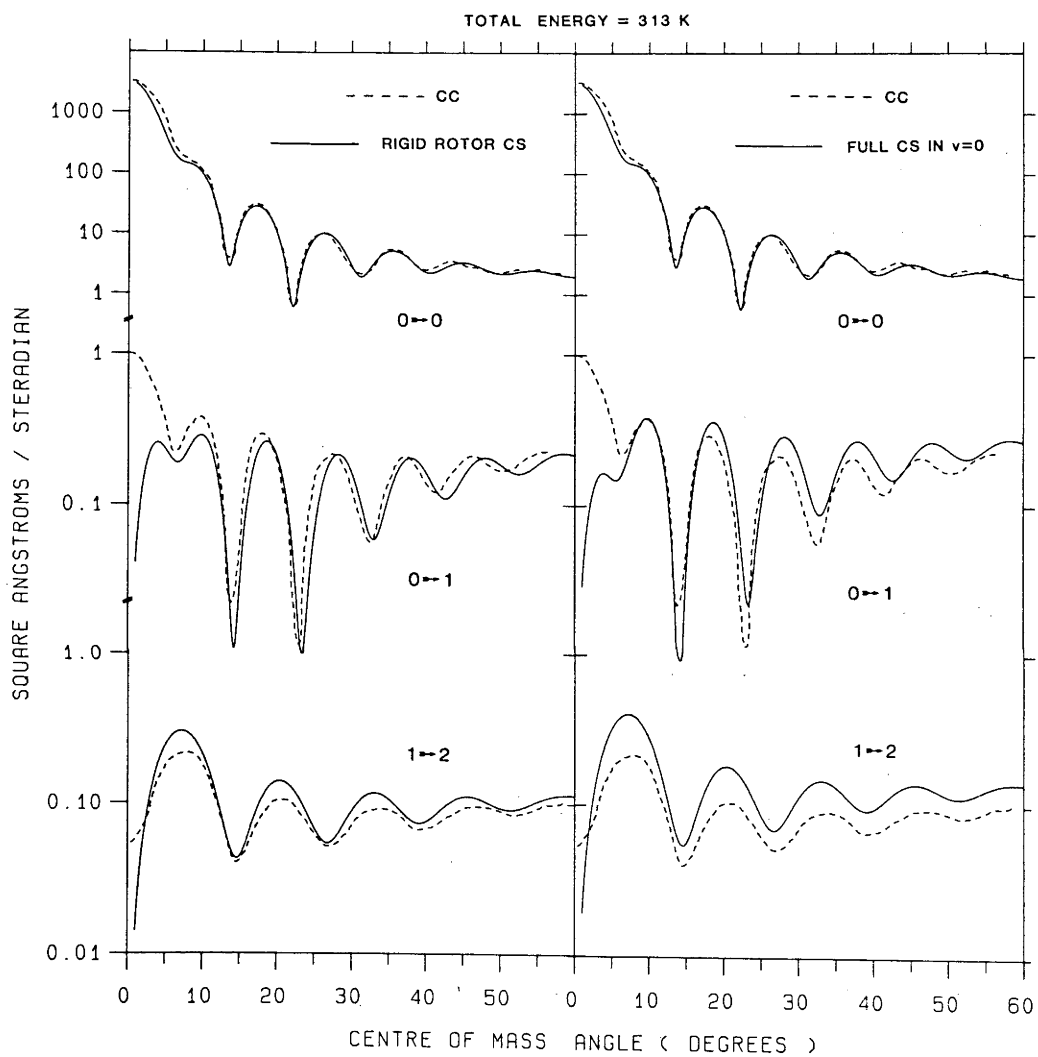


Figure 4.3

differential cross sections with the CC results reported by Battaglia *et al.* (1984b). Consider first the rigid rotor calculations. The integral cross sections are in good agreement, with only small differences between the corresponding $0 \rightarrow 1$, $0 \rightarrow 2$ and $1 \rightarrow 2$ processes. Although Battaglia *et al.* (1984b) obtained l -average IOS integral cross sections that were fairly close to the CC values, the corresponding differential cross sections were "grossly in error". The CS results, on the other hand, reproduce these CC differential cross sections rather well, differing only slightly in the positions and amplitudes of the diffraction oscillations, and underestimating the cross sections for centre of mass angles below about four degrees. Given that the CS results were converged as a function of both the integration algorithm and the maximum total angular momentum used in the summations, we attribute this disagreement at small scattering angles to a breakdown of the CS approximation.

When the zero-point ($v=0$) vibration is included in the CS calculations one finds that, whereas the elastic cross sections differ only slightly from the rigid rotor values, the inelastic cross sections are significantly increased. Indeed, the $0 \rightarrow 1$, $0 \rightarrow 2$ and $1 \rightarrow 2$ integral cross sections are 14, 39 and 24 percent larger than the corresponding CC cross sections obtained using the rigid rotor potential. This increase is reflected as an overall scaling of the $0 \rightarrow 1$ and $1 \rightarrow 2$ differential cross sections, with their shapes closely resembling those obtained from the rigid rotor CS calculations.

We now consider the value of the orbital angular momentum parameter \bar{l} and the phase choice used in the IOS and CS approximations (see Section 3.5). Within the CS approximation, the l -initial ($\bar{l}=1$) and l -final ($\bar{l}=1'$) choices lead to simpler (identical) expressions for the cross

sections than does the l -average ($\bar{l}=(l+l')/2$) choice (Khare et al. (1980)). For the systems He-CO, He-HCl and Ne-HD at low collision energies, both the IOS and CS degeneracy averaged differential cross sections are in reasonable agreement with the CC results only for the l -average and "correct phase" choices (Fitz et al. (1981) and Khare et al. (1980)). Other combinations of phase choice and \bar{l} , although often predicting accurate integral cross sections, lead to degeneracy averaged differential cross sections for odd Δj transitions whose diffraction oscillations are out of phase with the CC results. As noted above, the l -average "correct phase" CS differential cross sections (shown in Figure 4.3) agree rather well with the CC results, whereas the l -average IOS results were found to differ significantly (Battaglia et al. (1984b)). Although Battaglia et al. (1984b) report using an l -average algorithm, it is not clear which phase choice they used. The disagreement between the IOS and CC results may be due to an incorrect phase choice. Given the large separations between the HF energy levels (compared to the total energy) and the fact that the $j=2$ channel is almost closed (see Table 4.3), it is quite likely that the IOS approximation does not provide a good description of the inelastic scattering.

The comparison presented here with the close coupled results of Battaglia et al. (1984b) shows that the l -average CS approximation with the "correct phase" choice, unlike the l -average IOS method used by Battaglia et al. (1984b), is able to adequately predict both the integral and differential scattering behaviour in low energy He-HF collisions.

4.5 A Comparison Between Coupled States, IOS and Spherical Potential Calculations

Although the He-HF interaction potential is clearly anisotropic, the calculations of Rodwell et al. (1981) show that non-spherical terms in the surface are relatively small. Consequently, one might expect that the total differential scattering could be adequately described using a suitable spherical potential. In order to examine this possibility, four scattering calculations based on the HFD1 potentials were carried out. The first was coupled states calculation using the full vibration dependent HFD1 potential. Next, the rigid rotor HFD1 potential was used in an IOS calculation based upon semiclassical phase shifts calculated at sixteen orientations. A fully quantum single channel calculation was then carried out using the spherical term $V_{00}(r)$ of the HFD1 potential. In this case the log-derivative algorithm was used to solve the differential equations, and was optimised to give cross sections that were converged to within 0.5 percent (with respect to the integration scheme used). Finally, a single channel semiclassical calculation was performed using the same spherical potential. In all of the above investigations we included phase shifts (or S-matrices) for values of the total angular momentum quantum number from 0 to 120, giving total integral and differential cross sections that are converged to within 0.2 percent with respect to the maximum total angular momentum parameter used. This degree of convergence was confirmed by computing a number of cross sections using total angular momenta from 0 to 200. To facilitate a detailed comparison between these four methods, the calculations were carried out with no averaging over velocity distributions or detector geometry.

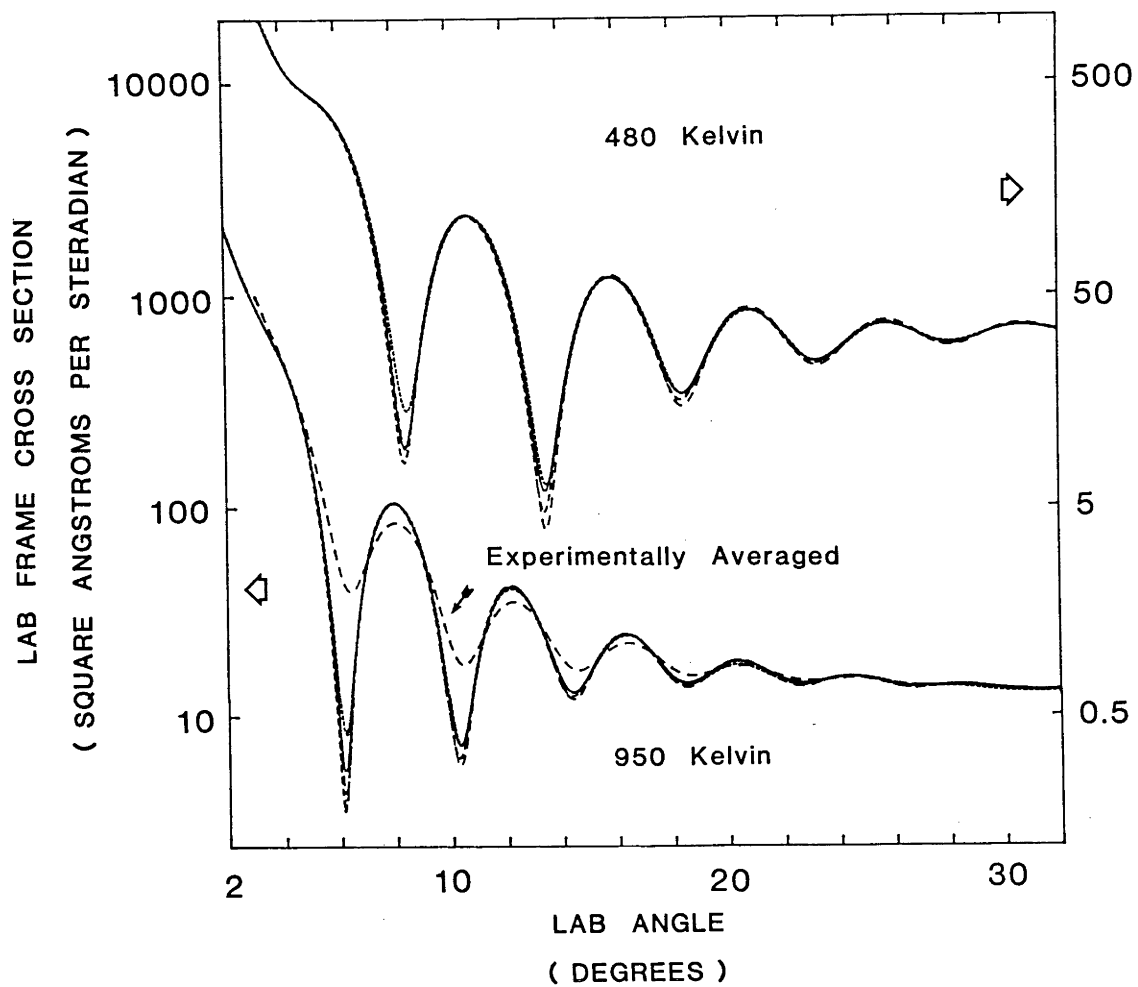


Figure 4.4

using the four methods. An enlargement of part of this figure, excluding the spherical potential semiclassical results, is given in Figure 4.5. The different techniques give very similar results, indicating that the total differential scattering can be well described by using the spherical part of the interaction potential. The main difference between the CS and IOS cross sections is that the diffraction oscillations in the latter are slightly more damped. On the other hand, the spherical potential calculations give more highly resolved oscillations than the CS method. The differences between the two single channel calculations are very small, indicating that it is satisfactory to use semi-classical methods to obtain the spherical potential phase shifts at the collision energies considered. Upon averaging over the experimental distributions, we expect the differences between the four differential cross sections to become negligible. Consequently, the analysis of the experimental data discussed in Section 4.7 was carried out using spherical potential semiclassical techniques. The total integral cross sections obtained from the four calculations are given in Table 4.5. As was the case for the differential cross sections compared above, the total integral cross sections are very similar for the different methods.

By averaging the 950 K total differential cross sections using a rectangular angular window 2.2° wide, one obtains a cross section with diffraction oscillations damped by about the same amount as those of the experimentally measured cross section. That this should be the case is somewhat fortuitous. To illustrate the degree of damping of the experimentally measured diffraction oscillations, the angle averaged CS cross section has been included in Figure 4.4 for a collision energy of 950 K.

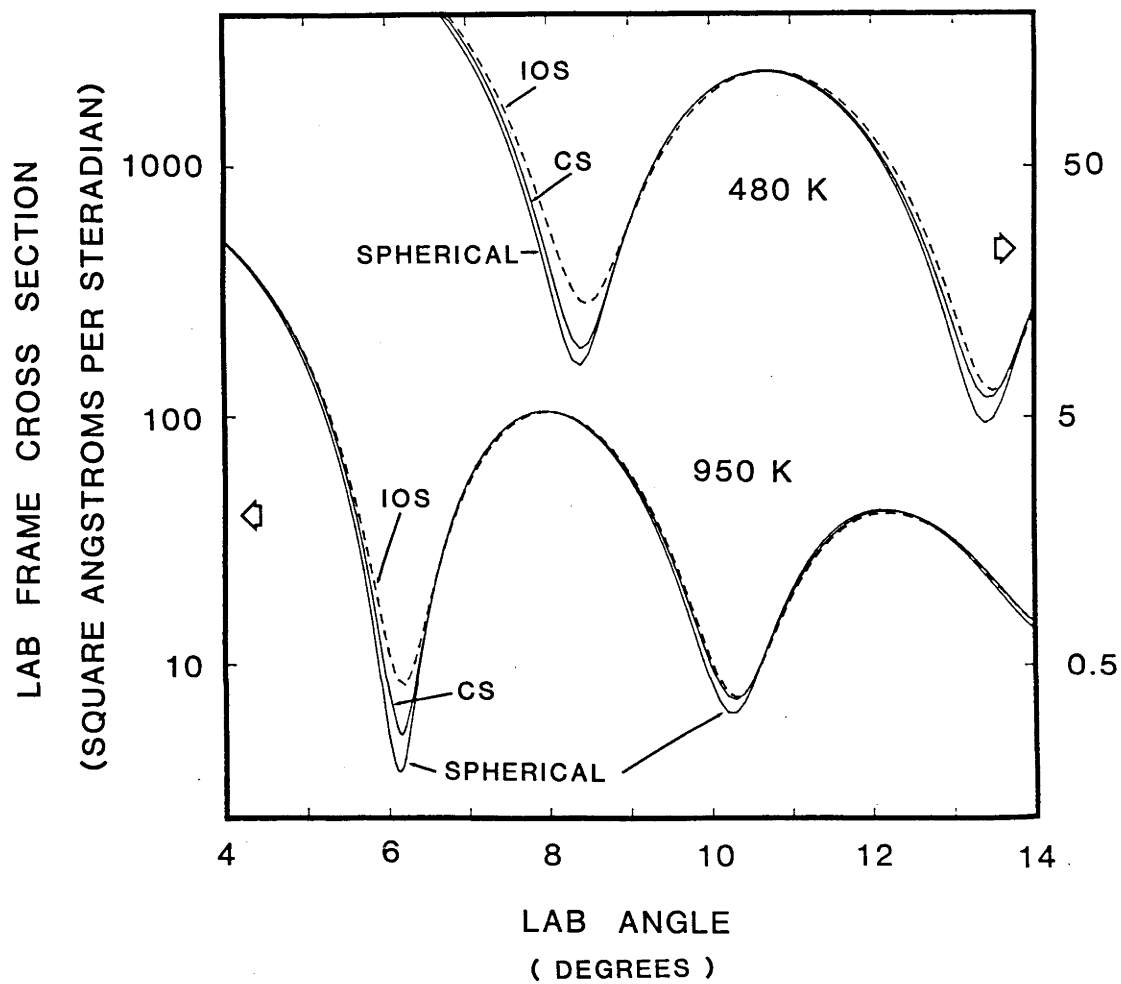


Figure 4.5

Table 4.5

Total Integral Cross Sections (\AA^2)		
collision energy		
method	480 K	950 K
coupled states	52.44	63.65
infinite order		
sudden	53.05	65.07
spherical potential		
quantum	52.27	63.03
spherical potential		
semiclassical	52.52	64.04

4.6 Inelastic Cross Sections Within the Coupled States Approximation

Newton diagrams for monoenergetic 90° He-HF collisions at the two energies studied are shown in Figures 4.6 and 4.7 (compare with Figure 3.2). The speeds of the He and HF molecules used in the calculations are similar to the most probable speeds given in Table 4.2. Final laboratory and centre of mass frame velocity vectors corresponding to a laboratory scattering angle of 30° are shown. For elastic collisions and $j=0 \rightarrow j=1$ or $j=1 \rightarrow j=0$ inelastic processes, the velocities of the scattered helium atoms terminate on the correspondingly labelled circular arcs. The speeds of the scattered helium atoms increase significantly as the laboratory scattering angle is varied from 0 to 30 degrees. It is therefore essential to include the velocity dependence of the detector response in calculations which attempt to simulate measured differential scattering intensities.

The rovibrational energies of the HF states included in the calculations are given in Tables 4.6 and 4.7 along with the asymptotic channel wavevectors and wavelengths. Four sets of wavevectors and wavelengths are shown in each table, corresponding to total energies $E_{\text{total}} = E_{\text{collision}} + E_{j\text{-initial}}$, where $j\text{-initial}$ is either 0, 1, 2 or 3. All existing open channels and at least one closed channel were included in every calculation. Convergence studies suggest that, except perhaps for the $j=3 \rightarrow j'$ transitions, the coupled states cross sections reported in this chapter are converged to within about 1%. Notice also that the asymptotic wavelengths, which determine the oscillatory behaviour of the solutions to the scattering equations, are all rather large. The asymptotic wavelengths for the elastic channels are 0.77 and 0.55 Å (1.0 and 1.5 atomic units) at collision energies of 480 and 950 K respectively.

Newton diagram for He-HF

collision energy = 950 K

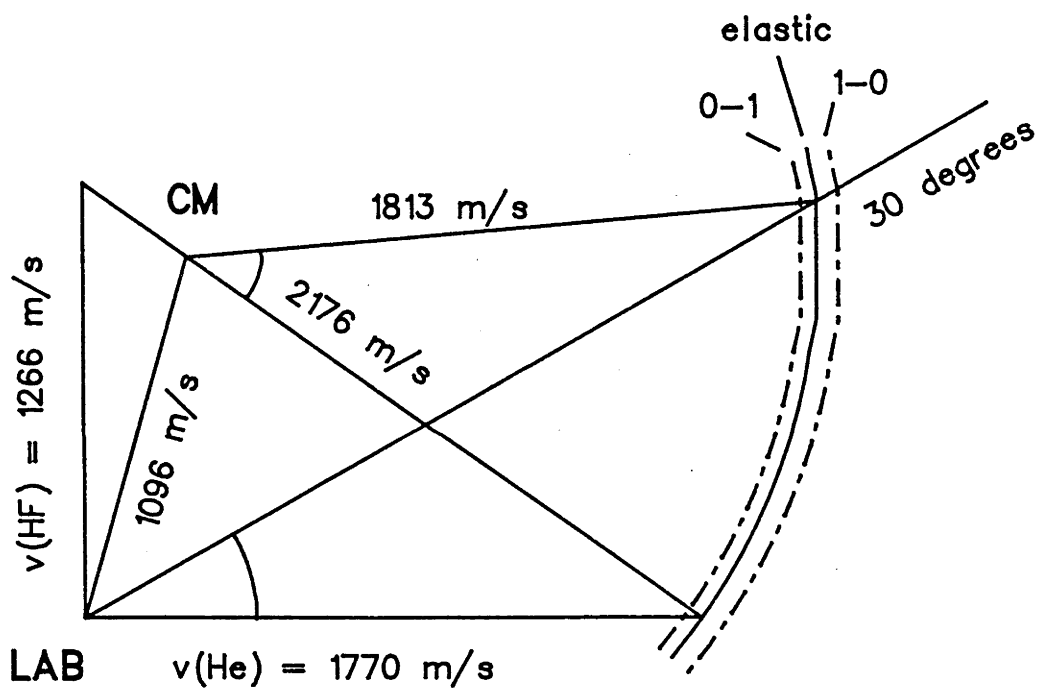


Figure 4.7

Table 4.6

Basis sets for He-HF calculations at a collision energy of 480 K

		j-initial = 0			j-initial = 1		
j	E_j (K)	k_j^2 (\AA^{-2})	k_j (\AA^{-1})	λ_j (\AA)	k_j^2 (\AA^{-2})	k_j (\AA^{-1})	λ_j (\AA)
0	0	65.99	8.124	0.774	74.18	8.610	0.730
1	59.15	57.89	7.608	0.826	65.99	8.124	0.774
2	177.4	41.60	6.452	0.974	49.74	7.052	0.891
3	354.5	17.25	4.154	1.513	25.39	5.038	1.247
4	590.4	-15.18	3.897	-	-7.049	2.655	-
5	884.7	-55.64	7.461	-	-47.53	6.894	-

		j-initial = 2			j-initial = 3		
j	E_j (K)	k_j^2 (\AA^{-2})	k_j (\AA^{-1})	λ_j (\AA)	k_j^2 (\AA^{-2})	k_j (\AA^{-1})	λ_j (\AA)
0	0	90.38	9.507	0.661	114.7	10.713	0.586
1	59.15	82.28	9.071	0.693	106.6	10.325	0.609
2	177.4	65.99	8.124	0.774	90.35	9.505	0.661
3	354.5	41.64	6.453	0.974	65.99	8.124	0.774
4	590.4	9.213	3.035	2.070	33.57	5.794	1.084
5	884.7	-31.25	5.592	-	-6.896	2.627	-

Table 4.7

Basis sets for He-HF CS calculations at a collision energy of 950 K

		j-initial = 0			j-initial = 1		
j	E_j (K)	k_j^2 (\AA^{-2})	k_j (\AA^{-1})	λ_j (\AA)	k_j^2 (\AA^{-2})	k_j (\AA^{-1})	λ_j (\AA)
0	0	130.6	11.43	0.550	138.8	11.78	0.533
1	59.15	122.5	11.07	0.568	130.6	11.43	0.550
2	177.4	106.2	10.31	0.610	114.4	10.69	0.587
3	354.5	81.88	9.048	0.694	90.03	9.488	0.662
4	590.4	49.46	7.032	0.894	57.57	7.589	0.828
5	884.7	8.981	2.997	2.100	17.11	4.137	1.519
6	1237.0	-39.46	6.283	-	-31.26	5.597	-
7	1647.0	-95.85	9.791	-	-87.71	9.365	-
8	2114.1	-160.1	12.65	-	-151.95	12.33	-

		j-initial = 2			j-initial = 3		
j	E_j (K)	k_j^2 (\AA^{-2})	k_j (\AA^{-1})	λ_j (\AA)	k_j^2 (\AA^{-2})	k_j (\AA^{-1})	λ_j (\AA)
0	0	155.0	12.45	0.505	179.4	13.39	0.469
1	59.15	146.9	12.12	0.519	171.3	13.09	0.480
2	177.4	130.6	11.43	0.550	155.0	12.45	0.505
3	354.5	106.3	10.31	0.610	130.6	11.43	0.550
4	590.4	73.85	8.593	0.731	98.20	9.910	0.634
5	884.7	33.37	5.777	1.087	57.74	7.599	0.827
6	1237.0	-15.12	3.883	-	9.281	3.046	2.063
7	1647.0	-71.46	8.453	-	-47.10	6.862	-
8	2114.1	-135.7	11.65	-	-111.3	10.55	-

These elastic channel wavelengths, λ_j , are important in determining the nature of the rainbow and diffraction oscillations for a given interaction potential. Indeed, the separation between the diffraction oscillations is determined by the ratio λ_j/r_m , where r_m is a measure of the position of the minimum of the potential (Loesch (1980)). The compression of the oscillations at the higher collision energy results primarily from a smaller value of λ_j .

The elastic and inelastic centre of mass frame integral cross sections are given in Tables 4.8a and 4.9a for collision energies of 480 and 950 K respectively. In order to assess their contributions to the measured intensities, we weighted each cross section by the fraction of molecules in the HF beam whose rotational states correspond to the initial state of the transition. These weighted cross sections, expressed as percentages of the weighted total integral cross section, are shown in Tables 4.8b and 4.9b. Laboratory frame differential cross sections, which have also been weighted by the appropriate rotational populations, appear in Figure 4.8. The comparison given in Section 4.4 with the close coupled results obtained by Battaglia et al. (1984b) suggests that the CS cross sections presented in this section are close to the exact cross sections for the vibration dependent HFD1 potential surface.

The results presented in Tables 4.8 and 4.9 show that, at the energies considered here, He-HF scattering is dominated by elastic processes. Inelastic integral cross sections are all one or two orders of magnitude smaller than the elastic ones. The population weighted 0 \rightarrow 1 integral cross section, which is the largest population weighted inelastic cross section, represents 3.7% of the population weighted total integral cross section at 950 K and 2.7% at 480 K, whereas the contributions from

Table 4.8

(a) Integral cross sections at a collision energy of 480 K (\AA^2).

initial j	final j				
	0	1	2	3	4
0	58.10	4.70	.73	.06	closed
1	1.83	58.71	2.86	.30	closed
2	.34	2.32	58.78	2.15	.05
3	.05	.53	2.57	59.14	1.40

(b) Population weighted integral cross sections at a collision energy of 480 K expressed as percentages of the total population weighted integral cross section.

initial j	final j				
	0	1	2	3	4
0	33.44	2.70	.42	.04	closed
1	1.23	39.55	1.92	.20	closed
2	.09	.61	15.39	.56	.01
3	.003	.03	.16	3.57	.08

Table 4.9

(a) Integral cross sections at a collision energy of 950 K (\AA^2).

Initial j	final j				
	0	1	2	3	4
0	44.70	5.33	2.07	.21	.11
1	1.88	46.07	3.40	1.04	.10
2	.59	2.31	45.97	3.01	.57
3	.05	.80	2.63	46.10	2.65

(b) Population weighted integral cross sections at a collision energy of 950 K expressed as percentages of the total population weighted integral cross section.

initial j	final j				
	0	1	2	3	4
0	31.20	3.72	1.45	.15	.07
1	1.51	37.67	2.73	.85	.08
2	.19	.73	14.59	.95	.18
3	.004	.06	.19	3.38	.19

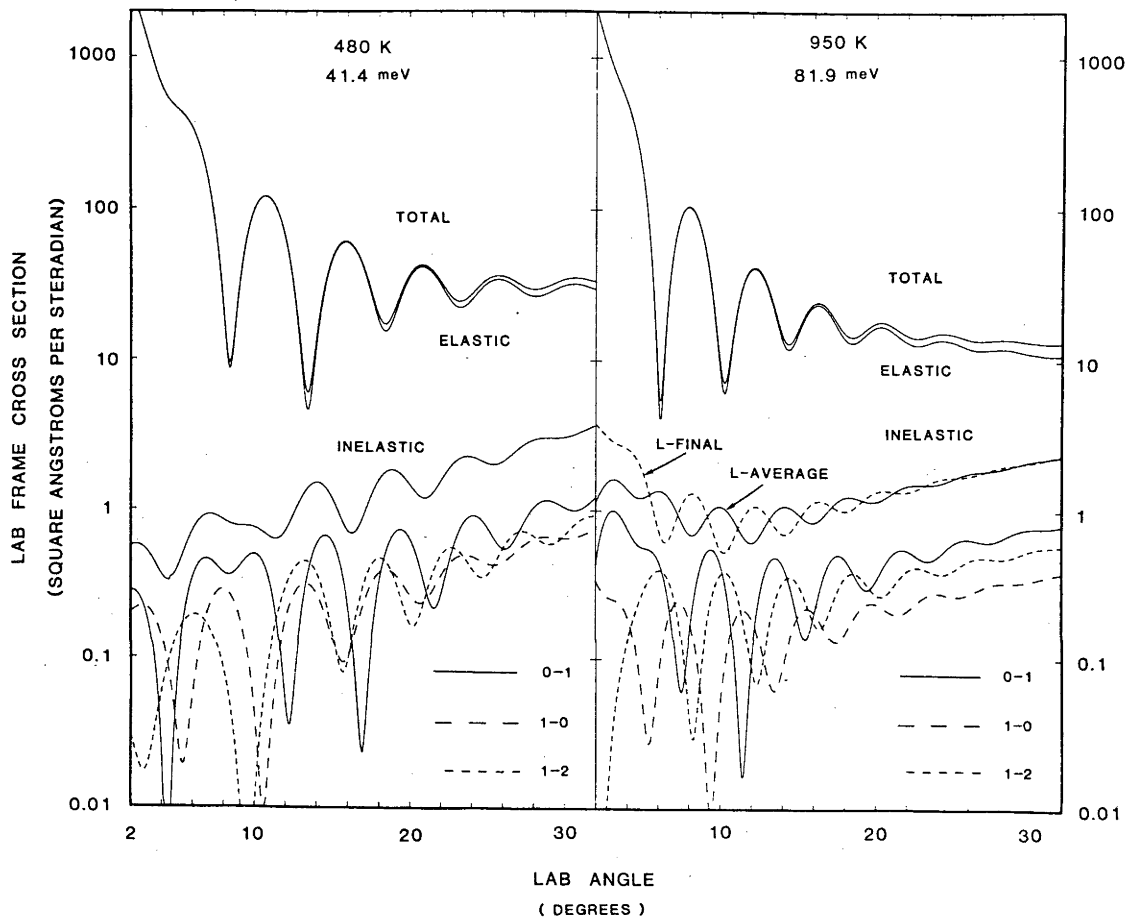


Figure 4.8

all elastic processes are 87% and 92% respectively.

Consider the differential cross sections shown in Figure 4.8. As expected on the basis of the integral cross sections, elastic processes dominate the scattering at both energies. The individual elastic differential cross sections were each found to have the same shapes as the total elastic cross sections shown in the figure. Although the inelastic cross sections are small, their contribution to the population weighted total differential cross sections can be significant at certain angles. In Table 4.10 we give these contributions, for scattering at a collision energy of 950 K, at the first three minima in the total differential cross section and at 32° . The upper numbers are the percentages for the unaveraged cross sections, and the lower figures resulted from averaging the cross sections using a 2.2° angular window. As noted in Section 4.5, the damping of the diffraction oscillations resulting from such averaging is similar to that observed experimentally. The largest inelastic contribution, namely 8%, is seen for the $0 \rightarrow 1$ excitation near the first minimum in the total differential cross section. After angle averaging, however, this figure drops below 1%. At a laboratory scattering angle of 32 degrees, the total contribution from inelastic processes is about 17% after angle averaging. The $0 \rightarrow 1$ transition accounts for 3.7% of the total differential cross section at 32° after angle averaging.

An investigation of the coupled states state-to-state integral and differential cross sections obtained using the l-final and "correct phase" choices was also undertaken. The individual even Δj inelastic differential cross sections were found to agree fairly well with the l-average "correct phase" results, whereas those for odd Δj transitions were not in agreement. The breakdown of the l-final CS approximation has been discussed in

Table 4.10

percentages of the total differential scattering cross
section at a collision energy of 950 K

cross section	first minimum	second minimum	third minimum	32 degrees
total	24.7	14.4	8.1	17.6
inelastic	3.0	5.3	6.0	16.6
0→1	8.0	5.1	3.0	6.0
	.9	1.8	2.0	5.8
1→0	2.0	1.5	1.2	2.9
	.4	.7	1.0	2.7
1→2	7.3	5.5	2.8	4.4
	.8	1.8	1.9	4.3

Sections 3.5 and 4.4. The total inelastic differential cross section, calculated using the l-final and correct phase choices, is shown in Figure 4.8 at a collision energy of 950 K. Given that it is dominated by $\Delta j = \pm 1$ transitions, it is not surprising that the diffraction oscillations present in this cross section are 180° out of phase with those of the l-average "correct phase" cross section. We note that the integral state-to-state cross sections calculated using the l-final and "correct phase" choices are identical to those obtained with the l-average and "correct phase" choices.

In Section 2.8 we noted the possibility that two centre of mass scattering angles may lead to forward scattering at the same laboratory angle. At a collision energy of 950 K this did not occur for the range of inelastic processes considered. For the low energy collisions there were situations in which two centre of mass scattering angles contributed to scattering at the same laboratory angle. In nearly all such cases the scattered intensity resulting from the slower of the two scattered helium atoms was negligible. The exceptions are the $0 \rightarrow 2$, $2 \rightarrow 3$ and $3 \rightarrow 4$ inelastic transitions for angles near the minimum laboratory scattering angles. These angles are approximately 4.6° for the $0 \rightarrow 2$ and $2 \rightarrow 3$ differential cross sections and 20.6° for the $3 \rightarrow 4$ cross section. As one approaches the minimum scattering angle from above, the computed laboratory frame differential cross section increases without bound (although the integrated intensity is finite). To understand this behaviour consider the last equation in Table 3.1. As the threshold is approached the two allowed values of η (which correspond to the two contributing centre of mass scattering angles) approach 90° and the Jacobians for the angle transformations, and hence also the cross sections, increase without bound. The noticeable discontinuity (albeit a tiny one) seen in the 480 K total

inelastic differential cross section at 4.7° results from the divergence of the $0 \rightarrow 2$ and $2 \rightarrow 3$ cross sections as the threshold angle is approached. A similar jump was noticed for the $3 \rightarrow 4$ cross section at 20.7° although, inadvertently, this cross section was omitted when calculating the cross sections shown in Figure 4.8 at a collision energy of 480 K. Apart from a tiny bump at 20.7° , the $3 \rightarrow 4$ population weighted differential cross section is completely negligible as far as the total inelastic cross section is concerned.

4.7 Comparing Theory with Experiment

In this section we discuss a reanalysis of the cross sections measured by Boughton (1986). The reanalysis was done because (1) a number of errors were discovered in the original computer programs, and (2) a reanalysis of the velocity distributions produced slightly different results. The velocity distributions used in the present analysis are given in Table 4.2. Algorithms used to average the computed cross sections over the velocity distributions and the angular view of the detector are given in Section 3.8. While the present results agree qualitatively with those of Boughton's original analysis, the differences were sufficient to warrant a discussion of the reanalysis in this thesis.

The experimentally measured total differential scattering intensities, which have been discussed in Section 4.2, are shown in Figure 4.9. Four sets of cross sections calculated using potentials surfaces which are discussed below are also shown. The computed cross sections were averaged over the experimental conditions and based upon semiclassical calculations using the spherical parts of the interaction potentials. In each case the scaling parameter λ which appears in Eq. (3.72) was chosen to minimise the fitting parameter S .

Cross sections predicted using the spherical parts of HFD1 and HFD2 potentials are shown in Figure 4.9. Both models give good fits to the experimental data at a collision energy of 990 K and reasonable fits at 516 K. It was not possible to obtain a unique potential surface from the present measurements alone. The lack of additional experimental data for the He-HF system meant that it was not possible to attempt a simultaneous fit to the differential cross sections and other experimental data.

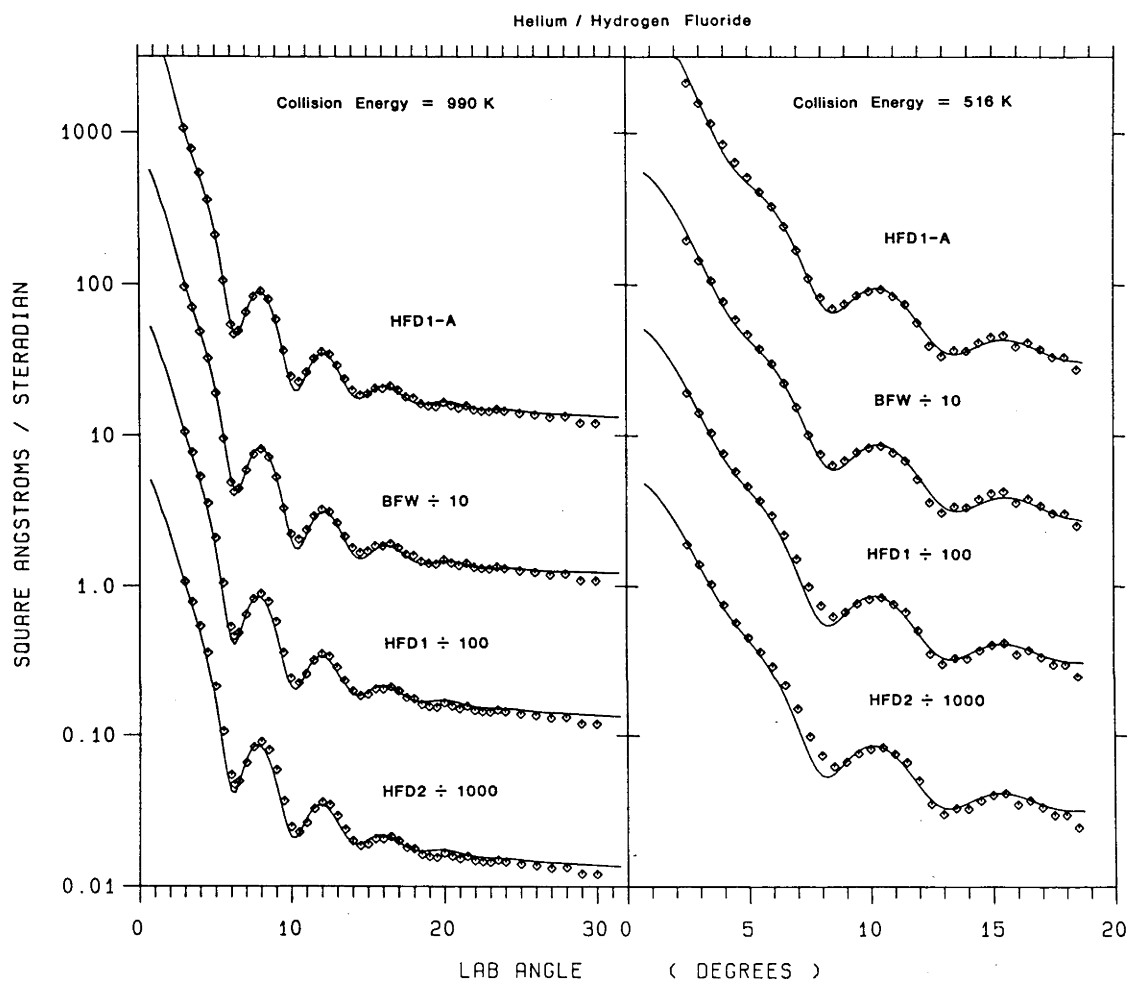


Figure 4.9

Instead, we chose to examine the modified HFD1 and HFD2 potentials which Boughton (1986) considered in an attempt to improve the agreement with experiment.

A simple way to adjust the HFD potentials is to vary the dispersion coefficients in order to improve the fits to the measured intensities. In developing an HFD potential for Ar-HF, Douketis et al. (1984) used this approach and found that spectroscopic data for the Ar-HF van der Waals molecule were reproduced well when all of the dispersion coefficients for this system were increased by 27% (see Section 4.1). The results of the present investigations show that the agreement between the calculated and measured He-HF scattering intensities is improved by (1) increasing the C_6 spherical coefficient in the HFD2 model by 24% (HFD2-A), (2) increasing the spherical C_6 coefficient in the HFD2 model by 18% and recalculating the other dispersion coefficients using the method discussed by Rodwell et al. (1981) (HFD2-B), or (3) increasing the spherical C_6 coefficient in the HFD1 model by 18% (HFD1-A). Values of the well depths and other properties of the spherical parts of these potentials are included in Table 4.11. All of these modified potentials give better fits to the experimental data than do the unaltered HFD1 and HFD2 potentials. The differential cross sections predicted using the HFD1-A potential appear in Figure 4.9. We also considered modifying the HFD1 potential by increasing the parameter ρ , which appears in the damping functions, by 11% (HFD- ρ). As shown in Table 4.11, the resulting agreement with experiment is similar to that obtained from the other modified potentials.

It is stressed that scaling the dispersion coefficients and modifying the damping functions are simply convenient ways of altering the

Table 4.11

(a) Distances and energies in Ångstroms and Kelvin respectively.

potential	σ (Å)	r_m (Å)	ϵ (K)	$\Delta r_{\frac{1}{2}}$ (Å)	$S(990) \times 10^3$	$S(516) \times 10^3$
HFD1	2.82	3.16	29.4	0.95	7.5	9.2
HFD2	2.85	3.20	27.5	0.97	11.2	13.5
HFD2-A	2.79	3.13	35.2	0.96	2.9	4.4
HFD2-B	2.79	3.13	34.7	0.95	3.1	4.4
HFD1-A	2.77	3.11	35.7	0.93	2.6	4.7
HFD- ρ	2.76	3.09	33.5	0.93	3.4	5.8
BFW	2.76	3.09	33.5	0.94	2.9	4.7

(b) Distances and energies in atomic units (given for convenience).

potential	σ (a.u.)	r_m (a.u.)	ϵ (a.u. $\times 10^{-5}$)	$\Delta r_{\frac{1}{2}}$ (a.u.)
HFD1	5.33	5.97	9.31	1.80
HFD2	5.39	6.05	8.71	1.83
HFD2-A	5.27	5.91	11.15	1.81
HFD2-B	5.27	5.91	10.99	1.80
HFD1-A	5.23	5.88	11.31	1.76
HFD- ρ	5.22	5.84	10.61	1.76
BFW	5.22	5.84	10.61	1.78

HFD potentials. The results presented above suggest that there are inadequacies in the spherical parts of the HFD potentials of Rodwell et al. (1981). These could arise from inadequacies in either (1) the Hartree Fock calculations used to characterise the repulsive wall of the interaction, (2) the dispersion expansion used to model the large r behaviour, (3) the damping functions used to combine the Hartree Fock results with the dispersion expansion, or (4) the use of the HFD method to describe the He-HF interaction. The Hartree Fock calculations carried out by Rodwell et al. (1981) used a large basis set and the resulting SCF potential is in reasonable agreement with that obtained by Raimondi (1984). In the light of this agreement we expect the results of the Hartree Fock calculations of Rodwell et al. (1981) to be reliable. Rodwell et al. (1981) estimated dispersion coefficients for the He-HF interaction using available values for HF-HF and He-He in conjunction with various combination rules and judicious scaling. They note that the resulting dispersion expansion is unlikely to be an overestimate of the correct result. Although the He-He and HF-HF dispersion coefficients are expected to be reliable, it is not possible to assess the accuracy of the values determined for He-HF. The possibility that inadequacies may exist in either the functions used to damp the dispersion series or in the HFD model itself has been suggested by both Rodwell et al. (1981) and Raimondi (1984). Investigations of the Ar-HF interaction by Douketis et al. (1984) also support this conclusion (see Section 4.1). Given that the spherical parts of the HFD potentials of Rodwell et al. (1981) appear to be incorrect, it is fairly likely that the anisotropic components are also in error. Until experimental data which are sufficiently sensitive to the anisotropic part of the He-HF interaction become available, it will not be

possible to reliably assess the available ab initio potential surfaces. We note, however, that for the Ar-HF system, for which such data are available, both the spherical and anisotropic parts of the ab initio HFD potential were deepened in order to achieve agreement between the predicted and observed spectroscopic data (Douketis et al. (1984)). These results suggest that the non-spherical terms of the potentials of Rodwell et al. (1981) are also possibly too shallow although, in the absence of measurements which are sensitive to these anisotropies, it is not possible to make a definite statement.

In the present investigations we also obtained an analytic spherically symmetric potential function which gave a good fit to the measured intensities. The form chosen was that used by Barker and coworkers (see Section 4.3) to describe rare gas interactions. We fitted this model to the scattering data, using the dispersion coefficients determined by Rodwell et al. (1981) for the spherical part of the He-HF interaction. The parameters of the resulting potential (BFW) appear in Table 4.12, and the corresponding fits to the experimental data are shown in Figure 4.9.

Figure 4.10 shows the spherical parts of the potential surfaces used to calculate the cross sections shown in Figure 4.9. From this figure and from Table 4.11 it can be seen that there are significant differences between the potentials considered in this study. In the light of the results presented above we cannot recommend one model more than another. Note, however, that the modified HFD potentials and the BFW potential are all deeper than the HFD1 and HFD2 models and have smaller values of the positions of the zero in their spherical parts. The present studies suggest that the spherical part of the He-HF potential can be described

Table 4.12

Best fit BFW potential		
parameter	value	
r_m	3.09	Å
	5.84	a.u.
ϵ	33.5	K
	10.61×10^{-5}	a.u.
α	13.0	
δ	0.01	
A_0	0.6384	
A_1	-2.254	
A_2	-8.035	
A_3	-48.975	
C_6	1.2364	
C_8	0.41842	

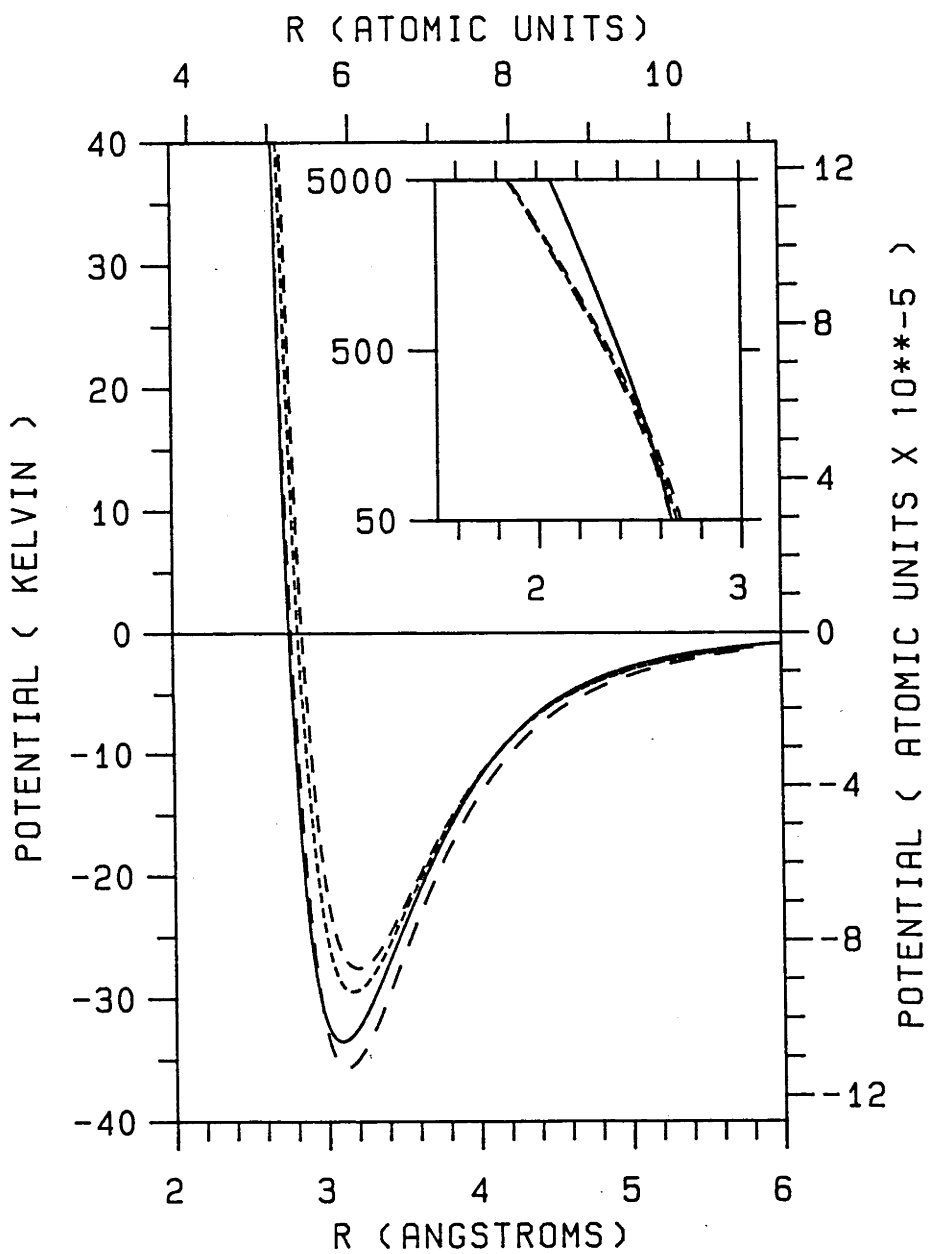


Figure 4.10

using the following parameters : zero crossing $\sigma = 0.278 \pm 0.003$ nm (5.25 ± 0.06 atomic units); position of minimum $r_m = 0.311 \pm 0.003$ nm (5.88 ± 0.06 atomic units); and well depth $\epsilon = 34.5 \pm 2.5$ K (10.9 ± 0.8 atomic units $\times 10^{-5}$). We note, however, that these three parameters give no explicit information about either the steepness of the repulsive wall or the attractiveness of the long range part of the interaction. From Figure 4.10 it is clear that the repulsive part of the BFW potential is steeper than those of the modified HFD potentials. It is not inconceivable that other spherical potentials whose σ , ϵ and r_m lie within the above ranges may also be consistent with the measured total scattering intensities.

The He-HF potentials proposed by Collins and Lane (1975,1976) and by Raimondi (1984) are both significantly shallower than, and have different anisotropies to, the HFD1 and HFD2 potentials of Rodwell et al. (1981). Both the repulsive wall and the minimum of the spherical part of the Raimondi (1984) potential occur at significantly larger values of the atom-molecule separation. Whilst the repulsive wall of the spherical part of the Collins and Lane (1975,1976) potential agrees rather well with those of the HFD potentials of Rodwell et al. (1981), the minimum occurs at slightly larger separations and the well depth is a factor of 3 smaller. The agreement between theory and experiment discussed in this section was improved by deepening the HFD potentials of Rodwell et al. (1981). Although no calculations were performed using the Collins and Lane (1975,1976) or Raimondi (1984) potentials, on the basis of the present investigations it seems unlikely that they would lead to differential cross sections which are in good agreement with Boughton's (1986) experimental results. In making this statement, we note that the measured scattering intensities are sensitive primarily to the spherical part of the

interaction which, for the Collins and Lane (1975,1976) and Raimondi (1984) potentials, differs significantly from those of the potentials considered in the present studies.

4.8 Conclusions

In this chapter we have reported the results of a thorough investigation of the scattering behaviour of the He-HF system at relatively low collision energies. Coupled states calculations were carried out using the HFD1 potentials of Rodwell et al. (1981). A comparison with the close coupled and IOS calculations of Battaglia et al. (1984b) showed that the l -average "correct phase" CS approximation, unlike the l -average IOS approximation used by Battaglia et al. (1984b), agrees reasonably well with the exact close coupled studies for both integral and differential state-to-state cross sections. As expected for such a weakly anisotropic system, elastic processes dominate the total integral and differential cross sections at collision energies of 41.4 and 81.9 meV. Laboratory frame total differential cross sections calculated using the CS, IOS and spherical potential approximations are all similar. Measured total differential scattering intensities are therefore only sensitive to the isotropic part of the He-HF interaction and can be analysed using the spherical potential approximation. A number of spherical potentials were used to analyse the total differential scattering intensities measured by Boughton (1986), and estimates of the well depth and of the positions of the zero crossing and the minimum of the He-HF potential were obtained. An analytic spherical potential which is able to reproduce the measurements was also given. Finally, a detailed study of the elastic and inelastic cross sections predicted by the HFD1 potential of Rodwell et al. (1981) was presented at collision energies similar to the mean energies determined by the experiments of Boughton (1986). The contributions from inelastic processes were found to be small.

Chapter FiveArgon - Hydrogen Fluoride Scattering Cross Sections

In this chapter we discuss the results of an experimental and computational study of the scattering of Ar from HF. The total differential cross section measured at a collision energy of 138 meV (1596 K) shows a broad, featureless, rainbow peak. Detailed scattering calculations were carried out for the anisotropic interaction potentials discussed by Douketis et al. (1984) using the spherical potential, infinite order sudden and coupled states approximations. These approximations are discussed in Chapter 2 of this thesis. The calculated cross sections were compared both with each other and with the measured scattering intensities.

After a brief introduction we: present the measured cross section; discuss the Ar-HF interaction potentials; compare the spherical potential, infinite order sudden and coupled states total cross sections; consider the agreement between the measured scattering intensities and the calculated ones; report the details of the coupled states investigations; discuss the behaviour of the partial integral cross sections (also referred to as the opacities); and make a number of concluding remarks.

5.1 Introduction

The use of molecular beam scattering techniques to investigate intermolecular potentials has been discussed in the introduction to Chapter 4. In that chapter we presented the results of a study of the scattering of He from HF. At collision energies of 44.5 and 85.3 meV (516 and 990 K), the He-HF total differential cross sections showed a number of broad diffraction oscillations, although the rainbow peaks were not resolved. In Section 5.2 we report measurements of the Ar-HF total differential cross section at a collision energy of 129 meV. In this case the diffraction oscillations were unresolved and the cross section was dominated by a broad primary rainbow peak.

A qualitative understanding of the dynamical processes responsible for both the diffraction oscillations and the rainbow features can be gained from a semiclassical description of the scattering process. Such a description involves propagating quantum mechanical oscillations (ie. de Broglie waves) along trajectories determined by classical mechanics (ie. Newton's equations of motion). Three classical trajectories which lead to scattering through the same angle are shown in Figure 5.1 for a hypothetical spherical interaction potential, the details of which are unimportant except that it must have an attractive region in order for trajectories 2 and 3 to exist. The de Broglie wavelength of the relative motion at any point along a trajectory depends upon the available kinetic energy at that point and the reduced mass of the system. All trajectories with the same impact parameter b , which is the distance of closest approach in the absence of an interaction potential, and the same collision energy, can be associated with a given orbital angular momentum quantum number l

typical classical trajectories

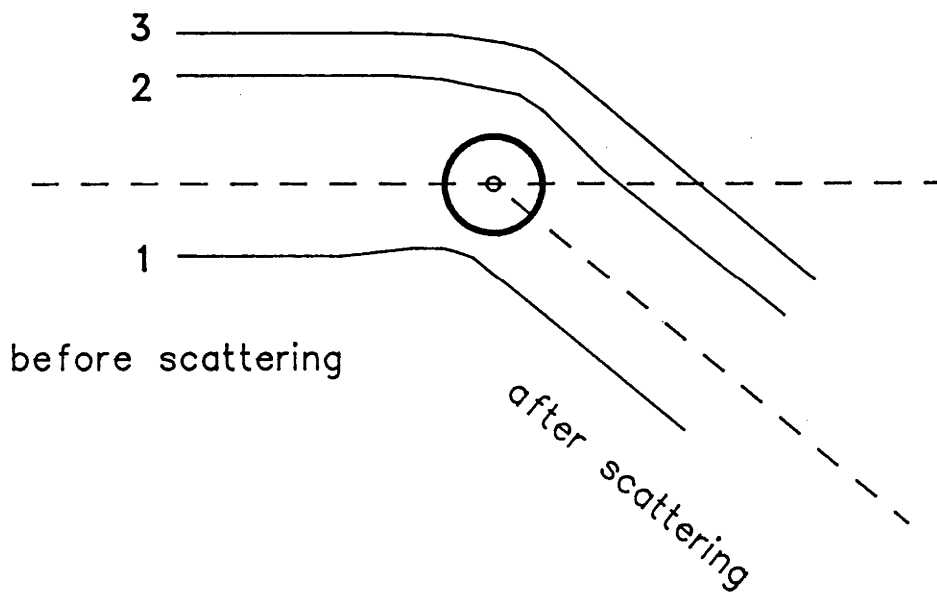


Figure 5.1

using the equation

$$b_1 \approx \frac{(1+\frac{1}{2})}{k_0} \approx \frac{(1+\frac{1}{2})\lambda_0}{2\pi} \quad (5.1)$$

where $k_0=2\pi/\lambda_0$ is the wavevector corresponding to the asymptotic de Broglie wavelength λ_0 . Consider the trajectories shown in Figure 5.1. Relative phases of the scattered de Broglie waves will depend upon the deflection angle, and the corresponding scattered amplitudes may interfere either constructively or destructively. The closer the interfering trajectories, the larger the change in the deflection angle required to cause a change of 2π in the phase difference between a given pair of scattered waves, and hence the greater the angular separation between the corresponding interference peaks.

Diffraction oscillations result from the interference of trajectories which pass the scattering centre on different sides (ie. 1 and 2 or 3). As noted in Chapter 4, the separation between adjacent diffraction oscillations is proportional to λ_0/r_m , where λ_0 is the asymptotic de Broglie wavelength and r_m is the position of the minimum of the interaction potential. Rainbow oscillations, on the other hand, are caused by the interference between trajectories which pass the scattering centre on the same side (ie. 2 and 3). The similarity between such trajectories results in the rather large separations typically observed between adjacent rainbow peaks. At a certain deflection angle, which depends upon the details of the interaction potential, trajectories 2 and 3 will coincide, and the corresponding maximum is referred to as the primary rainbow. When the primary rainbow occurs at a sufficiently small scattering angle, its approximate location (ie. centre of mass scattering

angle) is $2\epsilon/E$ radians, where ϵ is the well depth of the interaction potential and E is the collision energy (see Fluendy and Lawley (1973)). The other (supernumary) rainbow peaks are found at angles smaller than that of the primary rainbow. We note that the primary rainbow peak determined by an exact solution of the quantum mechanical scattering problem occurs at a slightly smaller deflection angle than the angle for which the two classical trajectories coincide.

For scattering angles larger than the primary rainbow angle the differential cross section is determined primarily by the repulsive part of the potential, and to a lesser extent by the attractive well. As the scattering angle is reduced below that of the primary rainbow, the differential cross section becomes increasingly sensitive to the details of the interaction potential in the region of the minimum and beyond (ie. to larger separations r). Experimentally measured total differential cross sections for which rainbow features are resolved are therefore useful in assessing, and in some cases determining, the behaviour of the corresponding interaction potentials in the vicinity of the attractive well. Both spherical and non-spherical interactions exhibit rainbow and diffraction oscillations. An investigation of the damping of rainbow and diffraction structure resulting from anisotropic potentials was carried out by Pack (1978). It was concluded that the anisotropy of the well depth determines the degree of damping of the rainbow oscillations and that the damping of the diffraction oscillations is related to the anisotropy of the the position of the well.

The rainbow phenomena discussed in this chapter are observed as variations in the differentially scattered intensities as a function of the scattering angle. Most books about molecular scattering consider such

rainbow structures. See, for example, Bernstein (1979), Child (1974) and Fluendy and Lawley (1973). We note here that other types of rainbow structures exist. These are the so-called 'rotational rainbows' and 'vibrational rainbows'. They correspond to oscillations in a given scattering cross section as a function of the final rotational or vibrational quantum number. For discussions of rotational rainbows see Gianturco and Palma (1985), Hoffbauer et al. (1983a) and Schinke et al. (1982). The theory of the different types of rainbow structures is discussed by Schinke and Bowman (1983).

One of the earliest observations of rainbow oscillations was reported by Morse et al. (1962) for Cs and K colliding with Hg. As noted in the Section 4.1, accurate atom-atom interaction potentials can be obtained by inverting suitable differential cross section measurements. Ideally, such experimentally measured cross sections would include well resolved rainbow and/or diffraction oscillations. In the remainder of this introduction we discuss the results of a number of recent atom-molecule and molecule-molecule systems for which rainbow features have been observed experimentally, and comment upon the information obtained about the interaction potentials.

$\text{CH}_4\text{-CH}_4$ total differential scattering cross sections were independently measured and analysed by both Boughton et al. (1985) and Reid et al. (1985). For a collision energy of about 1200 K (103 meV), obtained using supersonic beams with most probable speeds of roughly 1100 m/s meeting at 90° , the primary rainbow was clearly resolved. Indeed, the shape of the cross section is qualitatively similar to the Ar-HF cross section reported in this chapter. Both groups obtained effective spherical potentials, with almost identical values of the well depth and the position

of the minimum, which were able to reproduce the scattering data. In a similar study, O'Loughlin et al. (1985) reported total differential cross sections and effective spherical potentials for Ne-CH₄ and Ar-CH₄. In each case, cross sections were measured at three collision energies. Although a single spherical potential was able to reproduce the three Ne-CH₄ differential cross sections, such a fit could not be found for Ar-CH₄. The observed primary rainbow oscillation was more highly damped than that predicted using the best fit spherical potential. This was attributed to anisotropies in the Ar-CH₄ interaction, which were not included in the analysis.

By fitting simultaneously to measured total differential cross sections, viscosities and virial coefficients, Pack et al. (1982b,1984) were able to obtain anisotropic interaction potentials for SF₆ interacting with He, Ne, Ar and Kr. The degree of damping of the rainbow oscillations was used to estimate the anisotropy of the well depth for the Ne-SF₆ potential. For He-SF₆, the smaller reduced mass meant that rainbow peaks were not observed, although diffraction oscillations were seen. The damping of the latter enabled a reliable estimate of the anisotropy of the position of the minimum to be made. Both spherical potential and IOS techniques were used in these investigations.

Of more relevance to the results presented in this chapter are the studies of Xe-HF scattering by Becker et al. (1979) and of Ar-HCl scattering by Buck and McGuire (1976) and Buck and Schleusener (1981). Becker et al. (1979) measured the Xe-HF total differential cross section at two collision energies, obtaining both primary and secondary rainbow oscillations. By fitting to these data an effective spherical potential was determined. This spherical potential was combined with various

non-spherical terms to create four potentials with rather different anisotropies. Coupled states calculations were then used to study the centre of mass frame state-to-state differential cross sections resulting from the four potentials. The most important conclusion drawn from these investigations was that the total differential cross section for Xe colliding with an HF molecule in a given initial rotational state depends significantly upon both the chosen initial state and the details of the interaction potential. When analysing total differential cross sections for systems which exhibit such behaviour, it is therefore essential to have reliable estimates of the rotational state distributions of the collision partners.

The experimental and computational studies of the Ar-HCl system have been discussed in the introduction to Chapter 4. Buck and McGuire (1976) used the coupled states approximation to calculate differential scattering cross sections for a number of model interaction potentials with different anisotropies. Good agreement with the experimental results of Farrar and Lee (1974) could not be obtained. It was noted that (1) the total differential cross section for centre-of-mass angles greater than about 40° (at a collision energy of 77.4 meV) results mostly from inelastic processes, and (2) the total differential cross section for HCl molecules initially in $j=0$ differs considerably from that for $j=1$ molecules. Buck and Schleusener (1981) remeasured the total differential cross section for Ar-HCl and used coupled states calculations to assess two interaction potentials which had been determined by fitting simultaneously to available experimental data, such as rotational constants, line broadening cross sections, viscosities and virial coefficients (see Holmgren *et al.* (1978) and Hutson and Howard (1981)). Neither of the total differential cross

sections predicted by these potentials were in agreement with the measured one. For the potential developed by Hutson and Howard (1981) the total differential cross section from an initial state of $j=0$ was significantly different from that for an initial state of $j=1$, as had been found previously for both Ar-HCl and Xe-HF.

There have been a number of experimental investigations of the properties of the Ar-HF van der Waals molecule. Harris et al. (1974) and Dixon et al. (1981) used molecular beam electric resonance techniques to measure radio frequency and microwave spectra for Ar-HF and Ar-DF. Equilibrium rotational constants, dipole and quadrupole moments and hyperfine splitting constants were obtained. In other studies Keenan et al. (1981) and Cousins et al. (1984) used pulsed Fourier transform microwave spectroscopy to determine equilibrium structures for Ar-DF and Ar-HF. Investigations of van der Waals molecules give information about the interaction potential for geometries near the equilibrium geometry. Hutson and Howard (1982b) used these data to develop an anisotropic intermolecular potential for Ar-HF, which is referred to as the M5 potential. These authors noted that, although the shape of the potential is well determined near its absolute minimum, its validity elsewhere and the reliability of the absolute well depth are uncertain.

An anisotropic potential function for Ar-HF has also been reported by Douketis et al. (1984). They used the HFD formalism, discussed in Chapter 4, to combine the results of accurate Hartree Fock calculations with estimates of the dispersion coefficients. The resulting potential, referred to as the ArHF-HFD1 potential in this thesis, was unable to reproduce the known spectroscopic constants. By increasing all of the dispersion coefficients by 27%, however, a potential capable of reproducing

the spectroscopic constants was obtained. This potential, which is called the ArHF-HFD2 potential in the present thesis, is significantly different to the previously reported M5 potential, which also correctly predicts the spectroscopic data. In this chapter we compare the cross sections predicted using the ArHF-HFD1, ArHF-HFD2 and M5 potentials, both with each other and with experimentally measured values. The results of these calculations are also compared with those reported for He-HF in Chapter 4 and with those for Ar-HCl and Xe-HF discussed above.

We note finally that Barnes et al. (1980,1982) measured relative state-to-state integral cross sections for vibrationally excited HF molecules colliding with Ar. Laser excitation was used to state-select an HF containing molecular beam before collisions with Ar, and infrared fluorescence detection was used to probe the resulting distribution of HF rotational states within the initially excited vibrational manifold. The cross sections obtained by Barnes et al. (1982) are compared with the coupled states cross sections reported in this chapter.

5.2 Experimental Results

Total differential scattering cross sections were measured for HF-Ar using the techniques described in Chapter 2 of this thesis and in more detail below. Bolometer A (see Chapter 2) was used to record the scattered intensity resulting from the collision of a primary beam of pure HF with a secondary beam of pure Ar. The results of these experiments are given in Table 5.1. Characteristics of the expansions used to obtain these data appear in Table 5.2.

In order to assess the statistical significance of the scattered intensities reported in Table 5.1, it is necessary to consider in detail the method used to obtain these data. We note firstly that particle fluxes reaching the bolometer were detected by (1) chopping the secondary beam using a 50% duty cycle rotating chopper located between the nozzle and skimmer, (2) using a lock-in amplifier tuned to this chopping frequency to demodulate the bolometer output voltage, and (3) sampling and averaging the output of the lock-in amplifier with a microcomputer. The time constant and roll-off characteristics of the output filter of the lock-in amplifier were adjusted so that the fluctuations in the demodulated bolometer signal were not unreasonably large. Integration times used in averaging the lock-in amplifier output signal were chosen by considering the timescale and amplitude of these fluctuations. Typical integration times varied from 15 seconds at small scattering angles to about 10 minutes at the larger angles. To obtain the scattered intensity at a given angle requires four measurements of the particle flux reaching the bolometer. By recording the signal with the primary beam blocked (measurement 1), and subtracting this from the signal recorded with the beam unblocked (measurement 2), one

Table 5.1

Laboratory angle (degrees)	Intensity (arbitray units)	Laboratory angle (degrees)	Intensity (arbitrary units)
2.5	3500	17.5	34.4
3.0	2540	18.0	31.7
3.5	1955	18.5	30.9
4.0	1540	19.0	29.5
5.0	1000 (1%)	19.5	28.5
5.5	785	20.0	28.0 (10%)
6.0	655	20.5	29.2
6.5	525	21.0	27.5
7.0	433	21.5	26.6
7.5	350	22.0	26.6
8.0	288	22.5	24.4
8.5	236	23.0	25.9
9.0	193	23.5	24.0
9.5	163	24.0	23.6
10.0	135 (4%)	24.5	22.7
10.5	115	25.0	23.4
11.0	96.8	26.0	21.8
11.5	87.3	27.0	21.8
12.0	77.9	28.0	21.5
12.5	68.0	29.0	20.5
13.0	58.8	30.0	20.9 (15%)
13.5	54.4	31.0	19.3
14.0	48.1	32.0	18.8
14.5	45.2	33.0	18.9
15.0	42.2 (7%)	34.0	19.7
15.5	40.4	35.0	19.5
16.0	39.3	36.0	18.0
16.5	36.5	37.0 17.4	39.0 19.1
17.0	35.1	38.0 18.6	40.0 17.9

Table 5.2

Property	Value	
Mean collision		
energy (K)	1596 ± 16	
(meV)	138 ± 1.4	
Gas used	HF	Ar
Source pressure (kPa)	100	200
Source temperature (K)	~500	310
Stream velocity v_S (m/s)	1273	571
Most probable		
velocity v_{mp} (m/s)	1289	574
Velocity width		
parameter v_w (m/s)	177	32
Velocity spread		
FWHM (%)	22	9
Beam divergence		
FWHM (degrees)	2	6
Nozzle diameter (μm)	80	80
First skimmer		
diameter (μm)	1000	500
Second skimmer		
diameter (μm)	800	-

obtains a value proportional to the desired scattering intensity. To account for long term drifts in the beam intensities and/or the bolometer responsivity, this value must be divided by that determined at a suitable reference angle (measurements 3 and 4). The fluctuations in the scattered intensities obtained from this procedure depend inversely upon the square roots of the times used to integrate the output signal of the lock-in amplifier. For each integration the standard deviation of the points sampled was determined. Although this figure gives a measure of the spread of values sampled, its interpretation in those cases for which the timescale of the fluctuations in the amplifier output is longer than the separation between sampling points is somewhat obscured by the fact that the points in such samples are not independent estimates of the quantity being measured. Integration times were always chosen to be at least five times longer than the estimated correlation lengths in the signals being integrated. In order to check the reproducibility of the scattered intensities determined in this way, a number of measurements were made at most scattering angles. The data presented in Table 5.1 are the averages of such measurements. Estimates of the uncertainties are given in the table at a number of scattering angles. These rather conservative limits give an indication of the scatter of the intensities obtained from the separate determinations made at each scattering angle.

The quadrupole mass spectrometer was used to assess the degree of clustering present in the beams. In each case the signal corresponding to the dimer mass was less than a few percent of that observed at the monomer mass, suggesting that contributions from clusters were insignificant. The rotational distribution of the HF primary beam was assumed to be the same as that for the HF secondary beam reported in Chapter 4, which was operated

under similar conditions.

Finally we consider the possible adsorption energy contribution to the measured scattering intensities resulting from the accommodation of the detected HF molecules onto the bolometer surface. As noted in Chapter 4, this contribution is negligible when detecting helium atoms. HF molecules will clearly give up more energy when adsorbing onto the cold bolometer surface. The kinetic energies given up to the bolometer are ≥ 2000 K per molecule (see Table 2.4). Although the strength of the interaction between the HF molecules and the bolometer surface is not known, we expect the adsorption energy to be smaller than about 1000 K (on average) per molecule. Boughton et al. (1985) compared calculated differential cross sections (for CH₄-CH₄ scattering) obtained by assuming (1) that the kinetic energy \gg the adsorption energy, and (2) that the converse is true. Their results show that including an adsorption contribution in the calculation of a differential scattering intensity tends to lower the values obtained at large angles relative to those at small angles. This would tend to worsen the fits between the calculated Ar-HF scattering intensities and the experimental data (reported in Section 5.5). All of the calculated laboratory frame scattering intensities reported in this chapter were obtained using Eq. (3.59), which was derived by assuming that only the kinetic energies of the detected atoms or molecules contribute to the bolometer signal.

5.3 The Ar-HF Interaction Potential

Hutson and Howard (1982b) determined the analytic M5 potential by fitting to experimentally determined rotational constants and structural parameters for the Ar-HF van der Waals molecule. The equations defining this potential are given in Table 5.3. Angular cuts through the potential surface are shown in Figure 5.2. A potential angle of zero corresponds to the collinear Ar-H-F configuration. As expected, this potential is substantially deeper than the HFD1 potential developed by Rodwell et al. (1981) for the He-HF interaction which is shown in Figure 4.2. Notice that the form of the anisotropy is also qualitatively rather different. Whereas the He-HF potential has minima of similar depths at both zero and 180 degrees, the M5 potential has only a shallow relative minimum at 180 degrees compared to that at 0°.

The other potentials considered in these investigations are the HFD potentials reported by Douketis et al. (1984). Results of accurate solutions to the Hartree Fock equations were combined with estimates of the dispersion coefficients using the HFD formalism to obtain the ArHF-HFD1 potential. This potential was inconsistent with the known rotational constants. By increasing all of the dispersion terms by 27% good agreement with the available experimental data was obtained. This deepened potential is referred to as the ArHF-HFD2 potential in this thesis. The details of the analytic forms for these HFD potentials are given in the paper by Douketis et al. (1984) and are not reproduced here. For comparison with the M5 potential, angular cuts through these HFD surfaces are shown in Figures 5.3 and 5.4. The ArHF-HFD2 potential is the deepest of the three potentials and shows a pronounced double minimum structure like that seen

Table 5.3

The M5 Potential

$$V(r, \cos\gamma) = \varepsilon(\gamma) \left[\frac{6}{n-6} x^{-n} - \frac{n}{n-6} x^{-6} \right]$$

$$x = r/r_m(\gamma)$$

$$n = m(\gamma) + \eta(x-1)$$

$$m(\gamma) = m(0) + \Delta m f(\gamma, \zeta)$$

$$r_m(\gamma) = r_m(0) + \Delta r_1 f(\gamma, \kappa) + \Delta r_2 g(\gamma)$$

$$\varepsilon(\gamma) = \varepsilon(0) + \Delta \varepsilon_1 f(\gamma, \lambda) + \Delta \varepsilon_2 g(\gamma)$$

$$f(\gamma, \lambda) = 1 - \left[\frac{1}{2}(1 + \cos\gamma) \right]^\lambda$$

$$g(\gamma) = 0 \text{ for } \gamma \leq 90^\circ, \text{ and } g(\gamma) = \cos^2\gamma \text{ for } \gamma > 90^\circ$$

Parameter	Value
$\varepsilon(0)$	308.17 K
$\Delta \varepsilon_1$	-216.08 K
$\Delta \varepsilon_2$	23.02 K
$r_m(0)$	3.3904 Å
Δr_1	0.0653 Å
Δr_2	-0.1100 Å
$m(0)$	23.89
Δm	-9.60
λ	5.65
κ	12.70
ζ	16.40
η	9.0

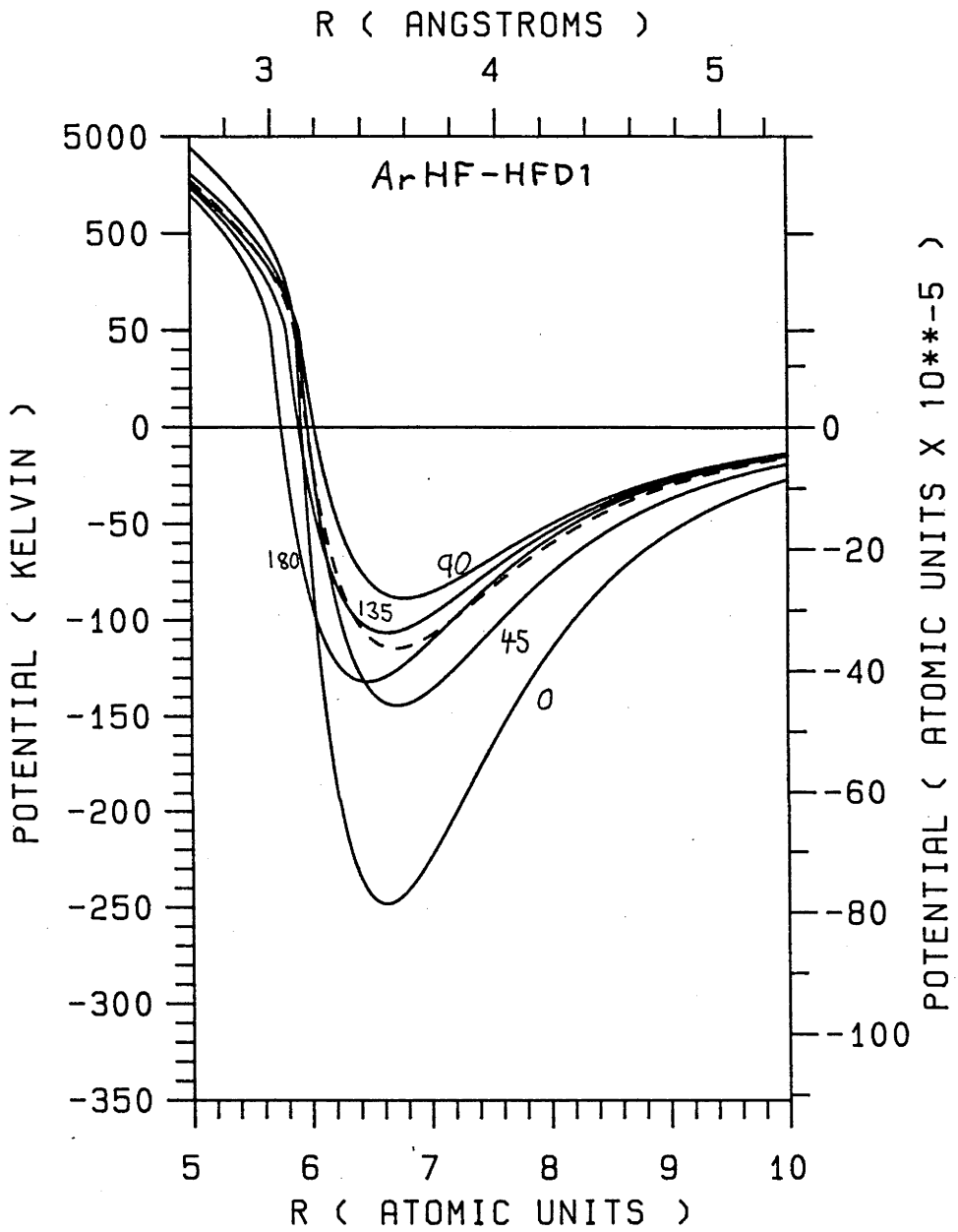


Figure 5.2

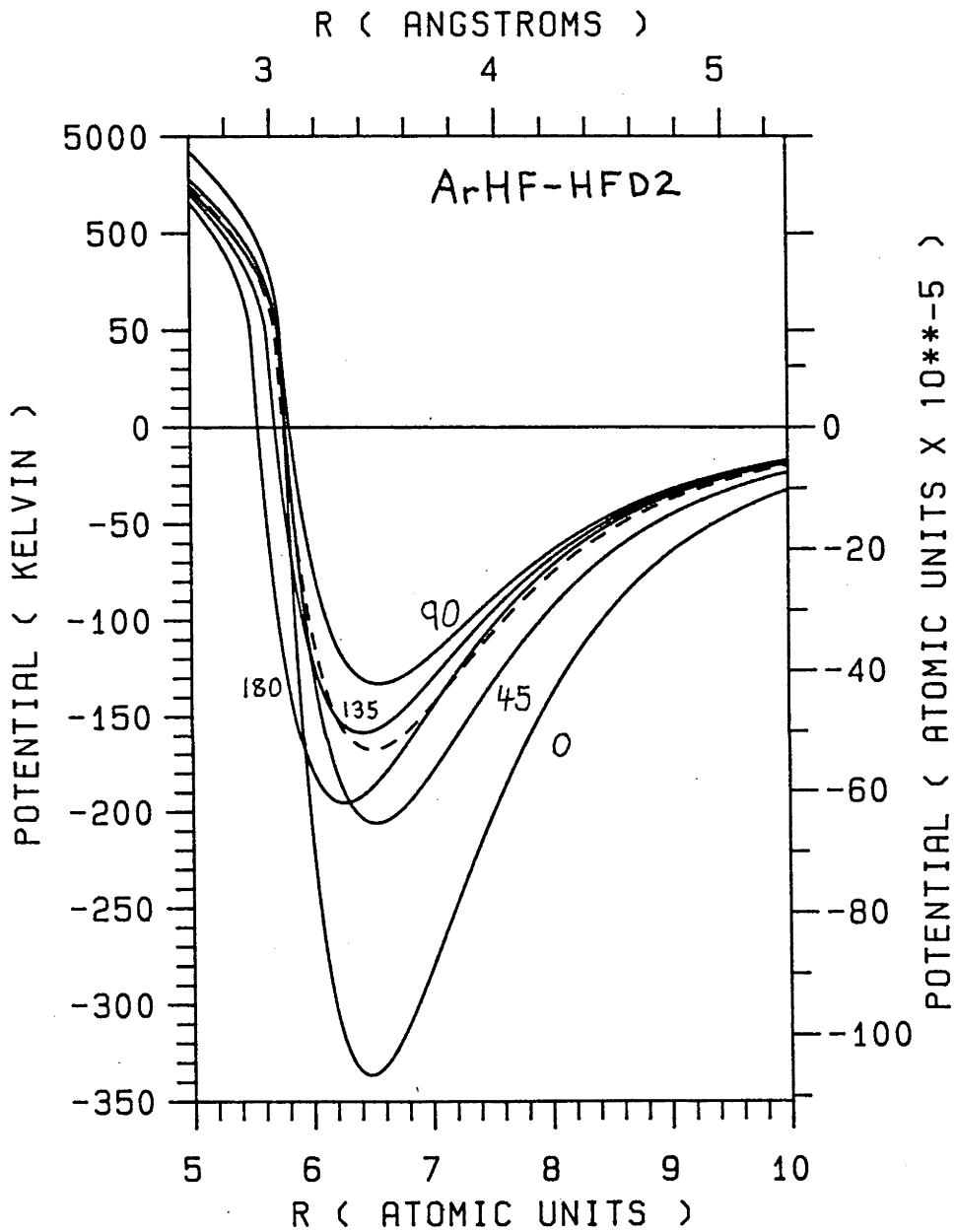


Figure 5.3

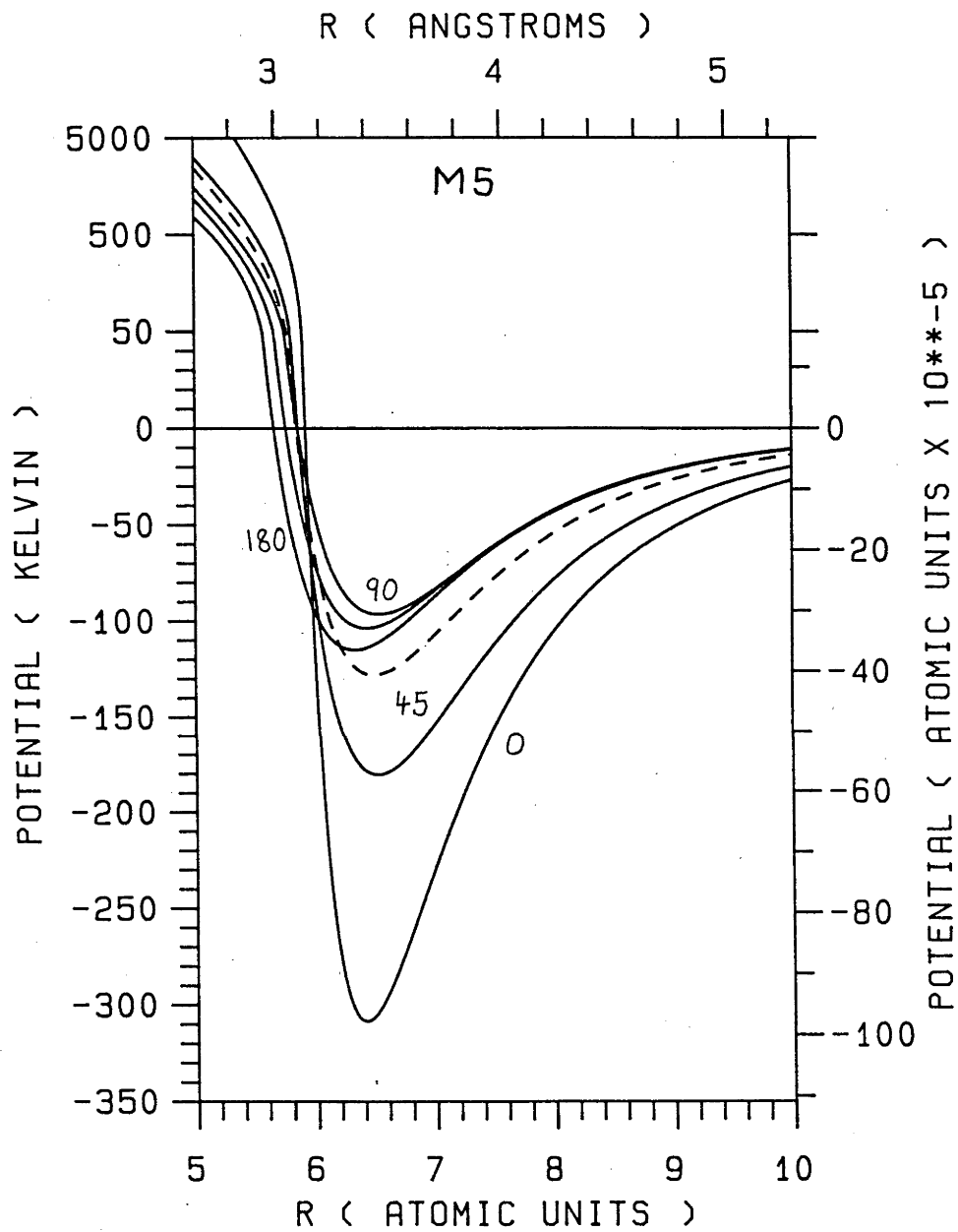


Figure 5.4

for the He-HF HFD1 potential shown in Figure 4.2. As expected, the ArHF-HFD1 potential is similar to the ArHF-HFD2 surface, only shallower.

In order to facilitate computation of the potential matrix elements needed for the coupled states calculations, the three Ar-HF potentials were expanded in the form (see Eq. (4.2))

$$V(r, \cos\gamma) = \sum_{\lambda=0}^9 V_{\lambda}(r) P_{\lambda}(\cos\gamma) \quad (5.2)$$

The desired expansion coefficients $V_{\lambda}(r)$ are given by

$$V_{\lambda}(r) = \left(\frac{2\lambda+1}{2}\right) \int_0^{\pi} V(r, \cos\gamma) P_{\lambda}(\cos\gamma) \sin\gamma \, d\gamma \quad (5.2)$$

A converged Gauss-Legendre quadrature was used to obtain the $V_{\lambda}(r)$ at intervals of 0.02 atomic units (0.01 Å) for each of the potentials. For values of r beyond the tabulated values, the potential expansion coefficients were expanded as series of inverse powers of r :

$$V_{\lambda}(r) = - \sum_n \frac{1}{r^n} C_n^{\lambda} \quad (5.4)$$

where the values of n used for a given λ are as follows:

$\lambda = 0$	$n =$	6	8	10	12	14
1		7	9	11	13	15
2		6	8	10	12	14
3		7	9	11	13	15
4		8	10	12	14	
5		9	11	13	15	
6		10	12	14		
7		11	13	15		
8		12	14			
9		13	15			

For the two HFD potentials, the tables of Legendre expansion coefficients extended to 31 atomic units (16.4 Å) and the series expansions were used to evaluate the potentials for larger r . The expansion coefficients C_n^λ evaluated near 30 atomic units (15.9 Å) differed negligibly from those evaluated near 60 atomic units (31.8 Å). For the M5 potential, unique series representations of the $V_\lambda(r)$ could not be found. In this case, the table of expansion coefficients was extended to 120 atomic units (63.5 Å), well beyond the largest separation for which potential evaluations were necessary.

The Ar-HF potentials considered in this chapter do not depend upon the HF stretching coordinate R , with the result that the coupled states calculations reported in this chapter are rigid-rotor calculations. Energies of the HF basis states were calculated using the potential reported by Huffaker (1977), which was also used in the He-HF scattering calculations reported in Chapter 4. These energies, which are for an HF molecule in its ground vibrational state differ only slightly from the rigid-rotor energies of an HF molecule in its equilibrium geometry.

5.4 A Comparison Between Spherical Potential, Infinite Order Sudden and Coupled States Calculations

For the He-HF system, the coupled states, infinite order sudden and spherical potential approximations all predict essentially the same total differential scattering cross sections (see Chapter 4). That this should be the case is perhaps somewhat surprising given the rather large energy separations between the HF rovibrational states compared to the collision energies considered. Both the collision energy and the reduced mass are larger for the Ar-HF collisions reported in this chapter than for the He-HF interactions discussed in Chapter 4. This means that the asymptotic de Broglie wavelength for the elastic channels, which is given by $\lambda_e = h^2 / (2\mu E_{\text{collision}})$, is significantly smaller for these Ar-HF collisions than for the He-HF collisions discussed in Chapter 4. The Ar-HF KoQnwehQKro potential is also significantly deeper than that for He-HF. In the light of these considerations, it is not surprising that the scattering behaviour for the Ar-HF and He-HF systems are qualitatively rather different.

Spherical potential, infinite order sudden and coupled states calculations were carried out for each of the three Ar-HF potentials. Semiclassical phase shifts were used to compute the cross sections within the spherical potential and infinite order sudden approximations, with orbital angular momenta from $l=0$ to 300 being summed. As was found for He-HF scattering, the results of an exact solution of the spherical potential equations were almost identical to the semiclassical results. A sixteen point Gauss-Legendre quadrature was used to evaluate the IOS integrals (see Section 3.4). All of the calculated differential scattering

intensities presented in this chapter were obtained using Eq. (3.59), and are given as a function of the laboratory scattering angle in units of square Ångstroms per steradian. Unless otherwise stated, the differential scattering intensities were been multiplied by $\sin(\theta) \cdot \theta^{4/3}$ in order to enhance the primary rainbow feature. All of the state-to-state differential cross sections were multiplied by the relative populations, in the HF beam, of their initial rotational states, as was done for the He-HF cross sections discussed in Chapter 4.

For the coupled states calculations reported in this chapter the l-average and "correct phase" choices were used (see Chapters 3 and 4). These calculations were done with the basis set $\{ |v,j\rangle : v=0, j=0, \dots, 7 \}$. As noted earlier, the Ar-HF interaction potentials considered in this thesis do not depend upon the HF stretching coordinate. The HF vibrational quantum number v is included in the basis set only because the energies used for the basis states are those for an HF molecule in its ground vibrational state. Asymptotic channel wavevectors and wavelengths corresponding to scattering from $j_{\text{initial}}=0$ through 3 are given in Table 5.4 for a collision energy of 1493 K (128.6 meV). We expect the resulting cross sections to be converged to within about 2% as a function of the size of the basis set used. The log-derivative method was used to integrate the coupled states equations from $r = 4$ atomic units to 50 atomic units (2.12 Å to 26.46 Å) with a step size of 0.0153 atomic units (0.008 Å), giving S matrix elements accurate to better than 1% for the basis set used in the calculations. All cross sections $j \rightarrow j'$ for $j=0, \dots, 3$ and $j'=0, \dots, 4$ were evaluated, averaging over the initial values of m , the rotor angular momentum projection quantum number, and summing over final values. Total angular momenta from $J=0$ to 220 were included in the calculation of the

Table 5.4

Basis sets for Ar-HF CS calculations at a collision energy of 1493 K

		j-initial = 0			j-initial = 1		
j	E_j (K)	κ_j^2 (\AA^{-2})	κ_j (\AA^{-1})	λ_j (\AA)	κ_j^2 (\AA^{-2})	κ_j (\AA^{-1})	λ_j (\AA)
0	0	820.3	28.65	0.219	852.8	29.20	0.215
1	59.15	787.8	28.06	0.224	820.3	28.65	0.219
2	177.4	722.8	26.89	0.234	755.3	27.48	0.299
3	354.5	625.7	25.00	0.251	658.1	25.64	0.245
4	590.4	496.0	22.26	0.282	528.5	22.98	0.274
5	884.7	334.3	18.27	0.334	366.7	19.14	0.328
6	1237.0	140.3	11.85	0.530	172.8	13.15	0.478
7	1647.0	-84.99	9.203	-	-52.14	7.238	-

		j-initial = 2			j-initial = 3		
j	E_j (K)	κ_j^2 (\AA^{-2})	κ_j (\AA^{-1})	λ_j (\AA)	κ_j^2 (\AA^{-2})	κ_j (\AA^{-1})	λ_j (\AA)
0	0	917.8	30.29	0.207	1015.	31.86	0.197
1	59.15	885.3	29.76	0.212	982.8	31.35	0.201
2	177.4	820.3	28.65	0.219	917.8	30.29	0.207
3	354.5	723.1	26.89	0.234	820.3	28.65	0.219
4	590.4	593.5	24.36	0.258	690.6	26.29	0.239
5	884.7	431.7	20.77	0.303	528.9	23.00	0.273
6	1237.0	237.8	15.42	0.407	335.3	18.31	0.343
7	1647.0	12.50	3.553	1.769	110.0	10.49	0.599

elastic cross sections. Although this was sufficient to converge the integral cross sections to within 0.5% as a function of the number of total angular momenta included, the neglect of higher J 's resulted in small oscillations (as a function of the scattering angle) in the large angle elastic differential cross sections. By including values of J up to 300, these oscillations disappear. After averaging the differential cross sections using a two degree angular window (discussed later in this section) the elastic cross sections calculated using $J_{\max}=220$ differ negligibly from the converged results. For inelastic processes, the contributions to the cross sections diminish far more rapidly with increasing J than for the elastic processes. The maximum J 's used in calculating the individual inelastic cross sections were chosen to converge the integral cross sections to within 0.1% as a function of the number of total angular momenta summed.

Most of the Ar-HF scattering calculations reported in this chapter were carried out at a collision energy of 1493 K (128.6 meV). Right angle collisions were assumed, with the HF molecules travelling at 1240 m/s and the Ar atoms at 569.4 m/s. These speeds are similar to the most probable speeds given in Table 5.2. The Newton diagram for HF-Ar collisions under these conditions appears in Figure 5.5.

Laboratory frame total differential cross sections predicted by the spherical potential, infinite order sudden and coupled states approximations are shown in Figures 5.6, 5.7 and 5.8 for the ArHF-HFD1, ArHF-HFD2 and M5 potentials respectively. Corresponding centre of mass frame integral cross sections are given in Table 5.5. No averaging was done over the experimental parameters, although the differential cross sections were smoothed out using a two degree angular window to damp the

Newton diagram for HF-Ar

collision energy = 1493 K

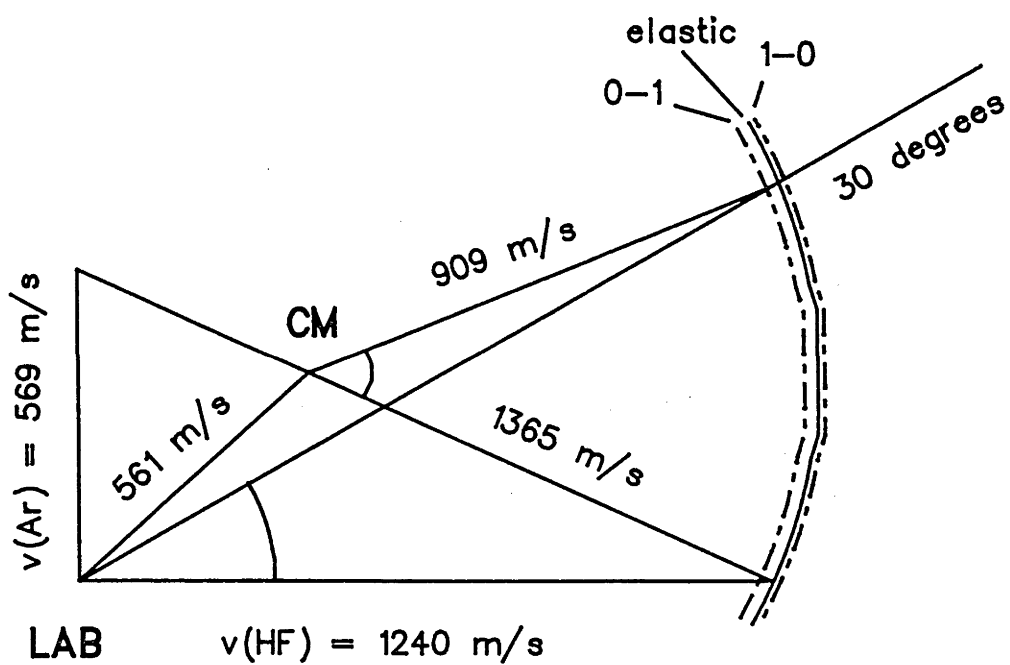


Figure 5.5

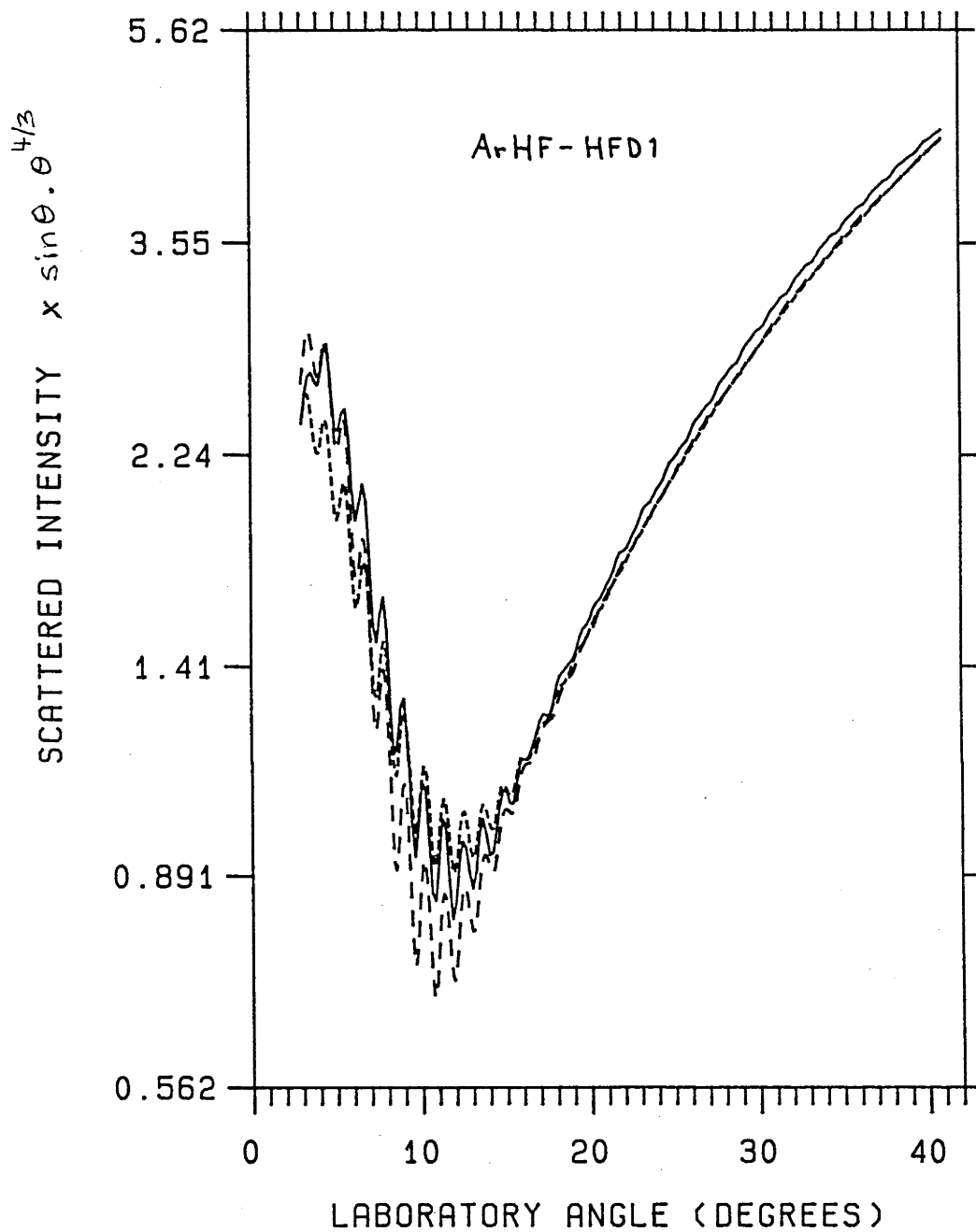


Figure 5.6

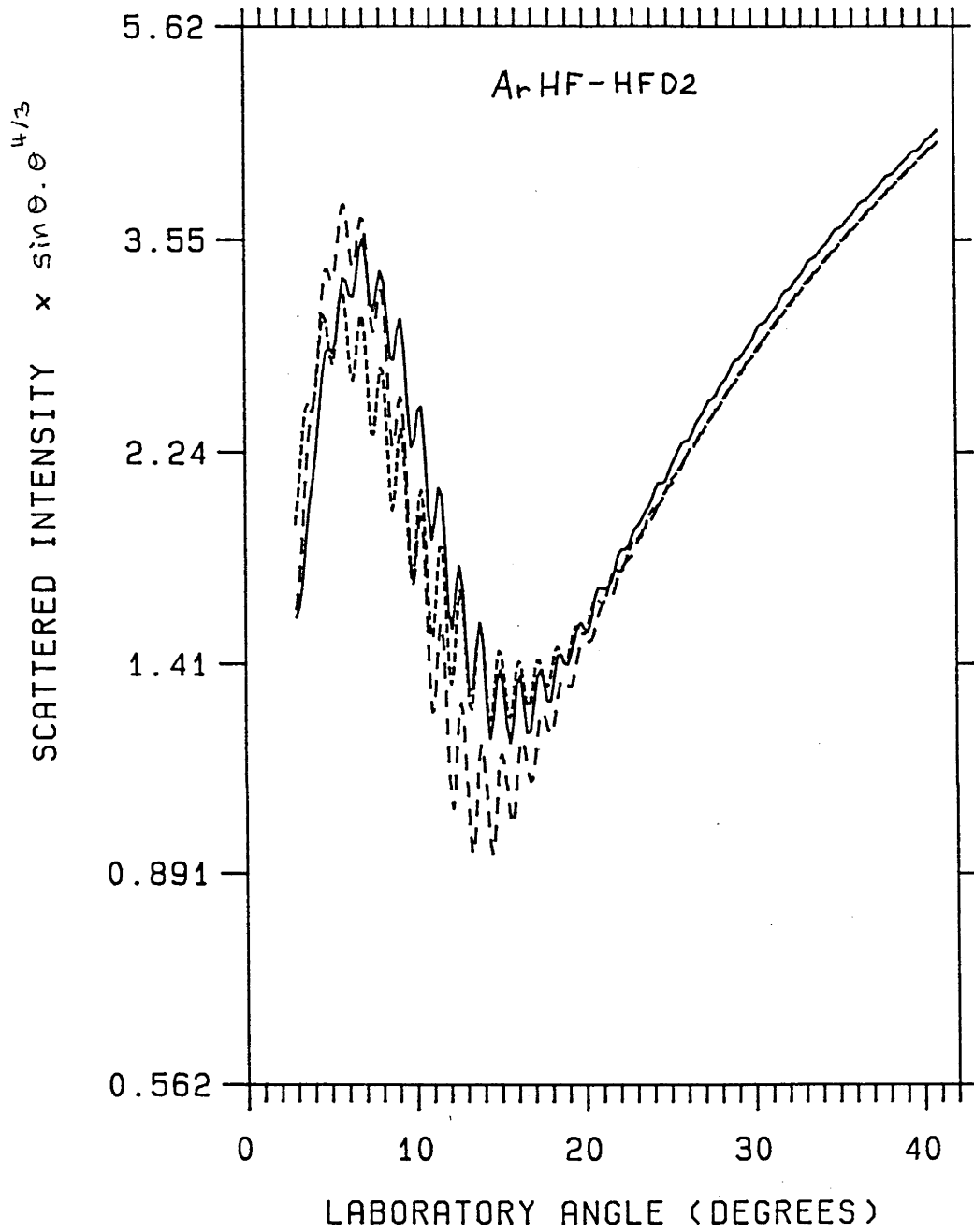


Figure 5.7

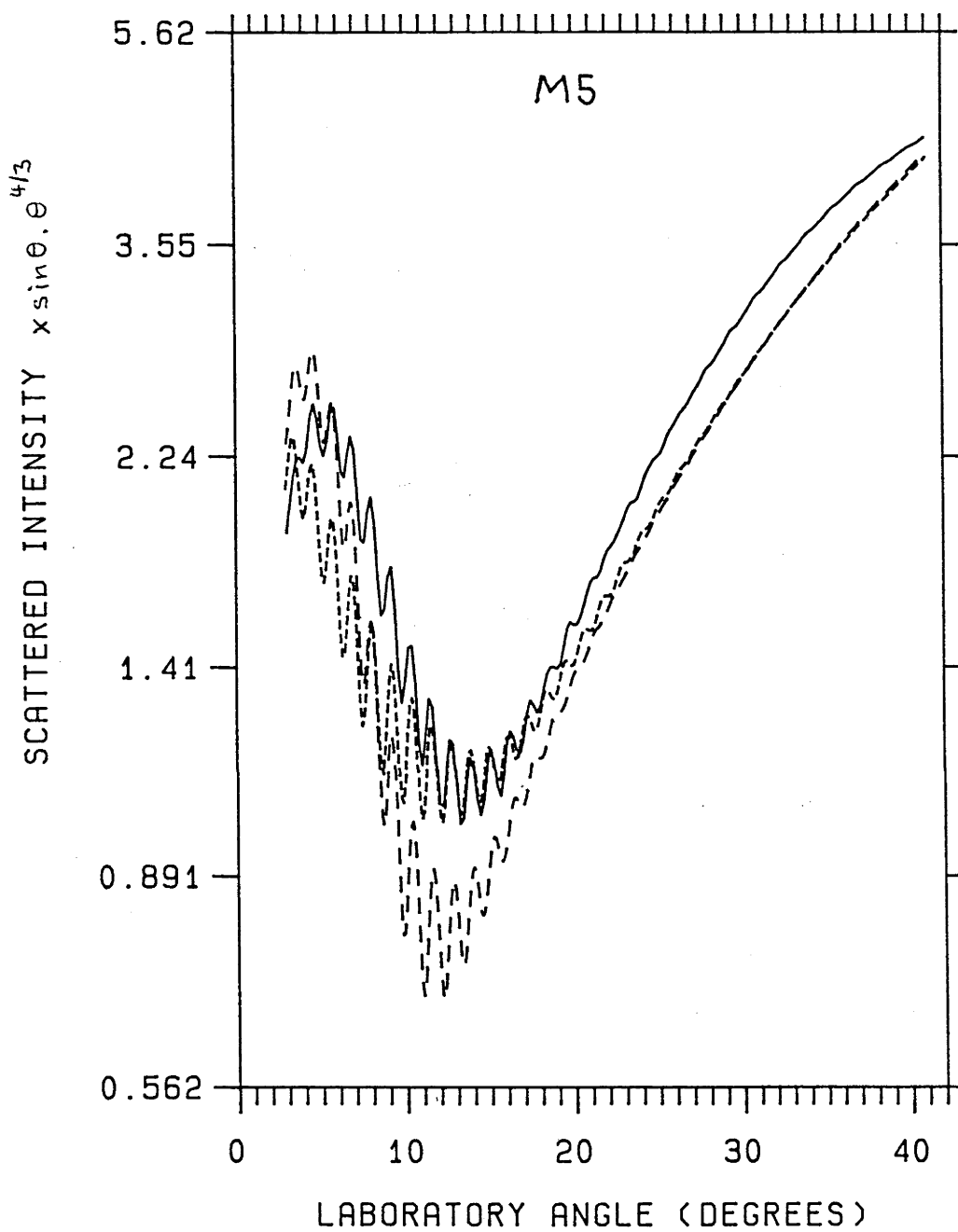


Figure 5.8

Table 5.5

Total Integral Cross Sections (\AA^2)			
Interaction Potential			
method	ArHF-HFD1	ArHF-HFD2	M5
spherical potential	190.7	215.5	178.6
semiclassical	191.3	216.5	179.1
infinite order	204.5	207.7	195.5
sudden	205.2	208.8	196.0
coupled states	193.8	218.0	182.2
	-	-	-

otherwise obscuring diffraction oscillations. The cross sections were multiplied by $\sin\theta.\theta^{4/3}$ in order to enhance the primary rainbow, which is the broad peak centred near 5 degrees. Coupled states total differential cross sections which have not been angle averaged are given in Figure 5.9 for the ArHF-HFD2 potential, both before and after having been multiplied by $\sin\theta.\theta^{4/3}$. These unaveraged cross sections show fading away diffraction oscillations characteristic of the dark (ie. large angle) side of a primary rainbow feature. The small oscillations seen for laboratory scattering angles greater than 23° are the result of neglecting J 's greater than 220 in calculating the elastic cross sections. Truncating the sums for the elastic cross sections at $J=220$ does not affect the discussions presented in this chapter.

Although the three approximate methods predict rather similar total differential cross sections for the ArHF-HFD1 potential, this is not so for the other potentials. This is almost certainly related to the fact that the ArHF-HFD1 potential is the shallowest, as far as its spherical part is concerned, and the least anisotropic of the three potentials. In all cases, the IOS cross sections are in better agreement with the coupled states results than are the spherical potential cross sections. The latter overestimate the heights of the primary rainbow peaks and significantly over resolve the minima on the dark sides of the rainbows. Rainbow peaks predicted using the coupled states approximations are shifted slightly to larger angles than those predicted using the other approximations.

Consider the integral cross sections given in Table 5.5. All of the coupled states results are similar to the spherical potential values. Whereas the ArHF-HFD1 and M5 IOS integral cross sections are about 15 \AA^2 larger than the spherical potential and coupled states results, that for

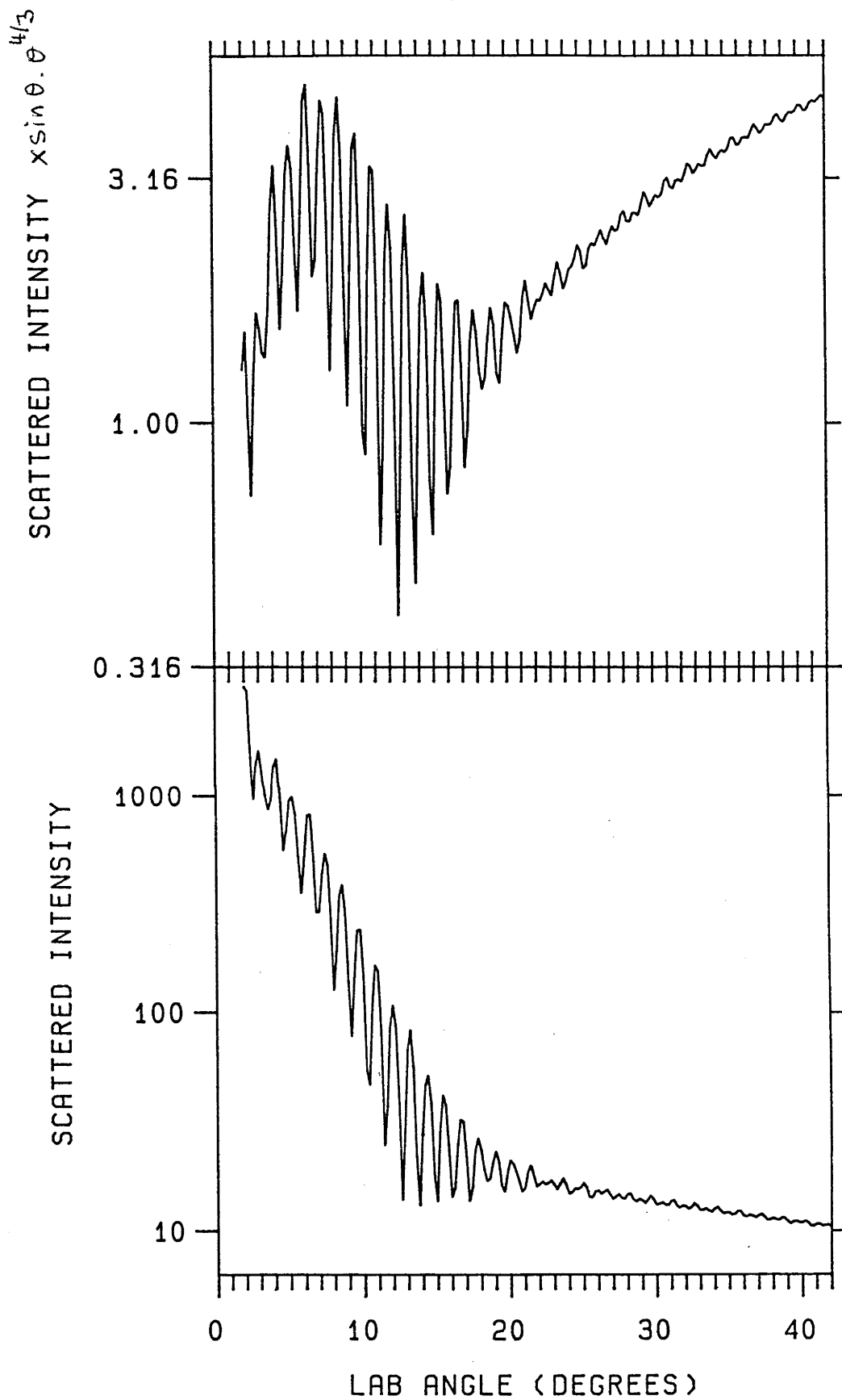


Figure 5.9

the ArHF-HFD2 potential is about 8 \AA^2 smaller. In Table 5.6 and Figure 5.10 we give the integral cross sections which were used to compute the IOS integrals as a function of the potential angle γ . The variations in the cross sections as a function of γ reflect the substantial anisotropies of the potentials. In view of these variations it is not surprising that the IOS integral cross sections behave as they do. By considering the contributions to the integral cross sections from the different orbital angular momentum quantum numbers, which are referred to as the opacities, it is found that the behaviour of the IOS cross sections between $\gamma=0$ and 45 degrees is related to rather dramatic changes in the opacities between $l=85$ and 110 . Orbital angular momenta in this range correspond to classical turning points which coincide with the attractive wells of the potentials. The opacities are discussed in more detail in Section 5.7. Given the differences between the IOS and coupled states integral cross sections, it is unclear why the spherical potential integral cross sections agree as well as they do with the coupled states results.

The rotational periods of the HF molecules are about 0.39 and 0.13 ps for $j=1$ and 2 respectively. These periods correspond to tangential speeds of about $5,400$ and $19,000$ m/s at a radial distance of 3.4 \AA (6.4 atomic units), which is roughly where the minima in the potentials are located. By comparison, the relative speed of the collision relevant to the calculations reported above is 1360 m/s. This speed gives a reasonable estimate of the tangential speed at the distance of closest approach. From these results we conclude that HF molecules with $j>1$ rotate many times during a single collision, and the tangential speed of the collision at the distance of closest approach is not well matched to the speed of the rotational motion. For molecules in $j=1$ the the tangential speed for the

Table 5.6

Infinite order sudden cross sections as a function of
the potential angle γ

			Integral Cross Sections (\AA^2)		
			Interaction Potential		
γ (degrees)	$\cos\gamma$	weight	ArHF-HFD1	ArHF-HFD2	M5
8.5	0.989	0.027	241.2	265.1	236.6
19.1	0.945	0.062	252.8	240.7	237.7
30.0	0.866	0.095	241.5	231.6	249.9
41.0	0.755	0.125	205.5	251.2	241.6
51.8	0.618	0.159	190.0	240.7	197.5
63.3	0.450	0.169	194.9	212.0	181.1
73.6	0.282	0.183	204.2	194.6	186.6
84.5	0.095	0.189	209.2	189.4	190.8
95.5	-0.095	0.189	210.9	188.8	191.8
106.4	-0.282	0.183	209.9	189.1	191.0
116.7	-0.450	0.169	206.1	191.1	189.0
128.2	-0.618	0.159	199.8	196.7	186.1
140.8	-0.775	0.125	192.3	206.4	182.6
150.0	-0.866	0.095	187.8	217.6	179.1
160.9	-0.945	0.062	183.7	226.4	176.3
171.5	-0.989	0.027	182.0	231.2	174.7

IOS integral cross sections
as a function of the potential angle

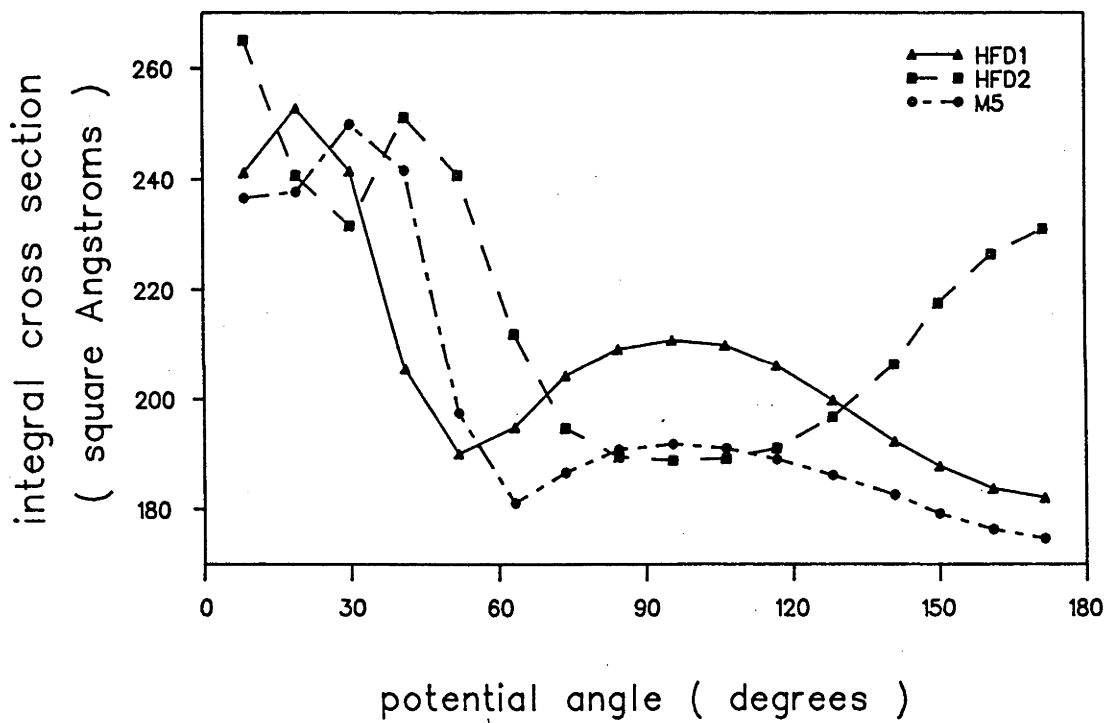


Figure 5.10

collision at the distance of closest approach is about four times smaller than that corresponding to the rotating HF molecule. Molecules in $j=1$ therefore rotate about twice in the time it takes the collision to occur. Given the rather rapid rotational motion compared to the duration of the collision, one might expect the scattering to be reasonably well described using an effective spherical potential. Although this seems to be the case for the integral cross sections, it is not so for the differential cross sections. The deep and strongly anisotropic attractive regions of the potentials are clearly important in determining the scattering behaviour.

It was noted in Section 5.1 that the primary rainbow occurs at a centre-of-mass scattering angle of about $2\epsilon/E_{\text{collision}}$ radians, where ϵ is a measure of the well depth of the potential. From the well depths of the spherical parts of the ArHF-HFD1 and ArHF-HFD2 potentials, namely 114.6 and 167.6 K, one obtains centre of mass scattering angles of 8.8 and 12.9 degrees respectively. Assuming elastic scattering, the corresponding laboratory scattering angles are 5.8 and 8.5 degrees. Noting that the above expression was derived from a spherical potential classical analysis, and that the quantum mechanically determined primary rainbow peak is expected to occur at slightly smaller angles than the classical one, these angles are in reasonable agreement with with the computed cross sections.

In summary, we conclude that both the spherical potential and IOS approximations are unable to adequately describe the total differential and total integral cross sections for HF scattered from Ar at a collision energy of 1493 K (128.6 meV). It is only possible to assess the accuracy of the coupled states results by comparing them with those of exact close coupling calculations, as done in Chapter 4 for the He-HF system. Unfortunately, we could neither carry out such calculations nor find

reference to the same in the literature.

5.5 Comparing Theory with Experiment

The results presented in the previous section suggest that the spherical potential and IOS approximations are unable to accurately describe the scattering of HF from Ar at the collision energies considered. In making a comparison between the measured total differential cross sections and the calculated ones, we therefore chose to use the coupled states results.

A full average over the molecular beam parameters and the detector geometry using the coupled states approximation was not feasible with the available computing facilities. To assess the effect of such averaging upon the calculated cross sections, we compared IOS total differential cross sections both before and after averaging over the velocity distributions of the beams. The ArHF-HFD2 potential was used in this study. Seventeen IOS calculations were carried out for a range of HF and Ar velocities, determined by the experimentally determined distributions whose parameters appear in Table 5.2. The resulting total differential cross sections were appropriately weighted and summed to give the desired velocity averaged cross section. Right angle collisions were assumed and the cross sections were smoothed using a 2 degree angular window. As shown in Figure 5.11, the only significant difference between the velocity averaged IOS cross section and that calculated using the most probable speeds given in Table 5.2 is that the diffraction oscillations in the former are more highly damped. The primary rainbow features seen in these cross sections are in good agreement.

Also shown in Figure 5.11 is a single energy IOS cross section (for the ArHF-HFD2 potential) calculated using the HF and Ar speeds which

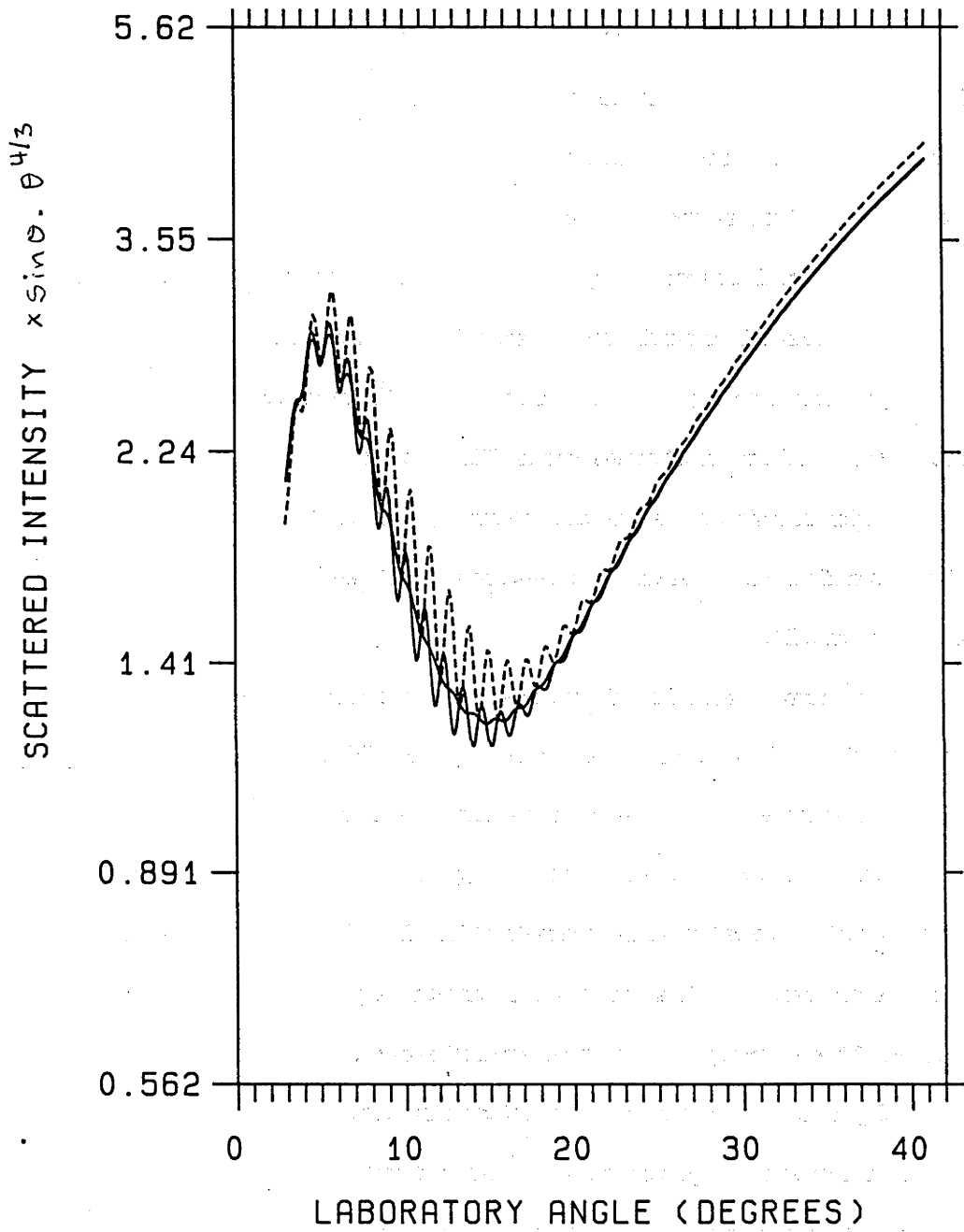


Figure 5.11

were used in the coupled states calculations. These latter speeds, which were chosen before the reanalysis of the velocity distributions (see Chapter 4), result in a collision energy 6% smaller than that obtained from the most probable speeds given in Table 5.2. The IOS differential cross section calculated using the experimentally determined most probable speeds, rather than those used in the coupled states calculations, has a primary rainbow which is shifted to slightly lower angles, but is otherwise quite similar. We conclude that, apart from a small shift in the position of the primary rainbow peak, the single energy coupled states total differential cross sections presented in this chapter are probably similar to those which would result from full velocity and angle averaged coupled states calculations.

Coupled states total differential cross sections for the three potentials are compared with each other in Figure 5.12 and 5.13. Those in Figure 5.13 have not been multiplied by $\sin\theta.0^{4/3}$. The experimentally measured data, which are shown as diamonds in the figure, have been scaled (by eye) to coincide as closely as possible with the M5 cross section. Differences between the three cross sections are substantial, with the M5 potential agreeing most closely with the measured data. The primary rainbow predicted by the ArHF-HFD2 potential occurs at too large a scattering angle, suggesting that this potential is either too deep or has the wrong anisotropy, or both. As noted above, the collision energy used in the coupled states calculations is about 6% smaller than the mean experimental collision energy. An increase in the collision energy would tend to improve the agreement between the ArHF-HFD2 cross section and the experimental results and worsen it for the other potentials. Assuming that the changes in the coupled states cross section resulting from the use of

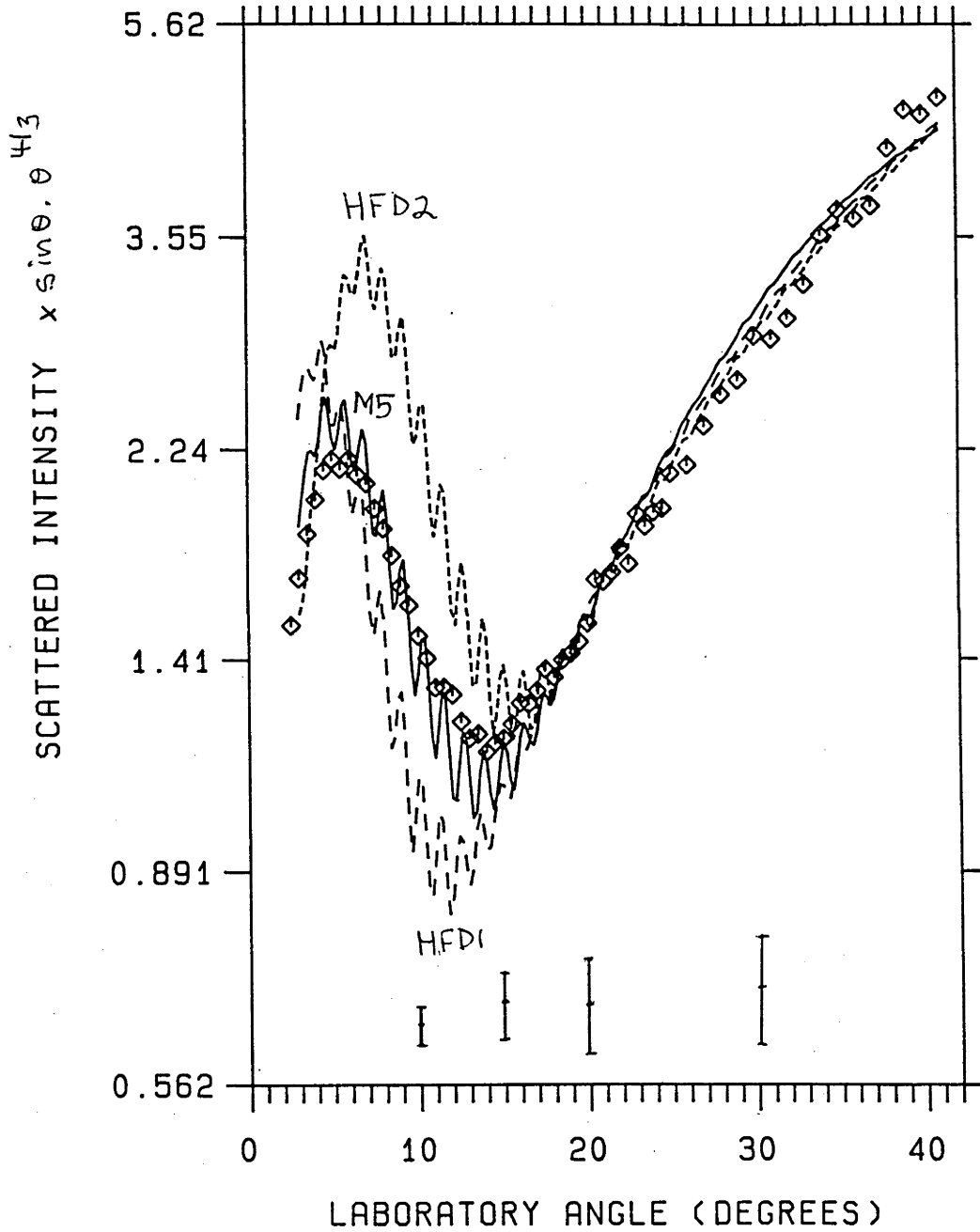


Figure 5.12

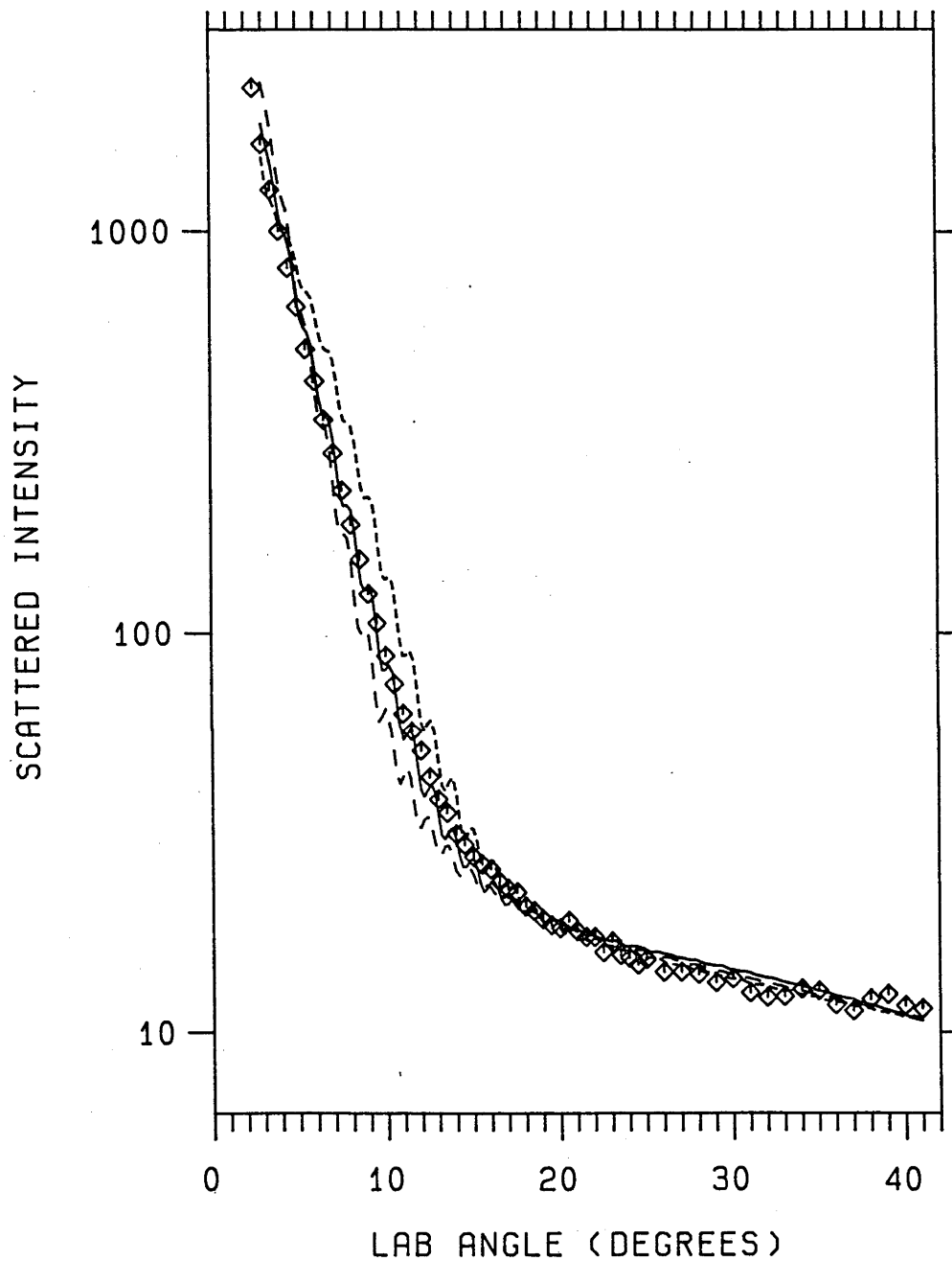


Figure 5.13

the experimentally determined most probable speeds are similar to those observed for the IOS cross sections (shown in Figure 5.11 for the ArHF-HFD2 potential), this energy correction is unlikely to alter the conclusions presented in this section.

If the cross sections are not weighted by $\sin\theta.\theta^{4/3}$ the differences between the ArHF-HFD1 cross section and the measured data appear to be smaller, whereas the ArHF-HFD2 cross section is still obviously unable to reproduce these data. Of the three potential surfaces considered in this study, only the ArHF-HFD2 and M5 surfaces are able to reproduce the known spectroscopic constants for Ar-HF and Ar-DF (Douketis et al. (1984)). Of these two potentials, only the M5 potential is consistent with the measured total differential scattering cross section.

Although our results show that, of the potentials considered, the M5 potential gives the best description of the Ar-HF interaction, we stress that the analysis was based upon the coupled states approximation, and that no averaging was done over the experimental parameters. In order to reliably assess the accuracy of the unaveraged coupled states cross sections one would need to compare them with averaged close coupled results.

5.6 State-to-state Cross Sections within the Coupled States Approximation

In this section we compare the state-to-state integral and differential cross sections resulting from the ArHF-HFD1, ArHF-HFD2 and M5 potentials. The results are those of the coupled states calculations reported earlier in this chapter. As noted previously, the state-to-state differential cross sections have been weighted by the appropriate experimentally determined HF rotational populations, and have been expressed as a function of the laboratory scattering angle, thereby allowing an assessment of their contributions to the measured total differential cross section. In all cases a two degree angular window was used to smooth the diffraction oscillations.

Differential cross sections for the three potentials, multiplied by $\sin\theta.\theta^{4/3}$, are given in Figures 5.14, 5.15 and 5.16. For comparison, results for the M5 potential which have not been multiplied by $\sin\theta.\theta^{4/3}$ are shown in Figure 5.17. The total and individual inelastic cross sections show primary rainbow peaks which are shifted to higher angles than those of the corresponding total elastic cross sections. In all cases the 0→1 cross sections are the major contributors to the total inelastic cross sections in the vicinity of the rainbow peak, followed by the 1→0 transitions. The maximum contributions to the total differential cross section from the 0→1 transition, which occur on the large angle side of the rainbow peak, are: 17% at 9° for the ArHF-HFD1 potential; 25% at 11° for the ArHF-HFD2 potential; and 25% at 10° for the M5 potential. The corresponding contributions from the total inelastic cross sections are: 25% at 9° for the ArHF-HFD1 potential; 35% at 11° for the ArHF-HFD2 potential; and 35% at 11° for the M5 potential. At a laboratory scattering

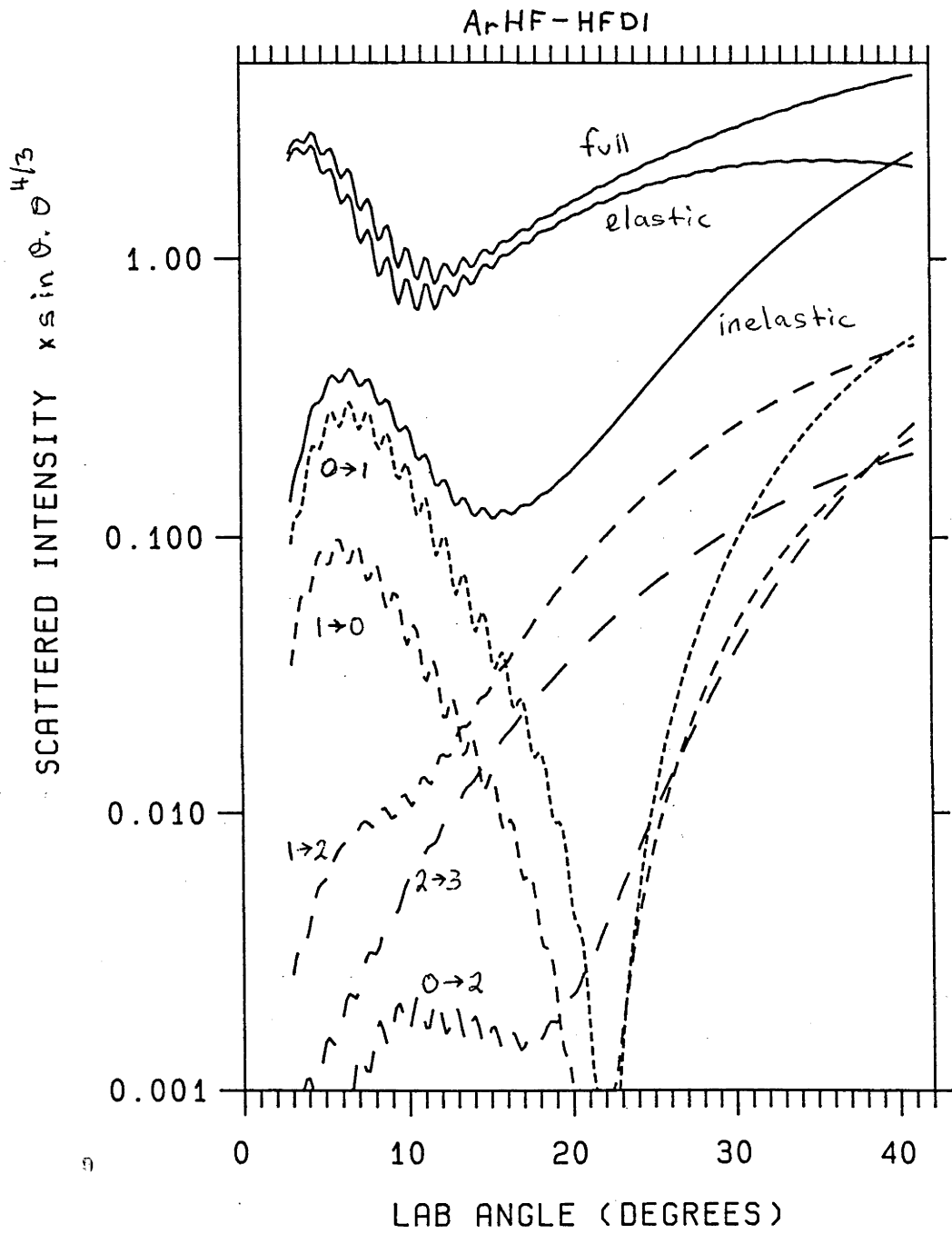


Figure 5.14

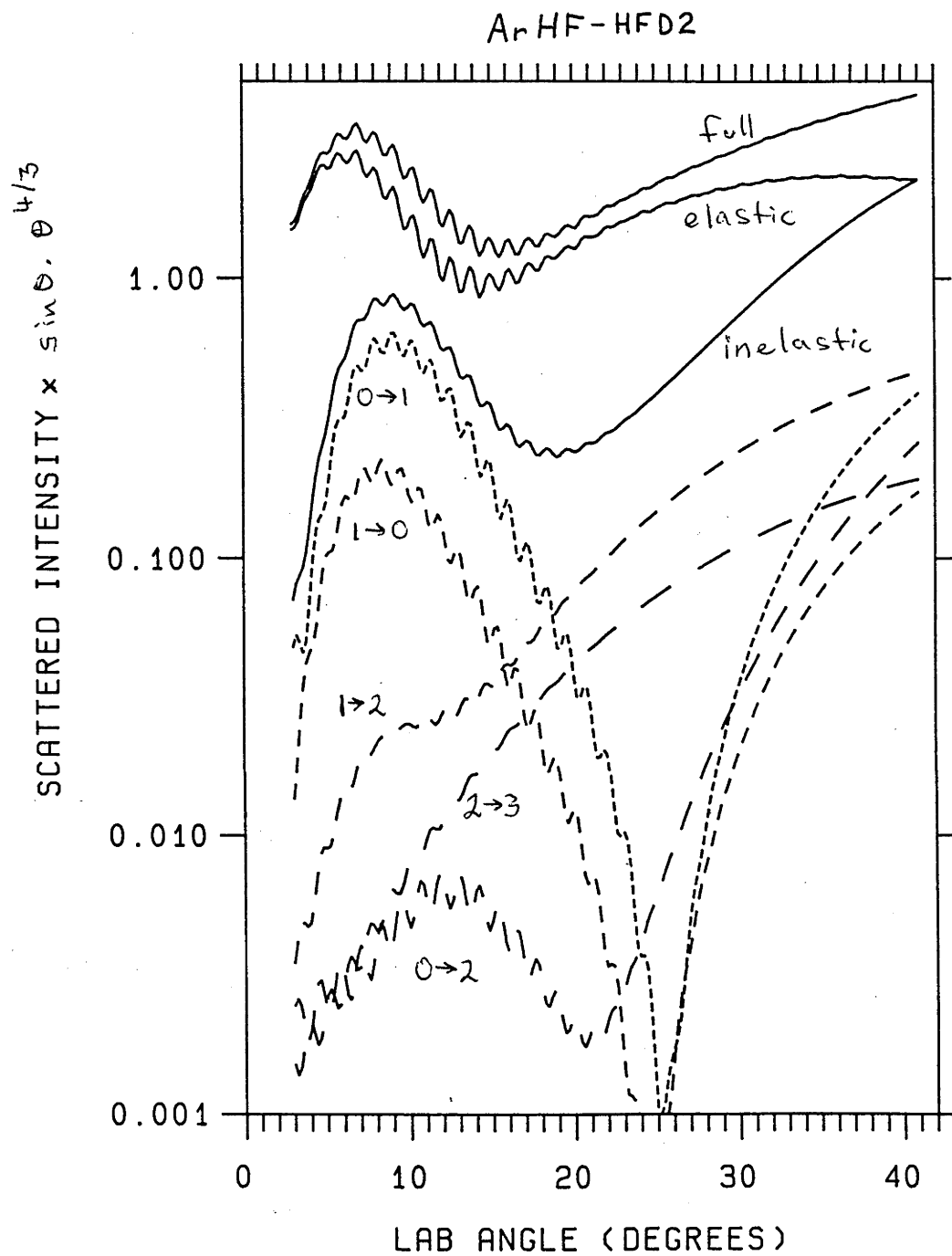


Figure 5.15

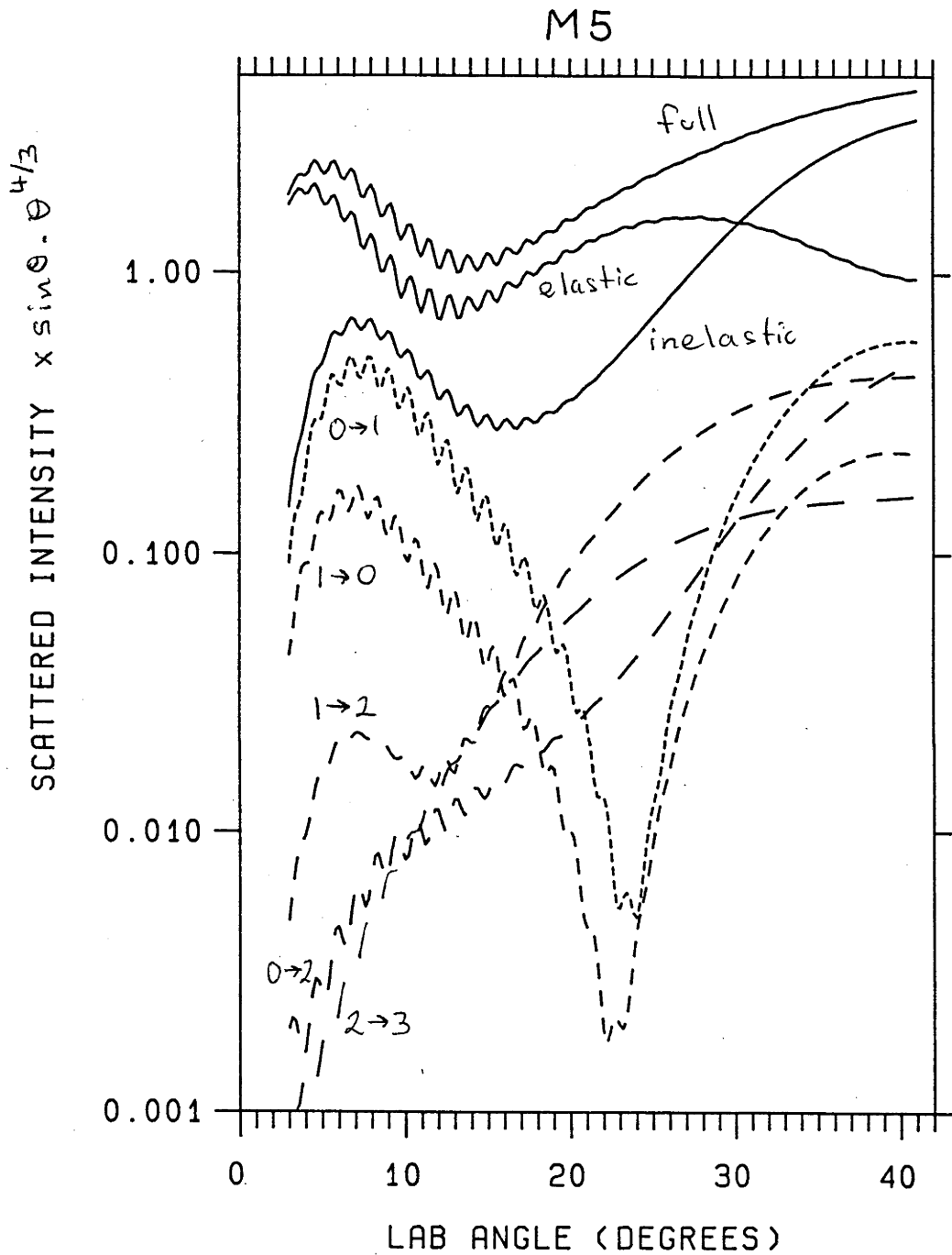


Figure 5.16

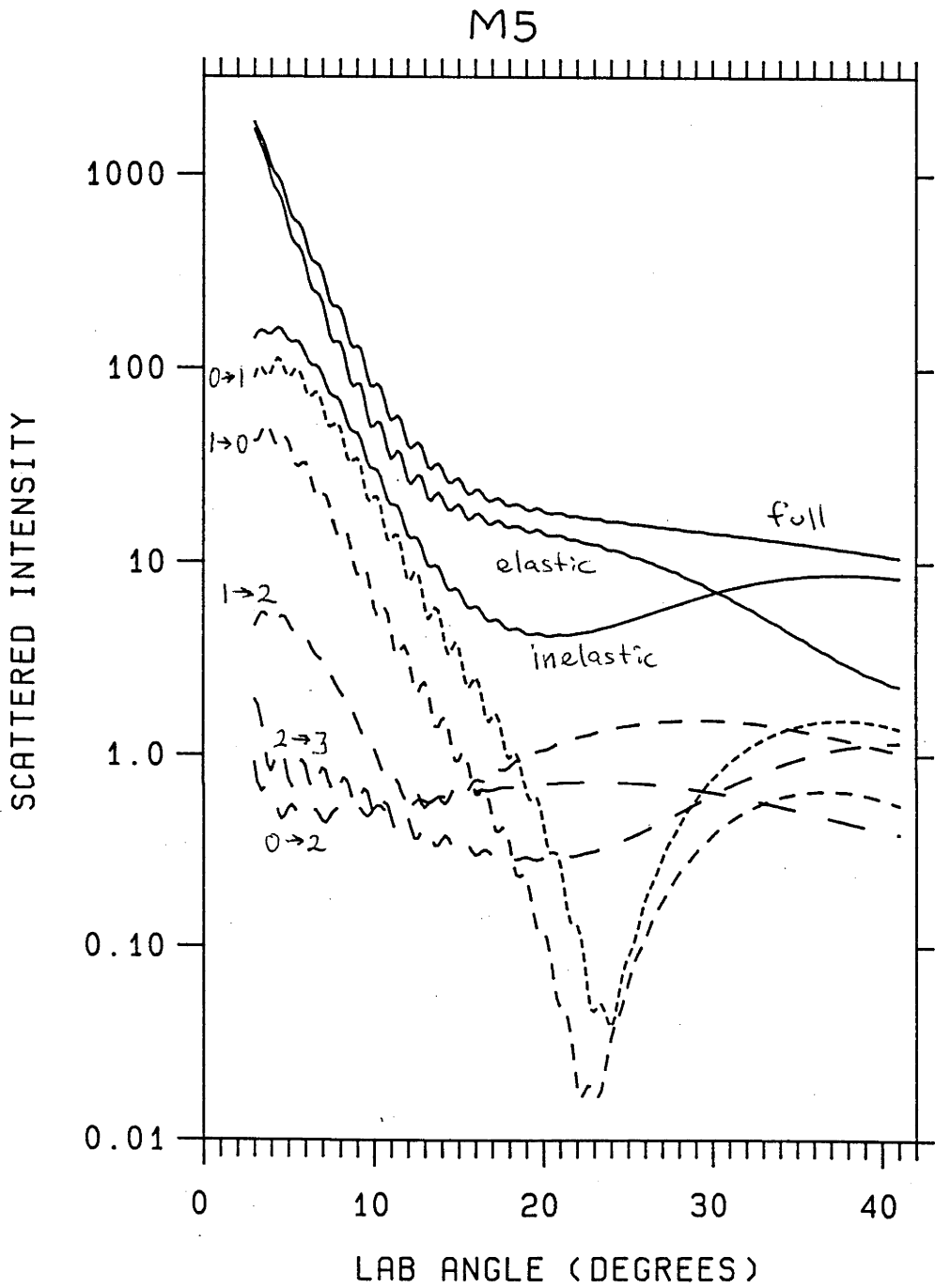


Figure 5.17

angle of 40° the total inelastic contributions are 50%, 48% and 78% for the ArHF-HFD1, ArHF-HFD2 and M5 potentials respectively.

The inelastic state-to-state differential cross sections predicted by the three potentials are all qualitatively similar. The major quantitative differences are (1) that they contribute less to the total differential cross sections for the ArHF-HFD1 potential, (2) that the $1 \rightarrow 2$ cross sections for the M5 potential shows a better resolved primary rainbow oscillation than do the $1 \rightarrow 2$ cross sections predicted by the other potentials, and (3) that the M5 potential predicts significantly larger inelastic cross sections at large scattering angles than do the other potentials. From the results presented above it is clear that inelastic processes, particularly the $0 \rightarrow 1$ and $1 \rightarrow 0$ processes, play a crucial role in determining the behaviour of the total differential cross section for the scattering of HF from Ar.

We now consider the differential cross sections for HF molecules in a given initial rotational state colliding with Ar. In Figures 5.18, 5.19 and 5.20 we show both the elastic ($j \rightarrow j'$) and total ($j \rightarrow \sum j'$) cross sections for initial HF rotational states $j=0,1,2$ and 3. These cross sections have been weighted by the measured HF rotational populations in order to assess the relative contributions of the different initial rotational states to the total differential cross section. Cross sections with $j_{\text{initial}}=0$ have been multiplied by $10^{\frac{1}{2}}$ (ie. shifted up half a decade) in order to disentangle them from the $j_{\text{initial}}=1$ results. Unshifted total cross sections from $j_{\text{initial}}=0$ are shown as dashed curves in the figures so that their contributions to the total scattering may be compared with those of the other population weighted cross sections. For all of the potentials

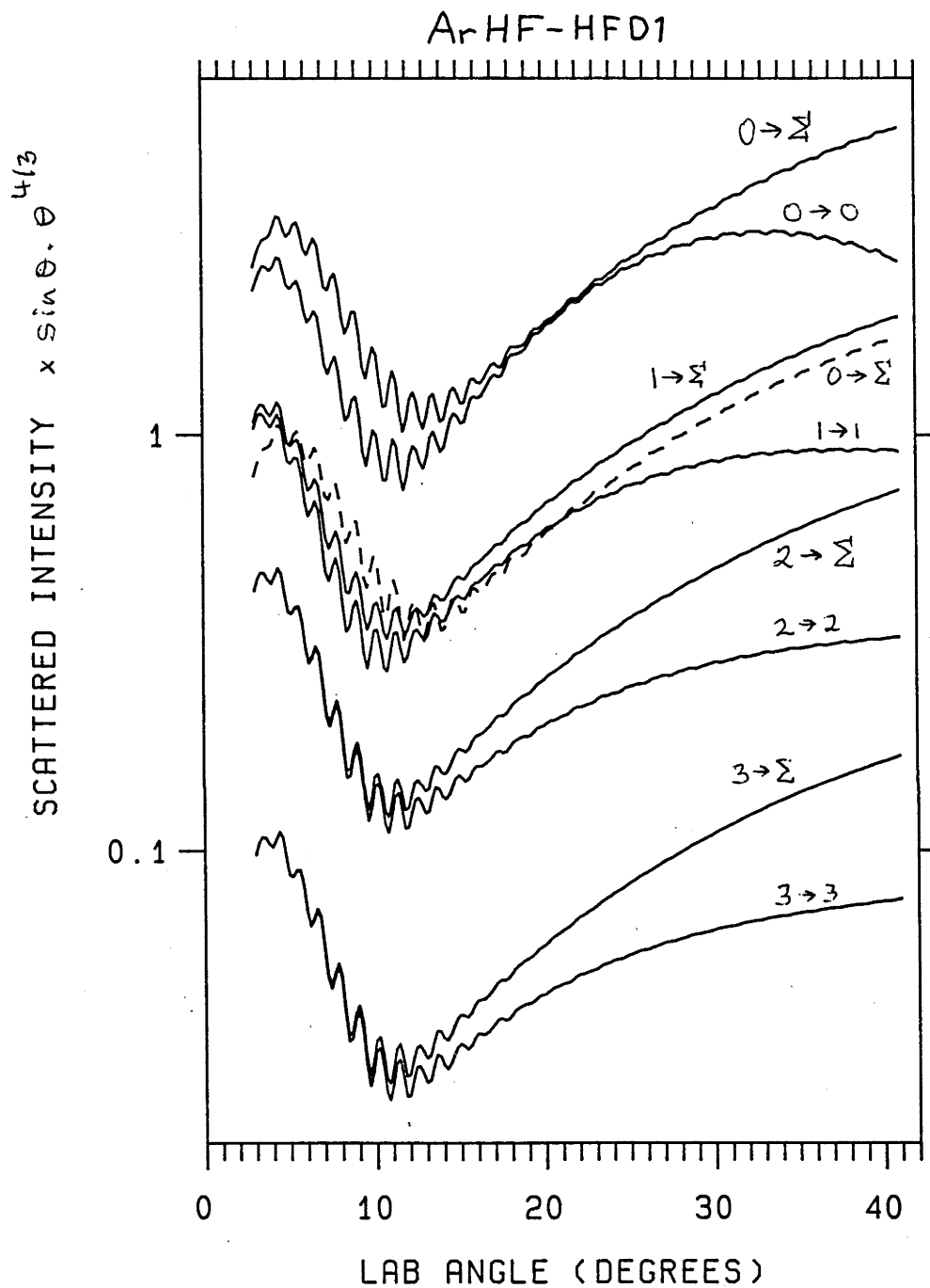


Figure 5.18

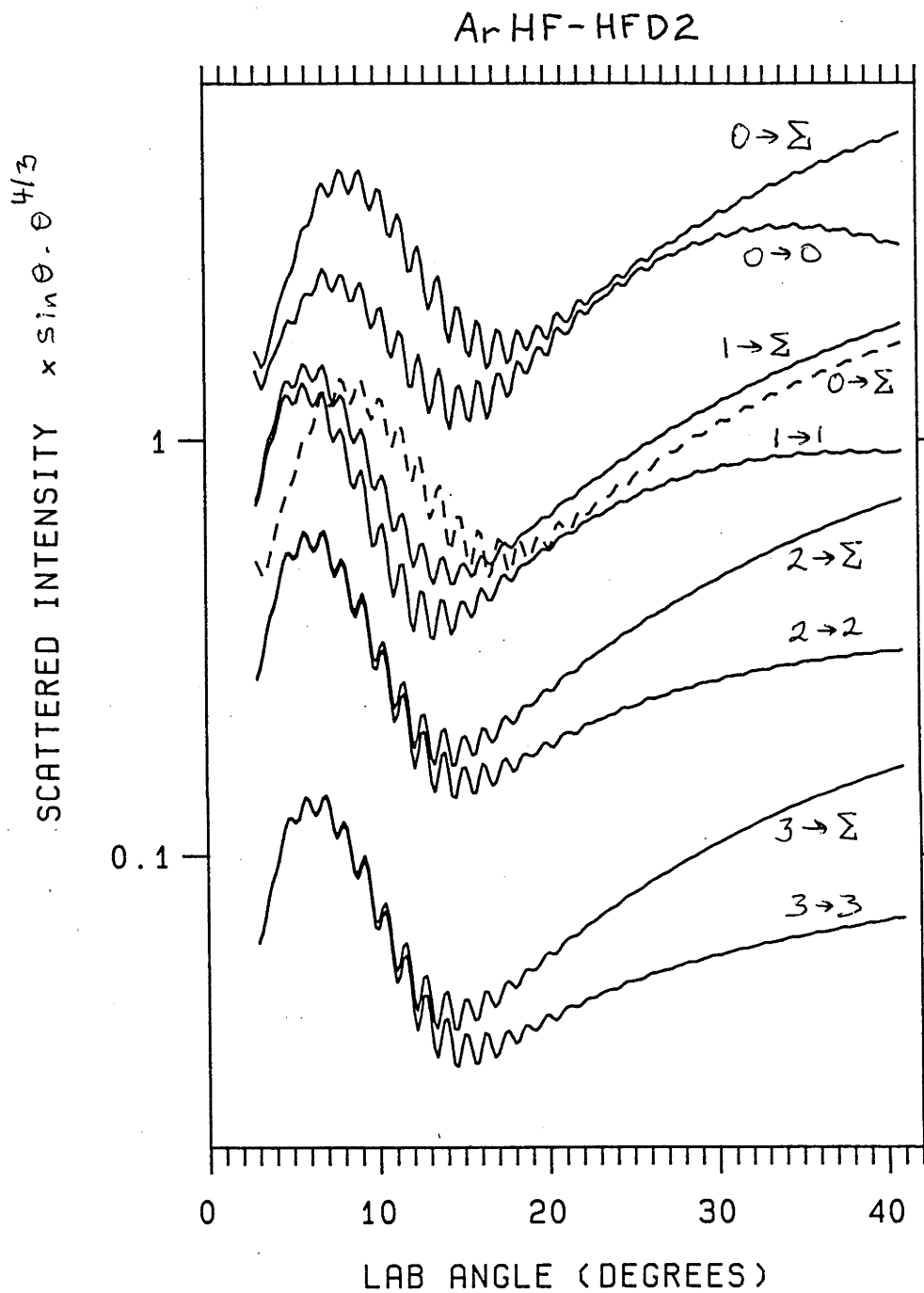


Figure 5.19

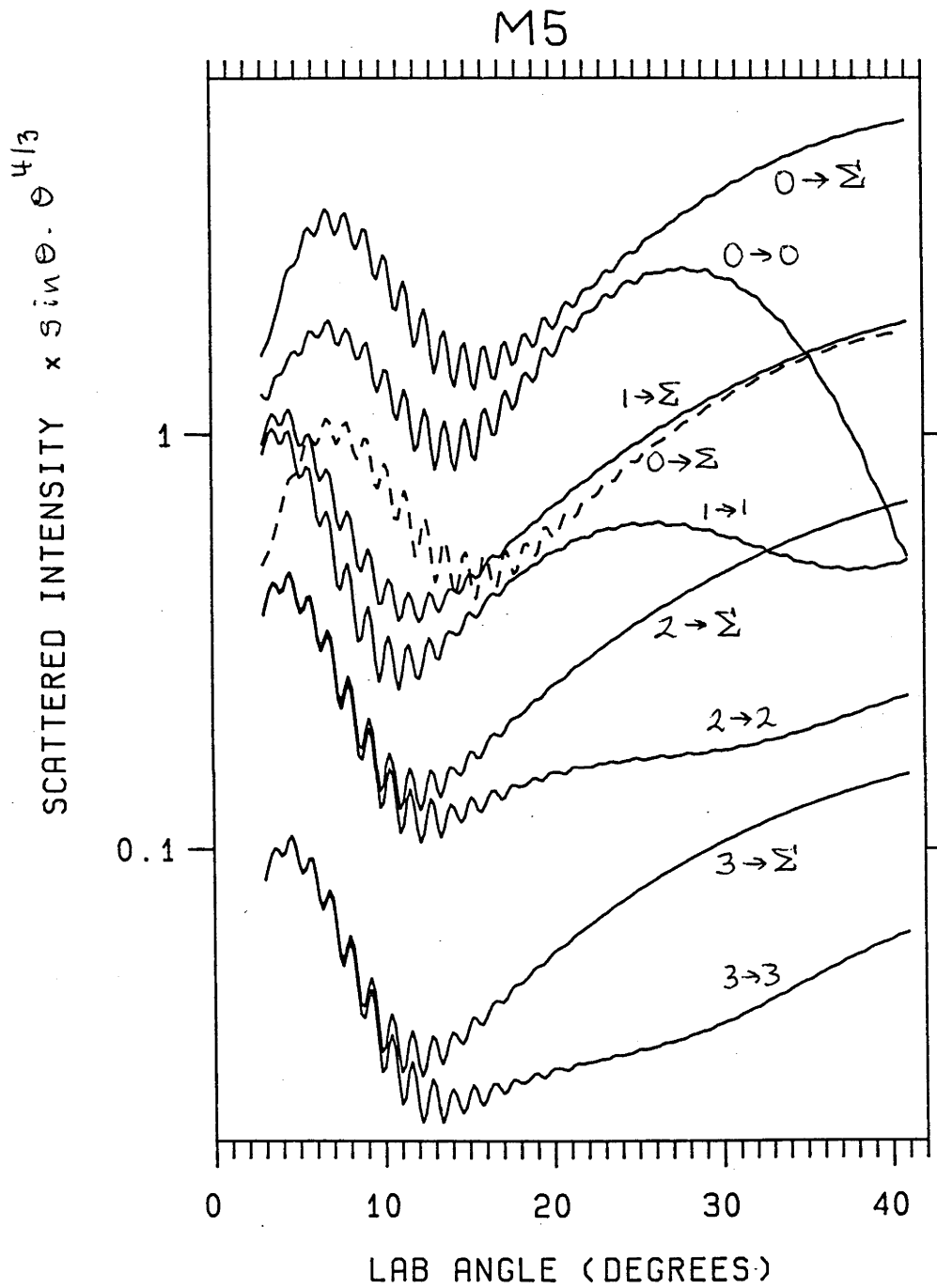


Figure 5.20

the $j_{\text{initial}}=0$ cross sections are almost the same in magnitude as those resulting from $j_{\text{initial}}=1$, although their primary rainbow oscillations are shifted to larger angles. The amount by which they are shifted depends upon the interaction potential. This behaviour is best understood by considering the shapes of the individual elastic and inelastic cross sections contributing to the total cross sections from a given initial HF rotational state. In the vicinity of the rainbow peaks, the only population weighted inelastic cross sections which are significant are those for the $0 \rightarrow 1$, $1 \rightarrow 0$ and $1 \rightarrow 2$ transitions, as can be seen from Figures 5.14, 5.15, and 5.16. This is clearly not the case at large scattering angles, for which many inelastic cross sections are significant. The contributions from these inelastic cross sections can be appreciated by comparing the $j \rightarrow j'$ elastic cross sections with the $j \rightarrow \sum j'$ total cross sections in the vicinity of the rainbow peak (see Figures 5.18, 5.19 and 5.20). Notice that

(1) the $3 \rightarrow j'$ and $2 \rightarrow j'$ cross sections are similar to the elastic $3 \rightarrow 3$ and $2 \rightarrow 2$ cross sections,

(2) the $1 \rightarrow \sum j'$ cross sections differ slightly from the $1 \rightarrow 1$ cross sections in that they fall away more slowly on the dark side of the rainbow, indicating a small contribution from the $1 \rightarrow 0$ and $1 \rightarrow 2$ transitions, and

(3) the $0 \rightarrow \sum j'$ cross sections are vastly different to the $0 \rightarrow 0$ cross sections, indicating large contributions from the $0 \rightarrow 1$ transitions. That these differences are larger for the ArHF-HFD2 and M5 potentials reflects the greater anisotropies resulting from these potentials. Note also that the $0 \rightarrow 0$ rainbow peaks are (a) broader than those of the other elastic cross sections, resulting in gentler declines on the large angle sides, and

(b) shifted to higher angles. Once again, these effects are more pronounced for the ArHF-HFD2 and M5 potentials. A discussion of this behaviour is given later in this section.

We conclude that the $0 \rightarrow \sum j'$ cross sections are different from the other $j \rightarrow \sum j'$ cross sections because of both substantial inelastic contributions (from the $0 \rightarrow 1$ transitions) and differently shaped elastic cross sections. Differences of this kind have also been noted by Becker et al. (1979) and Buck and Schleusener (1981) in their coupled states studies of Xe-HF and Ar-HCl scattering respectively.

Centre of mass frame integral cross sections predicted by the three potentials are given in Table 5.7. These results, which have not been weighted by the HF populations, refer to a fixed collision energy of 1493 K. The $0 \rightarrow 1$ cross sections are by far the largest inelastic ones, as was found for the differential cross sections near the primary rainbow peak. Elastic cross sections predicted by the three potentials differ considerably. The overall agreement between the inelastic cross sections, on the other hand, is rather good, except for the $0 \rightarrow 3$ and $j \rightarrow 4$ cross sections obtained from the M5 potential, which are significantly larger than those predicted by the other potentials. As we show in the next section, these cross sections result from small impact parameter collisions off the repulsive core of the potential. Given that the repulsive wall of the M5 potential is far more anisotropic than those of the HFD potentials (compare Figures 5.2, 5.3 and 5.4), it is not surprising that both the integral and differential inelastic cross sections predicted using the M5 potential differ from those obtained from the HFD potentials. In Section 5.1 we noted that Barnes et al. (1982) measured relative integral

Table 5.7Coupled states state-to-state integral cross sections (\AA^2)

initial j	potential	final j					sum
		0	1	2	3	4	
0	ArHF-HFD1	162.86	16.97	6.66	2.05	1.41	189.94
	ArHF-HFD2	193.76	21.41	7.12	1.94	1.69	225.92
	M5	152.99	21.03	5.37	3.41	3.32	186.12
1	ArHF-HFD1	5.86	178.76	6.76	3.99	1.60	196.96
	ArHF-HFD2	7.42	192.18	6.93	4.19	1.80	212.52
	M5	7.38	158.64	6.74	4.39	3.47	180.63
2	ArHF-HFD1	1.54	4.36	178.64	7.00	2.66	194.20
	ArHF-HFD2	1.65	4.49	199.28	7.05	2.99	215.45
	M5	1.18	4.37	162.14	6.91	4.30	178.90
3	ArHF-HFD1	0.42	2.08	5.48	179.06	6.12	193.15
	ArHF-HFD2	0.40	2.17	5.47	199.87	6.54	214.45
	M5	0.62	2.20	5.30	162.35	7.12	176.74

state-to-state cross sections for vibrationally excited HF molecules colliding with Ar. They considered three mean collision energies, the smallest of which was about 4 kcal/mole, or approximately 2000 K. The cross sections were found to be almost independent of both the vibrational state and the mean collision energy, except for the $j \rightarrow j' = 1 \rightarrow 0$ cross section, which increased 2.7 fold in going from 16 to 4 kcal/mole. By scaling their results at a mean collision energy of 2000 K to our $1 \rightarrow 0$ cross section of 7.4 \AA^2 at 1493 K (for the M5 potential) we obtain the following comparison, with cross sections in \AA^2 :

	$\sigma_{1 \rightarrow 0}$	$\sigma_{1 \rightarrow 2}$	$\sigma_{1 \rightarrow 3}$	$\sigma_{2 \rightarrow 0}$	$\sigma_{2 \rightarrow 1}$	$\sigma_{2 \rightarrow 3}$	$\sigma_{3 \rightarrow 0}$	$\sigma_{3 \rightarrow 1}$	$\sigma_{3 \rightarrow 2}$
Our M5 results	7.4	6.7	4.4	1.8	4.4	6.9	0.6	2.2	5.3
Barnes <u>et al.</u> (1982)	7.4	6.8	3.8	1.9	5.0	5.4	0.7	2.2	5.3

Given that Barnes et al. (1982) expect their results to be accurate to within 20%, the agreement between the measured and calculated values is rather good. We note, however, that the inelastic integral cross sections are rather insensitive to the details of the intermolecular potential. Indeed, except for the $0 \rightarrow 3$ and $j \rightarrow 4$ cross sections, both the ArHF-HFD2 and M5 integral cross sections agree well with the results of Barnes et al. (1982).

5.7 Partial Integral Cross Sections

Partial integral cross sections, also referred to as opacities, for the $0 \rightarrow j'$ and $1 \rightarrow j'$ transitions are shown in Figures 5.21, 5.22 and 5.23 for the three potentials. In these diagrams we have plotted

$$\sigma_1(j';j) = \frac{1}{(2j+1)} \frac{\pi}{k_0^2} \sum_{m,m'} |g_1(j'm';jm)|^2 \quad (5.5)$$

as a function of l . k_0 is the wavevector corresponding to the collision energy. Compare this equation with Eq. (3.38). Given that vibrational inelasticities were not studied, the vibrational quantum numbers have not been included in Eq. (5.5). The partial opacity $\sigma_1(j';j)$ is simply the contribution to the $j \rightarrow j'$ integral cross section from the orbital angular momentum l . By considering the effective potentials (ie. interaction potential + orbital angular momentum barrier) as a function of l one finds that (1) values of $l \leq 80$ correspond to turning points on the repulsive wall of the potential, (2) values of l in the range 90 to 120 correspond to classical turning points in the region of the attractive bowl of the potential, and (3) larger values of l result in glancing collisions off the attractive tail of the interaction potential. These observations are consistent with the estimates $b_{80} = 2.8 \text{ \AA}$ (5.3 atomic units) and $b_{100} = 3.5 \text{ \AA}$ (6.6 atomic units) obtained from Eq. (5.1).

Consider the elastic channel opacities, which are the largest curves shown in Figures 5.21, 5.22 and 5.23. In all cases a large peak is present for values of l greater than 100. These peaks account for about 60% of the respective integral cross sections and correspond to classical trajectories with turning points on the large r sides of the attractive wells of the interaction potentials. Another interesting feature of these

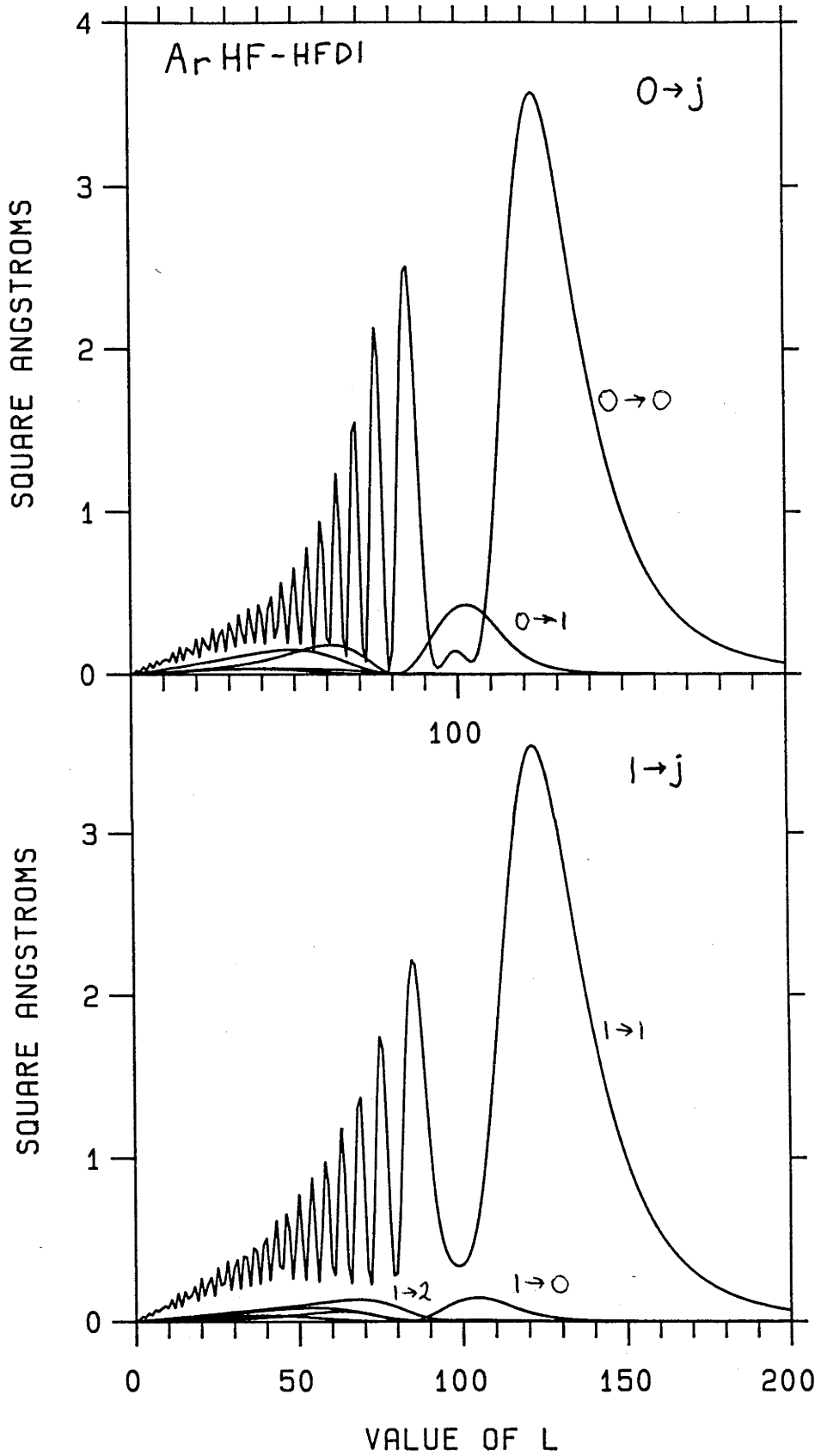


Figure 5.21

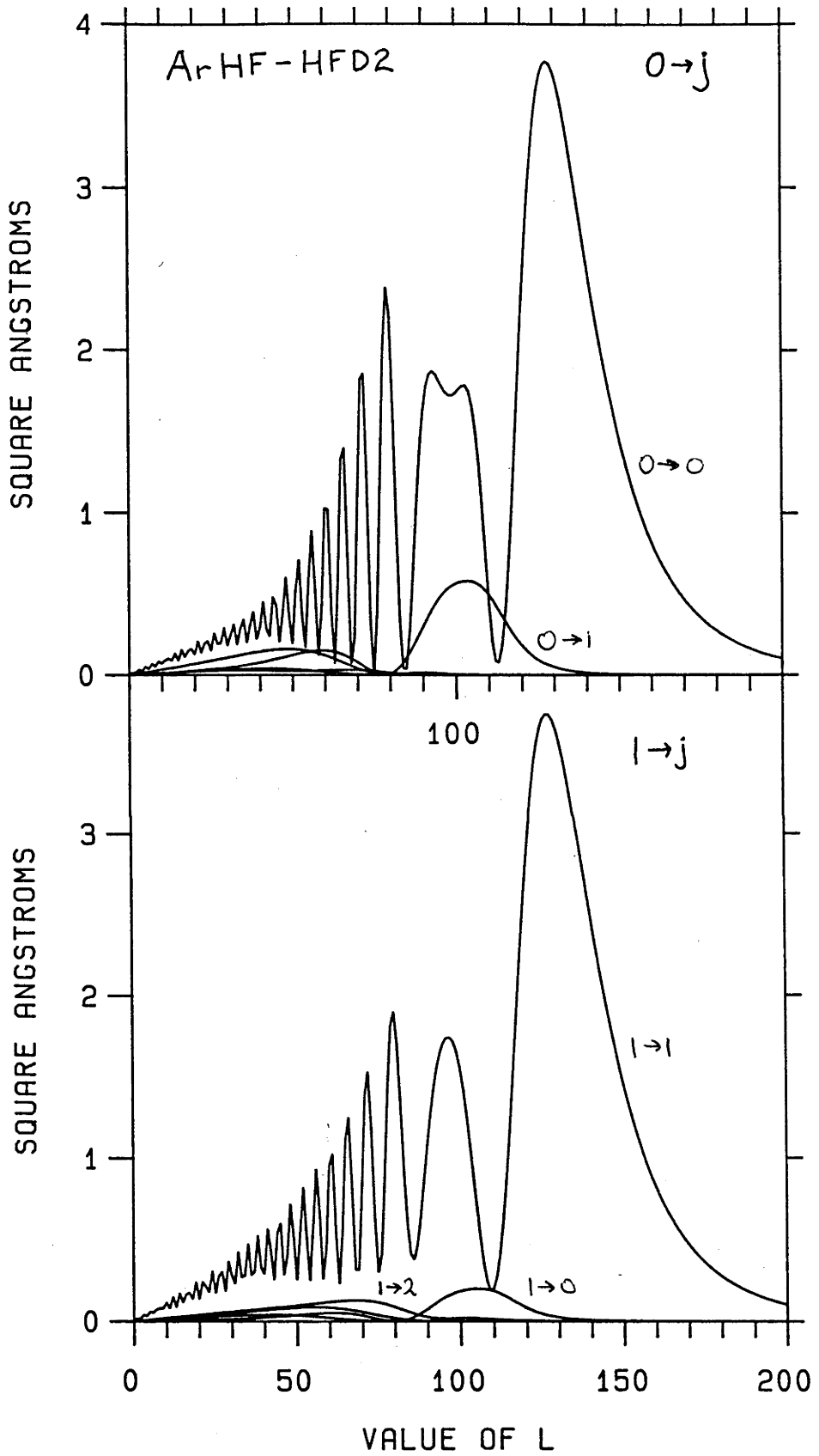


Figure 5.22

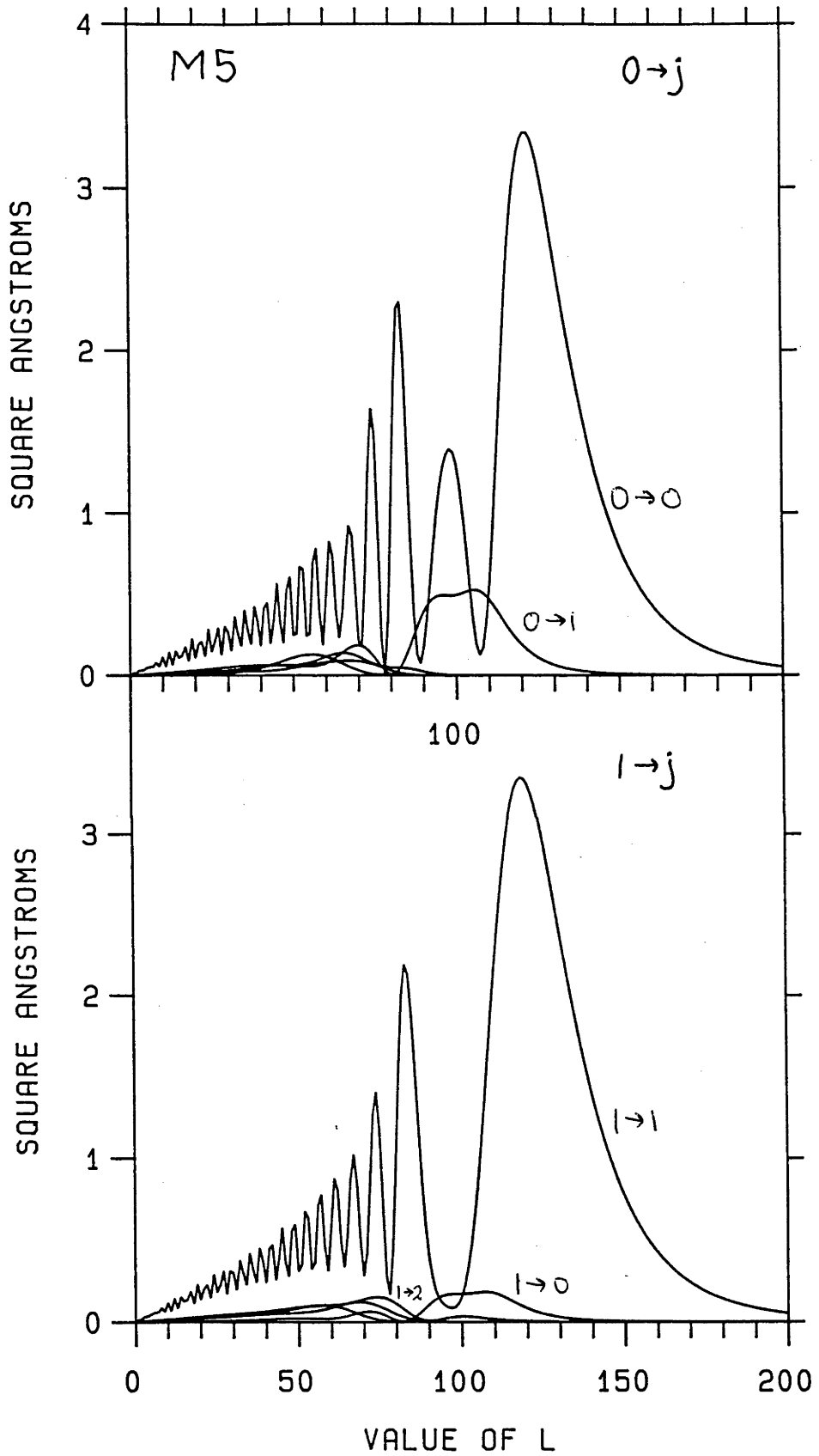


Figure 5.23

elastic opacities is seen between the largest and second largest peaks. For the ArHF-HFD1 potential there is no peak in this region for the 1→1 opacity function and only the tiny remnant of a peak for the 0→0 curve. A similar lack of structure is seen in the 1→1 partial opacity function for the M5 potential (see Figure 5.23). In contrast to these results, the 0→0 opacity function for the M5 potential and the 0→0 and 1→1 opacity functions for the ArHF-HFD2 potential (Figure 5.22) exhibit rather large peaks between $l=85$ and $l=110$. The 0→0 result for the ArHF-HFD2 potential shows two peaks which have almost completely merged. These results are for a collision energy of 1493 K. Coupled states opacities for the 0→0 transition were also calculated at collision energies of 1000 K and 2000 K for the ArHF-HFD1 potential. At 1000 K the two peaks had almost completely separated and were in fact both larger than the next peak to lower l . The higher energy opacity curve showed a single rather broad peak, which was the result of the two peaks shown in Figure 5.22 between $l=85$ and $l=110$ coalescing and diminishing in amplitude. We note that the opacity functions also stretch out towards larger l values as the collision energy is increased. This is because the wavevector k_0 is larger at higher energies, and thus larger orbital angular momenta are required to give the same classical turning point. It is clear from the results presented in Figures 5.21, 5.22 and 5.23, and from the investigations reported at the other collision energies, that the behaviour of the elastic opacities depends crucially upon both the details of the intermolecular potential and the collision energy.

As noted above, orbital angular momenta between about 90 and 120 correspond to classical turning points in the region of the attractive bowl of the potential. It is also possible to associate the different orbital

angular momenta with different scattering angles. In general, a large l means a large impact parameter and little deflection. Small orbital angular momenta correspond to head-on collisions and rather large scattering angles. As l , and therefore the impact parameter, increase from zero, the corresponding classical deflection function descends from 180° (back scattering) through zero (forward scattering) until it reaches the rainbow angle, after which it begins to increase and asymptotically approaches zero. Positive and negative deflection angles of the same magnitude both result in scattering at the same physical angle. In Figure 5.24 we show the results of a spherical potential study of the scattering predicted using the ArHF-HFD2 potential. The JWKB and Born approximations were used to evaluate the phase shifts. Velocities of the collision partners are the same as used for the coupled states calculations. The lower half of the figure shows the calculated opacities, which are not unlike those for the elastic channels seen in Figures 5.21, 5.22 and 5.23. Differential cross sections obtained by summing orbital angular momenta from 0 to 85, 110 and 300 are also shown in Figure 5.24. A two degree angular window was used to smooth out the diffraction structure. The rapid oscillations seen in the opacity function before the last two peaks (ie. between $l=0$ and 85) correspond to close encounters of the small impact parameter kind and large scattering angles. By including contributions from the peak between $l=85$ and 110, the differential cross section beyond the primary rainbow is almost completely accounted for. Nearly all of the scattering responsible for the primary rainbow results from values of l larger than 110, which constitute the largest peak seen in the partial opacity curve. In other words, the details of the rainbow are most sensitive to the interaction potential on the large r side of the minimum

SCATTERED INTENSITY $\times \sin^4 \theta$

132a

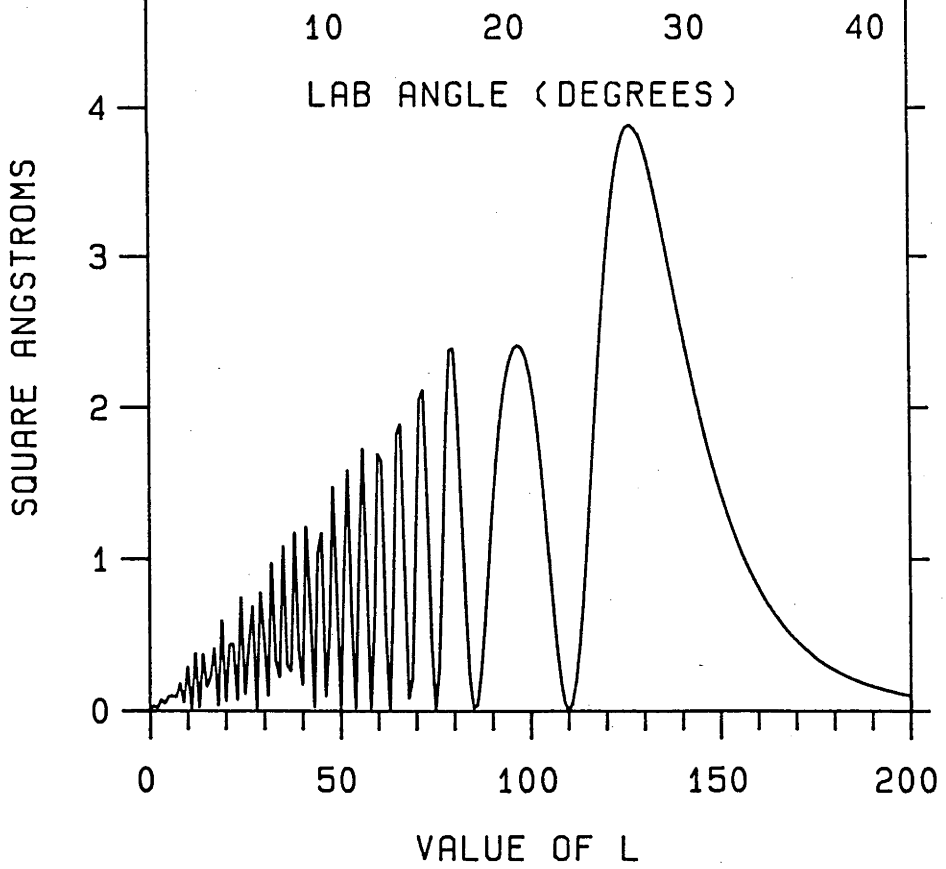
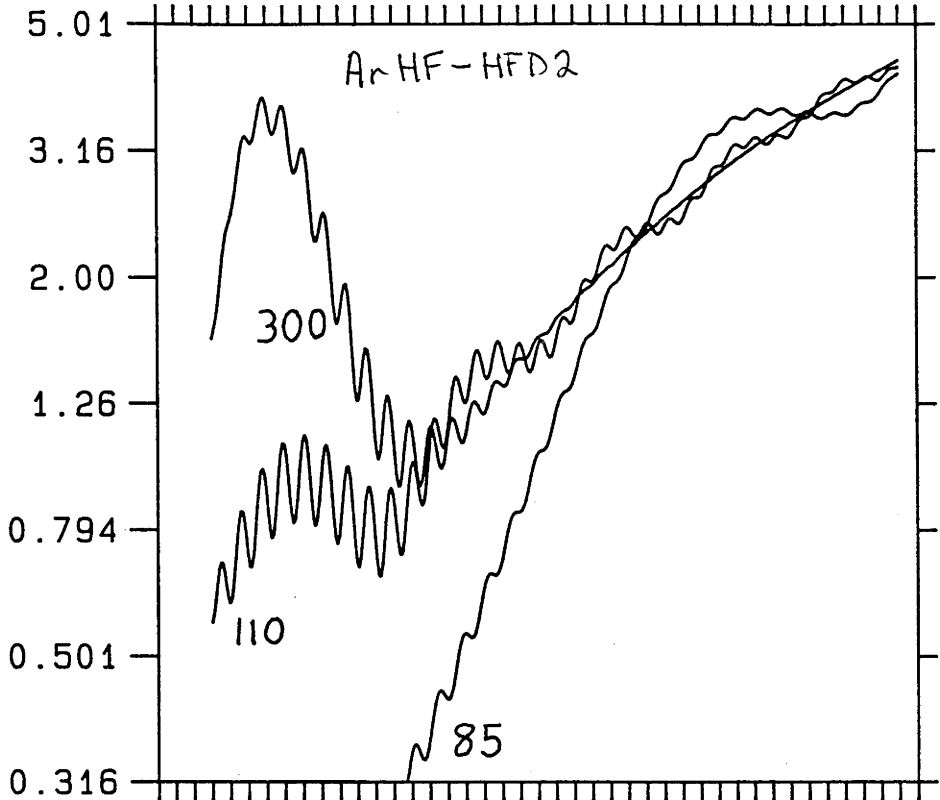
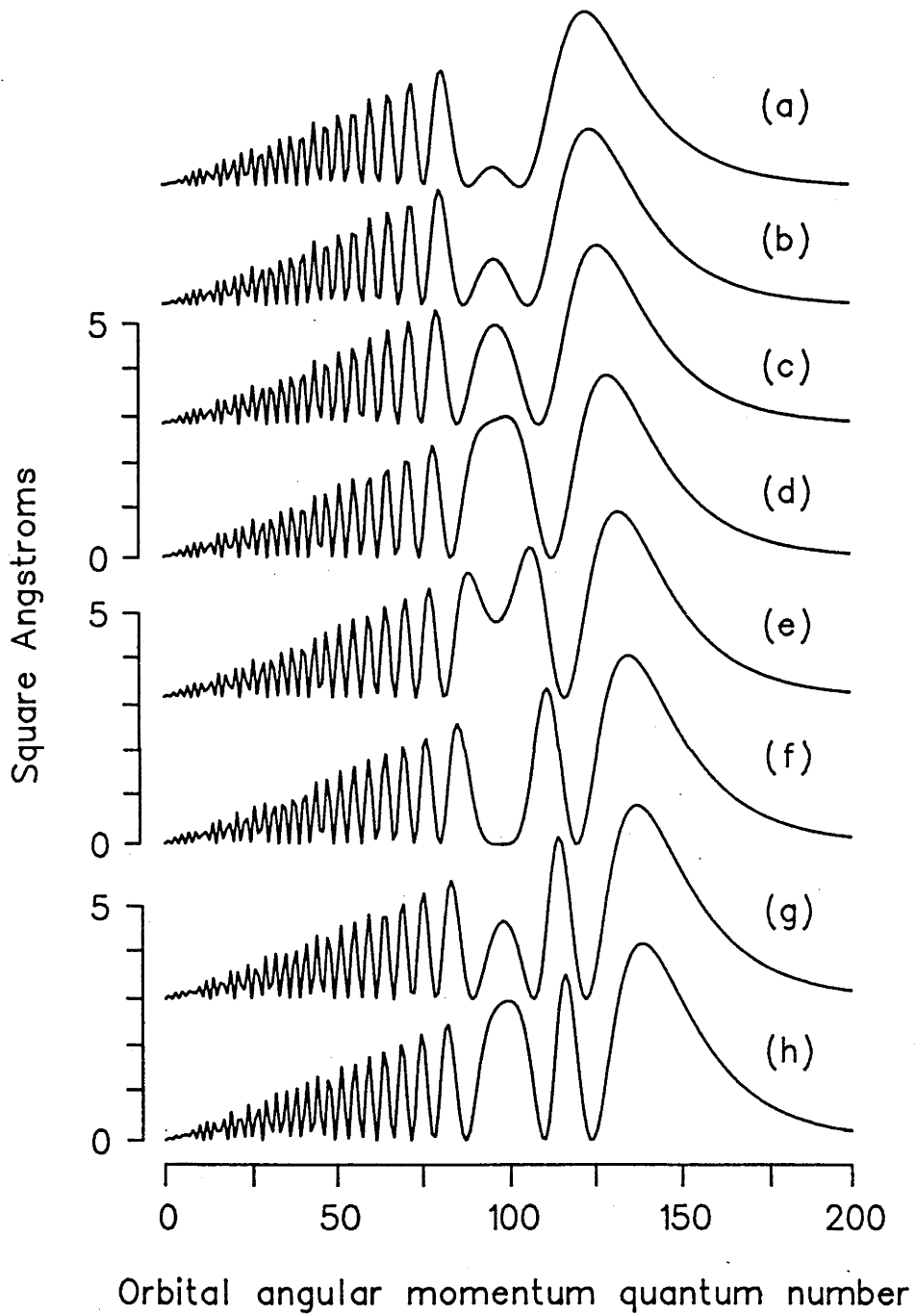


Figure 5.24

of the attractive well.

In Section 5.4 we discussed the behaviour of the integral cross sections computed for the three interaction potentials, using the IOS approximation, as a function of the potential angle γ (see Figure 5.10). These results were obtained at a fixed collision energy whilst varying the spherical interaction potential (by changing the value of γ) used to calculate the cross sections. As the potential angle is varied from $\gamma=90^\circ$ to $\gamma=0^\circ$, the angular slice of the potential surface used in the calculation deepens significantly (see Figure 5.5). As expected, an overall increase is seen in the integral cross sections as the potentials become more attractive. For all three potentials, however, a maximum occurs in the integral cross sections between $\gamma=45^\circ$ and $\gamma=0^\circ$. A study of the opacities corresponding to these integral cross sections was made for the ArHF-HFD2 potential for values of γ between 90° and 0° . The results of this study are shown in Figure 5.25. Curves (a) through (h) correspond to γ going from 90° to 0° . Notice (1) that the oscillations between $l=0$ and about 80, which are determined by the repulsive part of the potential, do not change significantly, and (2) that as the potential deepens (in going from (a) to (h)) new peaks are seen to develop near $l=100$. These peaks subsequently divide and separate, making way for more new peaks. The maximum in the ArHF-HFD2 integral cross section at a potential angle of $\gamma=41^\circ$ (see Figure 5.10) corresponds to the opacity function labelled (e) in Figure 5.25. Local maxima will be seen in the integral cross sections as the new peaks begin to separate and the area under them (ie. their contribution to the integral cross section) goes through a maximum. Oscillations in the integral cross section as a function of energy, referred to as glory

Ar HF-HFD2 10S

Figure 5.25

oscillations, are also related to the creation and division of new peaks in the opacity functions.

We are now in a position to relate the behaviour of the state-to-state differential cross sections to the opacities given in Figures 5.21, 5.22 and 5.23. Consider first the elastic cross sections shown in Figures 5.18, 5.19 and 5.20. As noted earlier in this section, the shapes of the $0 \rightarrow 0$ cross sections for the ArHF-HFD2 and M5 potentials differ from the other elastic cross sections for these potentials in that they do not fall away as rapidly or as much after the primary rainbow peak before increasing again at large angles. The investigations reported in the preceding paragraphs suggest that the enhancement of these elastic cross sections on the large angle side of the rainbow results primarily from collisions described by orbital angular momentum quantum numbers near $l=100$, which is where the new peaks are generated. The areas under the opacity curves near $l=100$ are larger for the $0 \rightarrow 0$ transitions than for the $1 \rightarrow 1$ transitions for both the ArHF-HFD2 and M5 potentials. This is clearly not the case for the ArHF-HFD1 potential (see Figure 5.21) for which the $0 \rightarrow 0$ and $1 \rightarrow 1$ differential cross sections differ only slightly.

Lastly, we consider the behaviour of the inelastic cross sections. Both the $0 \rightarrow 1$ and $1 \rightarrow 0$ opacity functions shown in Figures 5.21, 5.22 and 5.23 are double peaked, with most of the scattering resulting from the peaks centred around $l=100$. The dynamics of the Ar-HF interaction are therefore such that collisions for which the distance of closest approach coincides with the attractive bowl of the potential can readily cause transitions between the HF rotor states $j=0$ and $j=1$. The energy difference between these states is 59 K (5.1 meV), as compared to the collision energy of

1493 K (128.6 meV). Opacities for the other inelastic processes, including those for $j_{\text{initial}}=2$ and 3 not shown in the figures, were found to have negligible contributions for values of l greater than 80. These processes therefore correspond to scattering off the repulsive wall of the potential. The $0 \rightarrow 1$ and $1 \rightarrow 0$ opacities between $l=85$ and 120 are responsible for the rainbow peaks observed in the respective differential cross sections (see Figures 5.14, 5.15 and 5.16). That these rainbows are shifted to larger angles than the elastic rainbows reflects the different range of orbital angular momenta which contribute.

5.8 Conclusion

A detailed experimental and computational study of the scattering of HF from Ar has been reported in this chapter. The measured total differential cross section showed a clearly resolved primary rainbow oscillation. Coupled states, IOS and spherical potential calculations were carried out using the Ar-HF interaction potentials developed by Douketis et al. (1984) and Hutson and Howard (1982b). In summary, we found that:

(1) The coupled states, IOS and spherical potential total differential cross sections are all rather different. Consequently, we chose to use the coupled states approximation in making a comparison with the experimental data;

(2) Coupled states total differential cross sections predicted by the ArHF-HFD1 and ArHF-HFD2 potentials do not agree well with the measured scattering intensities. The M5 potential, however, gives rather good agreement. Of the available interaction potentials for Ar-HF which correctly predict the known spectroscopy for the Ar-HF and Ar-DF systems, namely the M5 and ArHF-HFD2 surfaces, we recommend the M5 potential for its ability to also reproduce the measured total differential scattering intensities;

(3) The relative state-to-state integral cross sections for Ar-HF measured by Barnes et al. (1982) are in surprisingly good agreement with our calculated values. Unfortunately, the three potentials considered in these investigations all predict similar inelastic integral cross sections, making it difficult to reliably distinguish between these potentials on the basis of such measurements.

(4) The calculated total differential cross sections for HF molecules

in a given initial rotational state colliding with Ar atoms depend significantly upon both the interaction potential used and the initial state. There are two factors responsible for this behaviour. Firstly, the shapes of the various elastic differential cross sections differ considerably, and secondly, the $0 \rightarrow 1$ transitions make a large contribution to the $0 \rightarrow \sum j'$ cross sections, whereas the other $j \rightarrow \sum j'$ cross sections are dominated by elastic processes. The different shapes of the elastic cross sections are related to the behaviour of the interaction potentials in the region of the minimum.

Lastly, we compare the magnitudes of the inelastic differential cross sections obtained for He-HF with those obtained for Ar-HF. In Figures 4.8 and 5.17 are given the population weighted differential cross sections for the He-HF HFD1 potential and for the Ar-HF M5 potential respectively. These cross sections have not been multiplied by $\sin\theta \cdot \theta^{4/3}$. Notice that the $0 \rightarrow 1$ cross section for Ar-HF is about two orders of magnitude larger than that for He-HF for small laboratory scattering angles, although their magnitudes are rather similar at large angles. The large value of the $0 \rightarrow 1$ cross section for Ar-HF at small angles is the result of the primary rainbow peak, and is therefore associated with the relatively strong attraction of the Ar-HF potential.

Chapter SixInfrared Spectroscopy of Small Clusters of Acetylene,Methyl Acetylene and Ethylene

In this chapter we present and discuss the results of a study of the infrared spectra of small van der Waals clusters of acetylene ($\text{H-C}\equiv\text{C-H}$), methyl acetylene ($\text{H-C}\equiv\text{C-C}\langle\text{H}_3$) and ethylene ($\text{H}_2\rangle\text{C}=\text{C}\langle\text{H}_2$). In all cases the colour centre laser was used to interrogate supersonic molecular beams of dilute mixtures of the molecule of interest in helium, and bolometric detection was used to monitor the resulting change in the molecular beam energy. After an introduction to the structure and spectroscopy of van der Waals molecules the following are discussed: the monomer spectra for acetylene, methyl acetylene and ethylene; the experimental techniques used in the present studies; the results obtained for acetylene clusters; the results for methyl acetylene van der Waals molecules; those for the ethylene system; and the significance of our results in the light of the current knowledge of these and other van der Waals molecules.

6.1 Introduction

In recent years there have been large numbers of experimental and theoretical studies of the properties of van der Waals molecules. The structures of many weakly bound clusters have been accurately determined and their dynamical behaviour upon laser excitation has been investigated. Reviews of such investigations have been given by Janda (1985), Gentry (1984), Cassasa et al. (1984), Levy (1981), Beswick and Jortner (1981) and Le Roy (1984). In this introduction we discuss the techniques used to study van der Waals molecules and summarize a number of the more important experimental and theoretical findings.

Both cooled, low pressure gas cells and supersonic molecular beam techniques can be used to create useful concentrations of van der Waals molecules. In the former case, either Fourier transform, Stark or other spectroscopic techniques are available to study the species of interest. See, for example, the results obtained by Pine and Lafferty (1983) and Pine et al. (1984) for HF and DF dimers, the studies of acetylene clusters by Pendley and Ewing (1983), the work on the OC-HF dimer by Kyrö et al. (1983), the study of the HCl dimer by Ohashi and Pine (1984) and the investigations by Mc Keller (1982) of the Ar-H₂ complex. By forming a supersonic expansion of a suitable gas mixture it is possible to obtain isolated van der Waals clusters at temperatures as low as a few Kelvin, resulting in reduced rotational congestion in the observed spectra. Almost invariably, however, the beam will contain a wide range of cluster sizes, which may complicate the interpretation of the spectra. Such difficulties are discussed by Cassasa et al. (1983,1984) in relation to their studies of clusters containing both HF and C₂H₄.

A variety of methods can be used to interrogate a cluster containing molecular beam. In most cases one first irradiates the beam with suitable radiation (radio frequency, microwave, infrared or visible) and then observes either: (1) the radiation emitted by the excited molecules, (2) the change in total molecular beam energy (using bolometric detection), or (3) the depletion of a given mass component of the beam (via mass spectrometry). From such studies one hopes to obtain spectra of the clusters of interest interacting with the exciting radiation. Both the degree of resolution and the nature of the interactions determine the amount of information which can be extracted from the spectra. By fitting to a resolved rovibrational spectrum, or a partially resolved rovibrational contour, the effective rotational constants of the van der Waals molecule can be obtained. The structure of a cluster can often be inferred from such constants. Alternatively, one can compare a measured spectrum with that predicted using an existing potential in order to assess the goodness of the latter in describing the interaction.

Of the techniques used to investigate van der Waals molecules (with typical examples given in parentheses) are: (1) conventional gas cell absorption or Fourier transform spectroscopy (used by Mc Keller (1982) to measure the infrared spectrum of Ar-H₂); (2) Stark spectroscopy (Legon (1983) and Legon and Millen (1982) discuss the method); (3) pulsed molecular beam Fourier transform microwave spectroscopy (discussed by Legon (1983) and Balle et al. (1979,1980), and used by workers at the Noyes Chemical Laboratory, the University of Illinois, to characterise (methylacetylene)-HF, benzene-HF, HCN-HBr, HCN-C₂H₄, HCN-Kr, HCN-C₂H₂ and OC-HCl); (4) molecular beam electric resonance spectroscopy (as used by Klemperer and co-workers at Harvard University to study Ar-HF, C₆H₆-HF, H₂CO-HF,

$\text{CO}_2\text{-HF}$, $\text{N}_2\text{O-HF}$ and NH_3 containing complexes, and by Gutowsky et al. (1985) to study HF-HF); (5) laser induced fluorescence spectroscopy (used by Janda and co-workers at the California Institute of Technology to study Ne-Cl_2 and Ne-Br_2 , and by Levy and co-workers at the University of Chicago to study He-I_2 , He-NO_2 , Ar-I_2 and clusters containing either *s*-tetrazine or trans-stilbene); (6) gas cell Raman spectroscopy (used by Maroncelli et al. (1985) to study HCN clusters); (7) two colour time-of-flight mass spectroscopy (as used by Law and Bernstein (1985) in the study of (n-propyl benzene)-(small alkane) clusters); (8) laser-induced dissociation spectroscopy, by monitoring an excited molecular beam using a mass spectrometer (used by Janda and co-workers at the California Institute of Technology to study many ethylene containing clusters using a CO_2 laser, by Gentry and co-workers at the University of Minnesota to investigate both OCS and ethylene containing clusters, also using a CO_2 laser, and by Lee and co-workers at the University of California, Berkeley, to record infrared spectra of $(\text{NH}_3)_2$, $(\text{H}_2\text{O})_2$ and benzene clusters); and (9) laser-induced dissociation spectroscopy using a bolometer detector to monitor the molecular beam energy (pioneered by Gough et al. (1977,1978,1981) and used by Miller and Watts and co-workers at the Australian National University, using a colour centre laser, to study $(\text{CH}_3\text{F})_n$, $(\text{CH}_3\text{Cl})_n$, $(\text{CH}_3\text{Br})_n$, $(\text{C}_2\text{H}_2)_n$, $(\text{C}_3\text{H}_4)_n$, $(\text{C}_2\text{H}_4)_n$, $(\text{CO}_2)_n$, $(\text{N}_2\text{O})_n$, substituted ethene clusters, $(\text{H}_2\text{O})_n$ and $(\text{HF})_2$ and $(\text{HF})_3$).

The dynamics of an excited van der Waals molecule (ie. the rate at which the initial state decays, possibly leading to rupture of the van der Waals bond, and the mechanisms by which it does so) are not easily determined experimentally. Frequency domain measurements which yield the degree of homogeneous broadening present in a spectrum enable a lower bound

to be placed upon the lifetime of the decaying state, although little knowledge is gained about the decay mechanism. Information about the distribution of the available energy amongst the fragments resulting from the dissociation of a van der Waals cluster can be obtained from measurements of the velocity and angular distributions of the fragments. Experiments of this kind have been reported by Hoffbauer et al. (1983d) and Bomse et al. (1983) for $(C_2H_4)_2$, by Vernon et al. (1981) and (1982a,1982b) for benzene dimers and H_2O clusters, and by Hoffbauer et al. (1983c) and (1984) for OCS and methanol dimers respectively. In all cases it was found that most of the available energy appeared as internal excitation of the fragments, rather than as relative translational kinetic energy. These results are in qualitative agreement with the approximate treatments of van der Waals predissociation given by Ewing (1979a,1979b,1982) and Beswick and Jortner (1977,1978,1981), often referred to as the "momentum gap" and "energy gap" models, respectively. The models predict that the dominant pathways are those which minimize the total translational kinetic energy, (or the total linear momentum), of the products. Because the dynamics of the dissociation process are very sensitive to the details of the interaction potential, these and other approximate techniques are only qualitatively useful in describing the behaviour of an excited cluster. To obtain accurate (quantitative) estimates of effective rotational constants and lifetimes of van der Waals molecules from a given interaction potential, one must solve the relevant Schrödinger equation. Such calculations are time consuming and complicated and have only been done for a few simple systems for which suitable potential surfaces exist. Of the systems which have been studied using exact close-coupling methods are Ar- H_2 (Kidd and Balint-Kurti (1985), Le Roy et al. (1982), Hutson et al.

(1983) and Hutson and Le Roy (1983)), Ar-HCl (Ashton et al. (1983), Hutson et al. (1985)), and HF-HF (Halberstadt et al. (1986)). The results of a quasiclassical trajectory study of Ar-OCS by Gibson and Schatz (1985) suggest that "neither dissociation nor energy transfer is important in the dynamics of ArOCS clusters excited with two quanta of bend excitation on a time scale of at least 15 ps and very likely 100 ps". Should this be true, then the 5.3 ps lifetime obtained by Hoffbauer et al. (1983b) from linewidth measurements may be caused by processes other than dissociation or energy transfer. Further calculations may lead to a better understanding of the dynamics of this system.

Only recently, Mitchell et al. (1985) reported time-resolved measurements of the predissociation lifetime of the ethylene dimer. They concluded that dimers excited near the ν_7 mode of the monomer (near 950 cm^{-1}) dissociate in less than 10 ns. By comparing the results of such high resolution time domain measurements with the lifetimes corresponding to the homogeneous linewidths obtained from experiments in the frequency domain, our understanding of the dynamics of excited van der Waals clusters should certainly increase.

A detailed review of the many documented experimental and theoretical studies of van der Waals systems is beyond the scope of this thesis. In the remainder of this introduction we discuss primarily the dynamics and infrared spectra of ethylene and acetylene containing clusters.

As noted above, information on the rate of relaxation of an initially excited state can be obtained from the homogeneous broadening present in the observed spectrum. Infrared spectra have been measured for a number of ethylene containing clusters in the vicinity of the ν_7

out-of-plane wagging mode of the ethylene monomer near 950 cm^{-1} . Cassasa et al. (1981) and Western et al. (1984) reported spectra for $(\text{C}_2\text{H}_4)_n$, $n=2,3,5,7$, $\text{C}_2\text{H}_4\text{-Ne}$, $\text{C}_2\text{H}_4\text{-Ar}$ and $\text{C}_2\text{H}_4\text{-Kr}$; Cassasa et al. (1983) studied $\text{C}_2\text{H}_4\text{-HCl}$, $\text{C}_2\text{H}_4\text{-HF}$ and $\text{C}_2\text{H}_4\text{-NO}$; Bomse et al. (1983) considered the speed and angular distributions of the fragments resulting from the dissociation of ethylene clusters; and Hoffbauer et al. (1983d) obtained both infrared spectra and product distributions for C_2H_4 clusters and their deuterated analogues. In all of the above experiments, a CO_2 laser was used to excite a cluster containing molecular beam, and mass spectrometric detection was used to monitor the resulting dissociation. Continuous molecular beam and laser techniques were used for all but the studies by Hoffbauer et al. (1983d), for which pulsed methods were used. Homogeneous broadening effects were found to dominate the observed spectra for $(\text{C}_2\text{H}_4)_n$ clusters. Lifetime estimates obtained from these homogeneous widths are all less than 1 ps. Hole burning studies by Hoffbauer et al. (1983d) confirm that homogeneous broadening dominates these spectra. As noted previously, Mitchell et al. (1985) determined an upper bound of 10 ns for the lifetime of the C_2H_4 dimer excited near 950 cm^{-1} .

The spectra of $\text{C}_2\text{H}_4\text{-HCl}$, HF and NO are also dominated by homogeneous broadening, with corresponding lifetimes of a few picoseconds. Although revealing inhomogeneous structure, the spectra measured for $\text{C}_2\text{H}_4\text{-Ar}$, Ne are also homogeneously broadened, with corresponding lifetime estimates of 1.7 and >10 ps. In short, ethylene-containing clusters excited near 950 cm^{-1} seem to relax within picoseconds.

Hoffbauer et al. (1983d) and Bomse et al. (1983) have also shown that, upon dissociation, most of the available energy appears as internal excitation of the products, rather than as translational kinetic energy.

As discussed earlier, this behaviour is typical of many van der Waals molecules, and is in accord with the energy and momentum gap models of predissociation.

In another study of ethylene cluster containing molecular beams, using a CO₂ laser to excite the clusters near 950 cm⁻¹ and a bolometer to monitor the molecular beam, Baldwin and Watts (1986) observed a net dissociation signal resulting from cluster dissociation. A broad, featureless band was obtained. A similar study of ethylene clusters was carried out by Fischer *et al.* (1983) using a colour centre laser to excite the clusters near 3000 cm⁻¹. These studies also reveal what appear to be predominantly homogeneously broadened bands.

Whilst the results discussed above suggest that the ethylene dimer bands observed near 950 cm⁻¹ are dominated by homogeneous broadening, Huisken *et al.* (1986) reported spectra of the ethylene dimer near 950 cm⁻¹ in which considerable inhomogeneous structure is seen. The situation near 3000 cm⁻¹ is also unclear. Liu *et al.* (1984) studied the ethylene dimer near 3000 cm⁻¹ with a resolution of 0.5 cm⁻¹, and the observed bands show significant inhomogeneous rotational structure. The full widths at half maxima of the bands are about 5 cm⁻¹, as observed by Fischer *et al.* (1983). It appears as if both homogeneous and inhomogeneous effects may be important in determining the band shapes of small ethylene cluster absorptions. The differences in the measured spectra may in part result from the use of different beam conditions, and hence different temperatures and/or cluster size distributions.

In summary, the spectra of ethylene containing clusters all

exhibit considerable homogeneous broadening, suggesting the existence of highly efficient mechanisms by which the excited states decay. The nature of the relaxation pathways, and whether or not they lead directly to dissociation, will depend crucially upon the details of the interaction potential, the energy of the initial state relative to the van der Waals bond, and the number of states, both of the bound cluster and of the free products, through which the excited state can decay. Possible decay mechanisms have been discussed by Gentry (1984), Cassasa *et al.* (1984) and Janda (1985).

In this chapter we describe an experimental study of the infrared spectra of clusters of acetylene, methyl acetylene and ethylene between 3050 and 3350 cm^{-1} . A detailed investigation of the acetylene system was made, in the hope of gaining a better understanding of the processes occurring in excited van der Waals molecules. The density of available states in both the acetylene monomer and dimer is lower than for the similar, much studied, ethylene system. As a result one may expect the dynamical behaviour of these systems to differ. Another reason for studying acetylene was the existence of a potential surface (Sakai, Koide and Kihara (1977)) which has been used in a study of the infrared absorption spectra of $(\text{C}_2\text{H}_2)_2$ and $(\text{C}_2\text{D}_2)_2$ between 500 and 2200 cm^{-1} . In this study, Pendley and Ewing (1983) observed five dimer bands (three for C_2H_2 and two for C_2D_2) in the form of unresolved rotational contours. The band shapes measured are not inconsistent with the most likely dimer structure predicted by the Kihara potential. The anomalous shape of one of the bands was attributed to the existence of a fast vibrational energy

transfer process.

6.2 Monomer Spectroscopy

Monomer absorptions for acetylene, methyl acetylene and ethylene, in the vicinity of 3000 to 3300 cm^{-1} are given in Table 6.1. For acetylene and ethylene the ν_1 modes are infrared inactive in the monomer. The lower symmetry of the methyl acetylene molecule results in a strong infrared absorption at the ν_1 $\equiv\text{C-H}$ stretching frequency. The infrared spectrum of ethylene clusters has been measured and assigned by Fischer et al. (1983). Centre frequencies of the cluster bands for ethylene clusters (Fischer et al. (1983)) and methyl acetylene clusters (reported in this thesis) also appear in Table 6.1. Notice that the ν_1 mode, which is infrared inactive in the monomer, appears in the cluster spectra as a result of the asymmetry introduced by cluster formation. Frequencies of the assigned modes are all shifted to the red of the corresponding monomer frequencies.

In the case of acetylene, the ν_3 mode is in Fermi resonance with the $\nu_2+\nu_4^1+\nu_5^1$ combination mode and the frequencies reported in the table are those resulting from the resonance. The acetylene cluster spectra reported in the following sections are all shifted 10 to 50 cm^{-1} to the red of these resonating modes. It is likely that the cluster absorptions result from excitations of the monomer units within the cluster which are similar in character to the ν_3 or $\nu_2+\nu_4^1+\nu_5^1$ monomer modes.

For methyl acetylene there exists a Fermi resonance between ν_2 and $2\nu_7$, as indicated in the Table 6.1. The spectra reported in this thesis for methyl acetylene are shifted some 5 to 80 cm^{-1} to the red of the ν_1 monomer mode at 3334 cm^{-1} . Qualitatively, the spectra measured for acetylene and methyl acetylene are quite similar. Given that both spectra result from the acetylenic $\equiv\text{C-H}$ stretching mode (and possibly the

Table 6.1

(a) Acetylene $\text{H-C}\equiv\text{C-H}$ symmetry = $D_{\infty h}$

mode	type	description	band centre (cm^{-1})
ν_1	Σ_g^+	sym CH stretch	3374 (inactive)
ν_3	Σ_u^+	asym CH stretch	3294.9
$(\nu_2+\nu_4^1+\nu_5^1)$			3281.9

note: ν_3 is in Fermi resonance with $\nu_2+\nu_4^1+\nu_5^1$. The frequencies given in the Table are the result of this resonance.

(b) Ethylene $\text{H}_2>\text{C}=\text{C}<\text{H}_2$ symmetry = D_{2h}

mode	type	description	band centre (cm^{-1})	cluster band (cm^{-1})
ν_1	A_g	sym CH_2 stretch	3026 (inactive)	3013
ν_5	B_{1g}	asym CH_2 stretch	3103	-
ν_9	B_{2u}	CH_2 wag	3105.5	3100
ν_{11}	B_{3u}	sym CH_2 stretch	2988.7	2982
$\nu_2+\nu_{12}$	B_{3u}	-	3099	3073

(c) Methyl Acetylene $\text{H-C}\equiv\text{C-C}<\text{H}_3$ symmetry = C_{3v}

mode	type	description	band centre (cm^{-1})	cluster bands (cm^{-1})
ν_1	A_1	sym CH stretch	3334	A_1 3331 A_2 3328.7 A_3 3326.5 Y 3318 X 3302
ν_2	A_1	sym CH_3 stretch	2941	
$(2\nu_7)$			2881	
ν_6	E	degenerate sym CH_3 stretch	3008.3	

note: ν_2 is in Fermi resonance with $2\nu_7$. The two frequencies given are those resulting from the resonance.

$\nu_2 + \nu_4^1 + \nu_5^1$ mode in the case of acetylene), this similarity is not surprising.

In the following sections we present and discuss the results of our studies of van der Waals molecules.

6.3 Experimental

The experimental techniques used in this thesis have been described in Chapter 2. In this section we summarise and discuss the experimental methods used to study van der Waals molecules.

All of results reported in this chapter were obtained using beams formed from supersonic expansions of low concentrations of the molecules of interest in helium. The mixtures were expanded through a nozzle with a circular aperture about 40 μm in diameter maintained at a temperature of 310 K. A single skimmer was used to collimate the expansions, resulting in a beam profile with a full width at half maximum of about two degrees. By varying the concentration of the molecule of interest in helium and the stagnation pressure of the gas in the nozzle, it is possible to alter both the range of cluster sizes produced in the expansion and their effective temperature. For a given gas mixture, the degree of condensation and cooling increases with increasing stagnation pressure. By using a low concentration of the gas of interest in helium, and a high pressure to form the expansion, one obtains a beam composed primarily of small clusters at very low effective temperatures (ie., <5 K).

An electron impact ionization quadrupole mass spectrometer was used to monitor the cluster composition of the beams (see Chapter 2). It must be stressed measurements of this kind give only an indication of the cluster size distribution. The severe fragmentation resulting from electron bombardment of the weakly bound van der Waals molecules makes the quantitative interpretation of such spectra difficult, if not impossible. Buck and Meyer (1984) used differential scattering techniques to investigate the fragmentation patterns obtained from the electron

bombardment of argon clusters. They found that roughly half of the ionized dimers and trimers were detected at the monomer mass, with only a slight dependence upon the electron energy over the range 30 to 100 eV. Almost no trimers were detected at the trimer mass, indicating the catastrophic nature of the ionization process for weakly bound complexes. For all the gas mixtures used in the van der Waals studies reported in this chapter, the mass spectrometer showed no signs of any impurities which may have affected the interpretation of the results.

Infrared spectra were obtained in the region 3200 to 3350 cm^{-1} using the colour centre laser. The laser-induced change in the molecular beam energy were measured using the bolometer detectors described in Chapter 2. Parallel gold coated mirrors were used to obtain multiple near-orthogonal laser - molecular beam crossings. Figure 6.1 shows the positions of the bolometer and the multipass mirrors in relation to the rest of the beam apparatus. In all cases the laser output was modulated using a 50% duty cycle rotating chopper and phase sensitive detection was used to monitor the bolometer output. A 50 cm focal length CaF_2 lens was used to focus the laser radiation to a waist of about 0.5 mm at the laser - molecular beam intersection. When the laser frequency coincides with a monomer absorption, the excited monomers remain in the beam until they reach the bolometer, and one observes an increase in the signal. If one excites a van der Waals molecule, one of three things may happen: (1) the cluster may be able to accommodate the energy and reach the bolometer intact, resulting in an increased signal; (2) the cluster may dissociate and the fragments remain in the beam, also resulting in an increased signal; or (3) the van der Waals molecule may dissociate sufficiently violently that the fragments do not remain in the beam, resulting in a

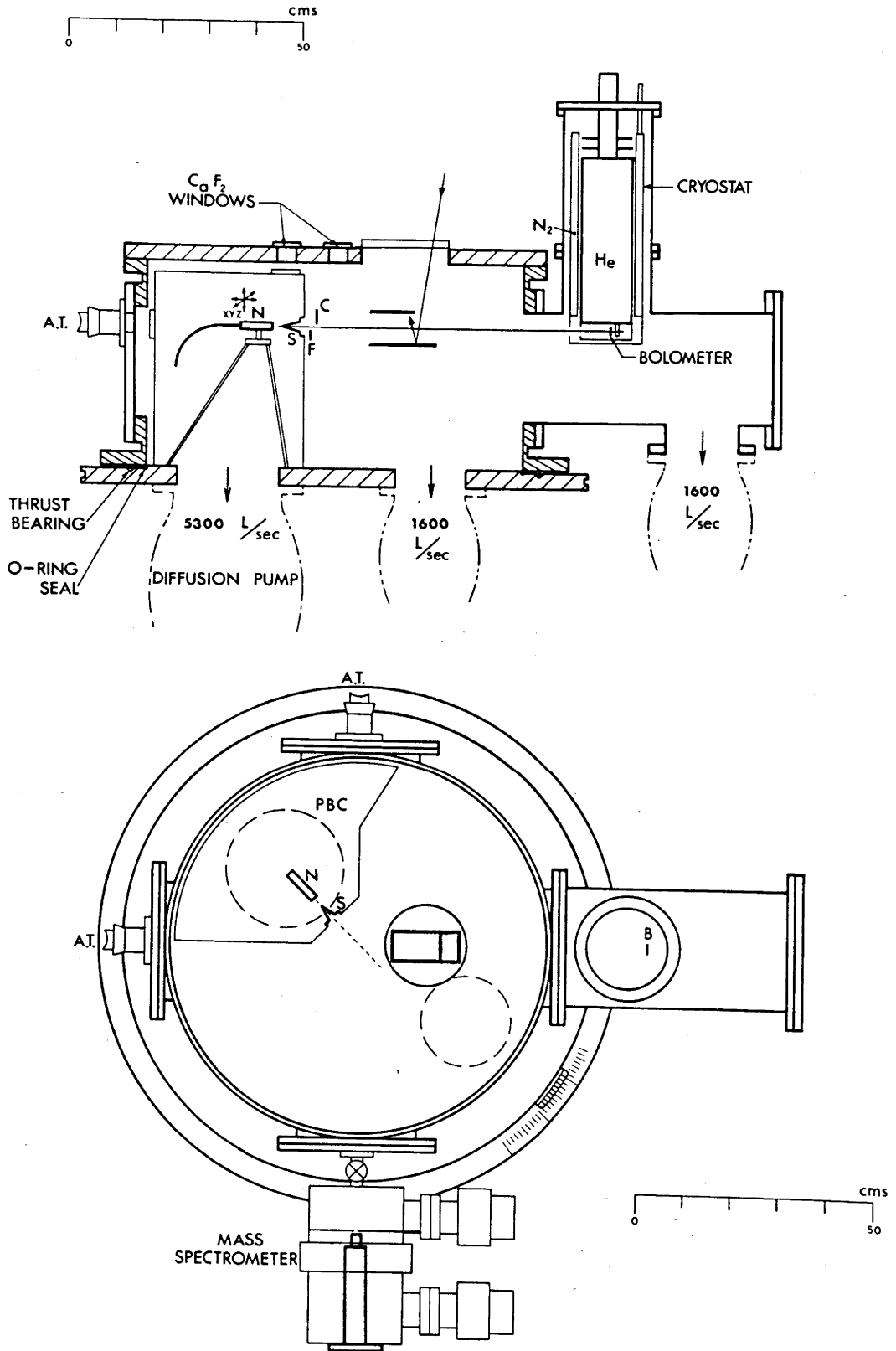


Figure 6.1

smaller bolometer signal. In practice, one obtains a spectrum which is a superposition of the spectra of all the species (monomers and clusters) present in the molecular beam. All of the infrared spectra reported in this chapter have been plotted so that a laser-induced decrease in the total molecular beam energy, as measured using the bolometer, corresponds to an upward going signal. Monomer absorptions are therefore seen as sharp, downward going features.

As described in Chapter 2, the colour centre laser can be used in either high or low resolution modes. When operated without the intracavity etalon, a number of longitudinal modes lase simultaneously. By rotating the grating one can scan the lasing modes across the tuning range of the crystal. A stepping motor was used to rotate the grating and a Grubb-Parsons monochromator was used to calibrate the spectra to within about 0.5 cm^{-1} . Although the overall resolution of such scans is about $1/3 \text{ cm}^{-1}$, the lasing modes have linewidths of about 1 MHz. This means that spectral features far narrower than the overall resolution can appear in a low resolution spectrum if, as the laser hops across the cavity modes, there are coincidences between the lasing modes and the said features.

By installing an intracavity etalon the laser can be scanned single mode through about 0.07 cm^{-1} (2000 MHz) at a time (see Chapter 2). In this case the laser linewidth is again 1 MHz, but the overall resolution is determined by the Doppler broadening resulting from the range of velocities present in the molecular beam and the geometry of the laser - molecular beam crossing. A single orthogonal laser - molecular beam crossing results in an effective resolution of about 4 MHz (as determined from the monomer absorption lineshape). The overall resolution obtained using the multipass mirrors is typically about 10 to 15 MHz. As described

in the next section, however, it is possible to deconvolute the Doppler broadening present in a given high resolution spectrum. A 150 MHz free spectral range confocal etalon was used to calibrate the high resolution scans.

The spectra and frequency markers were recorded using a Commodore microcomputer, with up to 2000 points per scan. The time constant and roll-off controls on the lock-in amplifier were chosen to reduce the noise on the bolometer signal to manageable levels. Most of the spectra reported in this chapter were recorded using bolometer B. Useful spectra having peak signals of about 0.5 μ V could be measured with this bolometer. By comparison, the total bolometer B signal resulting from a typical helium beam is about 100 to 200 mV. In comparing bolometer signal levels, however, it should be kept in mind that the bolometer operating point, which determines its responsivity, depends upon the total heat flux reaching the bolometer. As discussed in Chapter 2, this dependence was small for bolometer A and considerable for bolometer B for the range of load conditions typical of the molecular beam experiments discussed in this thesis.

6.4 Acetylene Clusters

6.4.1 Large clusters of acetylene

Initial investigations were performed using gas mixtures consisting of high concentrations (up to 20%) of acetylene in helium. Except at the lowest pressures, beams formed from such mixtures contain many large van der Waals clusters. Figure 6.2 shows the low resolution spectra obtained using an 11% mixture and bolometer A. Note that signals corresponding to both increases and decreases in the molecular beam energy are observed. The sharp negative features found at the higher frequencies correspond to increases in the molecular beam energy arising from the rotational structure associated with the ν_3 and $\nu_2+\nu_4^1+\nu_5^1$ bands of the acetylene monomer (see Section 6.2). On the other hand, the broad bands of opposite sign arise from vibrationally excited acetylene clusters which dissociate in a time which is shorter than their flight time from the laser crossing point to the bolometer, which is about 0.2 ms. This estimate of the flight time was obtained by assuming a speed of 1500 m/s over the distance of approximately 30 cm. Although time-of-flight distributions were not measured for these mixtures, we expect 1500 m/s to be within 10% of the actual speed.

A mass spectrum was also recorded at each of the source pressures represented in Figure 6.1. These spectra suggest that, at the lowest pressure indicated in the figure, the dimer, and possibly the trimer, were the only clusters present in any significant concentration. As the source pressure is raised, the proportion of larger clusters increases and the corresponding infrared spectrum shifts away from monomer frequencies

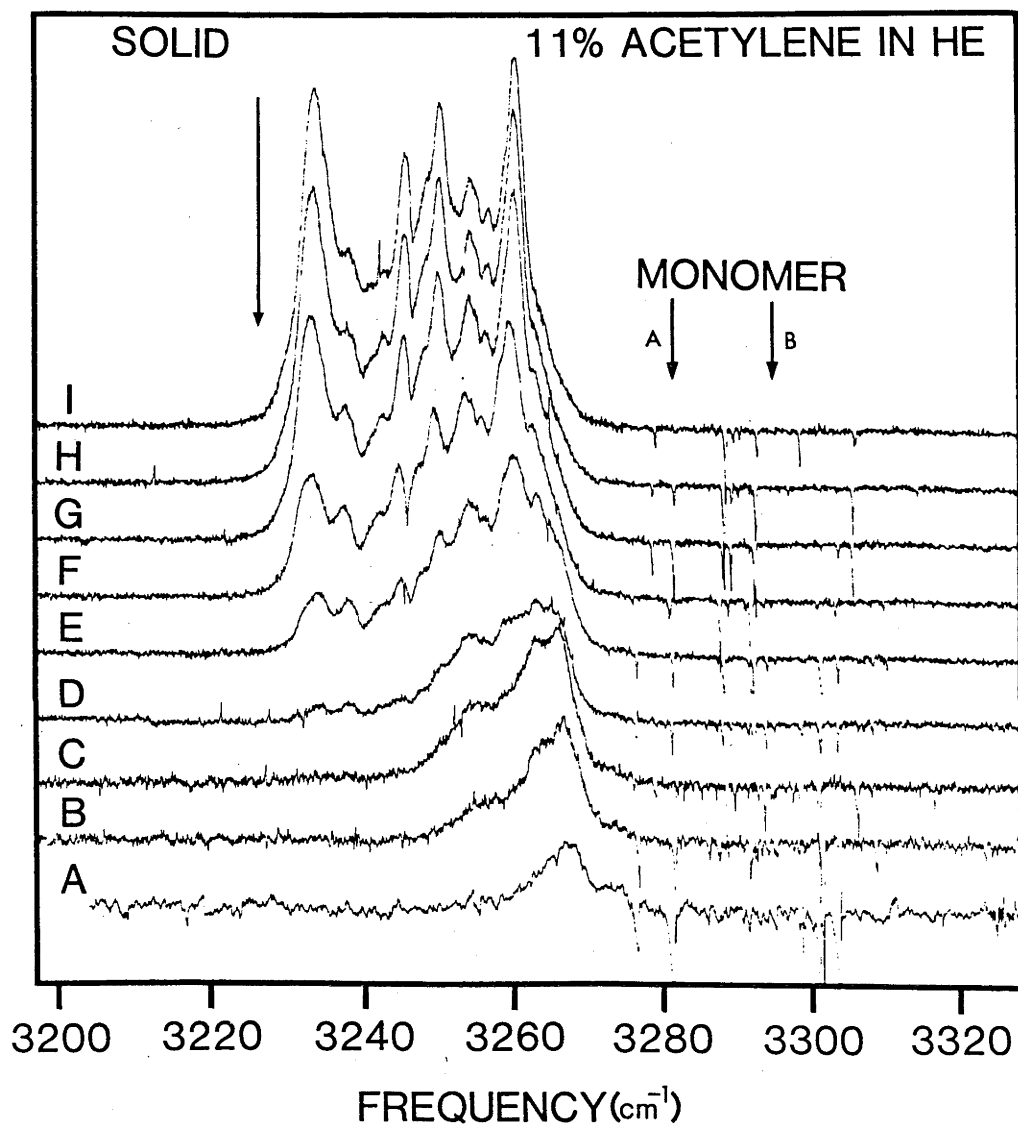


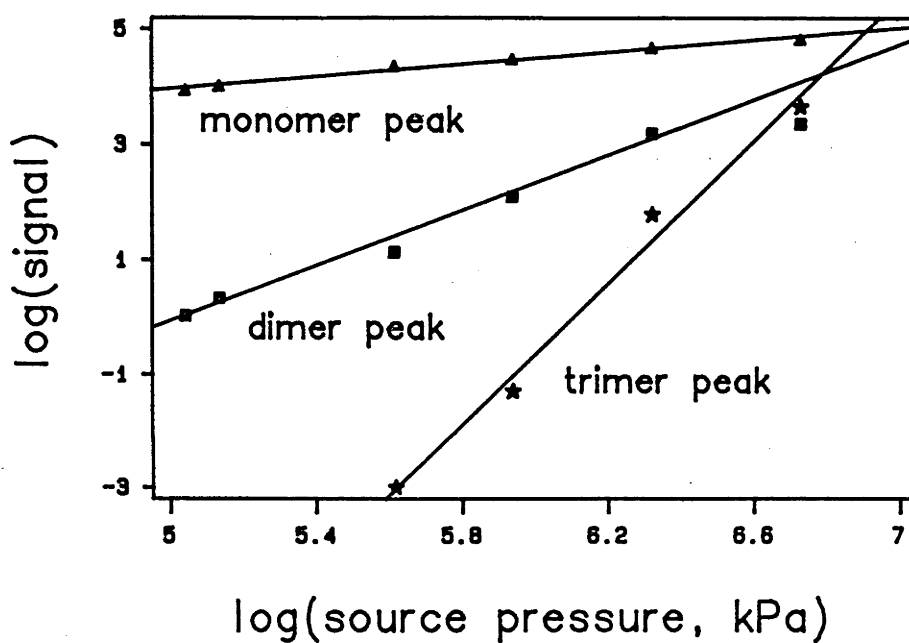
Figure 6.2

towards the frequency observed in the solid. The rich structure observed in the high pressure spectra is attributed to the overlap of features associated with a large range of cluster sizes. Even at the highest source pressure, the spectrum shows no features which are coincident with the solid state absorption. This suggests that either the molecular packing in the large clusters is different from that found in the solid, or that the maximum cluster size produced is such that surface effects remain important or both. Experimental and computational studies of N_2O clusters by Miller *et al.* (1984b) show that rather large clusters are required to obtain dissociation spectra with features coincident with the absorption frequency of the solid.

In view of the uncertainties inherent in interpreting electron impact ionization mass spectra, a study of the mass spectra of the 11% acetylene in helium mixture was carried out. The electron energy was set at 30 eV. Figure 6.3 shows the pressure dependence of the signals recorded at the monomer, dimer and trimer masses over the range 155 to 840 kPa, plotted on a log-log scale. Slopes of the lines of best fit are 0.5, 2.4 and 6.0 respectively. Similar slopes were obtained by Gough *et al.* (1981) for a 10% CO_2 in helium mixture. At the higher pressures the mass signals are expected to fall below the initial linear behaviour (on the $\log(\text{signal})$ vs $\log(\text{pressure})$ plot). Such a fall off is not clearly evident in Figure 6.3. Had we measured more points, or extended the range of pressures, we may have noticed such behaviour. The large slope of the trimer mass curve indicates a contribution from the fragmentation of larger clusters.

The data in Figure 6.3 were measured with a low mass resolution, so that a single peak about 3 or 4 amu wide was seen at each of the three masses. Under higher resolution, the signals at the dimer and trimer

11% acetylene in helium

**Figure 6.3**

masses were each found to consist of a number of separate peaks. Figure 6.4 shows the pressure dependence of the three mass peaks of highest intensity seen near the dimer mass. The slopes of the 49, 50 and 51 mass signals are 1.5, 1.7 and 4.2 respectively. Clearly, the mass 51 signal results from the fragmentation of clusters larger than the dimer. The ions corresponding to masses 49 through 51 are $[\text{C}_2\cdot\text{C}_2\text{H}]^+$, $[\text{C}_2\text{H}\cdot\text{C}_2\text{H}]^+$ and $[\text{C}_2\text{H}_2\cdot\text{C}_2\text{H}]^+$.

Figure 6.5 reproduces the low resolution infrared spectrum measured using the 11% mixture at 480 kPa, as well as spectra obtained using more dilute mixtures. In each case the source pressure was adjusted until the mass spectrometer indicated that few large clusters were present in the beam. It is seen that the infrared spectrum becomes considerably sharper as the concentration of acetylene is reduced and the source pressure increased. Since high source pressures and low concentrations favour the production of species with very low rotational temperatures, such behaviour suggests that the width of the overall spectrum is determined by a rotational contour. This suggestion is supported by the spectrum obtained using the 1% mixture, which shows structure resulting from individual rovibrational transitions. A more detailed discussion of this rotational structure is later in this chapter. By measuring the infrared absorption as a function of concentration and source pressure, as in Figure 6.5, one obtains valuable information about the principle source of broadening in a van der Waals spectrum. The data shown in the figure indicate that inhomogeneous broadening effects, resulting from rovibrational structure are more important than homogeneous broadening of the individual lines in determining the overall bandshape.

The spectra shown in Figure 6.5 for the 11% and 2.5% mixtures were

11% acetylene in helium

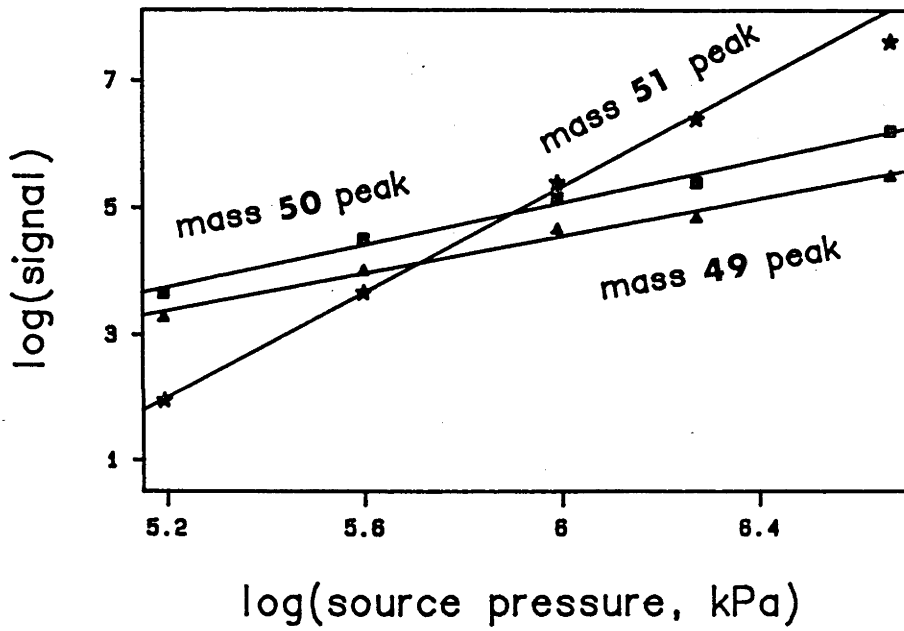


Figure 6.4

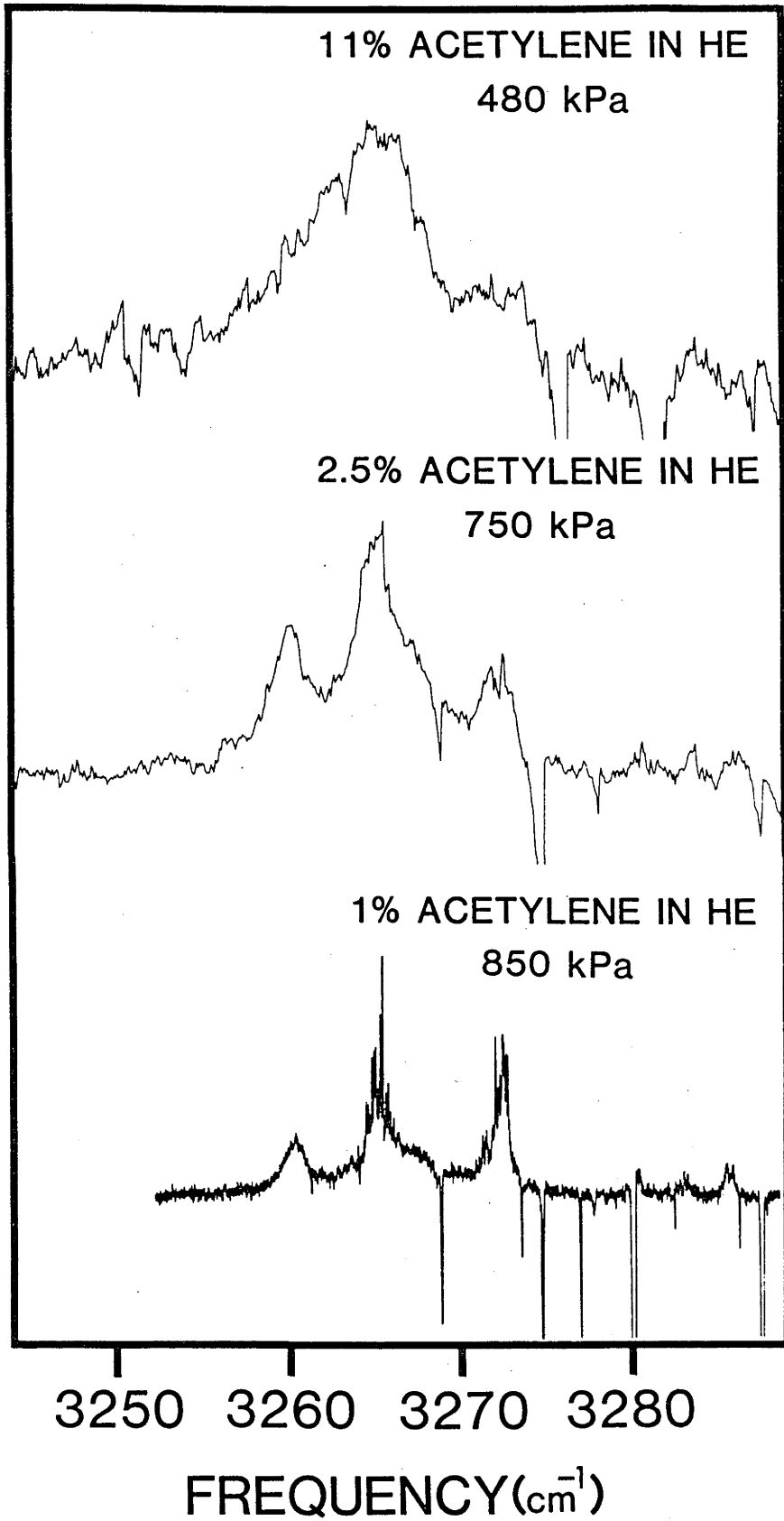


Figure 6.5

measured using bolometer A, whereas bolometer B was used for the 1% mixture. This may partly account for the differences between the spectra shown in the figure. In order to check this possibility, a more detailed study of the beam stagnation pressure and concentration dependence was carried out using bolometer B. Results of this study appear in Figure 6.6, with the following key giving the concentration/pressure values:

20% in He 400 kPa	10% in He 850 kPa	
20% in He 290 kPa	10% in He 380 kPa	2% in He 850 kPa
	10% in He 175 kPa	2% in He 500 kPa

a, b and c denote the positions of the three dominant bands seen in the 1% spectrum shown in Figure 6.5, with frequencies of approximately 3261, 3266 and 3272.5 cm^{-1} . The changes in the spectrum caused by varying the beam characteristics are clearly dramatic. Note that (1) the spectra narrow considerably with reduced concentration and pressure, (2) the spectrum of the 2% mixture at 850 kPa shows evidence of narrow structure in bands b and c, and (3) the relative intensities of the bands change considerably with pressure. Points (1) and (2) suggest that the bands represent inhomogeneously broadened rovibrational contours. The pressure dependence of the infrared band intensities, which is indicative of contributions from a range of cluster sizes, is discussed in more detail in a later section.

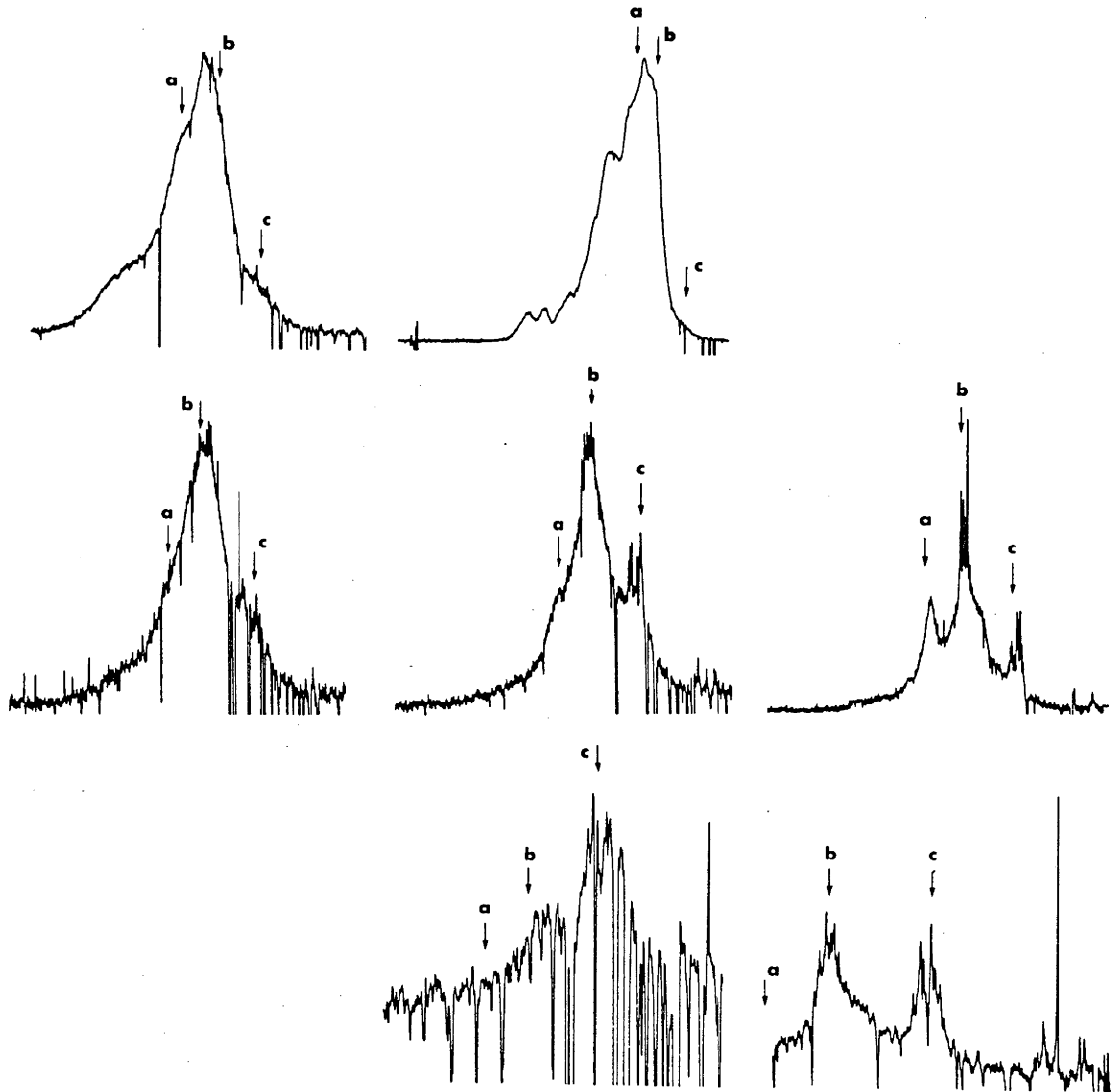


Figure 6.6

6.4.2 High resolution spectroscopy of small clusters of acetylene

In order to further our understanding of the dynamics leading to the infrared spectra of acetylene dimers and trimers, a detailed investigation of the behaviour of the 1% acetylene in helium mixture was undertaken. We first report the results of a high resolution spectroscopic study and then discuss the pressure dependence of both the mass spectrum and the infrared spectrum.

A low resolution spectrum of the 1% mixture is shown in Figure 6.7. Beam source pressures of 1100 to 1200 kPa were used to obtain this spectrum and all of the high resolution scans reported here for acetylene. Bands labeled A through F result from the dissociation of small acetylene van der Waals clusters. There is a striking difference between the spectrum shown in Figure 6.7 and many previously reported infrared cluster spectra. In previous studies, the spectra appeared as broad, relatively featureless bands. See, for example, Gough et al. (1978,1981), Fischer et al. (1983), Cassasa et al. (1981), Hoffbauer et al. (1983d) and Pendley and Ewing (1983). The present spectrum shows considerable sharp structure, which is particularly noticeable in band B, where the signal-to-noise ratio is the largest. As has already been noted, such fine structure was not observed in less dilute mixtures of acetylene in helium, for which the rotational temperature of the clusters would have been considerably higher and many large clusters would have contributed. Although the low resolution spectrum clearly shows that the spectrum can be resolved into rather narrow peaks, the details of this spectrum must be reviewed with some caution. As discussed in Chapter 2 and Section 6.3, the low resolution scanning mode of laser operation results from using the laser

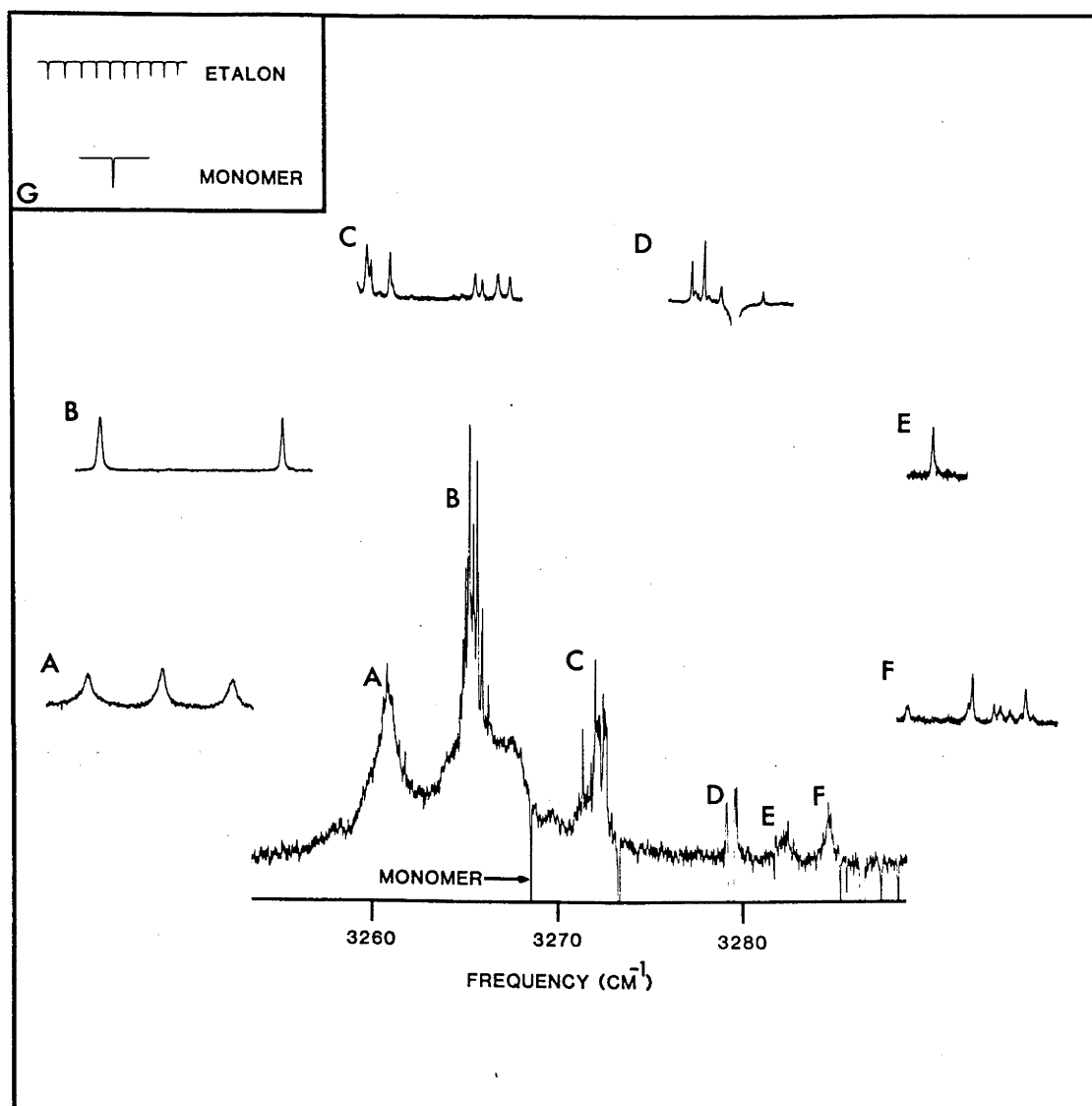


Figure 6.7

without the intracavity etalon and rotating the cavity grating. In this mode the laser does not scan continuously, but rather jumps discontinuously from one group of cavity modes to the next. As the widths of the rotational lines may be considerably less than the free spectral range of the cavity, the low resolution spectrum shows only a small portion of the narrow structure. This is the reason why the monomer spectrum obtained in low resolution mode is not in agreement with the known monomer spectrum.

To overcome these difficulties, small portions of the spectrum were recorded for each of the six bands with the laser operating in its high resolution mode. Typical examples of such spectra are shown as inserts in Figure 6.7. All of the inserts have been plotted using the same frequency scale, which is expanded by a factor of 155 in comparison to the low resolution scale. The high resolution scans shown in Figures 6.7 and 6.8 are plotted with wavelength increasing from left to right, which is in the opposite direction to the low resolution spectra reported in this chapter. Insert G shows a set of 150 MHz etalon frequency markers, as well as a monomer absorption, obtained under high resolution. As these are plotted using the same frequency scale as the other inserts, they serve to calibrate the frequency scale and indicate the instrumental resolution. All of these high resolution spectra were recorded using the parallel gold coated mirrors to obtain multiple near-orthogonal laser - molecular beam crossings. A striking feature of these spectra is that the linewidths depend upon the band excited. As the observed lines represent well resolved rovibrational transitions, the variations in the linewidths are most probably the result of differences in the relaxation rates of the excited modes. This point will be discussed in detail shortly. Note that some of the transitions are separated by less than 40 MHz (0.0013 cm^{-1}).

Given that the Doppler width for $(C_2H_2)_2$ at 300 K is about 170 MHz FWHM (0.0057 cm^{-1}), it is clear that sub-Doppler resolution (using, for example, the techniques described in this thesis) is required to obtain rotationally resolved spectra.

The longest continuous single mode scan we were able to obtain was about 2000 MHz, or 0.07 cm^{-1} (see Chapter 2). Had a sufficiently accurate absolute frequency calibration been available, for example a wavemeter giving a resolution of about 5 parts in 10^7 (or 50 MHz at 3300 cm^{-1}), it would have been possible to splice together an arbitrary number of 0.07 cm^{-1} scans, and thereby map out the complete rovibrational spectrum of the six cluster bands. Without such a calibration the best we could do was to link together consecutive overlapping scans by matching up the same spectral features from one scan to the next. [We note that it is also possible to match up consecutive high resolution scans by using two etalons with suitably chosen free spectral ranges to locate the frequency of the lasing mode to a sufficiently high accuracy. This method was used by Kasper *et al.* (1982) to routinely scan many wavenumbers using a colour centre laser.] Figure 6.8 shows such a composite spectrum from band D of the low resolution spectrum. Eleven single scans were required to map out the 0.4 wavenumber long section of band D shown in the figure. Four negative going transitions are seen. Although in principle they may correspond to clusters absorbing radiation and reaching the bolometer, either before or after dissociating, this is most unlikely given the large photon energy, the relatively low density of states in the acetylene system, the weak binding in the acetylene system, and the fact that the beam contains only small clusters. We therefore attribute them to monomer absorptions. The intense monomer line seen in both the low resolution and

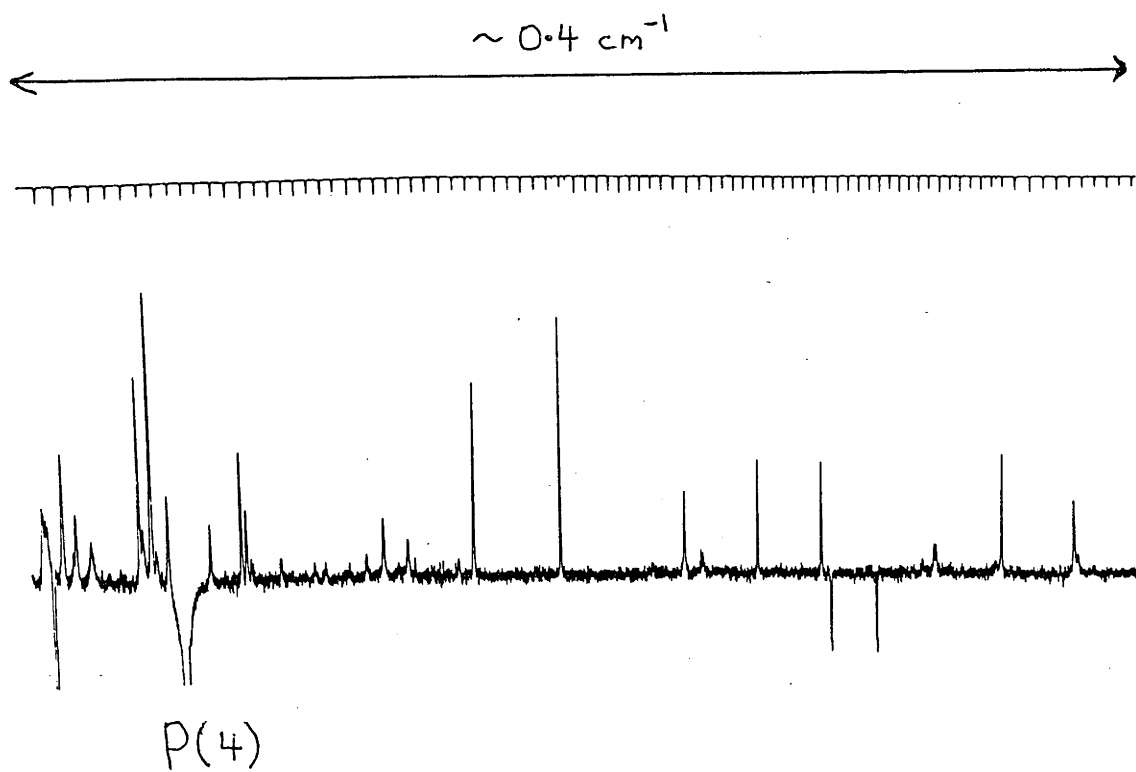


Figure 6.8

high resolution spectra of band D is most likely the P(4) line of C_2H_2 corresponding to the Fermi shifted $\nu_2+\nu_4^1+\nu_5^1$ absorption. The centre of this monomer band is at 3281.9 cm^{-1} (see Table 6.1), and the P(4) line is located at 3278.8 cm^{-1} . A most striking feature of the spectrum shown in Figure 6.8 is the narrowness of the cluster dissociation peaks. Indeed, except perhaps for the few lines at the very left of the scan, the cluster absorption lineshapes are seemingly as narrow as the monomer absorptions. A quantitative analysis of the cluster absorption lineshapes should reveal the degree of homogeneous broadening resulting from the relaxation (and/or dissociation) occurring in the excited cluster. This information would enable a lower bound to be placed upon the timescale of the corresponding dynamics. The analysis of the lineshapes from bands A to F is discussed below.

In order to isolate the lifetime broadening component of an observed rovibrational transition, it is necessary to identify all other sources of broadening and deconvolute these from the observed lineshape. This is most easily done by recording a monomer absorption profile and convoluting it with a lifetime broadened lineshape in order to fit the cluster absorption. Such a procedure is based on the assumption that the non-lifetime broadening effects affecting the cluster absorption are identical to those which broaden the monomer lines.

The Doppler effect resulting from the spread of molecular velocities in the beam is the major source of monomer broadening, and its magnitude will be similar for the cluster absorptions, given that the velocity distributions of the clusters are expected to be similar to the monomer distribution. Transit time broadening effects will also be the same in both cases. Power broadening, which depends upon the transition

moment squared, may vary between the monomer and the different clusters. For ethylene, Cassasa et al. (1983) report squared transition moments of 35.5×10^{-3} , 96×10^{-3} and $141 \times 10^{-3} D^2$ for the monomer, dimer and trimer respectively. Given that the ethylene and acetylene dimer and trimer equilibrium structures are probably quite similar, the power broadening effects for acetylene clusters are expected to be larger than for the monomer, and increase with increasing cluster size (ie. with increasing transition moment squared).

Unfortunately, there are too many unknowns to allow an accurate calculation of the power broadening. A rough estimate for the monomer was obtained by assuming: a single laser - molecular beam crossing; that the power P reaching the molecular beam was 1 mW; that the diameter of the laser beam was 0.5 mm; that the molecular speed was 1500 m/s; and that the squared transition moment μ^2 was $35 \times 10^{-3} D^2$. The transit time t is 0.33 μ s, resulting in a transit time broadening of 3 MHz. The rms electric field E can be obtained from energy density arguments using

$$\epsilon_0 E^2 = \frac{P}{c\pi(d/2)^2} \quad (6.1)$$

One obtains $E^2 = 1.9 \times 10^6 \text{ V}^2 \text{m}^{-2}$. The square of the Rabi frequency is given by (Cassasa et al. (1983))

$$\omega_R^2 = \frac{\mu^2 E^2}{3\hbar^2} \quad (6.2)$$

resulting in $\omega_R^2 = 0.9 \times 10^{14} \text{ rad}^{-2}$. The corresponding power broadening is $\omega_R/2\pi = 1 \text{ MHz}$. Both of these broadening effects are less than the 4 MHz FWHM observed for the monomer transition using an orthogonal laser - molecular

beam crossing. If we assume that the squared transition moment of the dimer is 96×10^{-3} , as was found for the ethylene dimer, we obtain $\omega_R^2 = 2.5 \times 10^{14} \text{ rad}^{-2}$. The corresponding power broadening is about 3 MHz. We stress that these estimates are qualitative at best.

That the sum of all non-lifetime broadening effects (excluding Doppler broadening) is less than 4 MHz for both the clusters and the monomer is supported by the lineshapes observed in band D. Using an orthogonal laser - molecular beam crossing the monomer and dimer lineshapes were each found to have a width of about 4 MHz. For this cluster the non-lifetime broadening is less than 4 MHz. This result leads us to conclude that, in all probability, if we deconvolute the monomer lineshape from a cluster absorption profile, we will be left with the lifetime broadened component of the latter.

It now remains to specify the form of the lifetime broadening component of the cluster lineshape. In their analysis of the infrared spectra of the HF and DF dimers, Pine *et al.* (1984) used a pure Lorentzian to represent the combined lifetime and pressure broadening (theirs was a gas cell experiment) contributing to the observed spectra. Alternatively, Cassasa *et al.* (1981, 1982, 1983) have described the dissociation process using a simple two level model in which the laser radiation couples the levels and, in addition, there exists a decay channel from the upper level into a dissociative continuum. The lineshape obtained from this latter model is the exponential of a Lorentzian multiplied by $\omega_R^2 \tau t$:

$$F(\omega, t) = \exp\left[\omega_R^2 \tau t \cdot \frac{-\tau^{-2}}{4(\omega - \omega_0)^2 + \tau^{-2}}\right] \quad (6.3)$$

where ω_R is the Rabi frequency, t the irradiation time, ω_0 the centre (angular) frequency, and τ is the half-life (ie., lifetime) of the excited

cluster state. The full width at half maximum of the Lorentzian (in cm^{-1}), $\Delta(1/\lambda)_{\text{FWHM}}$, is related to τ by

$$\tau \text{ (sec)} = \frac{1}{2\pi c \cdot \Delta(1/\lambda)_{\text{FWHM}}(\text{cm}^{-1})} \quad (6.4)$$

Equation (6.4) is related to the energy-time uncertainty principle, $\Delta E_{\text{FWHM}} \cdot \Delta t_{\text{half-life}} \geq \hbar$.

The value of $\omega_R t$ determines how significantly the actual lifetime τ differs from that determined by fitting a pure Lorentzian to the lifetime broadened lineshape. Because of the uncertainties in the laser power and the diameter of the laser where it crosses the molecular beam, it was not possible to reliably calculate ω_R or t . Using the values estimated earlier for the dimer gives $\omega_R^2 \tau t = 8.3 \times 10^7 \tau$. For lifetimes of 1, 10 and 100 ns $\omega_R^2 \tau t$ is 0.08, 0.83 and 8.3 respectively. These values suggest that, for lifetimes up to 10 ns, the neglect of the exponential in Eq. (6.3) will have a small effect upon the analysis (with deconvoluted lifetimes of 10 ns being about 25% too long), and that for lifetimes greater than 10 ns the use of a pure Lorentzian will be inadequate (see Casassa *et al.* (1982)). We initially chose to analyse the high resolution spectra using a pure Lorentzian to describe the lifetime broadening. All of the lifetimes obtained in this way were smaller than 10 ns, except for band D for which the lifetime broadening was too small to be resolved. On the basis of the model of Cassasa *et al.* (1981,1982,1983), we conclude that the neglect of the exponential in Eq. (6.3) is a good approximation for the analysis of the present experiments.

In summary, estimates of the lifetimes of the initially excited states of the acetylene clusters can be obtained by convoluting a Lorentzian with the monomer lineshape to reproduce the measured cluster

profile. The width of the Lorentzian needed to fit the cluster absorption determines the desired lifetime.

A typical monomer absorption is shown in Figure 6.9. The asymmetry of the lineshape results from a small misalignment of the multiple crossing mirrors, which gave two sets of laser - molecular beam crossings at slightly different angles. The Doppler profiles for each of these crossings are therefore not coincident. In order to allow for this effect, the monomer profile was fitted using two Gaussians, giving a total width (FWHM) of 15 MHz. The resulting function was convoluted with a Lorentzian function whose parameters were varied to obtain the best least squares fit to the cluster absorption under consideration. One of these fitted lineshapes is also presented in Figure 6.9. In this case the observed lineshape is well represented by a convoluted Lorentzian. Such agreement is consistent with the neglect of the exponential in Eq. (6.3). The widths of the Lorentzians obtained for the different bands using this procedure are given in Table 6.2, along with the corresponding values of the lifetimes of the excited states. For each band we fitted to one or two isolated rovibrational transitions to obtain the results presented in the table. We note, however, that between five and fifteen transitions were recorded from each band, and that the widths of the recorded lineshapes from a given band were all within $\pm 5\%$ of each other.

In all but band D, the lineshapes are broader than that of the monomer. Since band D gave essentially a Lorentzian width of zero using the fitting procedure described above, several spectra were recorded using a single orthogonal laser - molecular beam crossing in an effort to further increase the lower limit to the lifetime. Although the signal-to-noise ratio was reduced in this single crossing configuration, the width of the

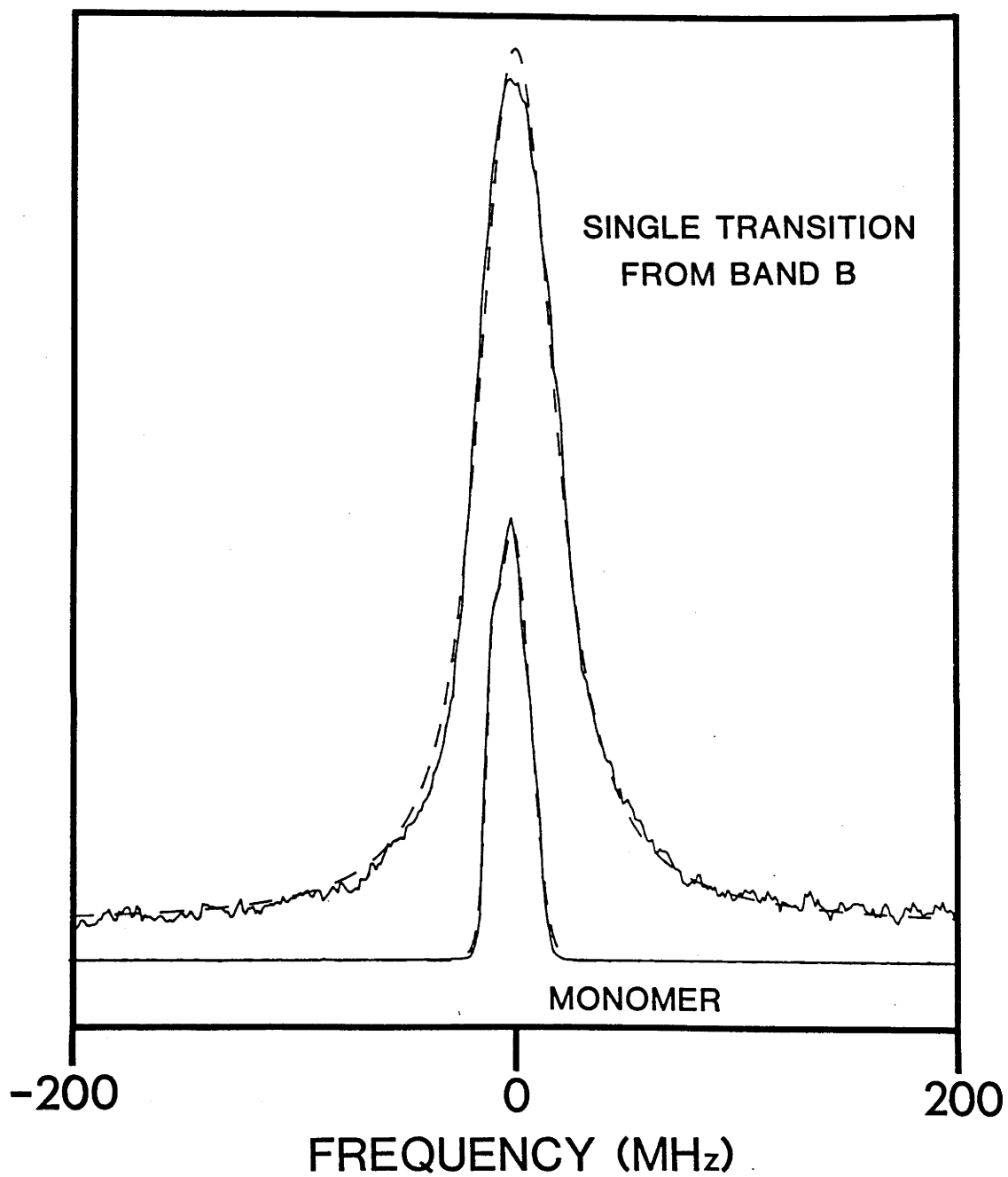


Figure 6.9

Table 6.2

acetylene cluster band	band centre (cm^{-1})	deconvoluted FWHM for the individual rotational lines (MHz)	half-life of corresponding relaxation process (nanoseconds)
A	3261	100.	1.6
B	3266	33.	4.8
C	3272.5	16.5	9.6
D	3279	< 2.0	> 80.
E	3282	19.5	8.2
F	3285	25.7	6.2

monomer transition was reduced to about 4 MHz. The results of this study are shown in Figure 6.10. As is the case for the spectra recorded using the multiple crossing configuration, the widths of the lines taken from band B are clearly greater than the monomer width. Band D, however, shows lines which are once again almost as narrow as the monomer lines. By deconvoluting these spectra using the methods described above, a lower limit of 80 ns is obtained for the clusters excited in band D. The width obtained for the band B line using the single pass configuration agrees well with those determined using multiple laser - molecular beam crossings.

The summary of the linewidths and corresponding lifetime estimates given in Table 6.2 suggests that lifetimes vary by a factor of up to 50, depending upon the mode and/or cluster excited. This result is in contrast to the broad infrared cluster spectra typical of polyatomic molecule van der Waals systems, which suggest that the homogeneous component of the lineshapes, and hence possibly the lifetimes, are rather independent of the molecule and mode excited. Further, the lifetimes of the acetylene clusters studied are all in the nanosecond range, rather than the picosecond lifetimes which have been estimated for many polyatomic molecule van der Waals systems, such as the ethylene dimer and other ethylene containing clusters.

6.4.3 Pressure dependence of the spectra of small acetylene clusters

Thus far we have not considered the possible interpretation and/or assignment of the bands A through F seen in the spectrum of Figure 6.7. Unfortunately, the data presented in this thesis are insufficient to allow

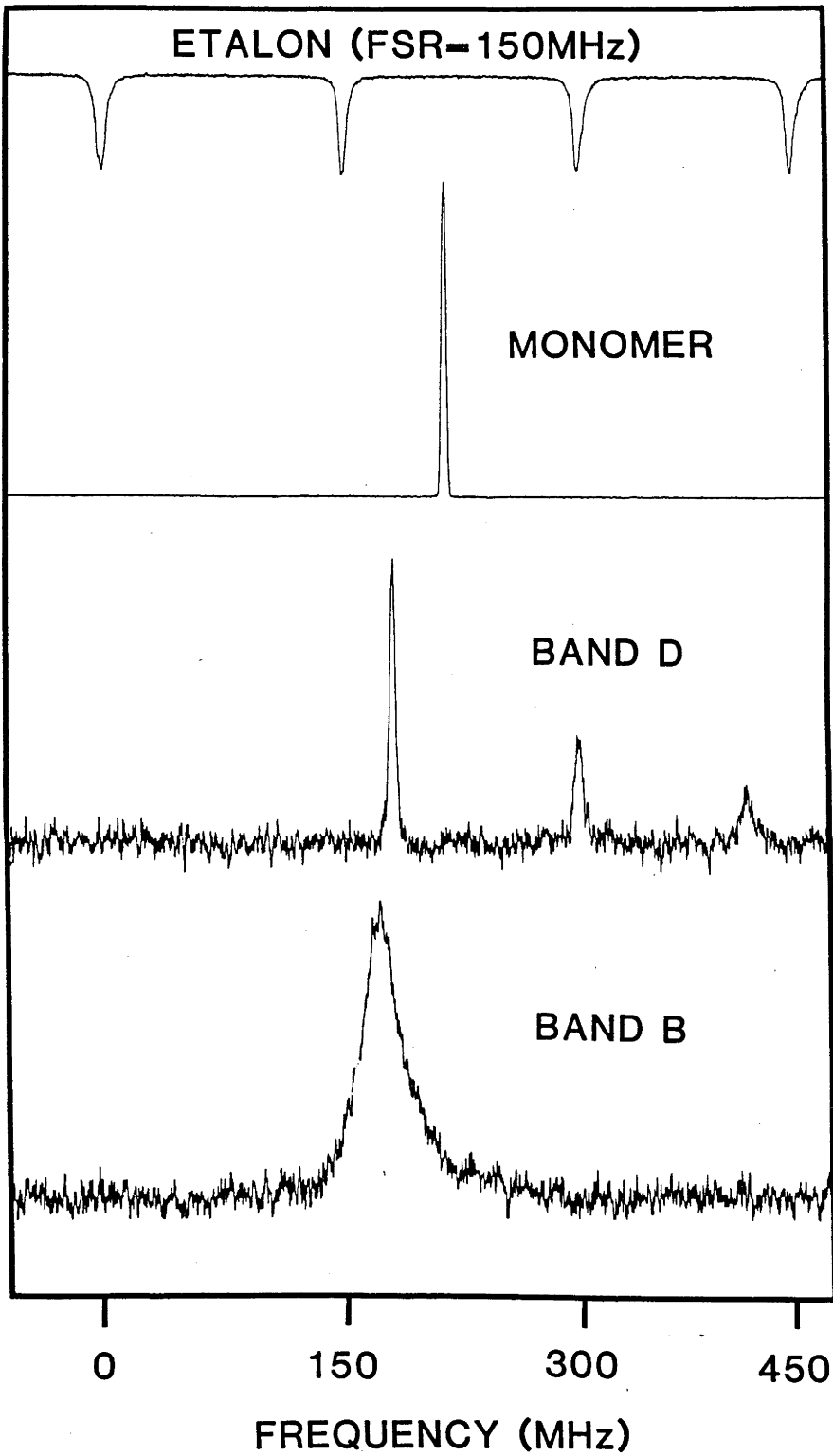


Figure 6.10

an unambiguous determination of the cluster structures, let alone the nature of the dynamics involved. A complete scan of the high resolution spectrum would give the necessary information. As noted earlier, to record such spectra requires a sufficiently accurate absolute frequency calibration, which was not available when these investigations were being carried out.

In an attempt to shed some light on the possible interpretation of these bands we made a detailed study of the changes in both the low resolution infrared spectrum and the mass spectrum, of the 1% mixture, as a function of the source pressure. Figure 6.11 shows a mass spectrum of the molecular beam formed using a source pressure of 1100 kPa. The energy of the ionizing electrons was set to 30 eV to minimise cluster fragmentation. As a result of this low energy, a peak associated with helium does not appear in the spectrum. The masses of the monomer, dimer and trimer are indicated in the figure, as are the vertical scale expansion factors used to offset the decreasing signals with increasing mass. It is tempting to associate the peaks observed at masses 49, 50 and 51 with fragments due to ionization of the dimer, leading to the conclusion that only the monomer and dimer were present at measurable concentrations. The results of the mass spectrometric study of the 11% mixture (presented earlier) suggest that this is probably not the case. Log-log plots of the pressure dependence of the four mass peaks shown in Figure 6.11 appear in Figure 6.12. The slopes decrease at higher source pressures as a result of condensation in the beam (ie. cluster formation) and, possibly, skimmer interference. Both of these effects become more important with increasing source pressure. As was found for the 11% mixture, the peaks at masses 49 and 50 have the same pressure dependence. For these masses, the slopes of

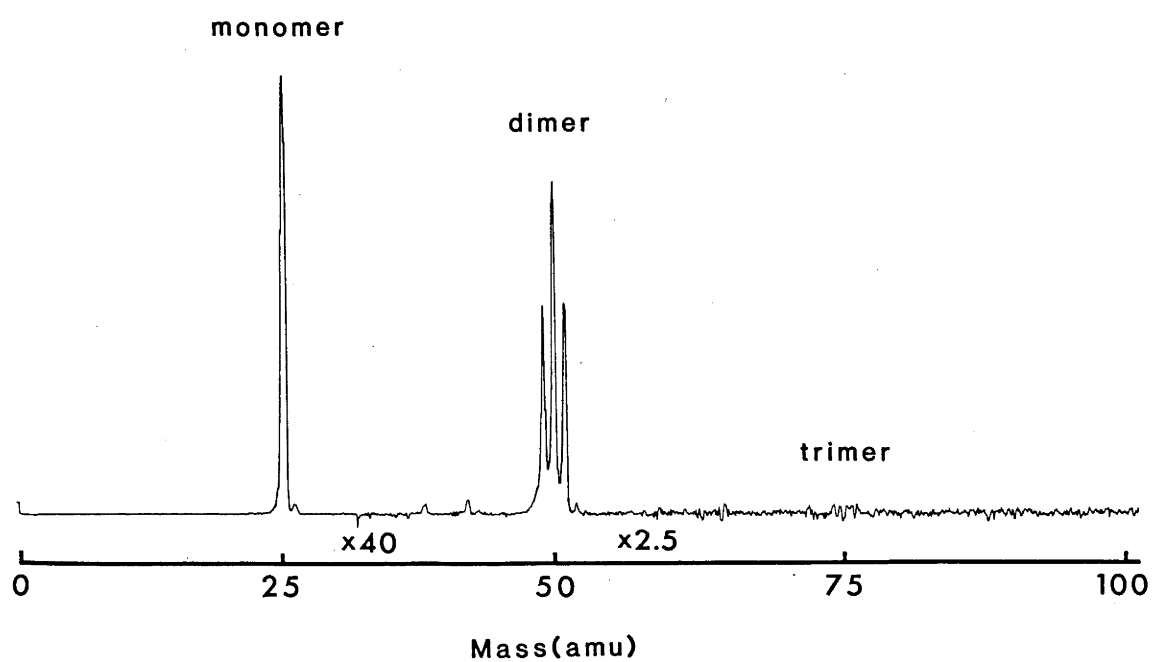
1% C₂H₂ in Helium at 1100kPa

Figure 6.11

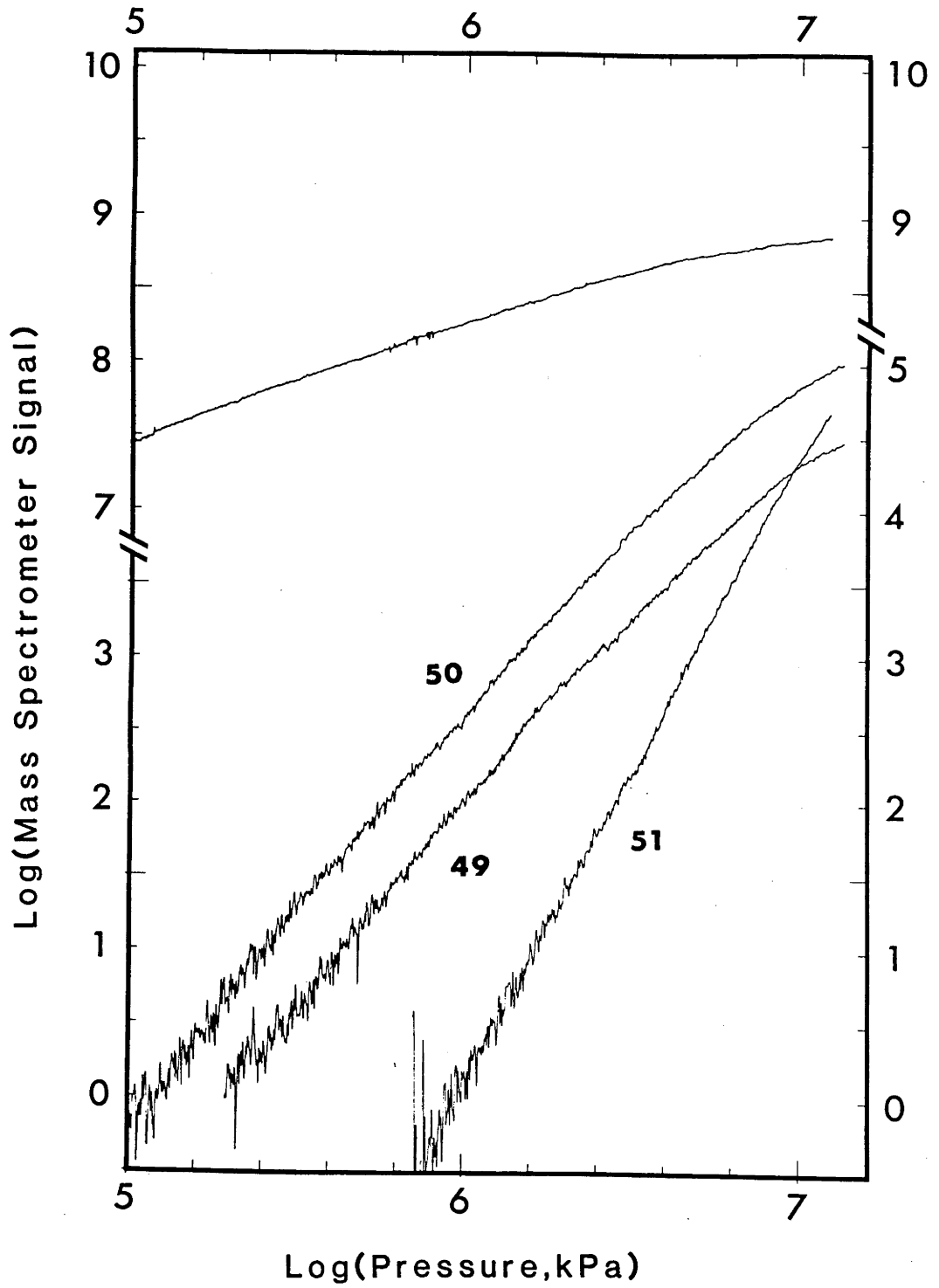


Figure 6.12

the log-log plots at low pressure are both 2.8, suggesting that the corresponding ions were formed from the acetylene dimer. On the other hand, the mass 51 peak has a slope of 4.5, indicating that it was most likely the result of trimer ion fragmentation. Notice that the mass 51 curve is linear over the entire range of pressures considered. It is indeed expected that the larger cluster signals should begin to deviate from linearity at higher source pressures. We also note that the deviations from linearity observed for the 1% mixture were not apparent for the 11% mixture. The reason for this is that, for the 11% mixture, measurements were only made at four or five discrete pressures, making a detailed assessment of the shapes of the curves impossible. A comparison of Figures 6.4 and 6.12 shows the greater contribution of trimers at the dimer mass expected for the 11% mixture.

When the source pressure of the 1% mixture was raised sufficiently, several small peaks were seen in the region around mass 78, presumably arising from the fragmentation of larger clusters. For the 11% mixture, the signals near mass 78 were relatively large at moderate pressures, with the heaviest ion peak exhibiting a greater pressure dependence than the others, rather like that of the mass 51 "dimer" peak.

A series of low resolution infrared spectra were also recorded for the 1% mixture as a function of the source pressure. These spectra are shown in Figure 6.13. It is clear from this figure that bands A and B decrease more rapidly with decreasing pressure than does band C, suggesting that they may also arise from clusters larger than the dimer. In order to obtain a useful log-log plot of the infrared band intensity vs pressure one would need to (1) take into account the variation in bolometer responsivity with the total gas load, and (2) use the integrated intensity

1% C₂H₂ IN HELIUM

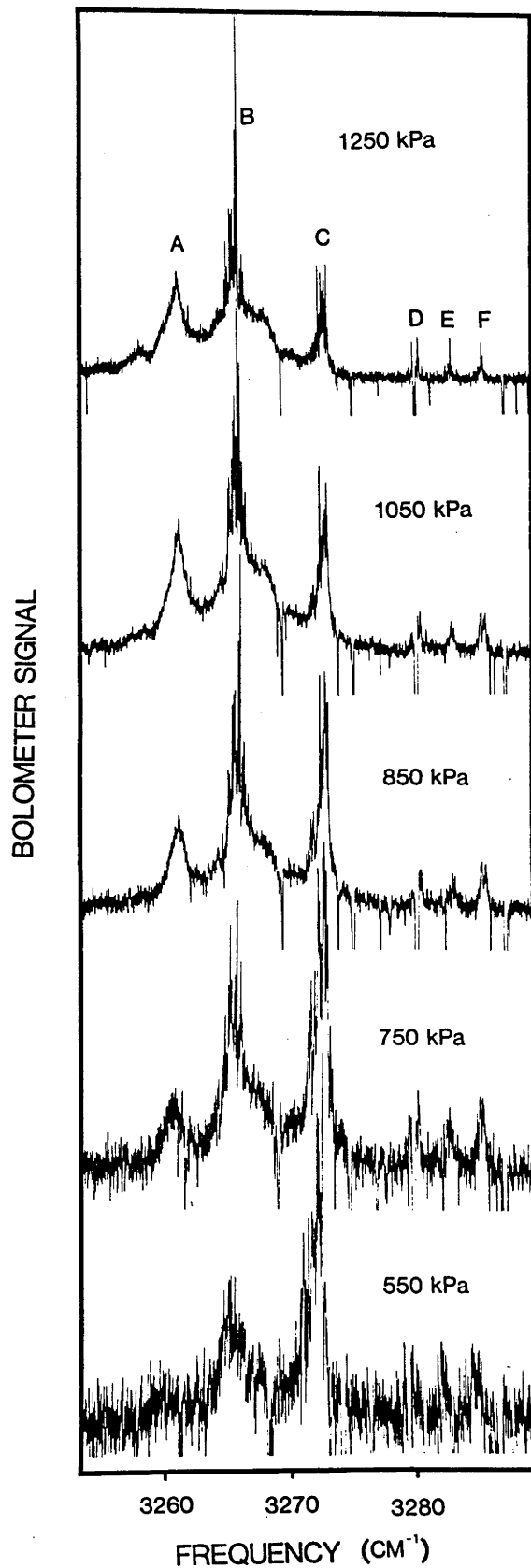
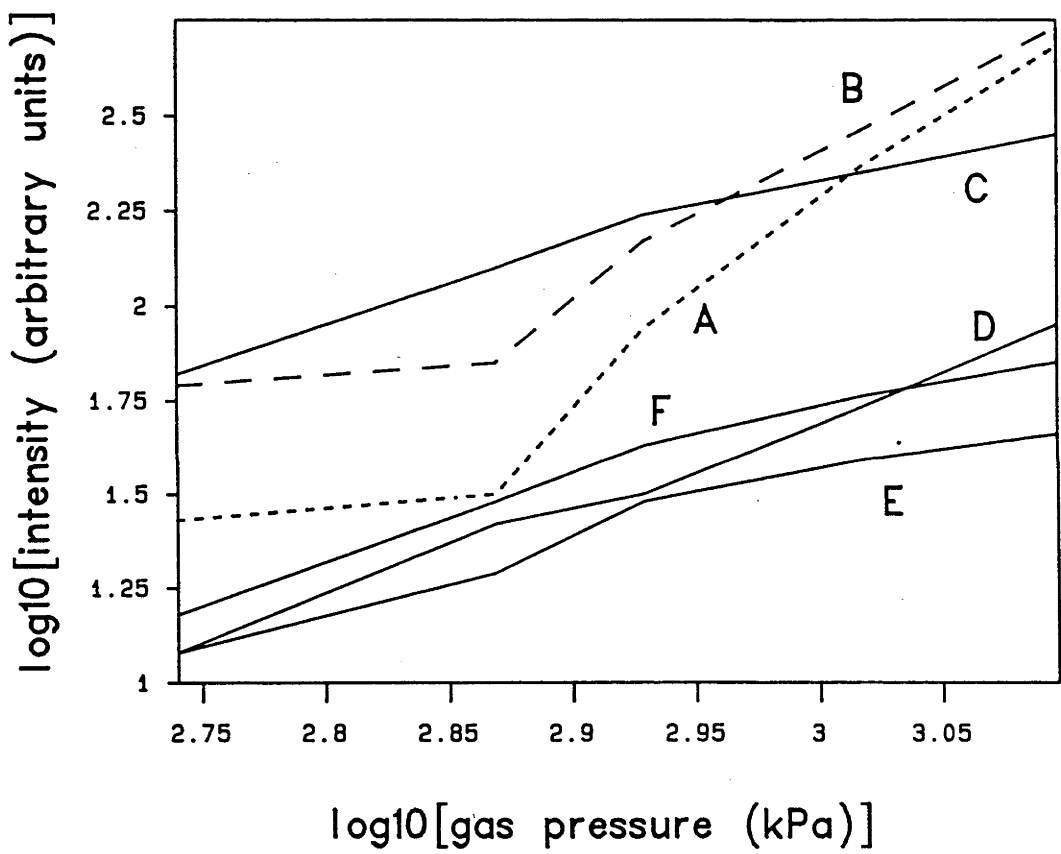


Figure 6.13

for the band, or for a chosen rovibrational transition within the band. For convenience we used the intensities of the bands shown in the low resolution spectra of Figure 6.13, estimated in as consistent a manner as possible, and corrected these values using the responsivity vs operating point characteristics for bolometer B given in Chapter 2. Figure 6.14 shows the corrected values for each band; the lines drawn simply join the points. Least squares linear fits to these points appear in Figure 6.15. Slopes of the lines of best fit, given in Table 6.3, indicate that bands B and A are probably not dimer bands, but result from the trimer, and perhaps the tetramer, respectively. This conclusion is supported by the spectra shown in Figure 6.2, which show how the infrared spectrum shifts to lower energy (ie., lower frequency) as the cluster size increases. The lifetimes reported in Table 6.2 also suggest that bands A and B result from larger clusters than do bands C to F. A larger cluster means a higher density of states through which the initial excitation can decay, with the result that the energy dumped into the complex can more readily migrate into the van der Waals mode responsible for dissociation. The fastest decays (ie., the largest linewidths) were indeed observed for bands A and B. We note that the interpretation of the pressure dependence of the infrared spectrum is complicated by the fact that the distribution of rovibrational cluster states present in the beam will depend upon the source pressure. It was not possible to account for this in the above analysis.

The pressure dependence of the high resolution spectrum of the 1% mixture was also investigated. A section of band C rich in cluster absorptions was recorded both at 1140 kPa and 760 kPa. Apart from a decreased overall signal at the lower pressure, the spectra were identical. The slope of the $\log(\text{signal})-\log(\text{pressure})$ plot determined by these two

acetylene dimer band intensities

Figure 6.14

acetylene dimer band intensities

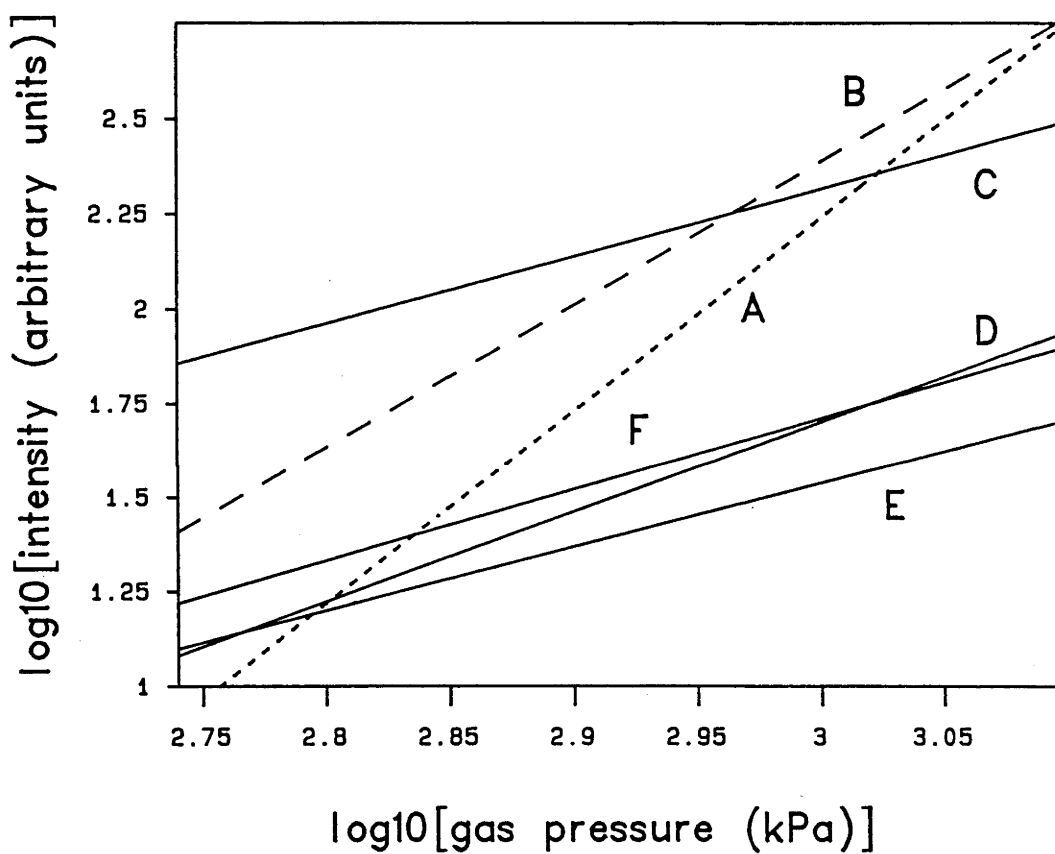
**Figure 6.15**

Table 6.3

acetylene cluster band	slope of $\log(\text{signal})$ vs $\log(\text{pressure})$ plot for the low resolution spectra	cluster size inferred on the basis of these slopes
A	5.1	tetramer ?
B	3.8	trimer
C	1.8	dimer
D	2.4	dimer
E	1.7	dimer
F	1.9	dimer

pressures is 2.0, in agreement with the value given in Table 6.3 for band C. The widths of the observed spectral features did not change as a function of pressure, as expected for individual rovibrational lines homogeneously broadened by a decay process from the initially excited state.

Having attributed bands A and B to higher clusters, it remains to consider the dimer bands C, D, E and F. Pendley and Ewing (1983) observed three dimer bands for $(C_2H_2)_2$ in the 600 to 2000 cm^{-1} range. Each observed band was the rovibrational contour of a dimer absorption corresponding to a different monomer mode (or combination of modes). As shown in Table 6.1, there are only two infrared active monomer bands near 3270 cm^{-1} , namely ν_3 and $\nu_2+\nu_4^1+\nu_5^1$. The combination band is strong in the monomer only because of a strong Fermi resonance with ν_3 . Given that the difference between the unperturbed frequencies in the monomer is only 0.55 cm^{-1} , compared with the monomer to dimer shift of up to ten wavenumbers for band C, it is likely that the near degeneracy responsible for the Fermi resonance will be lifted, and the intensity of the combination band reduced in the dimer. Nevertheless, it is possible that a number of the observed bands are associated with the $\nu_2+\nu_4^1+\nu_5^1$ vibration, and the remainder with the ν_3 vibration. Whether or not this is the case, one must still explain the presence of several peaks per vibrational band.

Given that the widths of the rovibrational lines depend upon the band to which they belong, and that all of the transitions observed in a given band have the same width, it is reasonable to suppose that bands C to F are separate rovibrational contours corresponding to different dimer modes and/or geometries. That there may exist a number of structures for dimers formed from a given molecule was verified for s-tetrazine by Haynam

et al. (1983). The possibility that the observed dimer bands may correspond to different structures is supported by Monte Carlo calculations of $(\text{N}_2\text{O})_2$, carried out by Miller et al. (1984), which show three peaks in the infrared spectrum corresponding to locally stable parallel, T, and crossed configurations. As pointed out by Pendley and Ewing (1983), the similarities between $(\text{C}_2\text{H}_2)_2$ and $(\text{CO}_2)_2$, and hence $(\text{N}_2\text{O})_2$, suggest that these dimers may form similar structures. Indeed, C_2H_2 , CO_2 and N_2O are all linear molecules having similar polarisabilities and quadrupole moments.

In an effort to test the plausibility of the suggestions given in the preceding paragraph, we generated band contours, using a contour analysis program attributable to Pierce, assuming both T and staggered parallel geometries. The structures considered were based upon the potential of Satai et al. (1977) and the analysis of $(\text{C}_2\text{H}_2)_2$ by Pendley and Ewing (1983). A rough estimate of the dimer temperature can be obtained from the results of Boughton (1986). The rotational temperature of the acetylene monomer in a beam formed from a mixture of 10% in helium at source pressures of 100 and 500 kPa was estimated from the measured relative P and R branch intensities. A nozzle with a 35 μm diameter hole was used in this study. Temperatures of 15.5 and 9.5 K were obtained. For a mixture of 1% acetylene in helium at 1100 kPa we expect the temperature of the monomer to be substantially lower, with the dimer temperature lower still. Using dimer temperatures in the range 2 to 5 K we obtained contours showing a single peak with a width of about 1 to 3 cm^{-1} , depending upon the band type and the dimer geometry. Although rather inconclusive, these results suggest that bands C to F are probably individual rovibrational contours.

The possibility that bands A, B and C represent a single rovibrational contour was also investigated, by attempting to simulate such a contour with plausible dimer geometries. Temperatures of 50 to 100 K were required to obtain contours resembling the A, B, C triplet. Given that we expect substantially colder clusters in the beam, and in the light of the evidence suggesting that these bands result from different cluster sizes, we discount the possibility that bands A, B and C are the P, Q and R branches of a single transition.

Lastly, we note that the lifetime estimate for band D excitations is larger than the estimates for bands C, E and F, which are all quite similar. The difference in relaxation rate reflects the ease with which the energy of the initial excitation is able to migrate to the dissociation coordinate. A $\equiv\text{C-H}$ stretching mode excited in one of the monomer units of a staggered parallel or crossed acetylene dimer is unlikely to couple strongly to the van der Waals bond. In a T structure, however, the stretching mode of the bonding monomer is directly coupled to the van der Waals bond and is likely to lead to fast dissociation. Whether or not the long lifetimes observed for band D can be explained by such arguments is, at present, purely speculative. Mode selective relaxation rates have been observed for the HF dimer by Pine *et al.* (1984).

In the remainder of this chapter we discuss the results obtained for methyl acetylene and ethylene clusters, and then summarise what has been learned from the present investigations.

6.5 Methyl Acetylene Clusters

In view of the dramatic changes in the acetylene cluster spectrum as a function of the concentration of the gas mixture and the source pressure, a similar study was carried out for methyl acetylene. Bolometer B was used to obtain the spectra presented in this section.

Methyl acetylene has four fundamental C-H stretching vibrations that lie within the tuning range of the colour centre laser (see Table 6.1). Three of these are associated with the methyl group and lie below 3000 cm^{-1} . Although it was possible to detect absorptions associated with these vibrations, the signal-to-noise ratios were too small to allow a detailed study of their characteristics. On the other hand, the cluster absorptions associated with the ν_1 acetylenic stretch, which is located at 3334 cm^{-1} in the monomer, are of a similar intensity to the A, B and C bands observed for acetylene clusters. In this thesis we report a study of the cluster bands in the vicinity of the ν_1 monomer mode.

The concentration and source pressure dependence of the low resolution spectrum of methyl acetylene was found to be similar to that of acetylene. Broad bands were observed at high concentrations and pressures, and as the concentration and pressure were reduced the spectral features became narrower. This behaviour is illustrated in Figures 6.16 and 6.17. The rich structure seen in Figure 6.16 almost certainly results from the overlapping spectra of clusters of many different sizes. At the lowest pressure used with the 1% mixture one sees dissociation signals near 3330 cm^{-1} , and two weaker bands at lower energies labelled X and Y. The cluster bands seen in this spectrum are probably the result of dimers and trimers. A detailed study of the mass spectra was not carried out for the

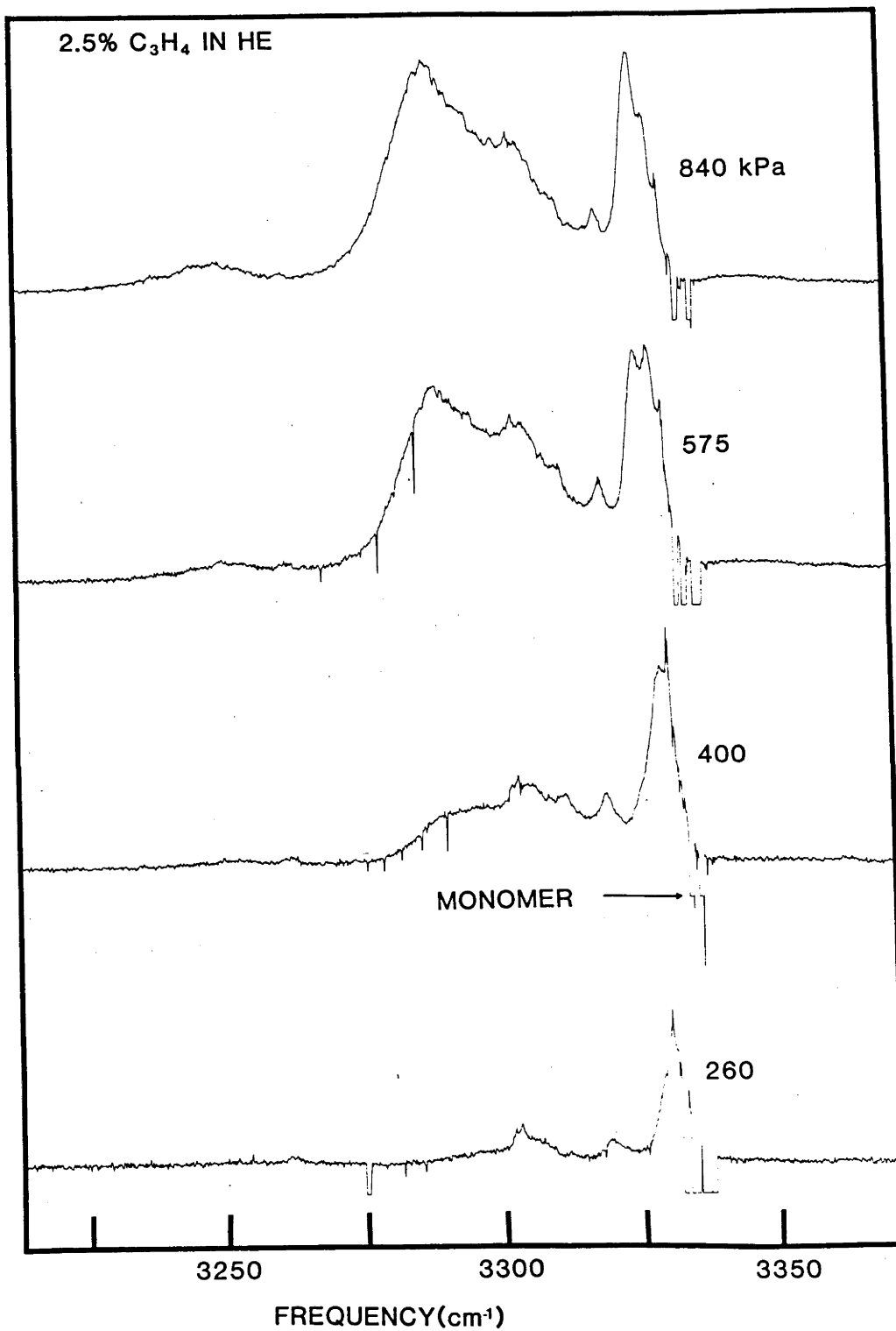


Figure 6.16

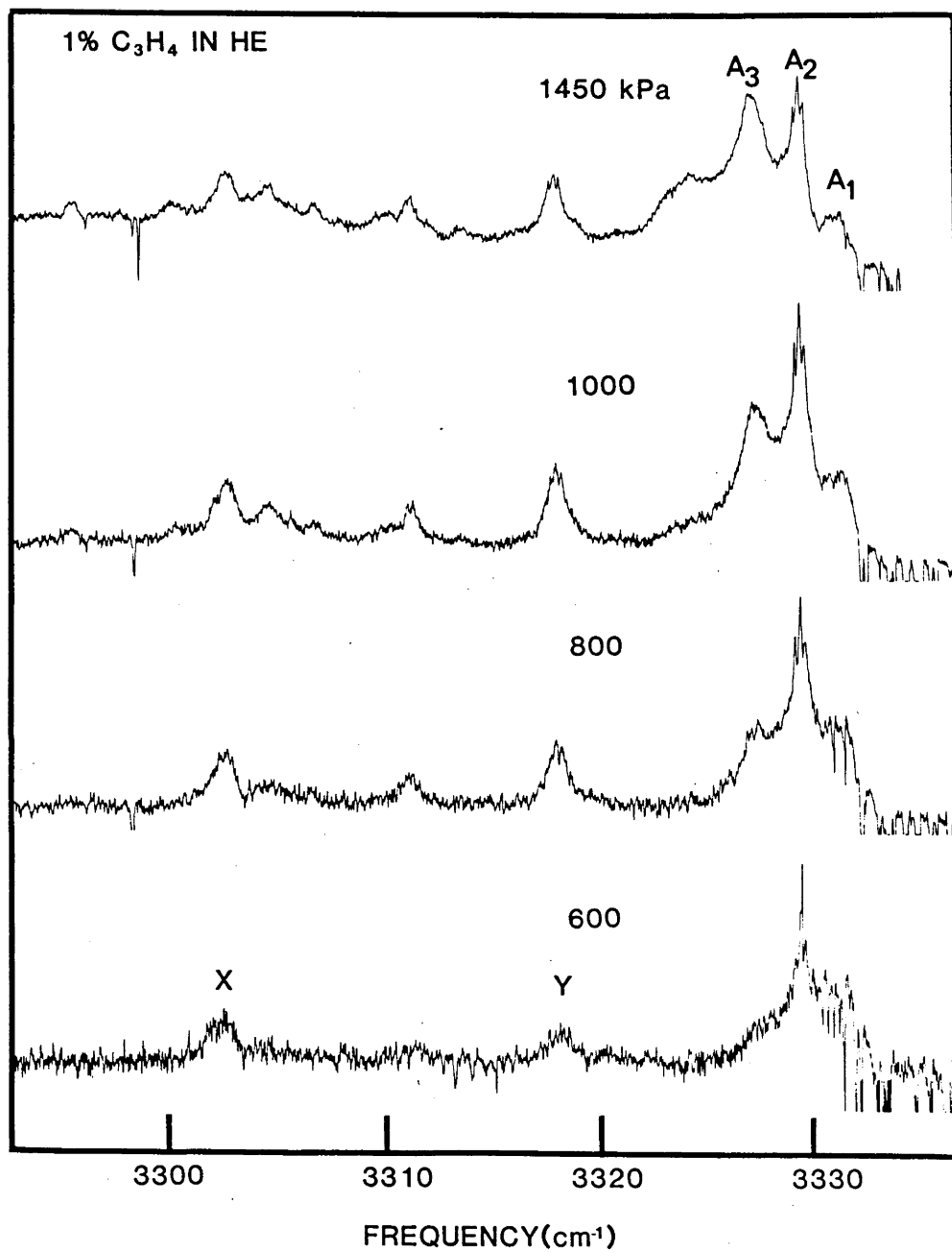


Figure 6.17

methyl acetylene mixtures.

A typical low resolution spectrum obtained using the 1% mixture is shown in Figure 6.18. It shows fine structure not unlike that observed for acetylene, which is particularly evident in band A_2 (compare with band B of the acetylene spectrum of Figure 6.7). Although a detailed investigation of the high resolution spectrum of methyl acetylene clusters was not undertaken, a number of single mode scans of the cluster transitions within band A_2 were obtained. Figure 6.19 shows one such scan, illustrating the broad lineshapes seen in band A_2 . If we assume that the three peaks shown in the figure represent single rovibrational transitions of a given cluster, then the degree of homogeneous broadening present can be used to place a lower bound upon the lifetime of the excited cluster, as discussed in the previous section for acetylene. Given that the observed cluster linewidths of about 350 MHz are all much larger than the 10 to 15 MHz widths of the monomer transitions, the lifetimes obtained by convoluting the monomer profile with a Lorentzian will be only slightly larger than those determined using unconvoluted Lorentzians. We therefore used three independent Lorentzians to obtain a best least squares fit to the high resolution spectrum, which appears as the solid curve in Figure 6.19. Full widths at half maximum determined in this way were all approximately 375 MHz, or 0.013 cm^{-1} , corresponding to a lifetime of 0.4 ns. The methyl acetylene clusters studied here seem to relax about one or two orders of magnitude faster than do acetylene clusters. This may be due to the fact that the density of states in a small methyl acetylene cluster is considerably higher than that in a similar sized acetylene cluster (as a result of the greater complexity of the methyl acetylene monomer).

The likeness between the low resolution spectra of acetylene and

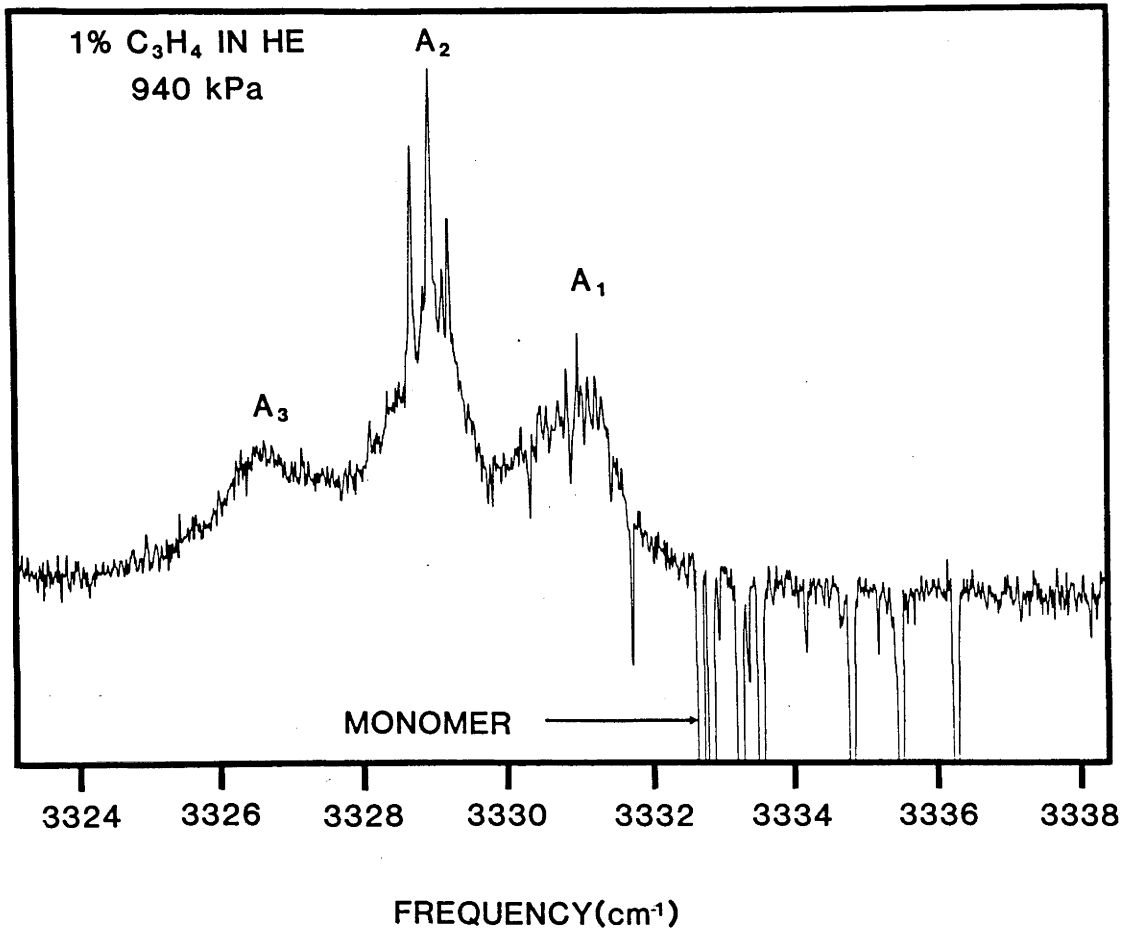


Figure 6.18

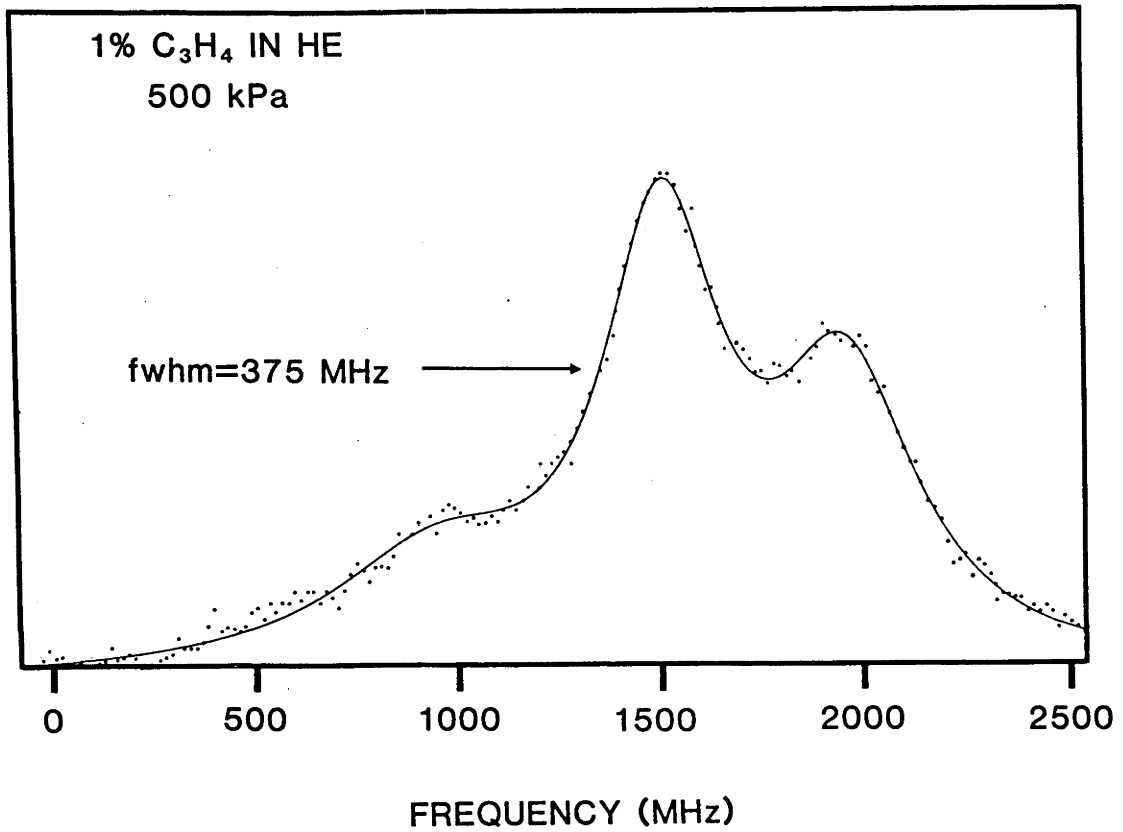


Figure 6.19

methyl acetylene suggests that the structures and/or relaxation mechanisms responsible for the two spectra are similar. That this should be the case is not surprising given that both spectra are probably the result of exciting an acetylenic $\equiv\text{C-H}$ stretching mode of one of the monomers in the cluster, and that the monomers are rather alike. Peaks corresponding to bands D, E and F of acetylene (see Figure 6.7) are not evident for methyl acetylene (Figure 6.18). Possibly bands A, B and C of acetylene and bands A_1 , A_2 and A_3 of methyl acetylene are the result of exciting the acetylenic $\equiv\text{C-H}$ stretch, whereas bands D, E and F of acetylene result from excitations of the $\nu_2+\nu_4^1+\nu_5^1$ monomer mode, whose Fermi resonance with ν_3 is expected to be reduced upon cluster formation.

Although we assumed that the peaks shown in Figure 6.19 are individual homogeneously broadened rovibrational transitions, we cannot rule out the possibility that they may represent separate bands, each substantially homogeneously broadened, or indeed that they are a single rotational contour. Such explanations, however, seem highly unlikely.

6.6 Ethylene Clusters

There has been a great deal of controversy regarding the degrees of homogeneous and inhomogeneous broadening present in the infrared spectra of ethylene containing van der Waals molecules (see Section 6.1). Fischer *et al.* (1983) concluded that the cluster bands near 3000 cm^{-1} were dominated by homogeneous broadening. The spectra reported were obtained using a mixture of 10% ethylene in helium, a $35\text{ }\mu\text{m}$ nozzle and source pressures between 505 and 2000 kPa. Our studies of the acetylene system suggest that a wide range of cluster sizes were present in the beams used by Fischer *et al.* (1983).

Figure 6.20 shows spectra recorded for 10%, 3% and 1% mixtures of ethylene in helium at source pressures similar to those used to obtain the results shown in Figure 6.5. The 10% spectrum, reported by Fischer *et al.* (1983), was obtained with bolometer A, and the lower spectra were measured using bolometer B. A spectrum recorded for a 0.5% mixture differed from that obtained for the 1% mixture only in the signal-to-noise ratio. For the 0.5% mixture we expect that dimers and trimers were the only clusters present in significant amounts. Fischer *et al.* (1983) assigned the two bands seen in the figure to the $\nu_2+\nu_{12}$ and ν_9 monomer modes (see Table 6.1). The width of the ν_9 cluster absorption (the larger of the two absorptions) is rather independent of the beam conditions, and there is no evidence of narrow structure of the kind seen in the spectra of small acetylene and methyl acetylene clusters.

High resolution scans of the ν_9 band of the 1% mixture were also made. In all cases a constant signal was observed, indicative of a large homogeneous broadening component superimposed upon a much narrower

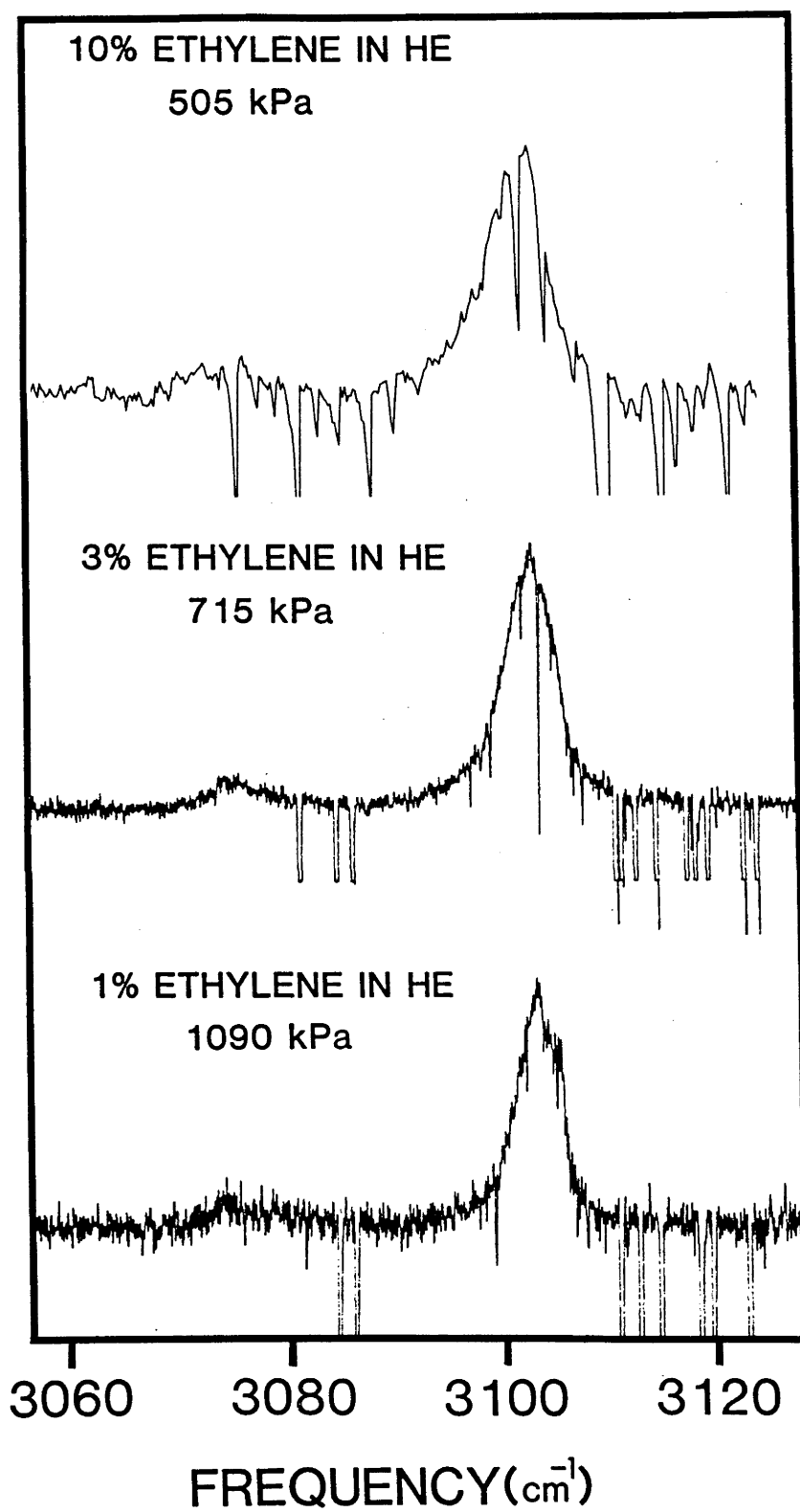


Figure 6.20

rotational contour. If we assume that the 5 cm^{-1} width (FWHM) of the 1% spectrum is due mainly to lifetime broadening effects, we obtain a lifetime estimate of 1 ps.

The results presented here for ethylene show that, unlike the acetylene and methyl acetylene systems, homogeneous broadening effects dominate the infrared spectra of small clusters excited near 3000 cm^{-1} . The nature of the relaxation processes leading to the broad homogeneous cluster absorptions cannot be determined solely on the basis of frequency domain measurements of the kind reported here. Perhaps time domain experiments like those of Mitchell *et al.* (1985) may help to uncover the mysteries of the dynamics of excited van der Waals molecules.

6.7 Summary and Conclusion

In this chapter we have reported the results of a detailed study of the infrared spectra of clusters of acetylene, methyl acetylene and ethylene in the range 3050 to 3350 cm^{-1} . The acetylene and methyl acetylene spectra were found to change dramatically as a function of the range of cluster sizes present. Six dissociation bands were observed for small acetylene clusters between 3260 and 3285 cm^{-1} , four of which we attribute to the dimer. By analysing the lineshapes of individual rovibrational transitions from each of the bands, we obtained estimates of 1.6 to >80 ns for the lifetimes of the of the initially excited states of the van der Waals molecules. The low resolution spectra of small methyl acetylene clusters were qualitatively similar to those observed for acetylene. A lifetime of 0.4 ns was determined from the excitations in one of the bands of the methyl acetylene spectrum. For both of these systems the homogeneous broadening associated with the individual rovibrational transitions of the clusters is small compared with their separation. As a result one can, in principle, obtain fully resolved rovibrational spectra for each of the cluster absorption bands. Such information, which is not reported in this thesis, would allow an unambiguous assignment of the cluster structures and transitions responsible for the observed bands.

The most interesting aspect of the present investigations is the range of relaxation times determined from the homogeneous broadening present in the observed spectra. Previous linewidth determined lifetimes of nanoseconds or more have been obtained for Ne-Cl₂ by Brinza et al. (1983,1984), for HF-HF by De Leon and Meunter (1984), Pine et al. (1984) and Bryant and Watts (1986), and for (rare gas)-OCS dimers by Hayman et al.

(1985). Miller and Watts (1984) also determined lower bounds of 50 ns for the lifetimes of $(\text{CO}_2)_2$ and $(\text{N}_2\text{O})_2$ excited by a colour centre laser. Most van der Waals molecules studied, however, seem to relax on the nanosecond timescale (see the reviews by Janda (1985), Gentry (1984) and Cassasa *et al.* (1984)). The results reported in this thesis show that the acetylene dimer, which is of a comparable complexity to $(\text{CO}_2)_2$ and $(\text{N}_2\text{O})_2$, also relaxes in nanoseconds, whereas ethylene clusters seemed to relax in less than a picosecond. Further, the linewidth derived lifetimes for acetylene clusters are found to depend upon the mode excited, varying from 1.6 to >80 ns.

Ethylene clusters excited near the ν_9 monomer frequency behave differently to acetylene and methyl acetylene clusters. We observed a single, broad (5 MHz FWHM) absorption which did not change significantly as a function of the range of cluster sizes present. The spectrum was dominated by substantial homogeneous broadening, so that it was not possible to resolve individual rovibrational transitions of the clusters. The lifetime estimated from the width of the spectrum is 1 ps. Ewing (1981) has suggested that curve crossing effects may lead to enhanced relaxation rates in van der Waals molecules. Whether or not such processes occur in ethylene is at present a matter for speculation.

The wide range of linewidth derived lifetimes determined in the present investigations suggests that the relaxation mechanisms are indeed rather complicated, and depend upon the nature of the initially excited mode, the geometry of the cluster and the monomer units comprising it. This is not surprising. Until the dynamics responsible for such relaxation is understood, and the observed cluster spectra can be unambiguously assigned, one can only speculate as to why, for example, acetylene dimers

and trimers excited near the $\nu_3/(\nu_2+\nu_4^1+\nu_5^1)$ monomer modes exhibit lifetimes in the nanosecond range, varying by up to a factor of 50, whereas ethylene dimers and trimers seem to relax in about 0.5 to 1 ps. In the present study we have considered a number of possible explanations consistent with the observed spectra, although a thorough understanding will only be possible when a complete rovibrational analysis is possible.

Chapter SevenResonant Rotational Energy Transfer in HF

In this chapter we discuss a series of experiments in which both molecular beam scattering techniques and infrared laser-bolometer spectroscopic methods were used to study the resonant transfer of rotational energy between HF molecules in the ground vibrational state. After an introduction to the scattering of polar molecules the following are discussed: the design of the experiment; the results obtained; the model used to analyse the experimental data; the analysis of the results; and the conclusions drawn from the analysis.

7.1 Introduction

Rotational energy transfer between polar molecules has long been a subject which has attracted considerable experimental and theoretical interest. This is due partly to the fact that interactions between polar molecules are dominated by the well known long range dipole-dipole potential. As a result, the associated rotational energy transfer cross sections are large and can be calculated using approximations which neglect the details of the intermolecular potential at small separations.

Interactions between polar molecules have been studied experimentally using a wide variety of techniques. In 1960 Schumacher *et al.* (1960) reported unusually large total integral cross sections for a beam of CsCl (dipole moment $\mu=10.42$ D) scattered by *cis*-C₂H₂Cl₂ ($\mu=1.90$ D) and CH₂F₂ ($\mu=1.97$ D). The results of a microwave double resonance study of rotational relaxation in ethylene oxide, (CH₂)₂O ($\mu=1.89$ D), lead Oka (1966) to conclude that transitions which obey the dipole selection rules are favoured.

By using pre- and post-collision quadrupole state selection, Toennies (1962,1965) measured large inelastic cross sections for a beam of TlF ($\mu=4.23$ D) interacting with a variety of gaseous targets. At about the same time, Cross and Gordon (1966) and Cross *et al.* (1966) calculated total integral cross sections of thousands of square Ångstroms for low energy polar collisions. Borckenhagen *et al.* (1976,1979) used state selection techniques similar to those used by Toennies (1962,1965) to study the interaction of a velocity selected beam of CsF ($\mu=7.88$ D) with a secondary beam target. They attributed the large cross sections observed with CF₃H ($\mu=1.65$ D), CF₃Cl ($\mu=0.5$ D) and CF₃Br ($\mu=0.6$ D) targets to dipole-dipole

collisions which are nearly energetically resonant.

Microwave double resonance experiments of collision induced linewidths in polar gases, carried out by Cohen and Wilson (1973a,1973b), showed that the dipole-dipole interaction is "overwhelmingly predominant". A cross section of 1570 \AA^2 was obtained for the corresponding radiation interruption process in HCN ($\mu=2.98 \text{ D}$). The role of "rotational resonance" effects in determining pressure broadening in polar gases was first considered by Anderson (1949).

Further evidence supporting the enhancement of dipole allowed cross sections as a result of near energy resonance comes from a series of experiments by Ding and Polanyi (1975) and Esche et al. (1979). Infrared luminescence spectroscopy was used to determine the distribution of rotational states in the $v=1$ vibrational manifold of a heated, seeded, supersonic beam of HCl ($\mu=1.08 \text{ D}$). By making such a measurement with and without a secondary beam of pure HF ($\mu=1.82 \text{ D}$) operating, it was possible to monitor the transfer of rotational energy between the beams. Enhanced efficiencies were indeed observed for dipole allowed transitions in which the energy lost by the HCl molecule is nearly equal to that gained by the HF molecule.

Although there is a large body of theoretical and experimental evidence suggesting that interactions between polar molecules are dominated by first order dipole allowed processes, there are situations in which higher order interactions seem to play a comparable role. Williams and Kukolich (1979) have looked at the OCS-OCS interaction ($\mu=0.71 \text{ D}$), with state selection of a molecular beam before a scattering chamber and microwave spectroscopic detection thereafter. Their results suggest that "the OCS cross sections are not dominated by the direct dipolar terms".

That $|\Delta j| > 1$ transitions are significant in OCS-OCS collisions is also supported by microwave double resonance studies by Lee (1978). Further support for the existence of large $|\Delta j| > 2$ cross sections comes from the results of a number of HF self relaxation studies (discussed below) and from IR-UV double resonance studies of rotational relaxation in D_2CO ($\mu = 2.33$ D) by Orr et al. (1984).

The rotational relaxation mechanisms of ro-vibrationally excited HF molecules interacting with HF in $v=0$ have been the subject of numerous investigations in recent years. Hinchey (1975) and Hinchey and Hobbs (1976, 1979) used two HF chemical lasers in a series of double resonance experiments to study relaxation processes. Rotational transfer rates three orders of magnitude larger than vibration-to-translation (V-T) rates were found. The transfer of rotational energy between HF($v=2$) and HF($v=0$) was observed and analysed by Copeland et al. (1981) and Copeland and Crim (1983, 1984). In order to obtain a good fit to their experimental results they required significant multiple-quantum transitions, with $|\Delta j| = 2$ interactions accounting for 20 to 30 percent of the total rate constant. Quantitative estimates were obtained for the rate constants involved.

Models based upon the energy defect in a collision have frequently been used to study inelastic energy transfer involving polar molecules. See, for example, Polanyi and Woodall (1972), Brunner and Pritchard (1982), Wilkins and Kwok (1983), Orr et al. (1984), Sentman (1977), Pritchard et al. (1979) and Alexander (1979). Alexander et al. (1980) assessed the validity of such energy gap models and noted that, although one is often able to obtain a good fit to a given set of experimental results, it is difficult to decide whether or not there is an underlying physical basis to such models. Another approach which has been used in the analysis of

experimental data is based upon the energy corrected sudden (ECS) approximation. De Pristo (1981) and De Pristo and Rabitz (1980) have shown that the predictions of the ECS method compare favourably with those of exact quantum calculations, and Copeland and Crim (1984) used the method to analyse their HF self relaxation results. The ECS approximation was also used by Bel Bruno et al. (1981) to obtain rotational relaxation rates in HF by the direct inversion of pressure broadened linewidths. It should be noted that the rates obtained by Copeland and Crim (1984) and those determined by Bel Bruno et al. (1981) differ considerably, suggesting that either improved analyses and/or more sensitive data are required. A comparison between the two sets of results is given by Copeland and Crim (1984).

Recently, Bullman and Dagdigian (1984) measured absolute state-to-state inelastic cross sections of hundreds of square Ångstroms for CaCl ($\mu=4.27$ D) interacting with CH₃Cl ($\mu=1.89$ D). Quadrupole state selection was used to prepare the incident beam and laser-induced fluorescence was used to monitor the product states. In similar studies of LiH ($\mu=5.88$ D) colliding with HCl, DCl ($\mu=1.08$ D) and HCN ($\mu=2.98$ D), Dagdigian et al. (1979) and Dagdigian and Alexander (1980) found large rotational energy transfer cross sections for $|\Delta j|=1$ changes in both molecules. The accompanying theoretical studies by Alexander (1979) show that, as expected, the largest cross sections are found for processes in which $j_1, j_2 \rightarrow j_1 \pm 1, j_2 \mp 1$. Interactions of this type minimise the translational energy gap and therefore tend to be more facile than dipole allowed processes of the type $j_1, j_2 \rightarrow j_1 \pm 1, j_2 \pm 1$. We note that the requirement that the total angular momentum be conserved does not imply that $j_1 + j_2 = j_1' + j_2'$, since the total angular momentum vector \underline{J} is the

vector sum of \underline{j}_1 , \underline{j}_2 and the orbital angular momentum \underline{l} .

For the case of identical molecule collisions it is convenient to separate the $j_1, j_2 \rightarrow j_1 \pm 1, j_2 \mp 1$ processes into two groups. The first group comprises the rotational exchange processes, in which the molecules simply interchange their rotational quantum numbers, as in $j_1, j_2 \rightarrow j_2, j_1$. For the case where the two molecules are in the same vibrational state, Alexander (1980) has referred to these as perfectly resonant energy transfer processes. The second group, of which $12 \rightarrow 03$ is an example, includes all other processes of the type $j_1, j_2 \rightarrow j_1 \pm 1, j_2 \mp 1$. These are referred to as the near resonant processes.

The HF-HF system is particularly interesting in that it is the only polar-polar system for which full quantum close-coupled calculations have been performed. Alexander (1980) and De Pristo and Alexander (1977) calculated a large number of first and higher order dipole allowed cross sections for HF-HF collisions in the energy range 0.5 to 1.5 eV. In their investigations they "did not, however, compute any $j_1, j_2 \rightarrow j_2, j_1$ cross sections, since these are not observables". Once again, the near resonant cross sections were found to be the largest.

The experimental and theoretical results summarised above indicate that the energy gap is important in controlling the size of the cross sections in polar-polar systems. One might therefore expect the perfectly resonant cross sections, for which the energy gap is zero, to be very large.

Mason and Monchick (1962) first suggested that, for polar molecules, exactly resonant rotational energy transfer processes could be used to explain why the thermal conductivities of such systems are anomalously low in comparison to their viscosities. This suggestion is

supported by the results of Baker and Brokaw (1965) and Nyeland et al. (1972). A theoretical study of this energy exchange process, and its relationship to rotational Raman line broadening, was reported by Fiutak and van Kranendonk (1962), van Kranendonk (1963) and Gray and van Kranendonk (1966). This theory was later used by Clifford and Dickinson (1976) to investigate the importance of resonant rotational exchange in the thermal conductivity of hydrogen fluoride. These calculations suggested that the cross sections associated with these processes were many times gas kinetic. In later studies of resonant and inelastic transitions in HCl-HCl collisions, Bhattacharyya et al. (1977) and Bhattacharyya and Saha (1978) obtained resonant cross sections of hundreds of square Ångstroms. More recent theoretical investigations of the resonant rotational energy transfer between polar molecules have been carried out by Alexander and Orlikowski (1984) and Takayanagi and Wada (1985). These studies predict cross sections of hundreds of square Ångstroms for the $01 \rightarrow 10$ process for low energy collisions between HF molecules in the ground vibrational state.

Despite all of the studies on polar-polar systems, there have been few direct experimental investigations of the perfectly resonant rotational exchange processes between like molecules. In one such study, discussed previously, Williams and Kukolich (1979) obtained cross sections of hundreds of square Ångstroms for OCS-OCS collisions. Their results could not be explained using first order dipole-allowed processes alone. In order to further our understanding of the resonant energy transfer between like polar molecules, a detailed investigation of such interactions between ground state HF molecules was made. We chose the HF-HF system for the following reasons: (1) the available colour centre laser was able to excite the $v=0 \rightarrow v=1$ transition; (2) HF possesses a reasonably large dipole moment

($\mu=1.83$ D); and (3) the HF-HF system has been studied extensively using exact quantum scattering calculations, and the relevant cross sections were therefore amenable to accurate calculation.

In the following sections we present and discuss the results of experiments in which we combined molecular beam methods with infrared laser spectroscopic techniques and bolometric detection to study the exactly resonant transfer of rotational energy between HF molecules in the ground vibrational state. Although similar to a number of the experiments discussed above, the aim of the present investigations was to study as directly as possible the exactly resonant processes, which are expected to dominate the rotational energy transfer between like molecules.

7.2 Experimental

The experimental arrangement is shown schematically in Figure 7.1. A primary beam was formed by expanding a mixture of about 1% HF in He through a 35 μm diameter nozzle maintained at a temperature of 310 K. By using high source pressures it was possible to cool the majority of the HF into $j=0$ and $j=1$. Further, by varying the source pressure used to form the expansion, one could change the amount of cooling of the HF molecules as a result of the expansion, and thereby alter the resulting distribution of rotational states. This rotationally cold beam was attenuated by a secondary beam formed by expanding pure HF, or Ar, at 1 atm (101 kPa) through an 80 μm diameter nozzle heated to about 500 K. The effective HF rotational temperature obtained in this case was considerably higher than those obtained for the various primary beams, corresponding to an appreciable population in each of the lowest three rotational states. By varying the secondary nozzle-skimmer distance (denoted by y in Figure 7.1) it was possible to adjust the primary beam attenuation in the range 0% ($\alpha=0$) to 100% ($\alpha=1$). The fractional attenuation α is defined so that $\alpha=0$ and $\alpha=1$ correspond to no attenuation and complete attenuation respectively.

Two detection systems were used to monitor the primary beam. Having been described in Chapter 2, only a brief summary of the salient features is given here. The first was a quadrupole mass spectrometer which, when tuned to the appropriate mass, gave a record of the total attenuation of the primary beam HF as a function of y . When used in conjunction with a time-of-flight chopper, the mass spectrometer also gave the velocity distributions for the beams, which were needed to determine the relevant collision energies and relative velocities. The energy of the

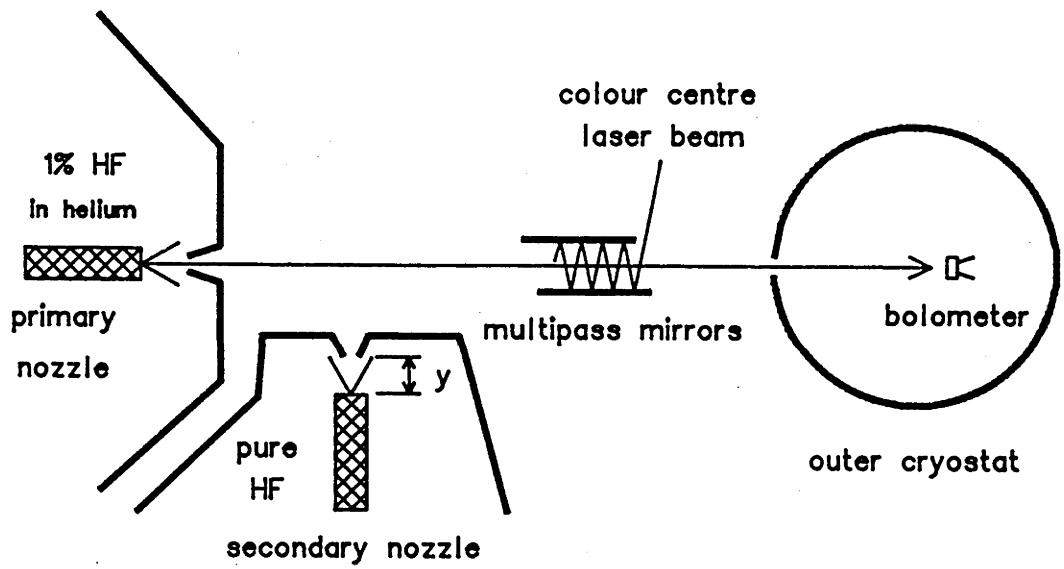


Figure 7.1

ionizing electrons used in these studies was 70 eV.

To obtain state specific information about the primary beam, a liquid helium cooled bolometer detector (bolometer A, as discussed in Chapter 2) was used in conjunction with the colour centre laser. In short, the bolometer monitors the increase in molecular energy corresponding to laser excitation from a specific rotational level. The magnitude of this signal, when corrected for laser power and dipole oscillator strength, is directly proportional to the population in the specified ground state (see Section 2.6). The multipass device shown in Figure 7.1 was used to increase the fraction of molecules excited by the laser. A room temperature pyroelectric detector was used, in much the same way as the bolometer, to measure the rotational distribution of the secondary beam HF. In order to monitor the number of molecules in a given rotational state for a time long enough to make the desired measurements, it was necessary to lock the output of the laser to a temperature stabilised 150 MHz FSR confocal etalon (see Section 2.5). To record a given population signal, the output of the bolometer (or pyroelectric detector) was detected using phase sensitive detection at the frequency used to chop the laser beam. A microcomputer was used to integrate the resulting signal for a time sufficiently long to average out the noise fluctuations. A discussion of the uncertainties associated with these measurements is given in the following section. For the $j=0$ and $j=1$ states the colour centre laser was tuned to the R0 and R1 transitions respectively. The P-branch lines P2 and P3 were used to monitor the $j=2$ and $j=3$ populations. Saturation effects were not included in obtaining the relative rotational populations from the monomer absorption signals. Gough and Miller (1983) measured the degree of saturation for supersonic beams of HF seeded in He interrogated by a colour

centre laser - bolometric detection system. The results of these studies indicate that saturation effects would be small under the conditions used to obtain the measurements reported in this chapter.

In summary, the experimental technique involves monitoring the populations of the primary beam j states as a function of the position of the secondary nozzle. If large resonant cross sections exist, the populations of the individual rotational states (in the primary beam) are expected to vary non-linearly as a function of the total attenuation of the primary beam HF. Examples of this behaviour are given in the following sections, along with the kinetic model used to extract the relevant cross sections.

We had originally intended to carry out the measurements using the crossed molecular beam geometry represented in Figure 7.1, so that the collision energy would be well defined. Indeed, the mean collision energy for the crossed beams was determined to be 240 ± 30 meV FWHM. However, it was found that most of the attenuation was attributable to background HF present in the scattering chamber, and not to the direct beam-beam interaction. This was partly a consequence of the fact that the nozzle-skimmer separations required to obtain attenuations greater than about 15 percent, (relative to the signal observed with the secondary beam off), were sufficiently small (less than 2 mm) to cause substantial skimmer interference. As a result, the HF beam was far from being an ideal supersonic beam, except for the smallest attenuations. In Figure 7.2 are shown the angular profiles of a low pressure secondary beam of argon for a number of different nozzle-skimmer separations, illustrating the onset of such beam degradation. At the smallest separation shown in the figure, the attenuation of the primary beam HF, resulting from an HF secondary beam,

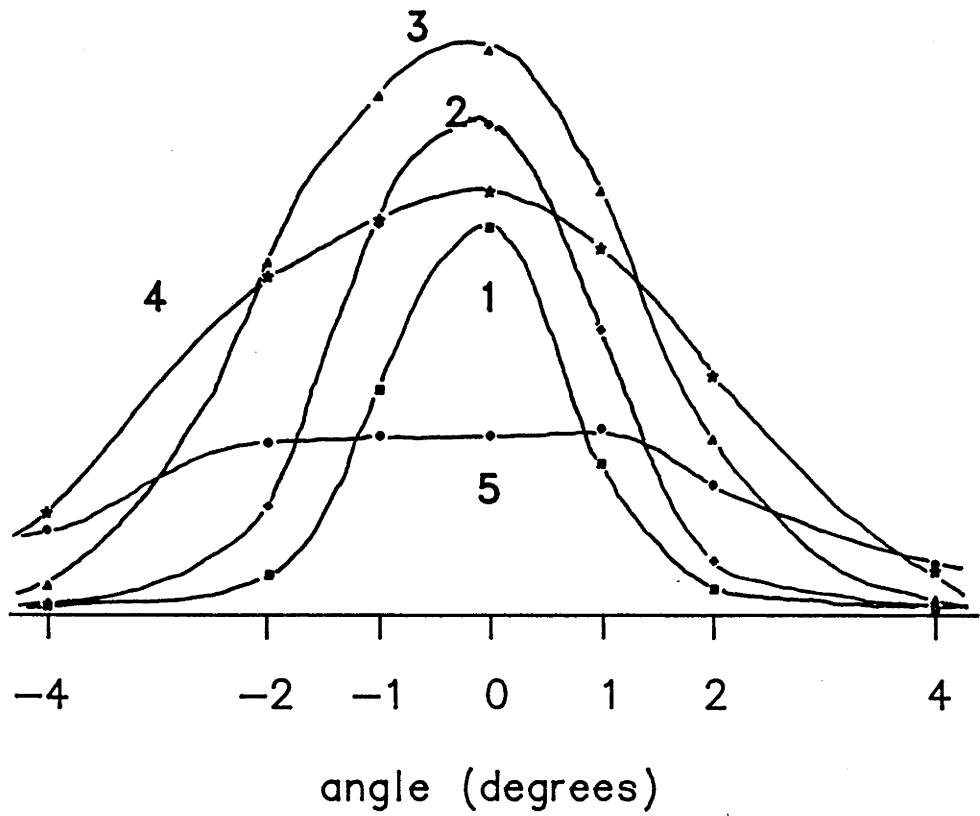


Figure 7.2

was about 15 percent. Other reasons for the large contribution from the background are the fact that a pure HF expansion does not produce an intense beam and that the scattering path length for the background gas was 15 to 20 times that for the direct beam-beam interaction. A liquid nitrogen cooled secondary beam dump was used to confirm that the majority of the attenuation was indeed attributable to the background HF. That the attenuation resulted primarily from background HF presented no problems, although it did mean that the collision energy was lower and less well defined than that for the crossed beam configuration. The mean collision energy can be calculated from the known velocity distributions. For the primary beam HF molecules we used the v^3 -Maxwellian distribution determined from a time of flight analysis (see Table 2.4), and the background HF molecules were assumed to obey a Maxwell-Boltzmann distribution $f_2(v) = v^2 \cdot \exp(-mv^2/2k_B T)$, with $T=300$ K. Averaging these distributions over the possible collision angles results in a mean collision speed of 1760 m/s and a mean collision energy of 170 meV. A summary of the relevant beam-beam and beam-background mean collision speeds and energies appears in Table 7.1.

Although it was not possible to obtain a reliable value for the background gas pressure in the scattering chamber, we estimate that at the higher attenuations it may have reached $4 \cdot 10^{-5}$ torr. The contribution to the background gas pressure from primary beam He or HF molecules was negligible. Noting that the scattering path length l for the background gas is about 0.7 m, and assuming a value of 230 \AA^2 for the effective HF-HF attenuation cross section σ , one predicts a value of 70 percent for the corresponding attenuation using the relation (see the following sections)

Table 7.1

System	μ (amu)	\bar{v} (m/s)	v_{rms} (m/s)	E (K)	E (meV)
HF/He + HF(boltz)	10	1760	1817	1985	171
HF/He + HF(beam)	10	2130	2142	2760	238
He + HF(boltz)	3.34	1860	1910	730	63.0
He + HF(beam)	3.34	2210	2221	990	85.3
HF/Ar + HF(boltz)	10	780	861	446	38.4
HF/Ar + HF(beam)	10	1420	1425	1221	105

$$\alpha = 1 - \exp(-n\sigma l) \quad (7.1)$$

where n is the number density of the scattering gas.

7.3 Results

A summary of the HF rotational population distributions for the secondary beam and the various primary beams is given in Table 7.2. The results for the secondary beam are those given in Chapter 4 for a supersonic expansion of pure HF under the same conditions as used in the present investigations. For the primary beam data two sets of figures are shown, the first corresponding to the populations obtained with the secondary beam operating with the largest nozzle-skimmer separation, and the second (shown in parentheses) giving the primary beam populations in the absence of any HF scatterers. The latter set was determined by extrapolating the attenuation curves to zero attenuation, using the measured value of approximately 5 percent obtained with the secondary beam operating and the largest nozzle-skimmer separation. In our original analysis we assumed that the attenuation corresponding to the largest nozzle-skimmer separation was zero. We note, however, that the results obtained by assuming zero attenuation at the largest nozzle-skimmer separation are identical to those obtained by assuming 5% attenuation. As expected, the number of molecules in the lower j states increases with the primary beam source pressure. For the background HF we assumed a Boltzmann distribution of rotational states corresponding to a temperature of 305 K. In Figure 7.3 we have plotted $\log[(2j+1)P_0/P_j]$ against $j(j+1)$ for these distributions, showing the characteristic deviation from linear behaviour resulting from a supersonic expansion.

The attenuation data obtained in these experiments can be used to extract the ratios of the exactly resonant cross sections to the total collision cross section. However, in order to obtain absolute cross

Table 7.2

primary beam source pressure (kPa)						
j	Boltzmann at 300 K	secondary beam	A 2170	B 1480	C 655	D 310
0	9.8	36.21	67.7 (68.8)	58.7 (59.7)	46.1 (46.5)	44.5 (45.2)
1	23.9	41.37	31.0 (30.6)	39.6 (39.4)	49.4 (49.8)	47.9 (48.2)
2	26.8	16.48	1.27 (0.46)	1.46 (0.67)	4.1 (3.3)	6.7 (5.9)
3	20.5	3.80	- (0.09)	0.26 (0.18)	0.47 (0.36)	0.87 (0.73)
4	11.8	1.14	- -	- -	- -	- -

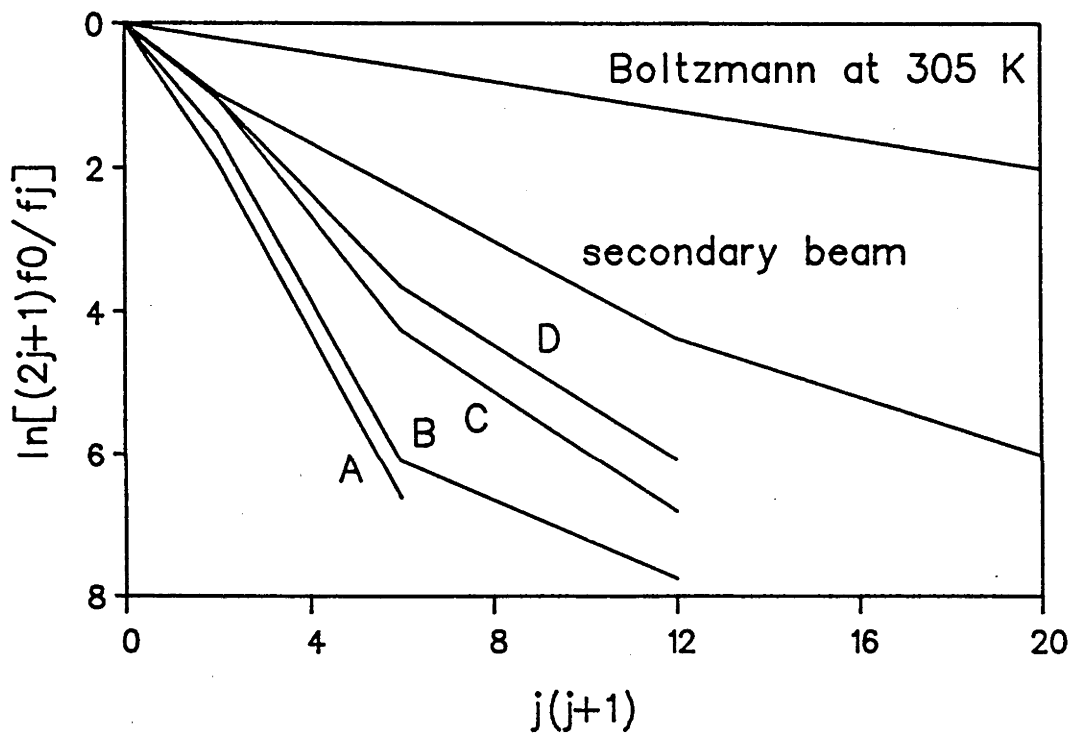


Figure 7.3

sections from these results, a value of the effective HF-HF total collision cross section was needed. We estimated its magnitude in the following way. A well collimated primary beam (FWHM = 0.4 degrees) was formed from a 1% mixture of HF in He. The mass spectrometer was used to measure the primary beam He and HF intensities with and without the secondary HF source operating and under conditions where the total HF-HF attenuation was between 5 and 10 percent. By using Eq. (7.1) to relate these measurements to the effective cross sections, the ratio of the HF-HF to the He-HF cross section was determined to be 3.3 ± 0.2 , with 0.2 representing two standard deviations in the spread of the measured values. It only remained then to determine the total collision cross section for He-HF. To estimate this latter cross section we used the HFD1A potential surface for the He-HF interaction reported in Chapter 4, which was determined by fitting to a series of total differential scattering intensities. Semi-classical calculations of the total integral cross section were made, as a function of the relative collision speed, for the spherical part of the HFD1A potential. When averaged over the possible collision angles and velocity distributions, the laboratory frame cross section was found to be 65.4 \AA^2 , assuming that the scattering was the result of background HF. If the scattering was assumed to be the result of the direct beam-beam interaction, a laboratory frame cross section of 68.6 \AA^2 was obtained. We note here that even at these low total HF-HF attenuations there was a significant amount of background attenuation present. An upper limit of 50 percent for this background contribution (at these low attenuations) was determined using a liquid nitrogen cooled secondary beam dump. By assuming the scattering to be wholly a result of the background, the total cross section for HF-HF, under conditions appropriate for comparison with the

attenuation measurements, was found to be approximately $216 \pm 15 \text{ \AA}^2$. If, on the other hand, the scattering at the low attenuations resulted purely from the direct beam-beam interaction, the predicted effective (primary beam HF) - (background HF) cross section was 263 \AA^2 . To obtain this last result we assumed that the effective total HF-HF cross section varies inversely with the relative collision speed. As the value $216 \pm 15 \text{ \AA}^2$ is expected to be a lower bound to the true effective (primary beam HF) - (background HF) cross section, we have used it in analysing these experiments.

Figure 7.4 shows state specific attenuation curves obtained at primary beam source pressures of 310, 655, 1480 and 2170 kPa. As indicated in the previous section, the total HF attenuation α was obtained as a function of the secondary nozzle-skimmer distance y using the mass spectrometer. The individual state populations P_j were measured over the same range of y using the laser-bolometer technique. The straight lines plotted for P_0 and P_1 represent the result expected if the individual states are attenuated in the same way as the total HF. In other words, they represent the case where all of the cross sections causing transfer between the primary beam rotational states are identically zero. It is seen that the experimental points deviate from this straight line behaviour. This deviation is substantial for $j=2$ and $j=3$, where the initial populations are very small. It is for these states, where $P_j \ll P_{j-1}$, that the effects of the resonant exchange processes are most clearly manifested and in fact lead to an increase in population with increasing attenuation.

It is important to note that cross sections associated with small impact parameter collisions do not contribute to the population transfer

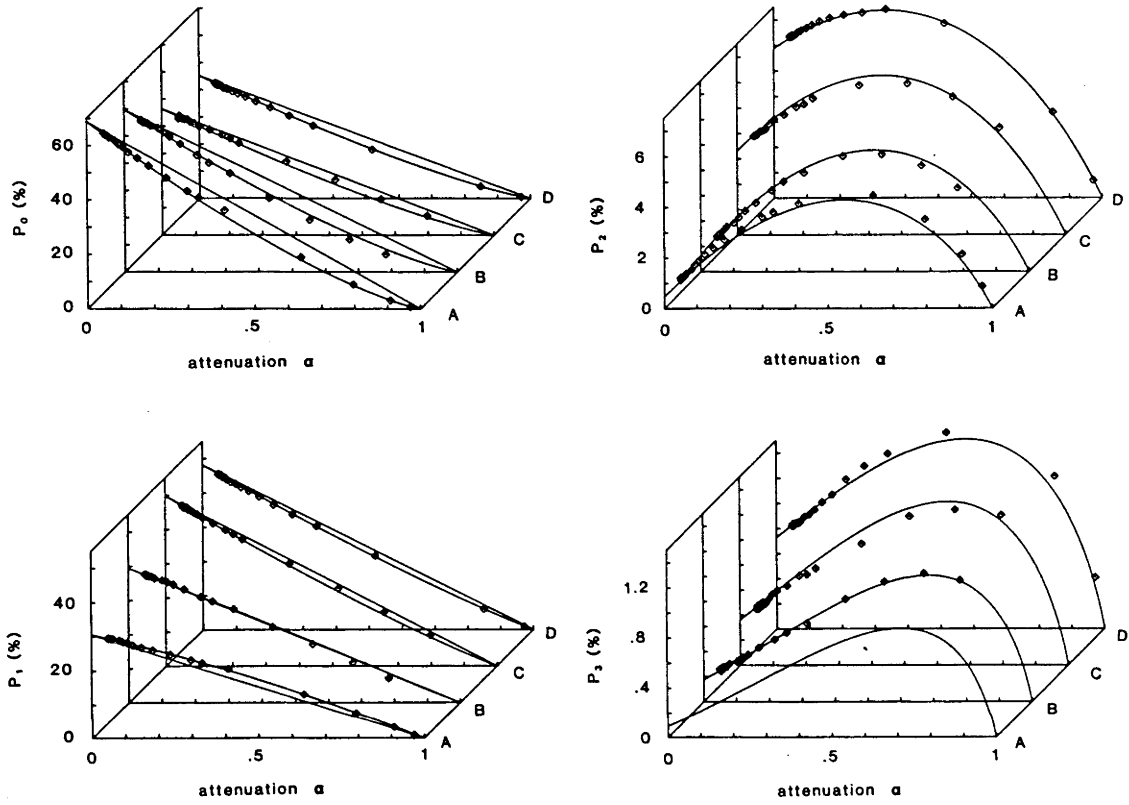


Figure 7.4

between primary beam rotational states, since collisions of this type cause the molecules to be deflected out of the beam. As a result, the important cross sections are those associated with the long range dipole coupled processes, which are strongly peaked in the forward direction ($\theta_{\text{LAB}} \approx 0$).

The following tests were performed in order to assess the reliability of the experimental techniques used. (1) The individual rotational populations were summed to give a laser-bolometer measurement of the total attenuation. When plotted against the total HF attenuation determined from the mass spectrometer measurements, the resulting plots were linear, as expected (see Figure 7.5). (2) By replacing the HF in the secondary beam by Ar, it was possible to check that the individual attenuation curves reproduced the results expected when all of the resonant cross sections are identically zero. As shown in Figure 7.6, linear attenuation curves were indeed obtained for the individual state populations. (3) To ensure that there was no direct contribution to the laser induced bolometer signal from the HF molecules in the background, the 1% HF in He mixture was replaced by pure He or Ar. In each case the laser induced bolometer signal was found to be zero under all attenuation conditions. This clearly indicates that there was no contribution to the signal from HF scattered from the background along the primary beam direction. These tests confirm that the non-linear attenuation curves, which were obtained with HF in both beam sources, resulted primarily from the rotational energy transfer between the cold primary beam HF and the room temperature Boltzmann distribution of the background HF molecules.

The major uncertainty in the measured rotational populations resulted from the uncertainty in the measured output power of the colour centre laser and from fluctuations of this power during a given attenuation

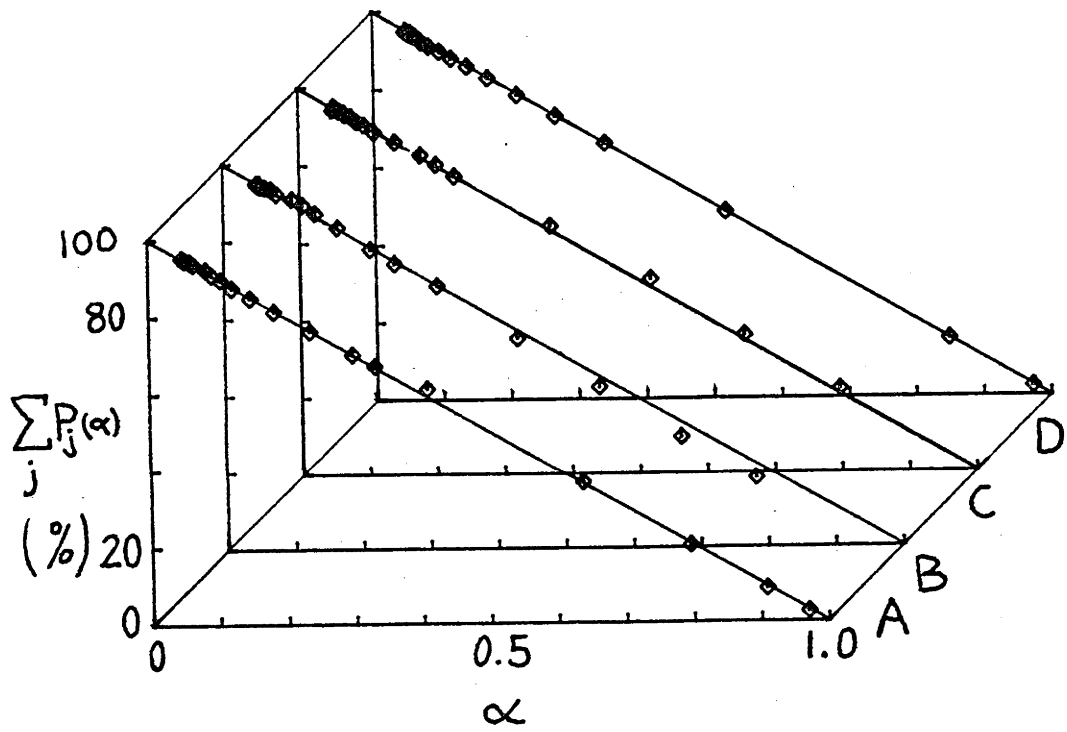


Figure 7.5

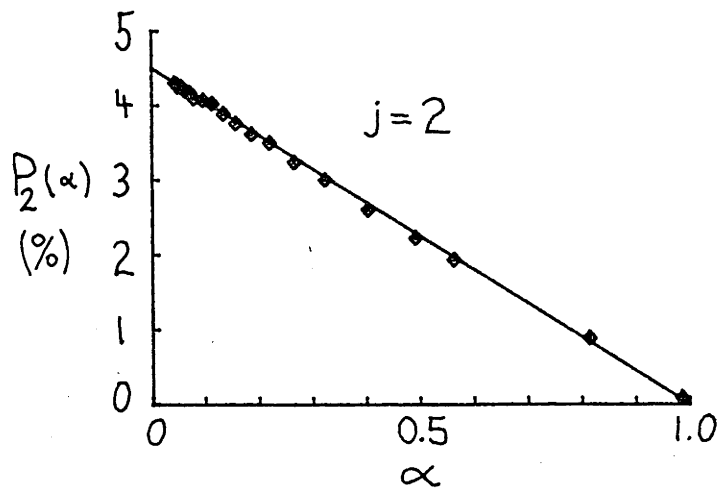
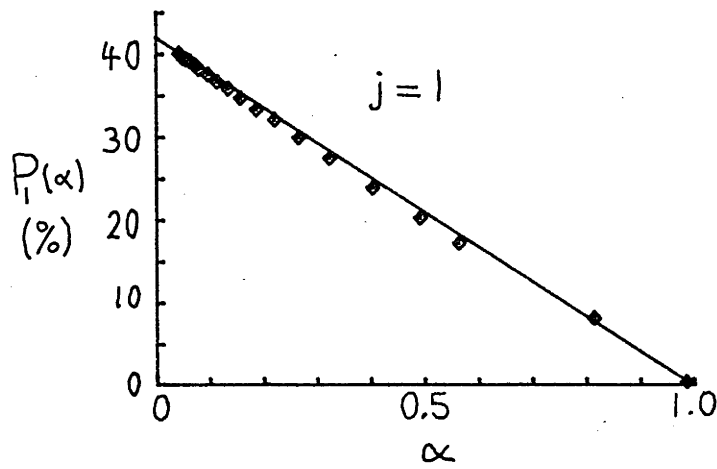
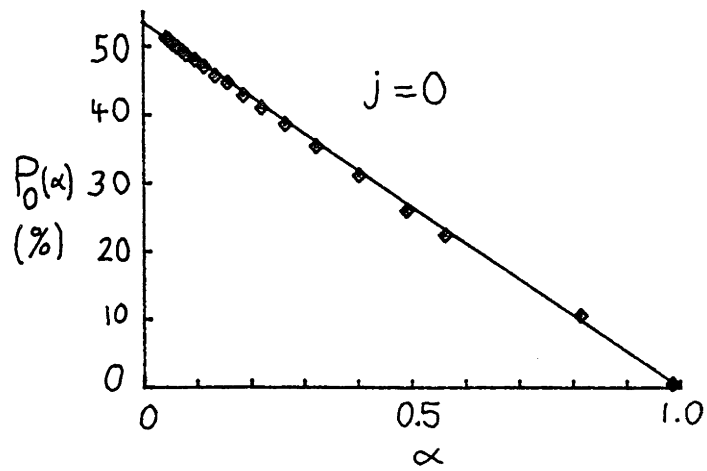


Figure 7.6

scan. Although it is also possible that the gain of the bolometer/lock-in amplifier detection system varied with time, we expect this latter variation to have been small. We note that when two successive attenuation scans were made for the same j , the results were found to be effectively identical. In view of the uncertainties involved in determining the laser power, we estimate that the true value corresponding to a given population datum lies within ± 5 percent of that datum.

Before discussing the analysis of the results, we consider the possible contribution from HF dimers and larger clusters formed in the primary beam expansions. Mass spectra of these expansions showed that the signals corresponding to the monomer mass were one or two orders of magnitude larger than those corresponding to the dimer and larger clusters, suggesting that most of the primary beam HF was present as monomer. Although the contribution to the monomer signals from the fragmentation of HF clusters is not known, we expect it to have been a small one. The total attenuation data recorded with the mass spectrometer set to the HF monomer mass therefore reflect the attenuation behaviour of the monomer component of the beam.

It is also possible that HF clusters present in the primary beam may have contributed to the laser-bolometer measurements. Except in the vicinity of the P2 transition, however, HF clusters do not absorb the wavelengths used to excite the HF monomer. Bryant and Watts (1986) measured linewidths of about 300 MHz for lines in the ν_2 band of the HF dimer, which are in the vicinity of the P2 monomer line. Given that the laser linewidth is much narrower than this value, we expect the dimer dissociation signal to be negligible compared to the the monomer absorption signal when the laser is tuned to the peak of the monomer transition.

7.4 Kinetic Model

In order to proceed further with the analysis of the data it is necessary to construct a model relating the observed attenuation curves to the appropriate cross sections. Defining $P_j(0)$ as the initial rotational population distribution of the primary beam (in the absence of the secondary beam) and n_j (where $\sum n_j = 1$) as the rotational state distribution of the scatterers, $P_j(x)$ can be shown to satisfy:

$$\begin{aligned} \frac{dP_j(x)}{dx} = & \left(-n \cdot \sigma_j - \sum_{i \neq j} n \cdot \sigma_{j \rightarrow i} \right) \cdot P_j(x) \\ & + \sum_{i \neq j} n \cdot \sigma_{i \rightarrow j} \cdot P_i(x) \end{aligned} \quad (7.2)$$

where x is the distance along the scattering path and n is the number density of the scattering gas, which is assumed to be constant throughout the scattering volume. The first term on the right hand side of Eq. (7.2) contains the rotational state dependent total cross sections σ_j which would, by themselves, lead to linear attenuation curves of the type obtained for HF scattered from Ar. This attenuation is the result of all processes deflecting molecules out of the primary beam. The second and third terms, on the other hand, represent processes which lead to a change in the rotational quantum number without deflecting the molecules out of the beam. In Eq. (7.2), $\sigma_{i \rightarrow j}$ has been defined as :

$$\sigma_{i \rightarrow j} = \sum_{k,l} n_k \cdot \sigma_{ik \rightarrow jl} \quad (7.3)$$

where $\sigma_{ik \rightarrow jl}$ represents the fully state resolved cross section for the process $\text{HF}_{\text{PB}}(i) + \text{HF}_{\text{bkgd}}(k) \rightarrow \text{HF}_{\text{PB}}(j) + \text{HF}_{\text{bkgd}}(l)$. The $\sigma_{i \rightarrow j}$'s are averaged

cross sections corresponding to the relaxation rate coefficients k_{ij} derived from the double resonance experiments discussed in Section 7.1.

Integrating Eq. (7.2) over the length of the scattering region gives the rotational populations in the primary beam downstream of the collision volume. By assuming that the rotational dependence of the total collision cross section is small, the σ_j 's can be replaced by a single effective cross section σ . This assumption was used previously in the analysis of polar-polar collision experiments by Dagdigian *et al.* (1979). The overall HF-HF attenuation α can then be expressed in terms of n, σ and l , the length of the scattering region, according to Eq. (7.1). To facilitate comparison with the experimental data, we can rewrite the expression for the primary beam populations in terms of α . Written in matrix form the final expression is:

$$\underline{P}(\alpha) = \exp(-\gamma \ln(1-\alpha)) \underline{P}(0) \quad (7.4)$$

where,

$$\gamma_{ij} = \begin{cases} -1 - \sum_{l \neq i} (\sigma_{i \rightarrow l} / \sigma) & i=j \\ (\sigma_{j \rightarrow i} / \sigma) & i \neq j \end{cases} \quad (7.5)$$

As expected, if all of the $\sigma_{i \rightarrow j}$'s are equal to zero then Eq. (7.4) reduces to:

$$P_j(\alpha) = (1-\alpha)P_j(0) \quad (7.6)$$

which reproduces the linear attenuation curves shown in Figure 7.3.

It is instructive to consider the solution for the simple case in which there are only two rotational states, so that $n_0 + n_1 = 1$. The only

rotational transfer present will be that which results from the cross section $\sigma_{01 \rightarrow 10}$. In this case, the populations of the two primary beam states, as a function of the attenuation α , are given by

$$P_0(\alpha) = n_0[P_0(0)+P_1(0)].(1-\alpha) + [n_1P_0(0)-n_0P_1(0)].(1-\alpha)^{1+\sigma_{01 \rightarrow 10}/\sigma} \quad (7.7)$$

and

$$P_1(\alpha) = n_1[P_0(0)+P_1(0)].(1-\alpha) - [n_1P_0(0)-n_0P_1(0)].(1-\alpha)^{1+\sigma_{01 \rightarrow 10}/\sigma} \quad (7.8)$$

We see that the magnitude of the cross section $\sigma_{01 \rightarrow 10}$ determines the functional form of the population transferred between the two states, namely $(1-\alpha)^{1+\sigma_{01 \rightarrow 10}/\sigma}$. The number of molecules transferred is directly proportional to both the primary beam population in the initial state and the number of scatterers present in the final state. If $P_0(0)$ is sufficiently greater than $P_1(0)$, then there will be a transfer of population from $j=0$ to $j=1$, with the $j=0$ curve, $P_0(\alpha)$, varying only slightly from the linear result expected in the absence of transfer. The $j=1$ population, being much smaller than that of the feeding state $j=0$, will be substantially perturbed by the molecules in $j=0$ which have resonantly transferred their rotational quanta with scatterers in $j=1$. Such large deviations from linearity are clearly shown in Figure 7.4 for $j=2$ and $j=3$, and are discussed further in the next section.

7.5 Analysis and Discussion

Strictly speaking, the state-to-state cross sections $\sigma_{ij \rightarrow kl}$ can only be obtained from a scattering experiment when both collision partners are state selected before the collision and the scattered molecules are selected thereafter. In the experiments discussed here the scatterers are distributed over a number of rotational states, so that in principle only the $\sigma_{i \rightarrow j}$'s can be determined from measurements of this type. At first sight it may appear as if even these cross sections are not directly probed, because of the distribution of rotational states initially populated in the primary beam. Indeed, in our initial attempts to extract a set of state-to-state cross sections from the data we were unable to determine a unique set without a prior knowledge of the relative importance of the cross sections used in the analysis. One might conclude from this that, in order to uniquely determine the state-to-state cross sections from experiments of this type, further state selection is required. However, as we will now show, if the near resonant processes can be neglected in comparison with the exactly resonant ones, the latter can be determined from the experimental results presented above.

Given that the first order dipole allowed transitions (which are expected to dominate polar-polar interactions), only involve changes of ± 1 in the rotational quantum numbers, and that the primary beam is sufficiently cold to make the ratio P_j/P_{j+1} large for all but $j=0$, the primary beam is effectively state selected. In other words, the population transfer into state j of the primary beam is primarily a result of transitions from $j-1$. Assuming that only the exactly resonant cross sections contribute, the background HF is also effectively state selected.

This is due to the fact that the transfer into a given state results entirely from background HF already in that state. For example, the transfer of primary beam molecules from the $j=1$ state to the $j=2$ state can only occur through interactions with $j=2$ in the background via $\sigma_{12 \rightarrow 21}$.

It must now be decided whether or not we are justified in neglecting the near resonant cross sections in comparison with the exactly resonant ones. On the basis of the energy gap arguments presented in Section 7.1 one would expect this to be the case. Further evidence supporting this proposition comes from the results of close coupled calculations performed by Alexander and Orlikowski (1984). These calculations were carried out at a collision energy of 228 meV. Their results show that, under conditions similar to those realised in our experiments, the exactly resonant cross sections are hundreds of square Ångstroms and the near resonant ones contribute only one or two square Ångstroms. A collision energy of 228 meV was used in these calculations because, when we supplied Alexander and Orlikowski with the collision energy, we assumed that the attenuation was due entirely to the direct beam-beam interaction, rather than the background HF. At the mean experimental energy of 170 meV, corresponding to primary beam HF molecules colliding with background HF molecules, the exactly resonant cross sections will, if anything, be larger while the near resonant ones should be smaller than at 228 meV. The near resonant cross sections can therefore be neglected in the analysis of our experiments.

A least squares minimisation algorithm was used to fit the model outlined in the previous section to the experimental data. For a given set of fitting parameters, the quantity minimised was the sum of squared relative deviations, the sum being taken over the experimental points. All

points were equally weighted, with the relative deviation defined by $(P_j(\alpha) - E_j(\alpha)) / E_{j,\max}(\alpha)$, where $E_j(\alpha)$ are the experimental points, $P_j(\alpha)$ the predicted values and $E_{j,\max}(\alpha)$ is the maximum experimental value of the curve to which the points in question belong. The data were found to be sufficiently sensitive to the values of the first and second order cross sections to allow their magnitudes to be estimated reasonably accurately, as determined by the degree of convergence of the least squares minimisation procedure. It was not possible, however, to determine the values of either the higher order resonant cross sections or the near resonant ones from these experimental data.

Although one might be tempted to allow all of the first and second order resonant cross sections to be varied independently in order to obtain a fit to the experimental data, when this is done one finds that one has too many free parameters to obtain a unique fit. To avoid this difficulty we considered a number of simplifying assumptions. The first of these was to allow the sizes of the first order cross sections to vary, but to fix their ratios according to the scaling relationship

$$\sigma_{j,j+1 \rightarrow j+1,j} = \frac{3(j+1)^2}{(2j+1)(2j+3)} \cdot \sigma_{01 \rightarrow 10} \quad (7.9)$$

which results from a sudden approximation treatment of the collision dynamics. A discussion of this result has been given by McFarlane and Richards (1981), and the same result has been used by Alexander and Orlikowski (1984) to determine rotational relaxation rates in HF. We also considered fixing the relative magnitudes of the second order resonant cross sections. As we were unable to find a scaling relationship similar to Eq. (7.9) for the second order processes, we chose either to make them

equal or to scale them according to the first order formula Eq. (7.9).

The results obtained by fitting independently to each of the four sets of data appear in Tables 7.3 and 7.4. These cross sections were determined using two adjustable parameters, namely a scaling factor for the first order cross sections and one for the second order ones. Ratios of the first order cross sections were determined by Eq. (7.9), and the analysis was done both with the second order processes equal (Table 7.3) and scaled (Table 7.4). Notice firstly that the second order cross sections for data set A are larger than those for the other data sets. The main reason for this is that the second order processes are determined primarily by the results for $j=3$, for which no experimental measurements were made for data set A. Secondly, it can be seen that, for a given data set, the size of $\sigma_{13 \rightarrow 31}$ is essentially independent of whether the second order cross sections are made equal or scaled. This reflects the fact that whereas $\sigma_{02 \rightarrow 20}$ and $\sigma_{24 \rightarrow 42}$ do not substantially affect the shapes of the attenuation curves, the shape of $P_3(\alpha)$ is quite sensitive to $\sigma_{13 \rightarrow 31}$.

By simultaneously fitting to all four sets of experimental data, one obtains the cross sections given in Table 7.5. From the fitting parameters given in the table it can be seen that one obtains slightly better agreement with the experimental data by scaling the second order cross sections, although both sets of cross sections give a good representation of the measured points. The solid lines through the data in Figure 7.4 correspond to the results given in Table 7.5 for the case of scaled second order cross sections. As discussed in Section 7.3, the effective HF-HF total collision cross section σ , needed to determine the absolute magnitudes of the resonant cross sections, was taken to be 216 \AA^2 .

Let us now consider the shapes of the attenuation curves more

Table 7.3

$ij \rightarrow ji$	A	B	C	D
01→10	336	309	308	335
12→21	270	248	248	269
23→32	258	237	237	257
34→43	254	234	233	253
02→20	53	42	36	41
13→31	53	42	36	41
24→42	53	42	36	41

Table 7.4

$ij \rightarrow ji$	A	B	C	D
01→10	288	286	295	319
12→21	232	230	237	256
23→32	222	220	227	245
34→43	218	217	223	241
02→20	70	54	47	54
13→31	56	43	37	43
24→42	54	42	36	42

Table 7.5

$ij \rightarrow ji$	second order equal	second order scaled
01→10	324	305
12→21	260	245
23→32	249	235
34→43	245	231
02→20	39	50
13→31	39	40
24→42	39	39
Σ	720	673

closely. The initial $j=0$ and $j=1$ populations are always sufficiently large for the overall attenuation σ to dominate. As a result, the curves for these states are almost linear. In all cases there is a net transfer of molecules out of the $j=0$ state, resulting in attenuation curves which lie slightly below the linear ones. The $j=1$ state, on the other hand, shows deviations both above and below the straight line. When its initial population is small, the transfer into $j=1$ exceeds the transfer out and the attenuation curve lies above the line (curve P_1 -A of Figure 7.4). As the source pressure is decreased, the population in $j=1$ increases and there is a net transfer out of $j=1$. At a primary beam source pressure of 1480 kPa the transfer rates into and out of $j=1$ clearly cancel (curve P_1 -B).

For the $j=2$ and $j=3$ states the initial populations are so small that rotational energy exchange processes from the more populous primary beam states, rather than the overall attenuation, dominate their behaviour. Since the population transfer into these states is substantially larger than the transfer out, the resulting attenuation curves lie well above the linear ones. Consider the $j=2$ state. The transfer of molecules from $j=1$ into $j=2$ is dominated by the term $P_1(\alpha) \cdot \sigma_{12 \rightarrow 21}$. Since $P_1(\alpha)$ has its maximum at $\alpha=0$ and decreases linearly with α , the $j=2$ attenuation curve has its maximum slope at $\alpha=0$ and is essentially quadratic in shape. Indeed, if only the $j=0$ and $j=1$ states of the primary beam contribute to the transfer into $j=2$, and $P_0(\alpha)$ and $P_1(\alpha)$ are linear with α , then $P_2(\alpha) = a(1-\alpha) - b(1-\alpha)^2$, where a and b are constants. This result follows from Eq. (7.4) if we use the best fit cross sections with the second order cross sections scaled. The contribution to the transfer of molecules into the $j=2$ state from the second order dipole allowed processes is proportional to $P_0(\alpha) \cdot \sigma_{02 \rightarrow 20}$. Since $P_0(\alpha) \approx P_1(\alpha)$ at all of the source pressures

considered here, and $\sigma_{02 \rightarrow 20} \ll \sigma_{12 \rightarrow 21}$, the contribution from the second order process can be neglected in this case.

Although a good fit could be obtained to the $j=0,1$ and 2 states without using the second order resonant cross sections, this was not possible for $j=3$. The reason for this is that the $j=3$ attenuation curve is more sensitive to the second order process because the state from which it is fed by the first order process, namely $j=2$, has only a small fraction of the total population. The second order process $13 \rightarrow 31$, on the other hand, couples $j=3$ to the much more populous $j=1$ state. As a result, even though the second order cross section is rather small, the population transferred from $j=1$ to $j=3$ cannot be neglected. Since the $j=1$ and $j=2$ attenuation curves have distinctly different shapes, the relative magnitudes of the first and second order cross sections will determine the shape of the $j=3$ attenuation curve. This is best seen by examining the $j=3$ attenuation results obtained at a source pressure of 1480 kPa. Each curve shown in Figure 7.7 was obtained by fixing the sizes of the second order cross sections and then adjusting the first order ones to obtain the best least squares fit to the four sets of data. The resulting cross sections appear in Table 7.6. Each set of cross sections was obtained by fixing the second order ones and using $\sigma_{01 \rightarrow 10}$, $\sigma_{12 \rightarrow 21}$ and $\sigma_{23 \rightarrow 32}$ as the free parameters in the fitting routine. $\sigma_{34 \rightarrow 43}$ was set equal to $\sigma_{23 \rightarrow 32}$. It was necessary to abandon the scaling relationship Eq. (7.9) and independently vary the first order cross sections in order to obtain reasonable fits to all of the data.

Consider the case where the second order processes are assumed to be zero. In this case the model curve increases rather slowly at small attenuations, with the slope increasing to an inflection point and the peak value occurring at a higher attenuation than obtained for $j=2$. The absence

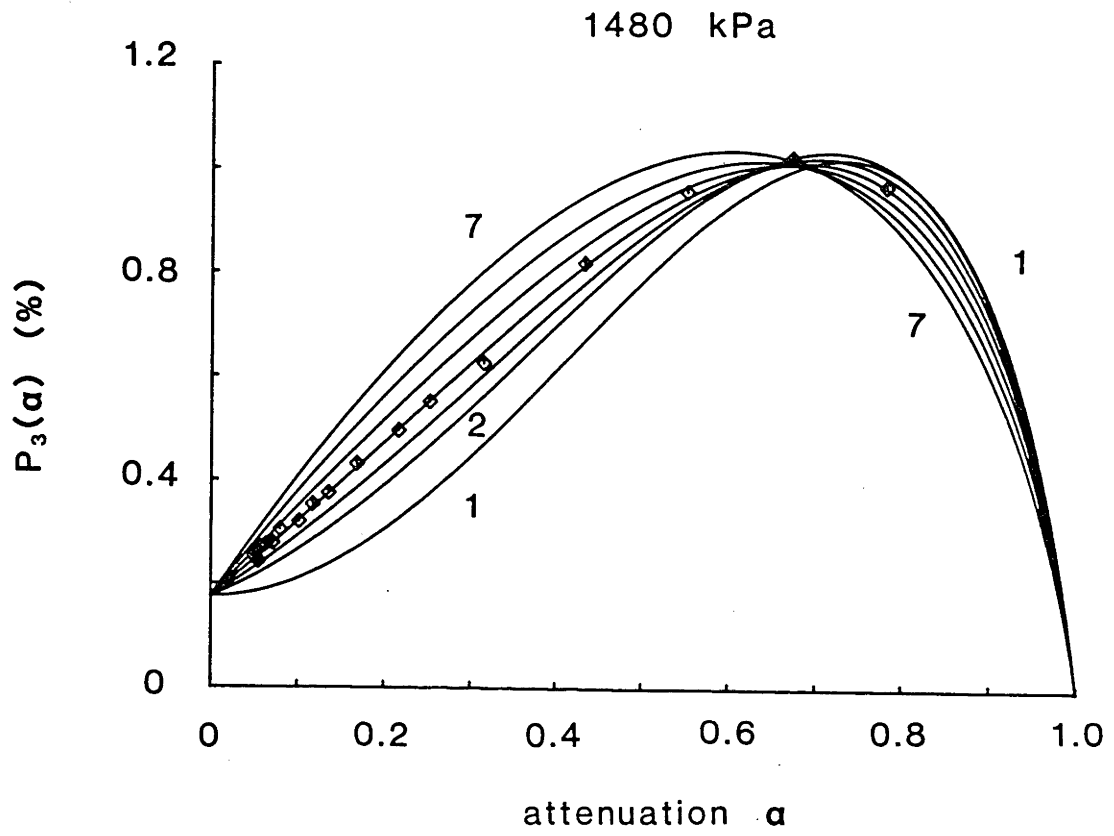


Figure 7.7

Table 7.6

$ij \rightarrow ji$	1	2	3	4	5	6	7
01→10	398	364	346	327	307	287	264
12→21	329	297	277	258	238	218	198
23→32	527	395	318	244	171	100	32
34→43	527	395	318	244	171	100	32
02→20	0	20	30	40	50	60	70
13→31	0	20	30	40	50	60	70
24→42	0	20	30	40	50	60	70
Σ	2159	1038	778	723	914	1402	2249

of second order cross sections means that only the $j=2$ state, which has its maximum population at non-zero attenuation, feeds into $j=3$. As the second order cross sections are increased, the inflection in the curve becomes less pronounced and the model curve reproduces the data rather well. If the second order resonant cross sections are made larger still, the increased flow from $j=1$ to $j=3$ results in a shape very similar to that seen for $j=2$ at the same pressure. The shapes of the attenuation curves can therefore be used to fix the relative magnitudes of the first and second order resonant cross sections.

The best fit to the experimental data is obtained when the second order cross sections are 40 \AA^2 . In this case, the independently fitted first order cross sections scale almost exactly according to Eq. (7.9), and the resulting cross sections are the same as those given in Table 7.5 for the case of equal second order processes. Note also that the ratio of second to first order cross sections giving the best fit to the data is approximately 0.1, which is similar to the ratios of the corresponding near resonant cross sections obtained by Alexander (1980). Although scattering experiments are often carried out under conditions of low attenuation, the wide range of attenuations used in these experiments enabled us to extract information which could not be determined from the low attenuation regime alone.

From the best fits to the experimental data given in Table 7.5, we obtain a value of approximately 310 \AA^2 for the $01 \rightarrow 10$ resonant cross section. When comparing this value with the results of other studies, experimental or theoretical, the following points should be borne in mind:

- (1) Most calculations predict integral cross sections, whereas the experiment probes the corresponding differential cross sections about

$\theta_{\text{LAB}}=0$. In view of the fact that the perfectly resonant processes are highly peaked in the forward direction, this difference should not be too great; (2) The experimentally derived cross sections are laboratory frame cross sections which have been averaged over the velocity distributions of the collision partners, whereas most calculations are reported at a single centre of mass frame collision energy; and (3) In view of the uncertainties involved in determining the absolute (as opposed to relative) sizes of the cross sections (see Section 7.3), the value of 310 \AA^2 should be treated as a lower bound to the true value of the $01 \rightarrow 10$ cross section. Laboratory frame integral cross sections are related to the corresponding centre of mass cross sections by the formula $\sigma_{\text{lab}} = (g/v_1) \cdot \sigma_{\text{c-of-m}}$, where g is the relative velocity and v_1 is the speed of the particle being detected (Pauly and Toennies (1968)). For primary beam HF molecules colliding with background HF molecules the average value of g/v_1 is unity. It is therefore not unreasonable to compare our laboratory frame cross sections with calculated centre of mass frame cross sections.

Consider the result of a simple linear trajectory calculation, discussed by Mason and Monchick (1962) and Nyeland *et al.* (1972), which predicts a cross section of approximately $0.47(2\pi^3\mu^2/hv)$ for the collision of two polar molecules with dipole moment μ travelling at a relative speed v . h is Planck's constant. For two HF molecules travelling at 1760 m/s, the mean collision speed of the present experiments, one obtains a cross section of about 840 \AA^2 . A calculation of this type is expected to overestimate the size of the cross section and, although it is rather crude, it does provide an upper bound to the true value. That this should be the case is supported by the close-coupled calculations of Alexander and Orlikowski (1984), who obtained a value of 241 \AA^2 for $01 \rightarrow 10$ centre of mass

frame integral cross section for HF-HF collisions at a 228 meV. The linear trajectory result at the same energy is 695 \AA^2 . If we scale the value obtained by Alexander and Orlikowski (1984) using the expected $1/v$ velocity dependence for dipole-dipole interactions, we obtain about 280 \AA^2 for the $01 \rightarrow 10$ cross section at 170 meV, in reasonable agreement with our value, albeit a lower bound, of 310 \AA^2 . Finally we note that the impact parameter close-coupling studies carried out by Takayanagi and Wada (1985) give a $01 \rightarrow 10$ cross section of approximately 395 \AA^2 at a mean collision energy of 170 meV.

In their reanalysis of their earlier double resonance experiments on the rotational self-relaxation of HF, Copeland and Crim (1984) were able to fit their data with, among others, the rate constants $k_{0 \rightarrow 1} = 8.37 \times 10^{-10}$, $k_{1 \rightarrow 2} = 4.8 \times 10^{-10}$ and $k_{2 \rightarrow 3} = 2.35 \times 10^{-10} \text{ cm}^3/\text{molecule/s}$. In view of the beam results presented here, it would be instructive to estimate the sizes of the $ij \rightarrow ji$ cross sections corresponding to these rate constants, assuming that these $ij \rightarrow ji$ cross sections completely dominate the relaxation. The possibility that the double resonance results of Copeland and Crim might be explained using first order resonant cross sections alone was first considered by Alexander and Orlikowski (1984). We can use the expression $k = v\sigma$ to relate the rate constants to cross sections, using the mean relative velocity $v = 775 \text{ m/s}$ for a 300 K sample of HF, and then use Eq. (7.3) to determine the desired resonant cross sections. By scaling the resulting values to our mean experimental relative velocity of 1760 m/s , assuming the $1/v$ dependence characteristic of dipole coupled processes, we obtain $\sigma_{01 \rightarrow 10} = 200 \text{ \AA}^2$, $\sigma_{12 \rightarrow 21} = 90 \text{ \AA}^2$ and $\sigma_{23 \rightarrow 32} = 65 \text{ \AA}^2$. These values are substantially lower than our estimates, which we expect to be lower bounds to the true values. It is important to note that our cross sections cannot

be compared directly with those derived from the double resonance experiments since, in the latter studies, the two HF molecules are in different vibrational states, with the result that the $ij \rightarrow ji$ processes are not exactly resonant.

Two points pertaining to the quantitative analysis of the experimental results deserve mention. Firstly, we assumed that all of the attenuation resulted from the background gas in the scattering chamber. Clearly, there was a contribution from the direct beam-beam interaction. Since the secondary beam rotational distribution is not the same as that for the background, this may have had some effect on the derived cross sections. Although our experiments with a secondary beam cryotrap indicated that this contribution was small, its exact value and its dependence upon nozzle-skimmer separation are uncertain. Secondly, it was assumed that the processes causing population transfer acted over the same distance as those resulting in the removal of primary beam HF (ie. those determining the attenuation α). After laser excitation, however, only the attenuation processes are effective in altering the experimental results. Whilst this is probably the greatest uncertainty present in determining the absolute magnitudes of the cross sections, we note that including this effect would increase the sizes of the cross sections obtained. In view of this second point and of the problems involved in determining the effective HF-HF attenuation cross section, discussed earlier, we stress that the absolute magnitudes of the cross sections presented here are lower bounds to the true values. The relative magnitudes of the cross sections, however, are independent of these considerations, and we expect their accuracy to depend primarily upon the uncertainties present in the experimental data.

7.6 Conclusion

Molecular beam techniques have been used in conjunction with laser-bolometer detection to study the rotational energy transfer between HF molecules in the ground vibrational state. The results of these experiments are consistent with the hypothesis that resonant rotational energy transfer cross sections dominate the observed interactions. Indeed, the first order ($\Delta j=1$) exactly resonant cross sections were found to be several hundred square Ångstroms. A lower bound of 310 \AA^2 was obtained for the $0_1 \rightarrow 1_0$ cross section at a mean collision speed of 1760 m/s. Second order ($\Delta j=2$) resonant cross sections were also required in order to obtain a good fit to the experimental data. The second order cross sections were found to be about 13 percent the size of the first order ones. Our results are in qualitative agreement with the close-coupled calculations carried out by Alexander and Orlikowski (1984).

In these experiments a beam containing HF was attenuated by a thermal distribution of HF scatterers. Effective state selection of the scatterers resulted from the fact that the first order, exactly resonant, cross sections were known to dominate the observed scattering. Further progress could be made by performing beam-beam measurements in which a second laser is used to modulate the secondary beam rotational population distribution. Since an experiment of this type does not rely upon the magnitudes of the cross sections to give state selection, it could be used to accurately determine the sizes of the near resonant and higher order cross sections.

Chapter Eight

Summary and Conclusions

Molecular beam scattering and spectroscopic techniques were used to study the behaviour of a number of atom-molecule and molecule-molecule systems. In this chapter we summarise the results reported in this thesis and discuss a number of avenues for further investigation.

A study of the scattering of He from HF is reported in Chapter 4. Total integral and differential cross sections were calculated using the spherical potential (single channel), infinite order sudden and l-average coupled states approximations. The anisotropic HFD1 interaction potential developed by Rodwell et al. (1981) was used, with collision energies of 480 and 950 K (41.4 and 81.9 meV) being considered. Cross sections calculated using the three approximations are in good agreement, indicating that the spherical part of the He-HF interaction potential leads to a good description of the total scattering at these collision energies. Total differential scattering intensities measured by Boughton (1986) were analysed using the spherical potential approximation. The HFD1 potential reported by Rodwell et al. (1981) leads to reasonable agreement with these experimental data. An analytic spherical potential resulting in better agreement was developed. By considering only total differential scattering measurements, it is not possible to assess the accuracy of the anisotropic parts of the He-HF interaction potential. The l-average coupled states approximation was used to investigate the role of inelastic processes. A comparison with the close coupled and infinite order sudden results reported by Battaglia et al. (1982b) showed that, unlike the infinite order

sudden approximation, the l -average coupled states method gives an adequate description of the inelastic differential scattering. Given the small magnitudes of the calculated inelastic differential scattering intensities, substantial improvements in the sensitivity of state selective scattering techniques will be required to enable their detailed experimental investigation.

Measured total differential scattering intensities for the scattering of Ar from HF are reported in Chapter 4. A clearly resolved primary rainbow peak was observed. Scattering calculations were carried out using the Ar-HF interaction potentials discussed by Hutson and Howard (1982b) and Douketis *et al.* (1984) for a collision geometry similar to the mean experimental geometry. Significant differences were found between the differential scattering intensities predicted using the spherical potential, infinite order sudden and l -average coupled states approximations, which was not the case for the He-HF system. We therefore chose to use the coupled states approximation to compare the measured intensities with the calculated ones. Of the potentials considered, only the M5 potential (Hutson and Howard (1982b)) gives an adequate representation of the measured scattering intensities. This potential is also able to correctly predict the known spectroscopy for the Ar-HF and Ar-DF systems (indeed, it was obtained by fitting to such data).

An investigation of the state-to-state cross sections was also carried out for the Ar-HF system using the l -average coupled states approximation. Inelastic integral cross sections predicted by the M5 potential are in good agreement with the measurements carried out by Barnes *et al.* (1982). The $0 \rightarrow 1$ differential cross section, which accounts for about 25% of the total differential cross section in the vicinity of the

primary rainbow peak, is two orders of magnitude larger than the corresponding cross section calculated for He-HF. Unfortunately, the difference between the laboratory frame velocities of elastically scattered HF molecules and those undergoing $0 \rightarrow 1$ excitation, which is about 2%, is too small to readily allow their resolution using time-of-flight techniques. Perhaps the use of sufficiently sensitive laser-based state selective methods will allow the measurement of these inelastic cross sections. Lastly, as was found for Xe-HF by Becker *et al.* (1979) and for Ar-HCl by Buck and Schleusener (1981), the shapes of the elastic $j \rightarrow j$ differential cross sections for Ar-HF depend significantly upon the value of j . By considering the behaviour of the partial integral cross sections, or opacities, as a function of the orbital angular momentum quantum number, it was possible to relate these differences, for a given interaction potential, to the details of the potential in the vicinity of the attractive bowl.

A colour centre laser was used in conjunction with molecular beam techniques and bolometric detection to study the behaviour of van der Waals clusters of acetylene (C_2H_2), ethylene (C_2H_4) and methyl acetylene (C_3H_4) upon laser excitation in the range 3000 to 3300 cm^{-1} . These results are reported in Chapter 6. The acetylene and methyl acetylene cluster spectra were found to change dramatically as a function of the conditions under which the expansions were formed, which determined both the range of cluster sizes present and their effective temperature. Six dissociation bands were seen in the low resolution spectrum of acetylene clusters (resolution $\approx 0.4 cm^{-1}$), four of which are attributed to the dimer. By analysing the lineshapes of individual rovibrational transitions from each of the bands (measured with the laser operating in single mode), estimates

ranging from 1.6 to >80 ns were obtained for the lifetimes of the initially excited states of the clusters. The pressure dependence of both the mass spectra and the infrared spectra of acetylene cluster containing molecular beams were used to assess the contributions from different cluster sizes. Although it was possible to associate the bands of the low resolution spectra with given cluster sizes, the structures of these clusters could not be obtained. An obvious next step in the analysis of these van der Waals systems is to measure the full rovibrational spectra of each of the bands observed under low resolution. The results of such investigations should allow the structures of the relevant clusters to be unambiguously determined. Low resolution spectra observed for methyl acetylene were qualitatively similar to those for acetylene. A linewidth derived lifetime of 0.4 ns was determined from the rovibrational transitions observed in one of the bands of the low resolution spectrum.

Although the spectra of small clusters of acetylene and methyl acetylene showed rather rich structure under both high and low resolution, this was not the case for ethylene clusters. The low resolution spectra obtained using molecular beams containing predominantly ethylene monomers and dimers show a single peak about 5 cm^{-1} wide, in agreement with the results obtained by Fischer *et al.* (1983). A high resolution investigation of this peak failed to uncover any structure, indicating the presence of substantial homogeneous broadening superimposed upon the much narrower rovibrational contour of the excited cluster. By assuming that the 5 cm^{-1} width of the observed ethylene cluster spectrum is due mainly to lifetime broadening effects, a lifetime estimate of about 1 ps is obtained.

The details of the dynamical processes responsible for the complex spectra observed for small acetylene and methyl acetylene clusters on the

one hand, and the rather simple spectra seen for ethylene clusters on the other are, at present, not well understood. It is not clear why small ethylene clusters, which are of a similar complexity to those of methyl acetylene, behave so differently. Perhaps direct investigations of the dissociation process using time domain techniques, such as those used by Mitchell *et al.* (1985), will help to uncover the details of the dynamical behaviour of small van der Waals molecules.

A study of the transfer of rotational energy between HF molecules in the ground vibrational state is reported in Chapter 7. Molecular beam scattering methods were combined with laser-bolometer spectroscopic techniques to estimate the magnitudes of some of these cross sections. The results are consistent with the hypothesis that resonant rotational energy transfer cross sections dominate the observed interactions. A lower bound of 310 square Ångstroms was obtained for the $j=0, j=1 \rightarrow j=1, j=0$ cross section at a mean collision speed of 1760 m/s. These results are in qualitative agreement with the close coupled calculations performed by Alexander and Orlikowski (1984). Second order resonant cross sections, with $\Delta j=2$, were also required to obtain a good fit to the experimental data. The second order cross sections were found to be about 40 square Ångstroms. The experiments reported in Chapter 7 were carried out by attenuating an HF containing primary beam with a thermal distribution of HF scatterers. Effective state selection of the scatterers resulted from the fact that the $j, j-1 \rightarrow j-1, j$ cross sections were known to dominate the scattering. Further progress could be made by performing beam-beam measurements in which a second laser is used to modulate the secondary beam rotational population distribution. Experiment of this kind could, in principle, be used to estimate cross sections for processes other than the

resonant processes. The small signals which would be obtained from such experiments, however, would make them rather difficult to carry out successfully. Another possibility would be to use a scattering cell containing pure HF to attenuate the primary beam, so that experiments could be carried out over a range of temperatures of the scatterers. By also varying the conditions used to form the primary beam (ie., the mixture used, the nozzle temperature and the pressure), one could obtain information about the energy dependence of the measured cross sections.

The major results and conclusions of the research work described in this thesis are summarised below:

(1) the total scattering cross sections for low energy He-HF collisions are well described using the spherical part of the interaction potential;

(2) the 1-average coupled states approximation, with the correct phase choice (Khare et al. (1980)) gives a good description of the inelastic scattering cross sections for He-HF;

(3) an analytic spherical potential was determined for the He-HF interaction by fitting to available scattering data;

(4) total differential scattering intensities measured for Ar-HF show a well resolved primary rainbow peak;

(5) the spherical potential and infinite order sudden approximations do not adequately describe the total scattering cross sections for the Ar-HF system;

(6) of the available interaction potentials for Ar-HF, the M5 potential developed by Hutson and Howard (1982b) is recommended for its ability to reproduce both the known spectroscopic data (Hutson and Howard (1982b)) and the total differential scattering intensities reported in this

thesis. Coupled states calculations were used to compare the calculated cross sections with the measured ones;

(7) the differences between the shapes of the total differential cross sections predicted using the available potential surfaces are related to the shapes of the elastic cross sections in the vicinity of the primary rainbow peak, which are in turn sensitive to the behaviour of the given potentials in the region of the minimum;

(8) the infrared spectrum of small clusters of acetylene (C_2H_2) in the vicinity of 3300 cm^{-1} was measured. Six bands were seen using a resolution of about 0.4 cm^{-1} , four of which were assigned to the dimer. Individual rovibrational transitions could be observed from each of the six bands. Estimates of the lifetimes obtained from the homogeneous widths of these transitions range from 1.6 ns to >80 ns;

(9) the low resolution spectrum observed for small clusters of methyl acetylene has features similar to those seen for acetylene clusters. Homogeneous widths of the individual rovibrational transitions resolved from one of the bands in the low resolution spectrum correspond to a lifetime of 0.4 ns;

(10) under conditions where the dimer is the only cluster present in significant concentrations, the observed ethylene spectrum is dominated by substantial homogeneous broadening, resulting in an estimate of 1 ps for the lifetime of the excited cluster;

(11) the observed rotational energy transfer between HF molecules was dominated by first order dipole allowed resonant processes of the type $j, j+1 \rightarrow j+1, j$. A lower bound of 310 \AA^2 was determined for the $j=0, j=1 \rightarrow j=1, j=0$ cross section. Second order cross sections are about 40 \AA^2 .

References

- Abramowitz M. and Stegun I.A. (1970), Handbook of Mathematical Functions,
Dover Publications, New York.
- Anderson P.W. (1949), Phys. Rev. 76, 647.
- Anderson J.B. and Fenn J.B. (1965), Phys. Fluids 8, 780.
- Andres J., Buck U., Huisken F., Schleusener J. and Torello F. (1980),
J. Chem. Phys. 73, 5620.
- Andres J., Buck U., Meyer H. and Launay J.M. (1982), J. Chem. Phys.
76, 1417.
- Alexander M.H. (1979), J. Chem. Phys. 71, 1683.
- Alexander M.H., Jendrek E.F. and Dagdigian P.J. (1980), J. Chem. Phys. 73,
3798.
- Alexander M.H. (1980), J. Chem. Phys. 73, 5135.
- Alexander M.H. (1984), J. Chem. Phys. 81, 4510.
- Alexander M.H. and Orlikowski T. (1984), private communication.
- Arthurs A.M. and Dalgarno A. (1960), Proc. Royal Soc. London A 256, 540.
- Ashton C.J., Child M.S. and Hutson J.M. (1983), J. Chem. Phys. 78, 4025.
- Aziz R.A., Presley J., Buck U. and Schleusener J. (1979a), J. Chem. Phys.
70, 4737.
- Aziz R.A., Riley P.W., Buck U., Maneke G., Schleusener J., Scoles G. and
Valbusa U. (1979b), J. Chem. Phys. 71, 2637.
- Aziz R.A. and van Dalen A. (1983), J. Chem. Phys. 78, 2413.
- BelBruno J.J., Gelfand J. and Rabitz H. (1981), J. Chem. Phys. 75, 4927.
- Baker C.E. and Brokow R.S. (1965), J. Chem. Phys. 43, 3519.
- Baldwin K.G.H. and Watts R.O. (1986), private communication.
- Balle T.J., Campbell E.J., Keenan M.R. and Flygare W.H. (1979), J. Chem.

Phys. 71, 2723.

Balle T.J., Campbell E.J., Keenan M.R. and Flygare W.H. (1980), J. Chem.

Phys. 72, 922.

Barker J.A. and Pompe A. (1968), Aust. J. Chem. 21, 1683.

Barker J.A. and Bobetic M.V. (1970), Phys. Rev. B 2, 4169.

Barker J.A., Fischer R.A. and Watts R.O. (1971), Mol. Phys. 21, 657.

Barnes J.A., Keil M., Kutina R.E. and Polanyi J.C. (1980), J. Chem. Phys.

72, 6306.

Barnes J.A., Keil M., Kutina R.E. and Polanyi J.C. (1982), J. Chem. Phys.

76, 913.

Battaglia F. and Gianturco F.A. (1981), Chem. Phys. 55, 283.

Battaglia F., Gianturco F.A. and Palma A. (1984a), Chem. Phys. 84, 233.

Battaglia F., Gianturco F.A. and Palma A. (1984b), J. Chem. Phys. 80, 4997.

Becker C.H., Tiedemann P.W., Valentini J.J., Lee Y.T. and Walker R.B.

(1979). J. Chem. Phys. 71, 481.

Beijerinck H.C.W. and Verster N.F. (1981), Physica C 111, 327.

Bergman K, Hefter U. and Witt J. (1980), J. Chem. Phys. 72, 4777.

Bernstein R.B. (1960), J. Chem. Phys. 33, 795.

Bernstein R.B. (editor) (1979), Atom-Molecule Collision Theory: "A Guide for the Experimentalist", Plenum Press, New York.

Bernstein R.B. (1982), Chemical Dynamics via Molecular Beam and Laser Techniques, Clarendon Press, Oxford.

Beswick J.A. and Jortner J. (1977), Chem. Phys. Letts. 49, 13.

Beswick J.A. and Jortner J. (1978), J. Chem. Phys. 68, 2277.

Beswick J.A. and Jortner J. (1981), Adv. Chem. Phys. 47, 363.

Bhattacharyya S.S., Saha S. and Barua A.K. (1977), J. Phys. B 10, 1557.

Bhattacharyya S.S. and Saha S. (1978), J. Chem. Phys. 69, 4292.

- Bomse D.S., Cross J.B. and Valentini J.J. (1983), J. Chem. Phys. 78, 7175.
- Bordenave-Montesquieu A., Gleizes A., Benoitt-Cattin P. and Boudjema M. (1980), J. Phys. E 13, 209.
- Borkenhagen U., Malthan H. and Toennies J.P. (1976), Chem. Phys. Letts. 41, 222.
- Borkenhagen U., Malthan H. and Toennies J.P. (1979), J. Chem. Phys. 71, 1722.
- Bottger G.L. and Eggers D.F. (1964), J. Chem. Phys. 40, 2010.
- Boughton C.V., Miller R.E. and Watts R.O. (1982), Aust. J. Phys. 35, 611.
- Boughton C.V., Miller R.E. and Watts R.O. (1985), Mol. Phys. 56, 363.
- Boughton C.V. (1986), PhD Thesis, Australian National University.
- Boughton C.V., Miller R.E., Vohralik P.F. and Watts R.O. (1986), "The Helium-Hydrogen Fluoride Differential Scattering Cross Section", accepted for publication in Mol. Phys.
- Brinza D.E., Swartz B.A., Western C.M. and Janda K.C. (1983), J. Chem. Phys. 79, 1451.
- Brinza D.E., Western C.M., Evard D.D., Thommen F., Swartz B.A. and Janda K.C. (1984), J. Chem. Phys. 88, 2004.
- Brunner T.A. and Pritchard D. (1982), Adv. Chem. Phys. 50, 589.
- Buck U. and Pauly H. (1969), J. Chem. Phys. 51, 1662.
- Buck U. (1971), J. Chem. Phys. 54, 1923.
- Buck U. and Pauly H. (1971), J. Chem. Phys. 54, 1929.
- Buck U., Kick M. Pauly H. (1972), J. Chem. Phys. 56, 3391.
- Buck U., Hoppe H.O., Huisken F. and Pauly H. (1974), J. Chem. Phys. 60, 4925.
- Buck U. and McGuire P. (1976), Chem. Phys. 16, 101.
- Buck U., Huisken F., Schleusener J. and Schafer J. (1980), J. Chem. Phys.

72, 1512.

Buck U., Huisken F., Schleusener J. and Schafer J. (1981), J. Chem. Phys.

74, 535.

Buck U. and Schleusener J. (1981), J. Chem. Phys. 75, 2470.

Buck U. (1982), Faraday Discuss. Chem. Soc. 73, 187.

Buck U., Huisken F., Kolhase A., Otten D. and Schafer J. (1983a), J. Chem.

Phys. 78, 4439.

Buck U., Huisken F., Maneke G. and Schafer J. (1983b), J. Chem. Phys.

78, 4430.

Buck U. and Meyer H. (1984), Phys. Rev. Letts. 52, 109.

Buck U., Meyer H. and LeRoy R.J. (1984), J. Chem. Phys. 80, 5589.

Bullman S.J. and Dagdigian P.J. (1984), J. Chem. Phys. 81, 3347.

Casassa M.P., Bomse D.S. and Janda K.C. (1981), J. Chem. Phys. 74, 5044.

Casassa M.P., Celii F.G. and Janda K.C. (1982), J. Chem. Phys. 76, 5295.

Casassa M.P., Western C.M., Celii F.G., Brinza D.E. and Janda K.C. (1983),

J. Chem. Phys. 79, 3227.

Casassa M.P., Western C.M. and Janda K.C. (1984), in Truhlar (1984),

page 305.

Cavallini M., Gallinaro G. and Scoles G. (1967), Z. Naturforsch. A 22, 413.

Cavallini M., Dondi M.G., Scoles G. and Valbusa U. (1971a),

Entropie 42, 136.

Cavallini M., Meneghetti L., Scoles G. and Yealland M. (1971b),

Rev. Sci. Instr. 42, 1759.

Child M.S. (1974), Molecular Collision Theory, Academic Press, London.

Clifford A.A. and Dickinson E. (1976), J. Chem. Phys. 64, 3703.

Cohen J.B. and Wilson E.B. (1973a), J. Chem. Phys. 58, 442.

Cohen J.B. and Wilson E.B. (1973b), J. Chem. Phys. 58, 456.

- Collins L.A. and Lane N.F. (1975), Phys. Rev. A 12, 811.
- Collins L.A. and Lane N.F. (1976), Phys. Rev. A 14, 1358.
- Copeland R.A., Pearson D.J. and Crim F.F. (1981), Chem. Phys. Letts. 81,
541.
- Copeland R.A. and Crim F.F. (1983), J. Chem. Phys. 78, 5551.
- Copeland R.A. and Crim F.F. (1984), J. Chem. Phys. 81, 5819.
- Cousins B.L., O'Brian S. and Lisy J.M. (1984), J. Phys. Chem. 88, 5142.
- Cross R.J. Jr. and Gordon R.G. (1966), J. Chem. Phys. 45, 3571.
- Cross R.J. Jr., Gislason E.A. and Herschbach D.R. (1966), J. Chem. Phys.
45, 3582.
- DeLeon R.L. and Muentner J.S. (1984), J. Chem. Phys. 80, 6092.
- DePristo A.E. and Alexander M.H. (1977), J. Chem. Phys. 66, 1334.
- DePristo A.E. and Rabitz H. (1980), J. Chem. Phys. 72, 4685.
- DePristo A.E. (1981), J. Chem. Phys. 74, 5037.
- Dagdigian P.J., Wilcomb B.E. and Alexander M.H. (1979), J. Chem. Phys. 71,
1670.
- Dagdigian P.J. and Alexander M.H. (1980), J. Chem. Phys. 72, 6513.
- Ding A.M.G. and Polanyi J.C. (1975), Chem. Phys. 10, 39.
- Dixon T.A., Joyner C.H., Baiocchi F.A. and Klemperer W. (1981), J. Chem.
Phys. 74, 6539.
- Douketis C., Hutson J.M., Orr B.J. and Scoles G. (1984), Molec. Phys. 52,
763.
- Edmonds A.R. (1974), Angular Momentum in Quantum Mechanics, Princeton
University Press, Princeton, New Jersey.
- Ellenbroek T., Toennies J.P. and Wilde M. (1981), J. Chem. Phys. 75, 3414.
- Engelhardt R., Lorenz Th., Bergmann K., Mietzner Th. and Palczewski A.
(1985), Chem. Phys. 95, 417.

- Esche B.A., Kutina R.E., Lang N.C., Polanyi J.C. and Rulis A.M. (1979),
Chem. Phys. 41, 183.
- Ewing G.E. (1979a), J. Chem. Phys. 71, 3143.
- Ewing G.E. (1979b), J. Chem. Phys. 72, 2096.
- Ewing G.E. (1982), Faraday Discuss. Chem. Soc. 73, 325.
- Farina J.E.G. (1973), Quantum Theory of Scattering Processes, Pergamon
Press, Oxford.
- Farrer J.M. and Lee Y.T. (1974), Chem. Phys. Letts. 26, 428.
- Faubel M. and Toennies J.P. (1978), Adv. At. Mol. Phys. 13, 229.
- Faubel M., Kohl K.H and Toennies J.P. (1980), J. Chem. Phys. 73, 2506.
- Faubel M., Kohl K.H., Toennies J.P. and Gianturco F.A. (1983), J. Chem.
Phys. 78, 5629.
- Faubel M. (1983), Adv. Atom. Molec. Phys. 19, 345.
- Faubel M., Frick J., Kraft G. and Toennies J.P. (1985), Chem. Phys. Letts.
116, 12.
- Fischer G., Miller R.E. and Watts R.O. (1983), Chem. Phys. 80, 147.
- Fischer G., Miller R.E. and Watts R.O. (1984), J. Phys. Chem. 88, 1120.
- Fischer G, Miller R.E., Vohralik P.F. and Watts R.O. (1985), J. Chem. Phys.
83, 1471.
- Fitz D.E. (1978), Chem. Phys. Letts. 55, 202.
- Fitz D.E., Khare V. and Kouri D.J. (1980), J. Chem. Phys. 73, 4147.
- Fitz D.E., Khare V. and Kouri D.J. (1981), Chem. Phys. 56, 267.
- Fiutak J. and van Kranendonk J. (1962), Can. J. Phys. 40, 1085.
- Fluendy M.A.D. and Lawley K.P. (1973), Chemical Applications of Molecular
Beam Scattering, Chapman and Hall, London.
- Frick J. (1984), "Rotationsinelastische Streuung von He-Atomen an HF-, HCl-,
CH₄-, SF₆-, C₂H₆-, und C₂F₆-Molekülen", PhD Thesis, Max-Planck-Institut

für Strömungsforschung, Göttingen.

- Gentry W.R. and Giese C.F. (1977), J. Chem. Phys. 67, 5389.
- Gentry W.R. (1984), in Truhlar (1984), page 289.
- Gianturco F.A., Lamanna U.T. and Petrella G. (1983), Chem. Phys. 78, 81.
- Gianturco F.A., Lamanna U.T. and Petrella G. (1984), Nuovo Cimento 3, 561.
- Gianturco F.A. and Palma A. (1985), J. Chem. Phys. 83, 1049.
- Gibson L.L. and Schatz G.C. (1985), J. Chem. Phys. 83, 3433.
- Goldflam R., Green S. and Kouri D.J. (1977a), J. Chem. Phys. 67, 225.
- Goldflam R., Green S. and Kouri D.J. (1977b), J. Chem. Phys. 67, 4149.
- Goldflam R. and Kouri D.J. (1977), J. Chem. Phys. 66, 542.
- Goldflam R., Kouri D.J. and Green S. (1977c), J. Chem. Phys. 67, 5661.
- Gough T.E., Miller R.E. and Scoles G. (1977), Appl. Phys. Letts. 30, 338.
- Gough T.E., Miller R.E. and Scoles G. (1978), J. Chem. Phys. 69, 1588.
- Gough T.E., Miller R.E. and Scoles G. (1981), J. Phys. Chem. 85, 4041.
- Gough T.E. and Miller R.E. (1983), J. Chem. Phys. 78, 4486.
- Grey C.G. and van Kranendonk J. (1966), Can. J. Phys. 44, 433.
- Gutowsky H.S., Chuang C., Keen J.D., Klots T.D. and Emilsson T. (1985),
J. Chem. Phys. 83, 2070.
- Halberstadt N., Brechignac Ph., Beswick J.A. and Shapiro M. (1986),
J. Chem. Phys. 84, 170.
- Harris S.J., Novik S.E. and Klemperer W. (1974), J. Chem. Phys. 60, 3208.
- Hayman G.D., Hodge J., Howard B.J., Muenter J.S. and Dyke T.R. (1985),
Chem. Phys. Letts. 118, 12.
- Haynam C.A., Brumbaugh D.V. and Levy D.H. (1983), J. Chem. Phys. 79, 1581.
- Helbing R.K.B. (1968), J. Chem. Phys. 48, 1.
- Held W.D., Piper E., Ringer G. and Toennies J.P. (1980). Chem. Phys. Letts.
75, 260.

- Hepburn J.W. and Le Roy R. (1978), Chem. Phys. Letts. 57, 304.
- Hinchen J.J. (1975), Appl. Phys. Letts. 27, 672.
- Hinchen J.J. and Hobbs R.H. (1976), J. Chem. Phys. 65, 2732.
- Hinchen J.J. and Hobbs R.H. (1979), J. Appl. Phys. 50, 628.
- Hoffbauer M.A., Burdinski S., Giese C.F. and Gentry W.R. (1983a), J. Chem. Phys. 78, 3832.
- Hoffbauer M.A., Giese C.F. and Gentry W.R. (1983b), J. Chem. Phys. 79, 192.
- Hoffbauer M.A., Liu K., Giese C.F. and Gentry W.R. (1983c), J. Phys. Chem. 87, 2096.
- Hoffbauer M.A., Liu K., Giese C.F. and Gentry W.R. (1983d), J. Chem. Phys. 78, 5567.
- Hoffbauer M.A., Giese C.F. and Gentry W.R. (1984), J. Phys. Chem. 88, 181.
- Holmgren S.L., Waldman M. and Klemperer W. (1978), J. Chem. Phys. 69, 1661.
- Huffaker J.N. (1977), J. Molec. Spectrosc. 65, 1.
- Huisken F., Meyer H., Lauenstein C., Sroka R. and Buck U. (1986), 1042.
- Hutson J.M. and Howard B.J. (1980), Molec. Phys. 41, 1123.
- Hutson J.M. and Howard B.J. (1981), Molec. Phys. 43, 493.
- Hutson J.M. and Howard B.J. (1982a), Molec. Phys. 45, 769.
- Hutson J.M. and Howard B.J. (1982b), Molec. Phys. 45, 791.
- Hutson J.M. and LeRoy R.J. (1983), J. Chem. Phys. 78, 4040.
- Hutson J.M., Ashton C.J. and LeRoy R.J. (1983), J. Phys. Chem. 87, 2713.
- Janda K.C. (1985), Adv. Chem. Phys. 60, 201.
- Johnson B.R. (1973), J. Comp. Phys. 13, 445.
- Johnson B.R. (1977), J. Chem. Phys. 67, 4086.
- Jones R.C. (1953), J. Opt. Soc. America 43, 1.
- Kantrowitz A. and Grey J. (1951), Rev. Sci. Instr. 22, 328.
- Kasper J.V.V., Pollock C.R., Curl R.F. Jr. and Tittel F.K. (1982), Appl.

Optics 21, 236.

Keenan M.R., Buxton L.W., Campbell E.J., Legon A.C. and Flygare W.H.

(1981), J. Chem. Phys. 74, 2133.

Khare V. (1977), J. Chem. Phys. 67, 3897.

Khare V., Kouri D.J. and Pack R.T. (1978), J. Chem. Phys. 69, 4419.

Khare V. and Kouri D.J. (1978), J. Chem. Phys. 69, 4916.

Khare V. and Kouri D.J. (1980a), J. Chem. Phys. 72, 2007.

Khare V. and Kouri D.J. (1980b), J. Chem. Phys. 72, 2017.

Khare V., Fitz D.E. and Kouri D.J. (1980), J. Chem. Phys. 73, 2802.

Khare V., Kouri D.J., Hoffman D.K. (1981), J. Chem. Phys. 74, 2275.

Kidd I.F. and Balint-Kurti G.G. (1985), J. Chem. Phys. 82, 93.

Kistiakowsky G.B. and Slichter W.P. (1951), Rev. Sci. Instr. 22, 333.

Kouri D.J. (1974), Chem. Phys. Letts 31, 599.

Kouri D.J. (1975), Chem. Phys. Letts. 31, 599.

Kouri D.J. and Shimoni Y. (1976), J. Chem. Phys. 65, 5021.

Kouri D.J., Heil T.G. and Shimoni Y. (1976a), J. Chem. Phys. 65, 226.

Kouri D.J., Heil T.G. and Shimoni Y. (1976b), J. Chem. Phys. 65, 1462.

Kouri D.J. and Shimoni Y. (1977), J. Chem. Phys. 67, 86.

Kyrö E.K., Shoja-Chagervand P., McMillan K., Eliades M., Danzeiser D. and
Bevan J.W. (1983), J. Chem. Phys. 79, 78.

LeRoy R.J., Corey C.C. and Hutson J.M. (1982), Faraday Discuss. Chem. Soc.
73, 339.

LeRoy R.J. (1984), in Truhlar (1984), page 231.

Law K.S. and Bernstein R.B. (1985), J. Chem. Phys. 82, 2856.

Lees R.M. (1978), J. Mol. Spectroscopy 69, 225.

Legon A.C. and Millen D.J. (1982), Faraday Discuss. Chem. Soc. 73, 71.

Legon A.C. (1983), J. Phys. Chem. 87, 2064.

- Levy D.H. (1981), Adv. Chem. Phys. 47, 323.
- Linse C.A., van den Biesen J.J.H, van Veen E.H. and van den Meijdenberg C.J.N. (1979a) Physica A 99, 166.
- Linse C.A., van den Biesen J.J.H, van Veen E.H., van den Meijdenberg C.J.N. and Beenakker J.J.M. (1979b), Physica A 99, 145.
- Liu W., Kolenbrander K. and Lisy J.M. (1984), Chem. Phys. Letts. 112, 585.
- Loesch H.J. (1980), Adv. Chem. Phys. 42, 421.
- McCourt F.R., Fuchs R.R and Thakkar A.J. (1984), J. Chem. Phys. 80, 5561.
- McFarlane S.C. and Richards D. (1981), J. Phys. B 14, 3423.
- McGuire P. (1973), Chem. Phys. Letts. 23, 575.
- McGuire P. and Kouri D.J. (1974), J. Chem. Phys. 60, 2488.
- McGuire P. (1975), J. Chem. Phys. 62, 525.
- McKeller A.R.W. (1982), Faraday Discuss. Chem. Soc. 73, 89.
- Maroncelli M., Hopkins G.A., Nibler J.W. and Dyke T.R. (1985), J. Chem. Phys. 83, 2129.
- Mason E.A. and Monchick L. (1962), J. Chem. Phys. 36, 1622.
- Miller R.E. (1980), "Infrared Laser Spectroscopy of Molecular Beams", PhD Thesis, University of Waterloo, Canada.
- Miller R.E. (1982), Rev. Sci. Instr. 53, 1719.
- Miller R.E., Vohralik P.F. and Watts R.O. (1984a), J. Chem. Phys. 80, 5453.
- Miller R.E. and Watts R.O. (1984), Chem. Phys. Letts. 105, 409.
- Miller R.E., Watts R.O. and Ding A. (1984b), Chem. Phys. 83, 155.
- Mitchell A., McAuliffe M.J., Giese C.F. and Gentry W R. (1985), J. Chem. Phys. 83, 4271.
- Mollenauer L.F. (1985), the copy of a manuscript entitled "Colour Centre Lasers" was made available to us by the author prior to publication.
- Morse F.A., Bernstein R.B. and Hostettler H.U. (1962), J. Chem. Phys. 36,

1947.

- Morse F.A. and Bernstein R.B. (1962), J. Chem. Phys. 37, 2019.
- Mulder F., Thomas G.F. and Meath W.J. (1980), Mol. Phys. 41, 249.
- Mullaney N.A. and Truhlar D.G. (1979), Chem. Phys. 39, 91.
- Munn R.J., Mason E.A. and Smith F.J. (1964), J. Chem. Phys. 41, 3978.
- Nyeland C., Mason E.A. and Monchick L. (1972), J. Chem. Phys. 56, 6180.
- O'Loughlin M.J., Reid B.P. and Sparks R.K. (1985), J. Chem. Phys. 83, 5647.
- Ohashi N. and Pine A.S. (1984), J. Chem. Phys. 81, 73.
- Oka T. (1966), J. Chem. Phys. 45, 754.
- Orr B.J., Haub J.G. and Haines R. (1984), Chem. Phys. Letts. 107, 168.
- Pack R.T. (1973), J. Chem. Phys. 60, 633.
- Pack R.T. (1978), Chem. Phys. Letts. 55, 197.
- Pack R.T. (1978), Chem. Phys. Letts. 55, 197.
- Pack R.T., Valentini J.J., Becker C.H., Buss R.J. and Lee Y.T. (1982a),
J. Chem. Phys. 77, 5475.
- Pack R.T., Valentini J.J. and Cross J.B. (1982b), J. Chem. Phys. 77, 5486.
- Pack R.T. (1984), J. Chem. Phys. 81, 1841.
- Pack R.T., Piper E., Pfeffer G.A. and Toennies J.P. (1984), J. Chem. Phys.
80, 4940.
- Page R.H., Frey J. G., Shen Y.R. and Lee Y.T. (1984), Chem. Phys. Letts.
106, 373.
- Parker G.A. and Pack R.T. (1978), J. Chem. Phys. 68, 1585.
- Parker G.A., Schmaltz T.G. and Light J.C. (1979), National Resource for
Computation in Chemistry, Proceedings No. 5, Volumes I and II.
- Parker G.A., Light J.C. and Johnson B.R. (1980a), Chem. Phys. Letts. 73,
572.
- Parker G.A., Schmulz T.G. and Light J.C. (1980b), J. Chem. Phys. 73, 1757.

- Parker G.A., Keil M. and Kuppermann A. (1983), *J. Chem. Phys.* 78, 1145.
- Pauly J.P. and Toennies J.P. (1968), Methods of Experimental Physics B, volume 7A, page 227. Academic Press, New York.
- Pendley R.D. and Ewing G.E. (1983), *J. Chem. Phys.* 78, 3531.
- Pine A.S. and Lafferty W.J. (1983), *J. Chem. Phys.* 78, 2154.
- Pine A.S., Lafferty W.J. and Howard B.J. (1984), *J. Chem. Phys.* 81, 2939.
- Polanyi J.C. and Woodall K.B (1972), *J. Chem. Phys.* 56, 1563.
- Pritchard D.E., Smith N., Driver R.D. and Brunner T.A. (1979), *J. Chem. Phys.* 70, 2115.
- Procaccia I. and Levine R.D. (1976), *Phys. Rev. A* 14, 1569.
- Raimondi M. (1984), *Molec. Phys.* 53, 161.
- Reid B.P., O'Loughlin M.J. and Sparks R.K. (1985), *J. Chem. Phys.* 83, 5656.
- Rodwell W.R., Sin Fai Lam L.T. and Watts R.O. (1981), *Molec. Phys.* 44, 225.
- Sakai K., Koide A. and Kihara T. (1977), *Chem. Phys. Letts.* 47, 416.
- Schinke R., Müller W. and Meyer W. (1982), *J. Chem. Phys.* 76, 895.
- Schinke R. and Bowman J.M. (1983), in Molecular Collision Dynamics, edited by Bowman J.M., Springer-Verlag, Berlin.
- Schumacher H., Bernstein R.B. and Rothe E.W. (1960), *J. Chem. Phys.* 33, 584.
- Secret D. (1975), *J. Chem. Phys.* 62, 710.
- Sentman L.H. (1977), *J. Chem. Phys.* 67, 966.
- Serri J.A., Morales A., Moskowitz W. and Pritchard D.E. (1980), *J. Chem. Phys.* 72, 6304.
- Serri J.A., Becker C.H., Elbel M.B., Kinsey J.L., Moskowitz W.P. and Pritchard D.E. (1981), *J. Chem. Phys.* 74, 5116.
- Shimanouchi T. (1972), Tables of Molecular Vibrational Frequencies., Vol.I, National Bureau of Standards, Washington.

- Shimoni Y. and Kouri D.J. (1976a), J. Chem. Phys. 65, 3958.
- Shimoni Y. and Kouri D.J. (1976b), J. Chem. Phys. 65, 3372.
- Shimoni Y. and Kouri D.J. (1977a), J. Chem. Phys. 66, 675.
- Shimoni Y. and Kouri D.J. (1977b), J. Chem. Phys. 66, 2841.
- Smalley R.E., Wharton L., Levy D.H. and Chandler D.W. (1978), J. Chem. Phys. 68, 2487.
- Smith F.J. and Munn R.J. (1964), J. Chem. Phys. 41, 3560.
- Smith F.J. (1964), Physica 30, 497.
- Smith K.M., Rulis A.M., Scoles G., Aziz R.A. and Nain V. (1977), J. Chem. Phys. 67, 152.
- Takayanagi K. and Wada T. (1985), J. Phys. Soc. Japan 54, 2122.
- Tennyson J. and Sutcliffe B.T. (1983), J. Chem. Phys. 79, 43.
- Thomas L.D., Johnson B.R., Lester W.A. Jr., Light J.C., McLenithan K.D., Parker G.A., Redmon M.J., Schmalz T.G., Secrest D. and Walker R.B. (1981), J. Comp. Phys. 41, 407.
- Thuis H., Stolte S. and Reuss J. (1979), Comments Atom. Molec. Phys. 8, 123.
- Thuis H.H.W., Stolte S., Reuss J, van den Biesen J.J.H and van den Meijdenberg C.J.N. (1980), Chem. Phys. 52, 211.
- Toennies J.P. (1962), Faraday Discuss. 33, 96.
- Toennies J.P. (1965), Z. Physik 182, 257.
- Toennies J.P. and Winkelmann K. (1977), J. Chem. Phys. 66, 3965.
- Travis D.N., McGurk J.C., McKeown D. and Denning R.G. (1977), Chem. Phys. Letts. 45, 287.
- Truhlar D.G. (1984), Resonances: In Electron Molecule Scattering, van der Waals Complexes and Reactive Chemical Dynamics, edited by D.G. Truhlar, American Chemical Society, Washington.

- van den Biesen J.J.H., Stokvis F.A., van Veen E.H. and van den Meijdenberg (1980), *Physica A* 100, 375.
- van den Biesen J.J.H., Hermans R.M. and van den Meijdenberg C.J.N. (1982a), *Physica A* 115, 396.
- van den Biesen J.J.H. and van den Meijdenberg C.J.N (1982b), *Physica A* 115, 375.
- van Kranendonk J. (1963), *Can. J. Phys.* 41, 433.
- Vernon M.F., Krajnovich D.J., Kwok H.S., Lisy J.M., Shen Y.R. and Lee Y.T. (1982a), *J. Chem. Phys.* 77, 47.
- Vernon M.F., Lisy J.M., Krajnovich D.J., Tramer A., Kwok H. and Lee Y.T. (1982b), *Faraday Discuss. Chem. Soc.* 73, 387.
- Vohralik P.F. and Miller R.E. (1985), *J. Chem. Phys.* 83, 1609.
- Watts R.O. and McGee I.J. (1976), Liquid State Chemical Physics, John Wiley and Sons, New York.
- Western C.M., Casassa M.P. and Janda K.C. (1984), *J. Chem. Phys.* 80, 4781.
- Wilcomb B.E. and Dagdigian P.J. (1977), *J. Chem. Phys.* 67, 3829.
- Wilkins R.L. and Kwok M.A. (1983), *J. Chem. Phys.* 78, 7153.
- Williams J.R., and Kukolich S.G. (1979), *Chem. Phys.* 36, 201.

"Hurry along there Alice,

we haven't got all day you know..."